

Washington University in St. Louis

## Washington University Open Scholarship

---

Arts & Sciences Electronic Theses and  
Dissertations

Arts & Sciences

---

4-3-2024

### Likelihood Ratio Test for Markov Switching Parameters

Li Zhang

*Washington University in St. Louis*

Follow this and additional works at: [https://openscholarship.wustl.edu/art\\_sci\\_etds](https://openscholarship.wustl.edu/art_sci_etds)

---

#### Recommended Citation

Zhang, Li, "Likelihood Ratio Test for Markov Switching Parameters" (2024). *Arts & Sciences Electronic Theses and Dissertations*. 3079.

[https://openscholarship.wustl.edu/art\\_sci\\_etds/3079](https://openscholarship.wustl.edu/art_sci_etds/3079)

This Dissertation is brought to you for free and open access by the Arts & Sciences at Washington University Open Scholarship. It has been accepted for inclusion in Arts & Sciences Electronic Theses and Dissertations by an authorized administrator of Washington University Open Scholarship. For more information, please contact [digital@wumail.wustl.edu](mailto:digital@wumail.wustl.edu).

WASHINGTON UNIVERSITY IN ST. LOUIS

Department of Chemistry

Dissertation Examination Committee:

Timothy Wencewicz, Chair

Jonathan Barnes

Guy Genin

Courtney Reichhardt

John-Stephen Taylor

Design, Synthesis, Self-Assembly, and Applications of Functional Bottlebrush Architectures  
through Ring-Opening Metathesis Polymerization

by

Yipei Zhang

A dissertation presented to  
Washington University in St. Louis  
in partial fulfillment of the  
requirements for the degree  
of Doctor of Philosophy

May 2024

St. Louis, Missouri

© 2024, Yipei Zhang

# Table of Contents

List of Figures .....	iv
List of Schemes .....	iv
List of Tables .....	xiii
Acknowledgments.....	xiii
Abstract of the Dissertation .....	xvi
Chapter 1: Introduction.....	1
1.1 Shear-Thinning Hydrogels .....	1
1.1.1 General Overview of Shear-Thinning Hydrogels .....	1
1.1.2 Host-Guest-based Shear-Thinning Hydrogels.....	4
1.2 Cyclodextrin Molecular Recognition.....	9
1.2.1 Cyclodextrin-based Inclusion Complexes .....	9
1.2.2 Cyclodextrin-based Supramolecular Materials and Applications .....	13
1.3 Common Controlled Polymerization Methods for Cyclodextrin-based Polymers .....	17
1.3.1 Cyclodextrin-based Polymers through ATRP .....	17
1.3.2 Cyclodextrin-based Polymers through RAFT .....	21
1.3.3 Cyclodextrin-based Polymers through ROMP.....	23
1.4 References .....	26
Chapter 2: Saltwater-Induced Rapid Gelation of Photoredox-Responsive Mucomimetic Hydrogels .....	31
2.1 Abstract .....	32
2.2 Introduction.....	32
2.3 Results and Discussion .....	37
2.3.1 Molecular Design of Photoredox-Responsive Viscous Hydrogels .....	37
2.3.2 Saltwater-Induced Mechanism of Gelation.....	40
2.3.3 Modulating Rheological Properties as a Function of Host-Guest Crosslinking and Water Content .....	44
2.3.4 Versatile Adhesive Properties of the Viscous Hydrogels .....	49
2.3.5 Photoredox-based Control Over the Mechanical Properties Using Visible Light.....	54
2.4 Materials and Methods .....	58
2.4.1 Experimental Methods .....	58
2.4.2 Synthetic Methods .....	61
2.4.3 Spectroscopic Characterization of Novel Compounds .....	92
2.4.4 Evaluation of Hydrogel Properties.....	105

2.5 Conclusions.....	122
2.6 References.....	124
Chapter 3: Mitigating <i>Pseudomonas aeruginosa</i> Biofilm Formation Using Self-Assembled Bactericidal Polymer Coatings .....	128
3.1 Abstract.....	129
3.2 Introduction.....	129
3.3 Results and Discussion .....	132
3.3.1 Self-Assembled Polymer Film Design, Preparation, and Properties.....	132
3.3.2 Flow Cell Experiments.....	135
3.3.3 Static Growth Experiments .....	138
3.3.4 Antibiotic Release Experiments .....	141
3.4 Materials and Methods .....	143
3.4.1 Experimental Methods.....	143
3.4.2 Synthetic Methods .....	145
3.4.3 Spectroscopy Characterization .....	150
3.4.4 Polymer Film Preparation and Evaluation of Properties .....	152
3.4.5 Biological Experiments .....	156
3.5 Conclusions.....	171
3.6 References.....	172
Chapter 4: Innovative Drug Delivery Strategies to Treat Pediatric Kidney Disease.....	175
4.1 Abstract.....	175
4.2 Introduction.....	176
4.3 Results and Discussion .....	178
4.3.1 Design, Synthesis, and Characterization of Biotinylated Diblock Copolymer.....	178
4.3.2 Characterization of mini-Agrin mSA.....	183
4.4 Materials and Methods .....	184
4.4.1 Experimental Methods.....	184
4.4.2 Synthetic Methods .....	185
4.5 Conclusions.....	190
4.6 References.....	191
Chapter 5: Summary, Future Directions, and Final Thoughts .....	193
5.1 Dissertation Summary .....	193
5.2 Future Directions .....	195
5.3 References.....	198
Appendix: NMR Spectra of Compound.....	199

# List of Figures

<b>Figure 1.1.</b> (a) Static polymer chains with covalently cross-linked networks. (b) Dynamic polymer chains with flexible, dynamic networks. Reused with permission. <sup>2</sup> .....	1
<b>Figure 1.2.</b> Illustration of a sample placed between the parallel plates with an oscillatory torsional shear applied. Reused with permission. <sup>4</sup> .....	2
<b>Figure 1.3.</b> Shear-thinning and self-healing hydrogels rely on dynamic and reversible interactions between polymers and polypeptides. Reused with permission. <sup>3</sup> .....	3
<b>Figure 1.4.</b> Fabrication of supramolecular host-guest polymer network. Reused with permission. <sup>16</sup> .....	4
<b>Figure 1.5.</b> Molecular structures of the four types of supramolecular macrocycles: (a) CDs, $n = 1-3$ ; (b) calix[n]arenes, $n = 1-3$ ; (c) CB[n]s, $n = 5-8, 10, 13-15$ ; (d) pillar[n]arenes, $n = 1-11$ ; and their cartoon depictions. Reused with permission. <sup>18</sup> .....	5
<b>Figure 1.6.</b> (a) Schematic of guest-host material synthesis through modification of hyaluronic acid with either adamantane (Ad-HA) or $\beta$ -cyclodextrin (CD-HA). (b) Graphic showing guest-host assembly of adamantane and $\beta$ -cyclodextrin groups and shear-thinning. Reused with permission. <sup>19</sup> .....	6
<b>Figure 1.7.</b> Hydrogel loading onto the rheometer stage. (a) When lowering the geometry onto the hydrogel, spin the geometry slightly for more even hydrogel loading. (b) Over-filling and under-filling of the sample results in increased and decreased forces, respectively. The hydrogel sample must fill the space between the geometry and the rheometer stage correctly for accurate measurements. Reused with permission. <sup>19</sup> .....	7
<b>Figure 1.8.</b> Results of (a) frequency sweep, (b) strain sweep, (c) continuous flow, and (d) cyclic strain time sweep rheology experiments for hydrogels of 5 and 7.5 wt % material concentration, using the described method and rheological parameters. For cyclic strain, shaded regions are high strain (500%) and unshaded regions are low strain (0.2%). Reused with permission. <sup>19</sup> .....	8
<b>Figure 1.9.</b> Chemical structures, approximate geometric, dimensions, and physical properties of $\alpha$ -, $\beta$ -, and $\gamma$ -CD. Reused with permission. <sup>21</sup> .....	9
<b>Figure 1.10.</b> $\beta$ -CD structures, $\beta$ -CD-based host/guest pairs, and their associated response to external fields: (a) Structures of common CD building blocks (azide, thiol, and amine), (b) thermoresponsive adamantyl complex, (c) redox-responsive ferrocene complex, (d) color-changing phenolphthalein complex, (e) metal-ion-responsive bipyridine complex, (f) pH-responsive benzimidazole complexes, and g) light-responsive azobenzene complexes. Reused with permission. <sup>22</sup> .....	11
<b>Figure 1.11.</b> Schematic illustration of the association of free cyclodextrin (CD) and drug to form drug-CD complexes. Reused with permission. <sup>32</sup> .....	12
<b>Figure 1.12.</b> Formation of poly(pseudo)rotaxane hydrogels from $\alpha$ -CD and high molecular weight PEG. Reused with permission. <sup>33</sup> .....	13
<b>Figure 1.13.</b> Self-healing experiments. Reused with permission. <sup>39</sup> .....	14
<b>Figure 1.14.</b> (a) Schematic representation of the formation of MD- $\beta$ CD gels. (b) Photographs of the formation of a MD- $\beta$ CD gel. Reused with permission. <sup>42</sup> .....	15
<b>Figure 1.15.</b> Conceptual illustrations for selectivity switching of Py gel as a function of $x_{\text{DMSO}}$ . Reused with permission. <sup>43</sup> .....	16

<b>Figure 1.16.</b> Mechanism of ATRP. Reused with permission. <sup>45</sup> .....	18
<b>Figure 1.17.</b> Synthetic route for $\beta$ -CD-PDMAEMA. Reused with permission. <sup>46</sup> .....	18
<b>Figure 1.18.</b> Synthesis of 21Br-CD. Reused with permission.....	19
<b>Figure 1.19.</b> Synthesis of mono-methyl methacrylate substituted cyclodextrin (MCD) and atom transfer radical polymerization of MCD from PEG–Br initiator. Reused with permission. <sup>50</sup> .....	20
<b>Figure 1.20.</b> Mechanism of RAFT. Reused with permission. <sup>45</sup> .....	21
<b>Figure 1.21.</b> Introduction of CD end group with CTA agent. Reused with permission. <sup>53</sup> .....	22
<b>Figure 1.22.</b> In a CD-RAFT agent, CD can be either part of the Z or the R group. Reused with permission. <sup>53</sup> .....	22
<b>Figure 1.23.</b> General mechanism of ROMP. Reused with permission. <sup>57</sup> .....	23
<b>Figure 1.24.</b> Grubbs' catalysts. Reused with permission. <sup>58</sup> .....	24
<b>Figure 1.25.</b> (a) Chemical structures and corresponding cartoon representations of $\gamma$ -CD-Nb <sub>8</sub> , Nb-HEG, and Nb-PEG. (b) Core-first/graft-from synthetic strategy for DBASCs (CD-(HEG <sub>m</sub> -PEG <sub>n</sub> ) <sub>8</sub> ). Reused with permission. <sup>59</sup> .....	25
<b>Figure 1.26.</b> Synthetic routes of norbornene functionalized monomers and polymers through ROMP. Reused with permission. <sup>60</sup> .....	26
<b>Figure 2.1.</b> Self-assembly of natural and synthetic hydrogels comprising bottlebrush polymers. (a) Graphical representation of mucin proteins cross-linked by disulfide linkages (yellow). Oligosaccharide side chains (green) appended to the polypeptide backbone (blue) give a bottlebrush-like architecture, which aids hydrogel network formation. (b) Example of dynamic host–guest molecular recognition between $\beta$ -cyclodextrin ( $\beta$ -CD, host; yellow) and adamantane (Ad, guest; black). In H <sub>2</sub> O, the equilibrium affinity constant ( $K_a$ ) is on the order of 10 <sup>4–5</sup> M <sup>-1</sup> . (c) This work: Ring-opening metathesis polymerization (ROMP) of norbornene-based functional monomers in DMF yielded a set of bottlebrush supramolecular copolymers that, after dialysis, self-assembled 1:1 in saltwater (but not deionized H <sub>2</sub> O) to afford a photoresponsive mucomimetic hydrogel with broad adhesive properties. <i>Note:</i> For copolymers <b>A<sub>x</sub>, P<sub>n</sub></b> and <b>B<sub>x</sub></b> , the x and n values are summarized in Table1 with detailed information on monomer units. ....	36
<b>Figure 2.2.</b> Demonstration of saltwater-induced gelation and illustration of copolymer architectures. (a) Comparison of copolymer mixtures <b>A<sub>3</sub>, P<sub>1</sub>+B<sub>3</sub></b> , <b>C<sub>1</sub>, P<sub>1</sub>+B<sub>3</sub></b> , <b>C<sub>2</sub>, P<sub>1</sub>+B<sub>3</sub></b> and <b>D<sub>P1</sub>+B<sub>3</sub></b> which were injected* separately into 10 mL deionized H <sub>2</sub> O and 100×10 <sup>-3</sup> M NaCl solutions at 50 mg·mL <sup>-1</sup> . Screenshots are chosen from timepoints: before injection, during injection, immediately after injection and a while after injection. (b) Cartoon structures of statistical copolymers ( <b>A<sub>3</sub>, P<sub>1</sub></b> ) poly(2V <sup>4+</sup> Ad <sub>30</sub> -TEG <sub>90</sub> -ZnTPP) <sub>stat</sub> , ( <b>B<sub>3</sub></b> ) poly(CD <sub>30</sub> -TEG <sub>90</sub> ) <sub>stat</sub> , ( <b>C<sub>1</sub>, P<sub>1</sub></b> ) poly(HexylAd <sub>30</sub> -TEG <sub>90</sub> -ZnTPP) <sub>stat</sub> , ( <b>C<sub>2</sub>, P<sub>1</sub></b> ) poly(TEGAd <sub>30</sub> -TEG <sub>90</sub> -ZnTPP) <sub>stat</sub> , and ( <b>D<sub>P1</sub></b> ) poly(2V <sup>4+</sup> Me <sub>30</sub> -TEG <sub>90</sub> -ZnTPP) <sub>stat</sub> . * <i>Note:</i> 18 G needle gauge was used for <b>A<sub>3</sub>, P<sub>1</sub>+B<sub>3</sub></b> and <b>D<sub>P1</sub>+B<sub>3</sub></b> , while 16 G needle gauge was used for <b>C<sub>1</sub>, P<sub>1</sub>+B<sub>3</sub></b> and <b>C<sub>2</sub>, P<sub>1</sub>+B<sub>3</sub></b> . Additionally, <b>C<sub>2</sub>, P<sub>1</sub>+B<sub>3</sub></b> were maintained at 4 °C in solution until injected. ....	44
<b>Figure 2.3.</b> Modulating rheological properties. (a) General reaction coordinate diagram showing the different material states (S1-S4): upon mixing (S1), addition to saltwater (S2), and exposure to heat (S3) or light (S4). The cartoon diagram illustrates the mechanism of water loss in response to addition to saltwater and in response to heating or visible-light irradiation. (b) Rheology strain sweep experiments at 25 °C at a frequency of 1 rad·s <sup>-1</sup> . (c) Rheology frequency sweep experiments at 25 °C at 1% strain. The hydrogels were prepared in an aqueous 100×10 <sup>-3</sup> M NaCl solution at a concentration of 50 mg·mL <sup>-1</sup> . All hydrogel samples were tested in triplicate pre- and post-heating*. * <i>Note:</i> Hydrogel samples tested immediately after mixing was labeled as “Pre-heat”.	

Then, each hydrogel sample was heated to 80 °C and held at this temperature for 10 min, followed by cooling the sample back to 25 °C, where it was held for an additional 10 min and tested again. This latter state was labeled as “Post-heat”.....47

**Figure 2.4.** Lap-shear adhesion testing for  $A_{3, P1}+B_3$  hydrogels on different substrates. (a) Pictures of copolymer mixtures applied to different surfaces in aqueous  $100 \times 10^{-3}$  M NaCl solutions. (b) Representative lap-shear adhesion tests of  $A_{3, P1}+B_3$  hydrogels on different surfaces including glass, metal, high density polyethylene (HDPE), and ham after 24 h air dry. *Note:* All samples tested were prepared at a concentration of  $30 \text{ mg} \cdot \text{mL}^{-1}$ .....51

**Figure 2.5.** Photoredox-based control over mechanical properties. (a) Chemical structures of hydrogel network components and corresponding proposed self-assembled structures after reduction of the oligoviologen subunits via the integrated zinc-tetraphenyl porphyrin (**ZnTPP**) photoredox catalyst and sacrificial reductant (**TEOA**, triethanolamine). (b) Images of photoreduction process before and after irradiation, as well as after rheological assessment. (c) Oscillatory shear rheology strain sweep data for three hydrogels ( $50 \text{ mg} \cdot \text{mL}^{-1}$ ) at 25 °C and  $1.0 \text{ rad} \cdot \text{s}^{-1}$ . Hydrogels were tested without light irradiation (gray), 30 min blue light irradiation (light purple), and 60 min blue light irradiation (purple). (d) Oscillatory shear rheology strain sweep data for one hydrogel ( $50 \text{ mg} \cdot \text{mL}^{-1}$ ) at 25 °C and  $1.0 \text{ rad} \cdot \text{s}^{-1}$ . The hydrogel was tested in sequence without light irradiation (gray), then 15 (light purple) and 30 min (purple) blue light irradiation. (e) Experimental setup and illustration of photoreduction process for lap-shear adhesion tests. (f) Lap-shear adhesion stress (kPa) vs extension (mm) for  $A_{3, P1}+B_3$  hydrogels ( $30 \text{ mg} \cdot \text{mL}^{-1}$ ) on glass with 3 h air dry (without light, gray) and 3 h blue light irradiation (purple). *Note:* All hydrogels tested for rheology (c, d) and lap-shear adhesion (f) were prepared in an aqueous  $3 \times 10^{-3}$  M TEOA/ $100 \times 10^{-3}$  M NaCl solution. ....56

**Figure 2.6.**  $^1\text{H}$  NMR (500 MHz, 25 °C,  $(\text{CD}_3)_2\text{SO}$ ) spectra of statistical copolymers  $B_x$ . The red box highlights the comparison of conversion to polymer between different statistical copolymers  $B_x$ .....93

**Figure 2.7.** DOSY NMR ( $\text{D}_2\text{O}$ , 25°C) of statistical copolymer  $A_{3, P1}$ .....94

**Figure 2.8.** DOSY NMR ( $\text{D}_2\text{O}$ , 25°C) of statistical copolymer  $B_3$ .....95

**Figure 2.9.** DOSY NMR ( $\text{D}_2\text{O}$ , 25°C) of copolymer complex  $A_{3, P1}+B_3$ . ....96

**Figure 2.10.** ITC of  $\beta$ -CD and **9** in (a)  $\text{H}_2\text{O}$ , (b) 100 mM NaCl solution.....97

**Figure 2.11.** GPC traces of (a) **19**, **9** and statistical copolymers  $A_{1, P1}$ ,  $A_{2, P1}$ ,  $A_{3, P1}$ ,  $A_{4, P1}$ , and  $A_{5, P1}$  (similar components with different units of monomers incorporated and increasing molecular weight theoretically). (b) **19**, **9** and statistical copolymer  $A_{3, P0}$ ,  $A_{3, P1}$ ,  $A_{3, P2}$ , and  $A_{3, P4}$  (copolymers with similar molecular weight theoretically but with different amounts of porphyrin incorporated per chain).....98

**Figure 2.12.** GPC traces of **19**, **16** and statistical copolymers  $B_1$ ,  $B_2$ ,  $B_3$ ,  $B_4$ , and  $B_5$  (similar components with different units of monomers incorporated and increasing molecular weight theoretically). ....99

**Figure 2.13.** GPC traces of (a) **19** and statistical copolymer  $C_{1, P1}$ . (b) **19**, **11** and statistical copolymer  $D_{P1}$ . (c) **19** and statistical copolymer  $E_{P1}$ . ....99

**Figure 2.14.** Solubility illustration for statistical copolymer  $C_{2, P1}$ . ....100

**Figure 2.15.** GPC traces of statistical copolymers  $C_{1, P1}$  and  $C_{2, P1}$ . ....100

**Figure 2.16.** Plots of dRI vs. Concentration to determine  $dn/dc$  of statistical copolymers (a)  $A_{3, P1}$ , (b)  $B_3$ , (c)  $C_{1, P1}$ , and (d)  $D_{P1}$ . ....101

<b>Figure 2.17.</b> Plot of dRI vs. Concentration to determine dn/dc of statistical copolymer $C_{2, P1}$ .	102
<b>Figure 2.18.</b> UV-vis absorbance of the supernatant at different time points from copolymer mixture (a) $A_{3, P1+B3}$ , (b) $C_{1, P1+B3}$ .	103
<b>Figure 2.19.</b> Comparison of UV-vis absorbance at 430 and 634 nm of the supernatant from copolymer mixture $A_{3, P1+B3}$ and $C_{1, P1+B3}$ at different time points.	104
<b>Figure 2.20.</b> Representative picture of H <sub>2</sub> O droplets on different surfaces: (a) metal, (b) glass, (c) HDPE.	104
<b>Figure 2.21.</b> Representative picture of copolymer $A_{3, P1}$ on different surfaces: (a) metal, (b) glass, (c) HDPE.	105
<b>Figure 2.22.</b> Representative picture of copolymer $B_3$ on different surfaces: (a) metal, (b) glass, (c) HDPE.	105
<b>Figure 2.23.</b> Representative picture of copolymer mixture $A_{3, P1+B3}$ on different surfaces: (a) metal, (b) glass, (c) HDPE.	105
<b>Figure 2.24.</b> Representative picture of copolymer $C_{1, P1}$ on different surfaces: (a) metal, (b) glass, (c) HDPE.	105
<b>Figure 2.25.</b> $A_{3, P1}$ and $B_3$ mixed at 25 mg·mL <sup>-1</sup> in different concentrations of (a) NaCl solutions, (b) LiCl solutions, (c) KCl solutions.	106
<b>Figure 2.26.</b> Oscillatory strain rheology (performed at 1 rad·s <sup>-1</sup> ) data (average) at 50 mg·mL <sup>-1</sup> in 100 mM NaCl at 25 °C for $A_{n, P1+Bn}$ (n=1, 2, 3, 4 and 5) hydrogels. (a) $A_{1, P1+B1}$ , (b) $A_{2, P1+B2}$ , (c) $A_{3, P1+B3}$ , (d) $A_{4, P1+B4}$ , (e) $A_{5, P1+B5}$ . (Note: The reason why hydrogel $A_{5, P1+B5}$ has a big error bar after heating is that polymerization of $B_5$ could not go to full completion and each batch of polymer $B_5$ was not exact same.)	108
<b>Figure 2.27.</b> Oscillatory strain rheology (performed at 1 rad·s <sup>-1</sup> ) data (average) at 50 mg·mL <sup>-1</sup> in 100 mM NaCl at 25 °C for $A_{3, Pn+B3}$ (n=0, 1, 2 and 4) hydrogels. (a) $A_{3, P0+B3}$ , (b) $A_{3, P1+B3}$ , (c) $A_{3, P2+B3}$ , (d) $A_{3, P4+B3}$ .	109
<b>Figure 2.28.</b> Pictures of $C_{1, P1+B3}$ for rheology tests. <b>a)</b> as prepared on stage, <b>b)</b> before the test covering the gap, <b>c)</b> after test.	110
<b>Figure 2.29.</b> Pictures of $C_{2, P1+B3}$ for rheology tests. <b>a)</b> as prepared on stage, <b>b)</b> before the test covering the gap, <b>c)</b> after test.	111
<b>Figure 2.30.</b> Oscillatory strain rheology (performed at 1 rad·s <sup>-1</sup> ) data (average) at 50 mg·mL <sup>-1</sup> in 100 mM NaCl at 25 °C for hydrogels. (a) $A_{3, P1+B3}$ , (b) $C_{1, P1+B3}$ , (c) $C_{2, P1+B3}$ .	111
<b>Figure 2.31.</b> SEM images of $A_{3, P1+B3}$ in H <sub>2</sub> O after air dried overnight. (a) 1000x, (b) 5000x, (c) 10000x, (d) 10000x.	112
<b>Figure 2.32.</b> SEM images of $A_{3, P1+B3}$ hydrogel (fresh) in 100 mM NaCl solution after air dried overnight. Region 1: (a) 1000x, (b) 5000x, (c) 10000x, (d) 10000x.	113
<b>Figure 2.34.</b> SEM images of $A_{3, P1+B3}$ hydrogel (pre-made) in 100 mM NaCl solution after air dried overnight. (a) 1000x, (b) 5000x, (c) 10000x, (d) 10000x.	114
<b>Figure 2.35.</b> Pictures of (a) the dual syringe method and different surfaces investigated with hydrogel materials: (b) glass, (c) steel ruler, (d) HDPE, (e) ham.	115
<b>Figure 2.36.</b> Solubility test of copolymer $A_{3, P1}$ and $C_{1, P1}$ in H <sub>2</sub> O (a) at room temperature, (b) after heating at 80 °C for 10 min, (c) cooled back to room temperature.	116

<b>Figure 2.37.</b> Lap-shear adhesion test on glass: (a) aqueous 100 mM NaCl solution, (b) statistical copolymer $E_{P1}$ in $H_2O$ , (c) statistical copolymer $E_{P1}$ in aqueous 100 mM NaCl solution, and (d) statistical copolymer $F_{P1}$ in $CH_2Cl_2$ .	117
<b>Figure 2.38.</b> Lap-shear adhesion test on glass: (a) $A_{3, P1}+B_3$ hydrogels in aqueous 100 mM NaCl solution, (b) $A_{3, P1}+B_3$ copolymer mixture in 90% $CH_3OH$ and 10% $H_2O$ , and (c) $A_{3, P1}+B_3$ hydrogels in 100 mM NaCl in 90% $CH_3OH$ and 10% $H_2O$ , (d) three replicates of $A_{3, P1}+B_3$ hydrogels in aqueous 100 mM NaCl solution with curing protocol 1.	118
<b>Figure 2.39.</b> Lap-shear adhesion test on glass: (a) $C_{1, P1}+B_3$ emulsion in $H_2O$ , (b) $C_{1, P1}+B_3$ emulsion in aqueous 100 mM NaCl solution.	118
<b>Figure 2.40.</b> Lap-shear adhesion test of $A_{3, P1}+B_3$ hydrogels in aqueous 100 mM NaCl solution on metal: (a) pneumatic grips, and (b) wedge grips.	119
<b>Figure 2.41.</b> Lap-shear adhesion test of $A_{3, P1}+B_3$ hydrogels in 100 mM NaCl in 90% $CH_3OH$ and 10% $H_2O$ on metal: (a) pneumatic grips, and (b) wedge grips.	119
<b>Figure 2.42.</b> Lap-shear adhesion test of $C_{1, P1}+B_3$ emulsion in aqueous 100 mM NaCl solution on metal: (a) pneumatic grips, and (b) wedge grips.	120
<b>Figure 2.43.</b> Lap-shear adhesion test of $A_{3, P1}+B_3$ hydrogels in aqueous 100 mM NaCl solution on HDPE.	120
<b>Figure 2.44.</b> Lap-shear adhesion test of $A_{3, P1}+B_3$ hydrogels in 100 mM NaCl in 90% $CH_3OH$ and 10% $H_2O$ on HDPE.	121
<b>Figure 2.45.</b> Lap-shear adhesion test of $C_{1, P1}+B_3$ emulsion in aqueous 100 mM NaCl solution on HDPE.	121
<b>Figure 2.46.</b> Lap-shear adhesion test of $A_{3, P1}+B_3$ hydrogels in aqueous 100 mM NaCl solution on ham.	122
<b>Figure 3.1.</b> Schematic illustration of antifouling and bactericidal polymer coatings against bacterial adhesion and biofilm formation (top). Illustrations of the self-assembled polymer network before and after antibiotic loading is also shown (bottom).	130
<b>Figure 3.2.</b> Ring-opening metathesis polymerization (ROMP) of norbornene-based functional monomers in DMF yielded a set of bottlebrush supramolecular copolymers <b>A</b> and <b>B</b> that, after dialysis, self-assembled 1:1 in a mixture of 90% MeOH and 10% $H_2O$ to afford a polymer coating, leading to a bactericidal polymer coating after couteranion exchange with tazobactam and piperacillin anions.	133
<b>Figure 3.3.</b> Flow cell biofilm experiments. (a) Representative confocal microscopy images of one replicate at 20 min, 48 h, and 96 h for control (no polymer) and polymer coated ( <b>A+B</b> ) experiments. The scale bar indicates 100 $\mu m$ . (b) Thickness of polymer film ( <b>A+B</b> ) on glass coverslip at 20 min, 48 h, and 96 h. (c) Biofilm height on glass coverslip for control and polymer coated ( <b>A+B</b> ).	136
<b>Figure 3.4.</b> Static growth experiments. (a) Confocal microscopy images show biofilm formation of one replicate for no polymer film, polymer film ( <b>A+B</b> ) and antibiotic-loaded polymer film ( <b>A<sub>t</sub>+A<sub>p</sub>+B</b> ) at 48 h. The scale bar indicates 50 $\mu m$ . (b) Thickness of polymer film ( <b>A+B</b> ) and antibiotic-loaded polymer film ( <b>A<sub>t</sub>+A<sub>p</sub>+B</b> ) at 0 h and 48 h. (c) Biofilm formation at 48 h for no polymer film, polymer film ( <b>A+B</b> ) and antibiotic-loaded polymer film ( <b>A<sub>t</sub>+A<sub>p</sub>+B</b> ). CFUs of three biological replicates at 0 h, 24 h and 48 h for no polymer film, polymer film ( <b>A+B</b> ) and antibiotic-loaded polymer film ( <b>A<sub>t</sub>+A<sub>p</sub>+B</b> ) with PAO1 $\Delta wspF$ Tn7 Gm::P(A1/04/03)::GFP (indicated as "PAO1 $\Delta wspF$ ") (d) and PAO1 $\Delta wspF \Delta pelF \Delta psl \Delta algD$ Tn7 Gm::P(A1/04/03)::GFP (indicated as "PAO1 $\Delta wspF \Delta EPS$ ") (e).	139

**Figure 3.5.** MIC assay experiments. (a) Graphical representation for the release of antibiotics via counteranion exchange for antibiotic-loaded polymer film ( $A_t+A_p+B$ ). (b-e) MIC assay results of aliquots collected at different time points from the solution with antibiotic-loaded polymer film ( $A_t+A_p+B$ ). ..... 142

**Figure 3.6.**  $^1H$  NMR (500 MHz, 25 °C,  $CD_3OD$ ) spectrum of tazobactam loaded statistical copolymer  $A_t$ . Each charged viologen side chain contained four positive charges and should bind to four tazobactam anions if fully loaded, when correlated with NMR integration, proton resonances a and b should be 8, and resonances c, d, e should be 4, 4, 12, respectively. By the integration shown above, copolymer  $A_t$  is about 60% loaded with tazobactam anion..... 151

**Figure 3.7.**  $^1H$  NMR (500 MHz, 25 °C,  $CD_3OD$ ) spectrum of piperacillin loaded statistical copolymer  $A_p$ . Each charged viologen side chain contained four positive charges and should bind to four piperacillin anions if fully loaded, when correlated with NMR integration, proton resonances a and b should be 8, and resonances c, d, e should be 4, 4, 4, respectively. By the integration shown above, copolymer  $A_p$  is about 45% loaded with piperacillin anion. .... 152

**Figure 3.8.** (a) Picture of polymer film on glass slide. (b) Summary of profilometry data for three replicates submerged in a salt solution (100 mM NaCl) over several days. .... 153

**Figure 3.9.** SEM images of  $A+B$  in 90%  $CH_3OH$  and 10%  $H_2O$  after being air dried overnight. (a) 1000x, (b) 5000x, (c) 10000x, and (d) 35000x..... 155

**Figure 3.10.** SEM images of  $A_t+A_p+B$  in 90%  $CH_3OH$  and 10%  $H_2O$  after being air dried overnight. (a) 1000x, (b) 5000x, (c) 10000x, and (d) 35000x. .... 155

**Figure 3.11.** Set up of flow cells. .... 158

**Figure 3.12.** Images at 20 min and 96 h for flow cell experiments using glass coverslips coated with polymer film  $A_0+B$  (no porphyrin included)..... 158

**Figure 3.13.** Representative z-stack images of each replicate at 20 min, 48 h, and 96 h for flow cell experiments using glass coverslips without polymer coating (control)..... 159

**Figure 3.14.** Representative z-stack images of each replicate at 20 min, 48 h, and 96 h for flow cell experiments using polymer-coated glass coverslips. .... 160

**Figure 3.15.** Images from the top of the wells for three replicates. In all three replicates, wells of lane “a” were with no polymer coating, wells of lane “b” were coated with polymer film ( $A+B$ ), and wells of lane “c” were coated with antibiotic-loaded polymer film ( $A_t+A_p+B$ )..... 164

**Figure 3.16.** Confocal microscopy images (Replicate 1) of polymer film ( $A+B$ ) and antibiotic-loaded polymer film ( $A_t+A_p+B$ ) at 0 h; bacteria growth of no polymer film, polymer film ( $A+B$ ) and antibiotic-loaded polymer film ( $A_t+A_p+B$ ) at 48 h..... 165

**Figure 3.17.** Confocal microscopy images (Replicate 2) of polymer film ( $A+B$ ) and antibiotic-loaded polymer film ( $A_t+A_p+B$ ) at 0 h; bacteria growth of no polymer film, polymer film ( $A+B$ ) and antibiotic-loaded polymer film ( $A_t+A_p+B$ ) at 48 h..... 166

**Figure 3.18.** Confocal microscopy images (Replicate 3) of polymer film ( $A+B$ ) and antibiotic-loaded polymer film ( $A_t+A_p+B$ ) at 0 h; bacteria growth of no polymer film, polymer film ( $A+B$ ) and antibiotic-loaded polymer film ( $A_t+A_p+B$ ) at 48 h..... 167

**Figure 3.19.** Confocal microscopy images of control experiments in the well plate: polymer film ( $A+B$ ) with bacteria in PBS, polymer film ( $A+B$ ) without bacteria in TSB, no polymer film with bacteria in PBS, and no polymer film with bacteria in TSB. .... 169

<b>Figure 3.20.</b> (a) Initial screening of MIC assay results of antibiotics released at 0 h, 0-4 h, 4-8 h, 8-12 h, 12-24 h, and 24-48 h. (b) MIC assay results of antibiotics released at 10-12 h, 12-24 h, and 24-48 h (three replicates). .....	171
<b>Figure 4.1.</b> Cartoon representation of a polymer-drug conjugate. ....	176
<b>Figure 4.2.</b> Schematic diagram shows the structure of the mini-Agrin protein (NtA; green + LG domains; gray) fused to mono-StreptAvidin (blue) to make mini-Agrin-mSA. The biotin (red) on the drug-carrying polymer at right binds to mSA, forming the complex that will be used to carry drugs to glomeruli <i>in vivo</i> . ....	178
<b>Figure 4.3.</b> (a) Chemical structures of Nb-PEG, Nb-TEG-ZnTPP, Nb-CD, Nb-Me, and Biotin TA. (b) Synthetic strategy for poly(PEG <sub>5</sub> -ZnTPP)-(CD <sub>5</sub> -Me <sub>15</sub> )-biotin. ....	179
<b>Figure 4.4.</b> <sup>1</sup> H NMR (500 MHz, 25 °C, (CD <sub>3</sub> ) <sub>2</sub> SO) spectra of Nb-PEG, Nb-TEG-ZnTPP, Nb-CD, Nb-Me, poly(PEG <sub>5</sub> -ZnTPP), poly(PEG <sub>5</sub> -ZnTPP)-(CD <sub>5</sub> -Me <sub>15</sub> ) (from top to bottom). ....	180
<b>Figure 4.5.</b> <sup>1</sup> H NMR (500 MHz, 25 °C, (CD <sub>3</sub> ) <sub>2</sub> SO) spectra of <b>Biotin-TA</b> , <b>poly(PEG<sub>5</sub>-ZnTPP)-(CD<sub>5</sub>-Me<sub>15</sub>)-biotin</b> after dialysis, <b>poly(PEG<sub>5</sub>-ZnTPP)-(CD<sub>5</sub>-Me<sub>15</sub>)</b> (from top to bottom).....	181
<b>Figure 4.6.</b> Overlay of analytical GPC traces in DMF with 0.025 M LiBr at 60 °C at 1.0 mL·min <sup>-1</sup> : (a) <b>Nb-PEG</b> , <b>Biotin-TA</b> , <b>poly(PEG<sub>5</sub>-ZnTPP)</b> , <b>poly(PEG<sub>5</sub>-ZnTPP)-(CD<sub>5</sub>-Me<sub>15</sub>)</b> , <b>poly(PEG<sub>5</sub>-ZnTPP)-(CD<sub>5</sub>-Me<sub>15</sub>)-biotin</b> before dialysis.(b) <b>Biotin-TA</b> , <b>poly(PEG<sub>5</sub>-ZnTPP)-(CD<sub>5</sub>-Me<sub>15</sub>)-biotin</b> before and after dialysis. ....	181
<b>Figure 4.7.</b> (a) SDS-PAGE results of streptavidin and diblock copolymer. Lane L: ladder; lane A: streptavidin; lane B: streptavidin mixed with diblock copolymer with a molar ratio of 1:50; lane C: streptavidin mixed with diblock copolymer with a molar ratio of 1:100; lane D: diblock copolymer. (b) SDS-PAGE results of streptavidin and small biotin molecule. Lane L: ladder; lane A: streptavidin; lane B: streptavidin mixed with small biotin molecule with a molar ratio of 1:50000; lane C: streptavidin mixed with small biotin molecule with a molar ratio of 1:5000; lane D: streptavidin mixed with small biotin molecule with a molar ratio of 1:500; lane E: streptavidin mixed with small biotin molecule with a molar ratio of 1:50; lane F: streptavidin mixed with small biotin molecule with a molar ratio of 1:5.....	183
<b>Figure 4.8.</b> Schematic diagram (top) shows the domains of mini-Agrin-mSA and the epitope tags used for its purification and detection. Four different mice were injected i.v. with either PBS (left) or increasing doses of mini-Agrin-mSA. Kidneys were collected 1 h after injection and stained for the Myc tag. Increasing amounts of injected protein were detected in glomeruli.....	184
<b>Figure 5.1.</b> Hyaluronic acid modified with both methacrylates (blue) and guest and host molecules (purple). Ad-MeHA and CD-MeHA macromers crosslink by both physical bonding upon mixing and through a secondary crosslinking of methacrylates with UV light exposure. Reused with permission. <sup>2</sup> .....	195
<b>Figure 5.2.</b> (a) Compound key showing copolymer <b>A</b> : poly(2V <sup>4+</sup> Ad <sub>30</sub> -TEG <sub>90</sub> -ZnTPP) <sub>stat</sub> , copolymer <b>B</b> : poly(CD <sub>30</sub> -TEG <sub>90</sub> ) <sub>stat</sub> , negatively charged ATRP initiator ( <b>I</b> ), crosslinker ( <b>XL</b> , i.e., PEG diacrylate: PEG-DA), and generic scheme showing photo-ATRP of an acrylate monomer ( <b>M</b> ). (b) Illustration showing the <b>A+B</b> viscous hydrogel in saltwater, where <b>I</b> has been electrostatically loaded onto the oligoviologen sidechains and <b>M</b> has been mixed in prior to a photoinduced ATRP to form <i>in situ</i> a second covalent polymer ( <b>D</b> ). (c) Illustration showing <b>A+B</b> hydrogel, where <b>M</b> , <b>I</b> , and <b>XL</b> have been mixed into the 'host' network prior to photo-ATRP to form a secondary covalent network ( <b>E</b> ). ....	197

# List of Schemes

<b>Scheme 2.1.</b> Synthesis of <b>Ad-Hexyl-OH</b> .....	61
<b>Scheme 2.2.</b> Synthesis of <b>Ad-Hexyl-OMs</b> .....	62
<b>Scheme 2.3.</b> Synthesis of <b>Nb-Ethyl-OH</b> .....	62
<b>Scheme 2.4.</b> Synthesis of <b>Nb-Ethyl-OMs</b> .....	63
<b>Scheme 2.5.</b> Synthesis of <b>Nb-1V•1PF<sub>6</sub></b> .....	64
<b>Scheme 2.6.</b> Synthesis of <b>Nb-1V•2PF<sub>6</sub></b> .....	65
<b>Scheme 2.7.</b> Synthesis of <b>Nb-2V•3PF<sub>6</sub></b> .....	66
<b>Scheme 2.8.</b> Synthesis of <b>Nb-2V-Ad•4PF<sub>6</sub></b> .....	67
<b>Scheme 2.9.</b> Synthesis of <b>Nb-2V-Ad•4Cl</b> .....	68
<b>Scheme 2.10.</b> Synthesis of <b>Nb-2V-Me•4PF<sub>6</sub></b> .....	69
<b>Scheme 2.11.</b> Synthesis of <b>Nb-2V-Me•4Cl</b> .....	70
<b>Scheme 2.12.</b> Synthesis of <b>Nb-Gly</b> .....	71
<b>Scheme 2.14.</b> Synthesis of <b>CD-OTs</b> .....	72
<b>Scheme 2.15.</b> Synthesis of <b>CD-NH<sub>2</sub></b> .....	73
<b>Scheme 2.16.</b> Synthesis of <b>Nb-CD</b> .....	74
<b>Scheme 2.17.</b> Synthesis of <b>Nb-DCI</b> .....	75
<b>Scheme 2.18.</b> Synthesis of <b>TEG-OTs</b> .....	76
<b>Scheme 2.19.</b> Synthesis of <b>Nb-TEG</b> .....	77
<b>Scheme 2.20.</b> Synthesis of <b>Nb-TEG-OTs</b> .....	78
<b>Scheme 2.21.</b> Synthesis of <b>TPP-OH</b> .....	79
<b>Scheme 2.22.</b> Synthesis of <b>Nb-TEG-ZnTPP</b> .....	80
<b>Scheme 2.23.</b> Synthesis of <b>Nb-Hexyl-Ad</b> .....	81
<b>Scheme 2.24.</b> Synthesis of <b>Nb-Me</b> .....	82
<b>Scheme 2.25.</b> Synthesis of <b>Ad-TEG-OH</b> .....	83
<b>Scheme 2.26.</b> Synthesis of <b>Nb-TEG-Ad</b> .....	84
<b>Scheme 2.27.</b> Synthesis of statistical copolymers <b>A<sub>x, Pn</sub>: poly(2V<sup>4+</sup>Ad<sub>m</sub>-TEG<sub>2-4m</sub>-ZnTPP<sub>n</sub>)<sub>stat.</sub></b> ..	85
<b>Scheme 2.28.</b> Synthesis of statistical copolymers <b>B<sub>x</sub>: poly(CD<sub>m</sub>-TEG<sub>2-4m</sub>)<sub>stat.</sub></b> .....	86
<b>Scheme 2.29.</b> Synthesis of statistical copolymer <b>C<sub>1, P1</sub>: poly(HexylAd<sub>30</sub>-TEG<sub>90</sub>-ZnTPP)<sub>stat.</sub></b> .....	88
<b>Scheme 2.30.</b> Synthesis of statistical copolymer <b>C<sub>2, P1</sub>: poly(TEGAd<sub>30</sub>-TEG<sub>90</sub>-ZnTPP)<sub>stat.</sub></b> .....	89
<b>Scheme 2.31.</b> Synthesis of statistical copolymer <b>D<sub>P1</sub>: poly(2V<sup>4+</sup>Me<sub>30</sub>-TEG<sub>90</sub>-ZnTPP)<sub>stat.</sub></b> .....	90
<b>Scheme 2.32.</b> Synthesis of statistical copolymer <b>E<sub>P1</sub>: poly(TEG<sub>120</sub>-ZnTPP)<sub>stat.</sub></b> .....	91
<b>Scheme 2.33.</b> Synthesis of statistical copolymer <b>F<sub>P1</sub>: poly(Me<sub>120</sub>-ZnTPP)<sub>stat.</sub></b> .....	92
<b>Scheme 3.1.</b> Synthesis of statistical copolymer <b>A<sub>0</sub>: poly(2V<sup>4+</sup>Ad<sub>30</sub>-TEG<sub>90</sub>)<sub>stat.</sub>•120Cl</b> .....	146

<b>Scheme 3.2.</b> Synthesis of statistical copolymer <b>A</b> : <b>poly(2V<sup>4+</sup>Ad<sub>30</sub>-TEG<sub>90</sub>-ZnTPP)<sub>stat</sub>•120Cl</b> ..	147
<b>Scheme 3.3.</b> Synthesis of statistical copolymer <b>A<sub>t</sub></b> : <b>poly(2V<sup>4+</sup>Ad<sub>30</sub>-TEG<sub>90</sub>-ZnTPP)<sub>stat</sub>•72Tazobactam•48Cl</b> .....	148
<b>Scheme 3.4.</b> Synthesis of statistical copolymer <b>A<sub>p</sub></b> : <b>poly(2V<sup>4+</sup>Ad<sub>30</sub>-TEG<sub>90</sub>-ZnTPP)<sub>stat</sub>•54Piperacillin•66Cl</b> .....	149
<b>Scheme 3.5.</b> Synthesis of statistical copolymer <b>B</b> : <b>poly(CD<sub>30</sub>-TEG<sub>90</sub>)<sub>stat</sub></b> .....	150
<b>Scheme 4.1.</b> Synthesis of <b>Nb-PEG</b> .....	185
<b>Scheme 4.2.</b> Synthesis of <b>Boc-Tyramine</b> .....	186
<b>Scheme 4.3.</b> Synthesis of <b>Boc-Amine TA</b> .....	187
<b>Scheme 4.4.</b> Synthesis of <b>Amine TA</b> .....	188
<b>Scheme 4.5.</b> Synthesis of <b>Biotin TA</b> .....	188
<b>Scheme 4.6.</b> Synthesis of diblock copolymer <b>poly(PEG<sub>5</sub>-ZnTPP)-(CD<sub>5</sub>-Me<sub>15</sub>)-biotin</b> .....	189

# List of Tables

<b>Table 2.1.</b> Summary of statistical copolymers synthesized in this investigation. <i>Note</i> , the $C_{1, P1}$ , $C_{2, P1}$ , and $D_{P1}$ are control copolymers lacking oligoviologen side chains ( $C_{1, P1}$ and $C_{2, P1}$ ) or Ad groups ( $D_{P1}$ ). .....	39
<b>Table 2.2.</b> Oscillatory shear rheology testing summary for $A_{x, P1}+B_x$ hydrogel and $C_{x, P1}+B_3$ control materials in aqueous $100 \times 10^{-3}$ M NaCl solutions. ....	49
<b>Table 2.3.</b> Lap-shear adhesion testing summary for $A_{3, P1}+B_3$ hydrogel and $C_{1, P1}+B_3$ emulsion in aqueous $100 \times 10^{-3}$ M NaCl solutions. <i>Note</i> : <sup>a</sup> Curing protocol: (i) 24 h air dry, (ii) 12 h air dry followed by 12 h oven dry at 80 °C, and (iii) 24 h oven dry at 80 °C. <sup>b</sup> Microscope slide (VWR brand 25 x 75 x 0.9 mm). <sup>c</sup> Stainless steel ruler (28 x 75 x 0.9 mm). <sup>d</sup> High density polyethylene (25 x 75 x 1.6 mm). ....	52
<b>Table 2.4.</b> Summary of monomer ratios for different statistical copolymers $A_{x, Pn}$ . ....	85
<b>Table 2.5.</b> Summary of monomer ratios for different statistical copolymers $B_x$ . ....	86
<b>Table 2.6.</b> Molecular weight and dispersity data for the different statistical copolymers described in this report. ....	102
<b>Table 2.7.</b> Summary of storage and loss moduli for different $A_{3, Pn}+B_3$ ( $n=0, 1, 2$ and $4$ ) hydrogels, where different units of porphyrin were incorporated per chain. (Data was collected from <b>Figure 2.27</b> at 1% strain.) .....	109
<b>Table 2.8.</b> Summary of curing protocols for lap-shear adhesion tests. ....	115
<b>Table 3.1.</b> Summary of profilometry data for three replicates. ....	154
<b>Table 3.2.</b> Summary of thickness of polymer film ( $A+B$ ) on glass coverslip at 20 min, 48 h, and 96 h. ....	161
<b>Table 3.3.</b> Summary of bacterial growth on glass coverslip without polymer coating at 20 min, 48 h, and 96 h. ....	161
<b>Table 3.4.</b> Summary of bacterial growth on glass coverslip with polymer coating ( $A+B$ ) at 20 min, 48 h, and 96 h. ....	161
<b>Table 3.5.</b> Summary of thickness of polymer film ( $A+B$ ) in well plates at 0 h and 48 h. ....	168
<b>Table 3.6.</b> Summary of thickness of antibiotic-loaded polymer film ( $A_t+A_p+B$ ) in well plates at 0 h and 48 h. ....	168
<b>Table 3.7.</b> Summary of bacterial growth (PAO1 $\Delta wspF$ ) at 48 h for no polymer film, polymer film ( $A+B$ ) and antibiotic-loaded polymer film ( $A_t+A_p+B$ ) in well plates. ....	168
<b>Table 3.8.</b> Summary of bacteria growth (PAO1 $\Delta wspF \Delta EPS$ ) at 48 h for no polymer film, polymer film ( $A+B$ ) and antibiotic-loaded polymer film ( $A_t+A_p+B$ ) in well plates. ....	169

# Acknowledgments

I have been fortunate to have had numerous outstanding mentors throughout my undergraduate and graduate studies. First, I would like to thank my undergraduate advisors, Prof. Bin Tan and Prof. Yuanzhu Zhang from Southern University of Science and Technology, for introducing me to research and providing support for my graduate school applications. When I started my graduate school at Washington University, I was fortunate to join the Barnes Lab. Specifically, I would like to express my sincere gratitude to my research advisor, Prof. Jonathan Barnes, thank you for your unwavering support, guidance, and mentorship throughout my research journey. I am truly grateful for the opportunities you have provided me, the invaluable insights you have shared, and the challenges you have helped me overcome. Your mentorship has not only enriched my research experience but has also inspired me to strive for excellence in all aspects of my academic pursuits. I am profoundly thankful for your patience, wisdom, and encouragement, which have been invaluable assets in my growth as a researcher. A special thanks goes to my committee members: Prof. Timothy Wencewicz, Prof. John-Stephen Taylor, Prof. Courtney Reichhardt, and Prof. Guy Genin. Thank you for providing feedback for my research and guiding my journey in graduate study. I would also like to thank our collaborators, Prof. Jeffrey Miner, and Dr. Kohei Omachi for working with us on the protein-polymer conjugation project, and Prof. Courtney Reichhardt, Kejdi Kurti for working with us on the bactericidal polymer coating project. I would like to thank the funding support provided by the David and Lucile Packard Foundation through Prof. Jonathan Barnes' Packard Fellowship for Science and Engineering, and the funding support from the Children's Discovery Institute (St. Louis Children's Hospital).

I would also like to thank all current and previous members in Barnes lab. I appreciate the mentorship and help from Dr. Ruihan Li and Dr. Nathan Colley in my early years of graduate school. I also want to thank Mason Wong and Alexa Ribatt for being my productive mentee.

Especially, I want to thank Tarryn Trick, Jovelt Dorsainvil, and Sheila Tran for your support and help, in both research and life. I am grateful for the journey we've shared and for the friendship we've formed along the way.

During my graduate study, I am fortunate to be supported by a lot of friends. Especially, I want to thank Lingjue (Mike) Wang, whose consistent support and understanding have been invaluable to me. I also want to thank Mengting (Ashley) Yu, whose support has been instrumental during my final year of PhD studies. I would also like to express my gratitude to Xuan Ni, Chunxi Wang, Xiangfeng Niu, Yi Li, Xiaofeng Hu, Sijia Ding, Zhaohan Zhang and all other friends who have supported me throughout my PhD journey.

Above all, I want to express my deepest gratitude to my parents for their unconditional support and love. I am grateful for the courage and strength you have instilled in me, allowing me to embrace my true self and fearlessly navigate the challenges of the world.

Yipei Zhang

*Washington University in St. Louis*

*May 2024*

## ABSTRACT OF THE DISSERTATION

Design, Synthesis, Self-Assembly, and Applications of Functional Bottlebrush Architectures  
through Ring-Opening Metathesis Polymerization

by

Yipei Zhang

Doctor of Philosophy in Chemistry

Washington University in St. Louis, 2024

Professor Jonathan C. Barnes

Shear-thinning hydrogels are a class of materials with unique rheological properties that enable them to undergo a reversible reduction in viscosity under shear stress, which allows for easy injection. The injectability of shear-thinning hydrogels is particularly important when considering their use in biomedical applications, such as drug delivery, tissue engineering, and wound healing. However, before advancing to these applications, it is crucial to evaluate the “injectability” of new shear-thinning hydrogels to avoid clogging of the needle for injection. Injectability is typically associated with determining suitable viscosity, storage/loss moduli, and other factors, such as injection force (e.g., needle length and gauge for injection), for a specific hydrogel composition. Cyclodextrin (CD)-based host-guest chemistry is a widely used method for creating functional shear-thinning hydrogels. Despite the versatility and functional group tolerance of ring-opening metathesis polymerization (ROMP), its utilization in CD-based polymer synthesis is limited. This is primarily attributed to the bulky and rigid structure of CDs, which may hinder efficient polymerization or affect the reactivity of the catalyst. In this dissertation, I describe my efforts to address issues associated with injectability of shear-thinning hydrogels by synthesizing CD-based polymers using ROMP and studying the resultant materials to establish a new approach to shear-thinning hydrogels, antibiotic-loaded coatings, and as a potential drug delivery platform. In

Chapter 2, I describe a novel stimuli-responsive hydrogel comprising CD- and adamantane-based bottlebrush polymers that is both saltwater- and photoredox-responsive and exhibits broad adhesive properties on multiple materials with polar and non-polar surfaces. The host-guest cross-linked network remained soluble in deionized water and only formed viscous hydrogels in saltwater. The unique gelation mechanism was not dependent on the concentration of the polymer in the pre-gel solution, and this implies that the cross-linked network could be readily ejected from the syringe as a soluble aqueous solution prior to rapid gelation in saltwater without having to optimize any parameters associated with the injection method. The shear-thinning properties of the hydrogel were then “switched on” with either heat or exposure to visible light. Following this work, I then expanded the applications of viscous hydrogels to include antibacterial polymer coatings, which is described in Chapter 3. The polymer coatings were loaded with negatively charged antibiotics via electrostatic interactions and we demonstrated the release from the coatings effectively mitigated the growth of *Pseudomonas aeruginosa*. In Chapter 4, I describe an investigation into the possibility of developing a CD-based drug delivery platform through protein-polymer conjugation. In Chapter 5, future directions for “curing” the viscous hydrogels with a secondary polymerization step for further use in biomedical applications is discussed.

# Chapter 1: Introduction

## 1.1 Shear-Thinning Hydrogels

### 1.1.1 General Overview of Shear-Thinning Hydrogels

Hydrogels, which were first reported in 1894,<sup>1</sup> are water-swollen three-dimensional (3D) polymer networks, that are either physically or chemically bonded. Over the years, various hydrogels have been investigated with targeted applications. Conventional hydrogels are usually formed by covalently crosslinked polymer networks, the crosslinks are irreversible and static (**Figure 1.1a**).<sup>2</sup> In contrast, shear-thinning hydrogels are formed by dynamic reversible crosslinked polymer networks (**Figure 1.1b**)<sup>2</sup> and have gained in popularity recently as they are a good candidate for use in biomedical applications due to their unique ability to be ejected from a syringe.<sup>3</sup>

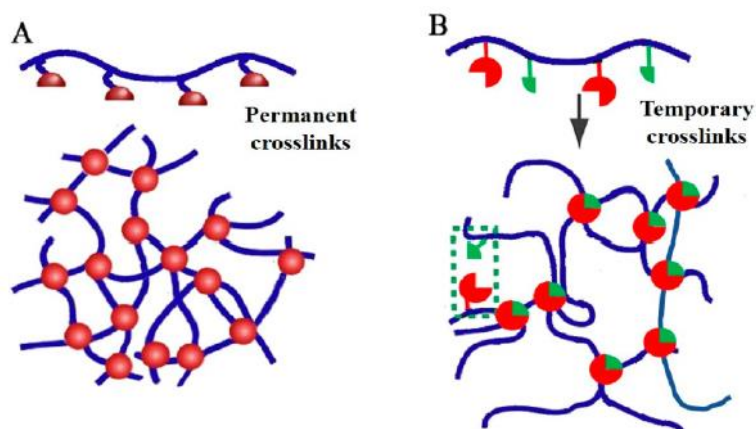


**Figure 1.1.** (a) Static polymer chains with covalently cross-linked networks. (b) Dynamic polymer chains with flexible, dynamic networks. Reused with permission.<sup>2</sup>

Shear-thinning is a property that is defined as the decrease in viscosity with increasing shear stress. Hydrogels possessing this property are liquid-like with agitation and solid-like at rest, thus providing easy access to injection. Typically, oscillatory shear rheology (**Figure 1.2**)<sup>4</sup> is the most

common tool to characterize the shear-thinning properties of hydrogels, where storage and loss moduli are measured throughout the process. Storage modulus ( $G'$ ) measures the stored energy, which is related to the elastic behavior of the hydrogel network in response to oscillatory shear forces; while the loss modulus ( $G''$ ) measures the released energy, which is related to the hydrogel's viscous behavior in response to oscillatory shear forces.

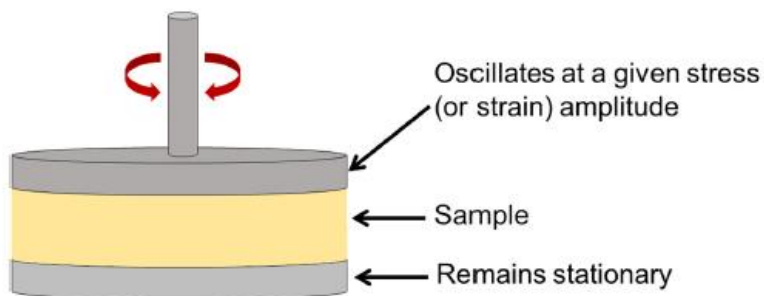


**Figure 1.2.** Illustration of a sample placed between the parallel plates with an oscillatory torsional shear applied. Reused with permission.<sup>4</sup>

It is challenging to identify the “first” example of a shear-thinning hydrogel due to the broad and interdisciplinary nature of the field, including chemistry, materials science, and biomedical engineering. However, the development and study of shear-thinning hydrogels have been a topic of interest since the late 20<sup>th</sup> century and evolved particularly rapidly during the past decade.<sup>5</sup> One of the early notable examples of shear-thinning behavior in hydrogels was reported by Kretsinger and co-workers in 2002, of which a designed peptide form pH-responsive hydrogels through intramolecular folding and self-assembly.<sup>6</sup> Currently, the design and development of shear-thinning hydrogels are mainly divided into two classes based on their dynamic nature as illustrated in **Figure 1.3**: (1) physical associations to assemble hydrogels (e.g., host-guest interactions, electrostatic interactions, metal-ligand interactions, or particle-based nanocomposite and granular systems), (2) dynamic covalent chemistry to form hydrogels (e.g., Schiff base, disulfide bonds, reversible Diels-Alder).<sup>3</sup> Regardless of the different chemistries and mechanisms involved in the formation of shear-thinning hydrogels, they share the similar properties that exhibit viscous flow

under shear stress (i.e., shear-thinning) and recovery when the applied stress is removed (i.e., self-healing).

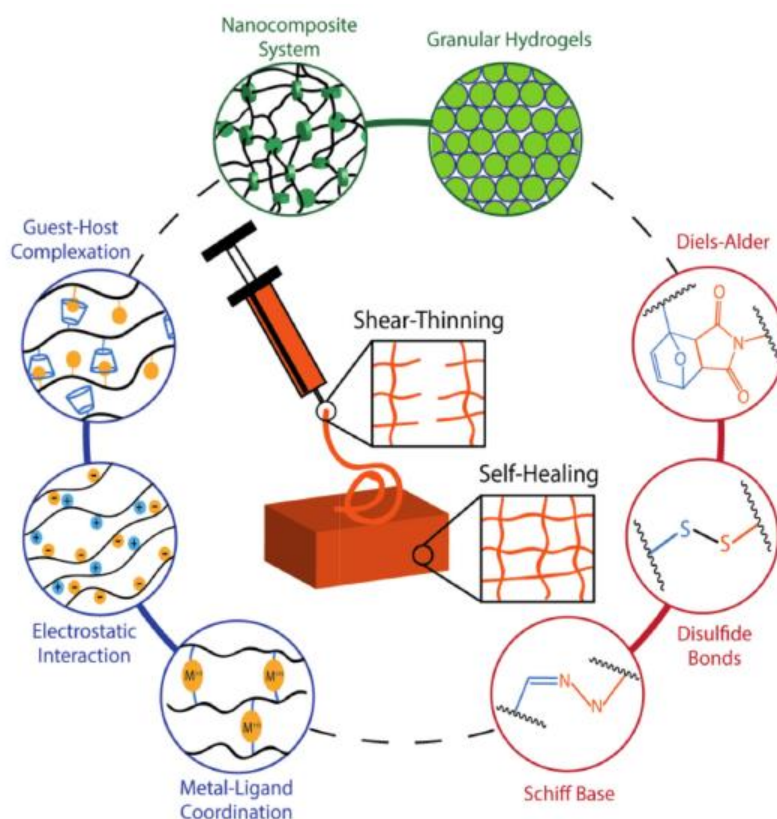


**Figure 1.3.** Shear-thinning and self-healing hydrogels rely on dynamic and reversible interactions between polymers and polypeptides. Reused with permission.<sup>3</sup>

As has been well-established in the literature, the main limitation of the traditional covalently crosslinked hydrogels that gelled during or after injection of the hydrogel precursors<sup>7</sup> is the crosslinking rate, as too rapid may clog the injection device<sup>8</sup> while too slow may lead to material dispersion.<sup>9</sup> Due to the dynamic bonding incorporated, shear-thinning hydrogels have gained more flexibility compared to the conventional covalently crosslinked hydrogels. Therefore, shear-thinning hydrogels have been widely used for biomedical applications, such as drug delivery,<sup>10, 11</sup> tissue regeneration,<sup>12, 13</sup> and 3D bioprinting.<sup>14, 15</sup>

## 1.1.2 Host-Guest-based Shear-Thinning Hydrogels

As has been illustrated in section 1.1.1, there are many different types of interactions that could lead to the formation of shear-thinning hydrogels. One of the most important ones relies on host-guest interactions that have been used frequently over the past few years to fabricate shear-thinning hydrogels for biomedical applications.

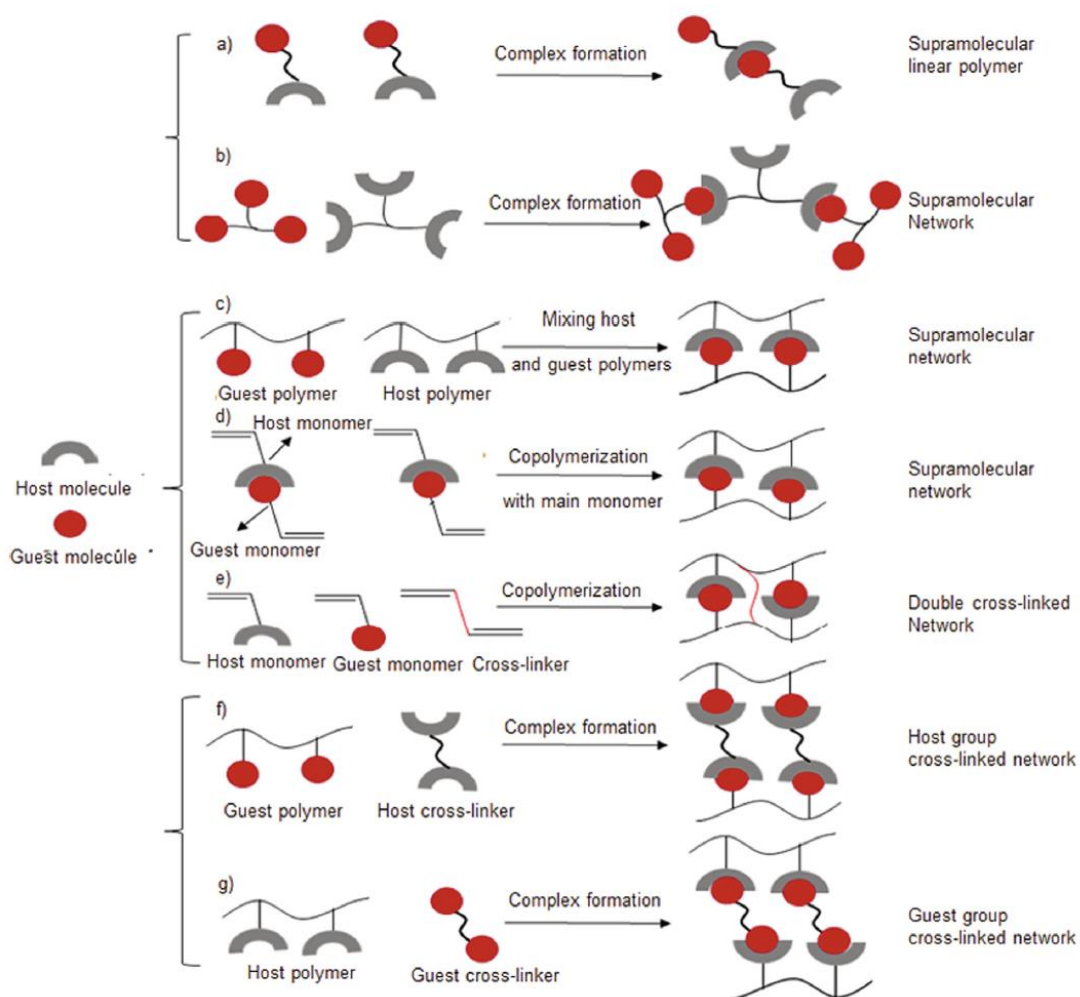


**Figure 1.4.** Fabrication of supramolecular host-guest polymer network. Reused with permission.<sup>16</sup>

Host-guest chemistry is an important field of chemistry that focuses on the interactions between host and guest molecules and has been widely used in the design of polymeric materials over the past few decades. In this context, a host molecule is usually a larger molecule that possesses a

cavity capable of accommodating a relatively smaller guest molecule. The interactions between the host and guest molecules are normally non-covalent, such as hydrogen bonding, hydrophobic interactions, and  $\pi$ - $\pi$  interactions. Several common methodologies used to form a host-guest polymer network are summarized in **Figure 1.4**.<sup>16</sup>

After Charles Petersen's pioneering synthesis of crown ethers in 1967,<sup>17</sup> a substantial number of macrocyclic compounds have emerged in this field, with four of them garnering significant attention. As shown in **Figure 1.5**, they are the naturally derived cyclodextrins (CDs) and the purely synthetic calix[n]arenes, cucurbit[n]urils (CBs) and pillar[n]arenes.<sup>18</sup> Due to their well-established synthetic methods, relatively high yields, and adaptable chemical modifications, the host-guest interactions and related applications for these macrocycles have been extensively explored in the field.

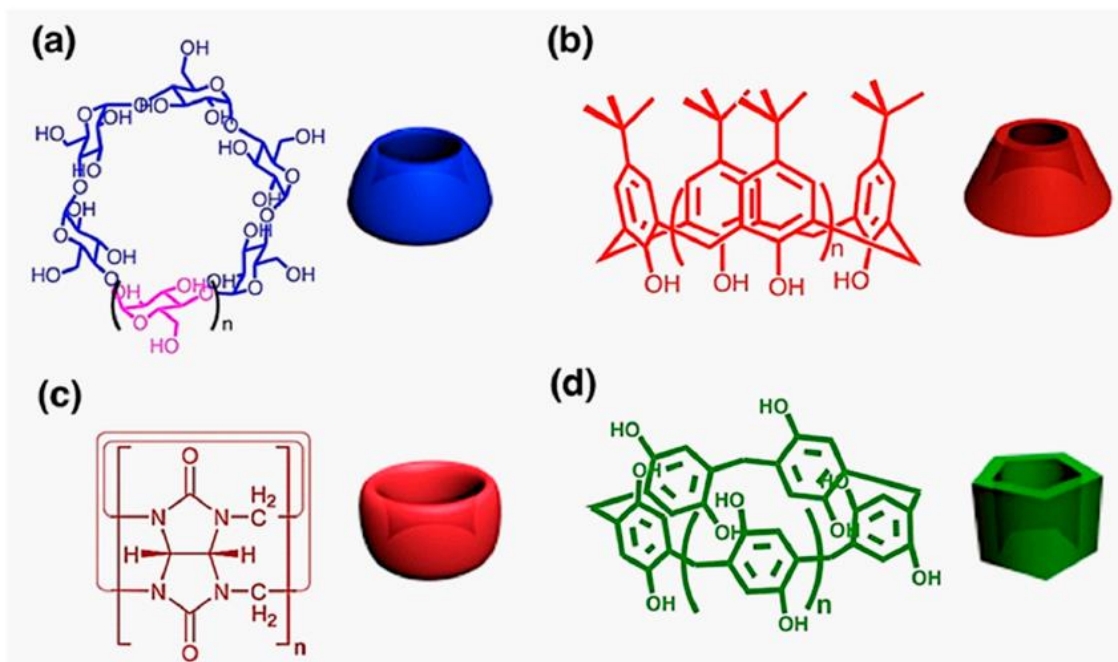


**Figure 1.5.** Molecular structures of the four types of supramolecular macrocycles: (a) CDs,  $n = 1-3$ ; (b) calix[n]arenes,  $n = 1-3$ ; (c) CB[n]s,  $n = 5-8, 10, 13-15$ ; (d) pillar[n]arenes,  $n = 1-11$ ; and their cartoon depictions. Reused with permission.<sup>18</sup>

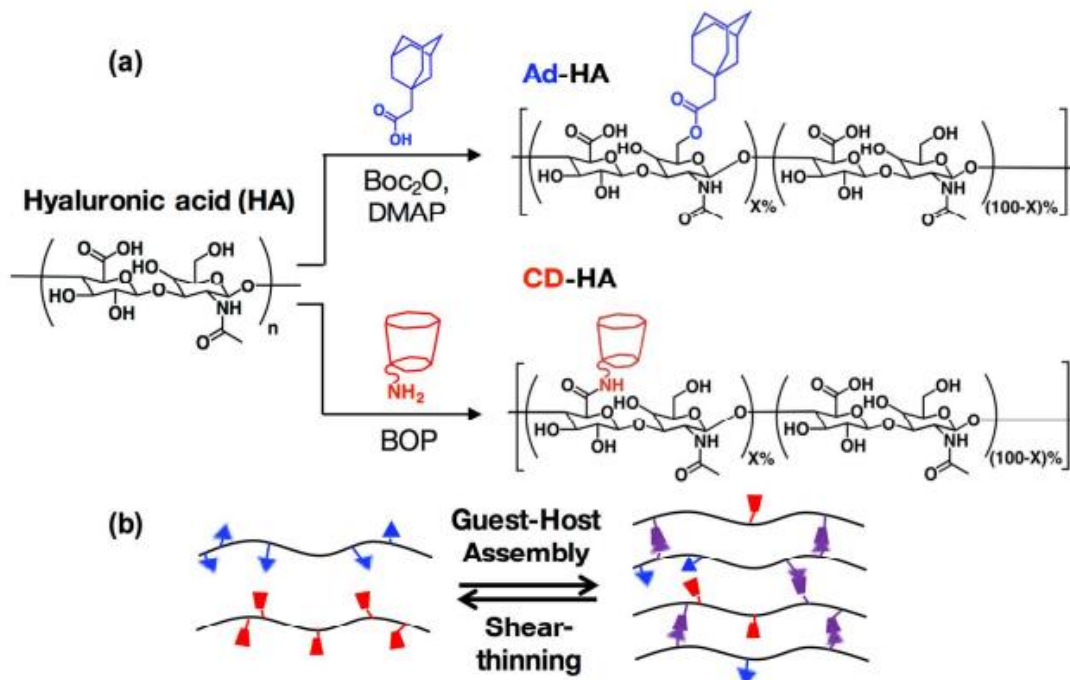


**Figure 1.6.** (a) Schematic of guest-host material synthesis through modification of hyaluronic acid with either adamantane (Ad-HA) or  $\beta$ -cyclodextrin (CD-HA). (b) Graphic showing guest-host assembly of adamantane and  $\beta$ -cyclodextrin groups and shear-thinning. Reused with permission.<sup>19</sup>

Burdick and colleagues have been investigating hydrogels with biomedical applications for almost 20 years, and his group's work helped establish the field of host-guest-based shear-thinning hydrogels and inspired many scientists. They developed their host-guest based shear-thinning hydrogel system utilizing hyaluronic acid (HA) as the polymer backbone, which is a naturally occurring polysaccharide with high biocompatibility. Specifically, HA-based polymers functionalized with either adamantane (Ad, guest) or  $\beta$ -cyclodextrin ( $\beta$ -CD, host) were self-assembled through host-guest interactions into shear-thinning hydrogels as illustrated in **Figure 1.6**.<sup>19</sup> Using this initial Ad/ $\beta$ -CD-crosslinked shear-thinning hydrogel, first reported in 2017, they demonstrated numerous applications, such as soft injectable hydrogels able to deliver a variety of therapeutic molecules (such as encapsulated proteins, growth factors, and small hydrophobic drugs) and cells (e.g., endothelial progenitor cells) for treating diseases.<sup>20</sup> However, due to the reversible nature of the host-guest crosslinking interactions, the initial hydrogel system exhibited limited utility in applications for mechanically demanding tissues. Thus, they incorporated

methacrylate groups into each polymer chain (both Ad and CD polymer) and the secondary crosslinking of methacrylates could be realized upon exposure to UV light in the presence of Irgacure 2959 (photoinitiator). This second crosslinking step allowed the system not only to be a printable 'bioink', but also with mechanical stability. The multifunctional hydrogel platform described above has provided a blueprint for scientists to continue investigating the field.

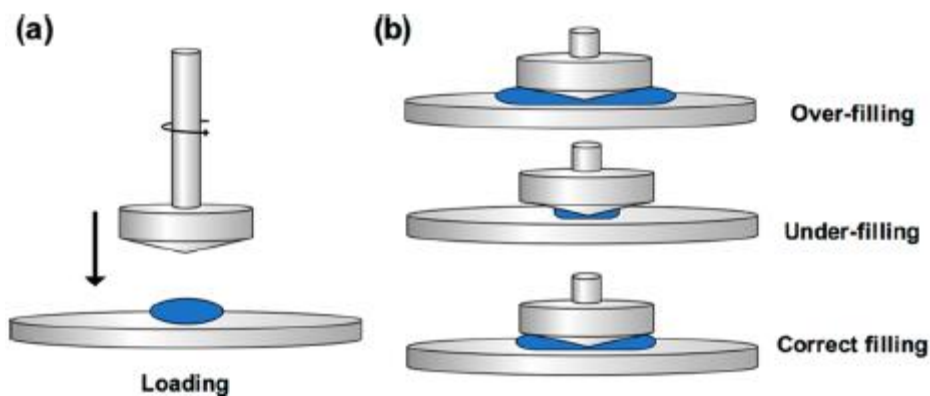


**Figure 1.7.** Hydrogel loading onto the rheometer stage. (a) When lowering the geometry onto the hydrogel, spin the geometry slightly for more even hydrogel loading. (b) Over-filling and under-filling of the sample results in increased and decreased forces, respectively. The hydrogel sample must fill the space between the geometry and the rheometer stage correctly for accurate measurements. Reused with permission.<sup>19</sup>

As mentioned earlier, oscillatory shear rheology is the standard method for characterizing shear-thinning hydrogels. Burdick and co-workers developed a detailed procedure for rheological analysis of shear-thinning hydrogels that is the go-to instructions for dynamic hydrogel analysis.<sup>19</sup> The general procedure for testing includes hydrogel preparation, rheometer set up and calibration, followed by hydrogel loading onto rheometer stage, acquisition, clean up, next sample preparation, and finally data analysis. Among these steps, choosing the right geometry and correctly loading the hydrogels are important to obtain reproducible data. As shown in **Figure 1.7**, accurate measurement needs correct filling of samples between the geometry and stage as otherwise the application of shear forces will be affected. Frequency sweeps, strain sweeps and continuous flow, and time sweeps are the methods used most often (protocols may vary under different conditions) for measuring the properties of hydrogels, as shown in **Figure 1.8**. One textbook

indication that a shear-thinning hydrogel has been prepared successfully is the observation of a crossover point between  $G'$  and  $G''$  with the increasing percent strain (for both hydrogels under this condition with different wt%) as observed in **Figure 1.8b**, which is also related to the injectability.

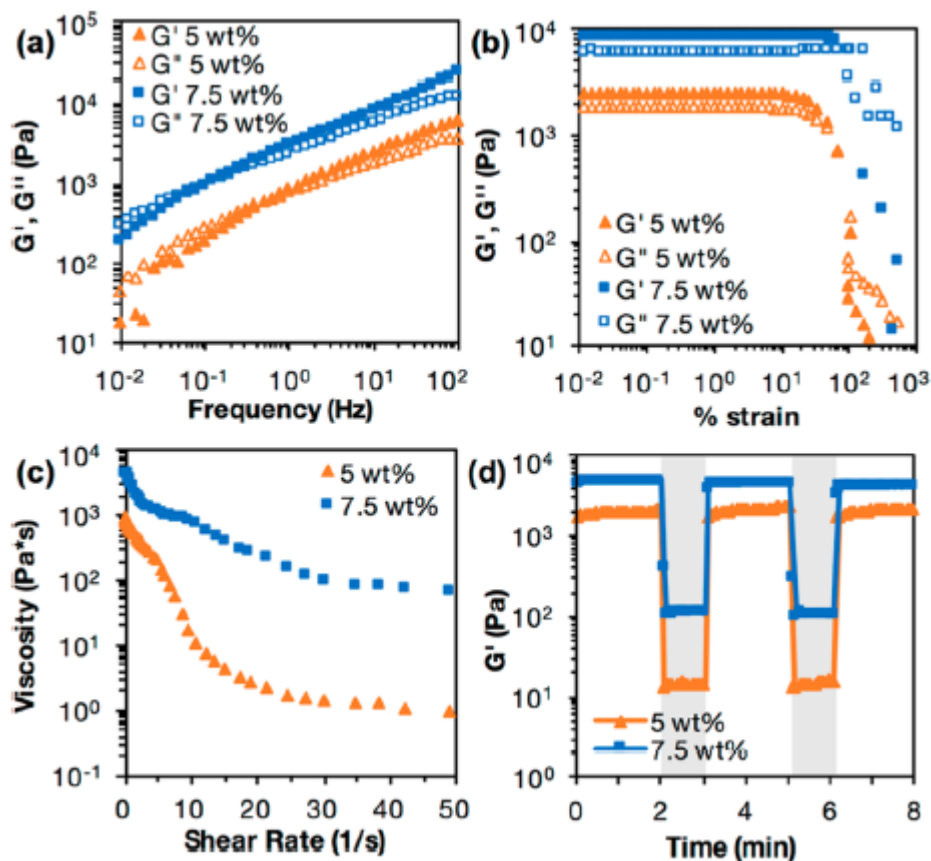


**Figure 1.8.** Results of (a) frequency sweep, (b) strain sweep, (c) continuous flow, and (d) cyclic strain time sweep rheology experiments for hydrogels of 5 and 7.5 wt % material concentration, using the described method and rheological parameters. For cyclic strain, shaded regions are high strain (500%) and unshaded regions are low strain (0.2%). Reused with permission.<sup>19</sup>

While the properties of shear-thinning hydrogels can simplify the injection process, some challenges still remain to obtain optimal injectability for bioengineering applications. For example, hydrogel composition (e.g., water percentage), injection forces, the latter of which is usually related to the length and gauge of the needle, along with the injection rate all need to be considered to achieve a consistent delivery and retention of the shear-thinning hydrogels.<sup>19</sup>

Therefore, we envision more research is required in the future to overcome these injectability challenges.

## 1.2 Cyclodextrin Molecular Recognition

### 1.2.1 Cyclodextrin-based Inclusion Complexes

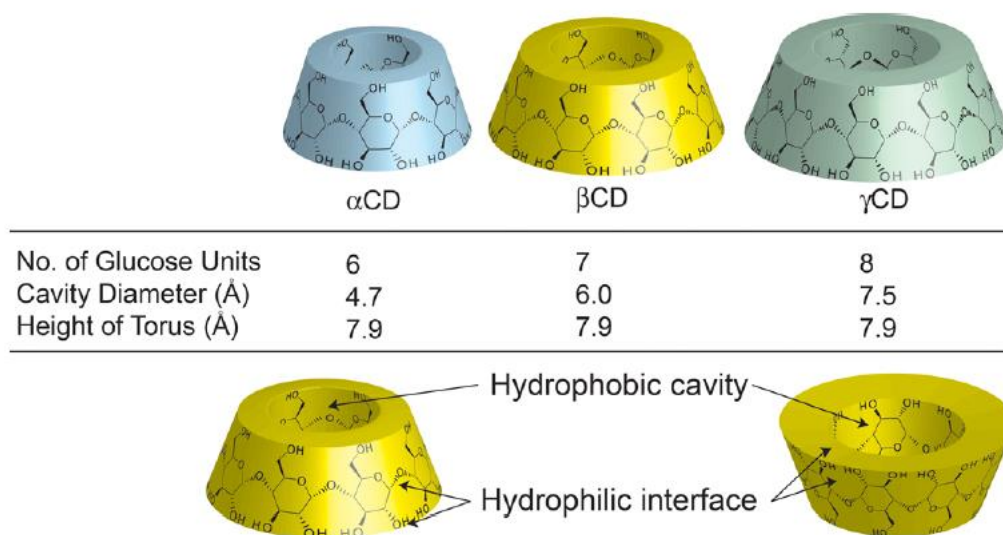


**Figure 1.9.** Chemical structures, approximate geometric, dimensions, and physical properties of  $\alpha$ -,  $\beta$ -, and  $\gamma$ -CD. Reused with permission.<sup>21</sup>

As mentioned in Section 1.1.2, the most commonly used hosts to form inclusion complexes in aqueous solutions are CBs, calix[n]arenes, pillar[n]arenes, and CDs. Currently, CDs are the most frequently used as they are commercially available, inexpensive, biocompatible, biodegradable, and easily modified for different applications.<sup>22</sup> CDs are cyclic oligosaccharides that are composed of glucose units joined together by  $\alpha$ -1,4 glycosidic linkages. They are typically classified into three categories ( $\alpha$ -,  $\beta$ -,  $\gamma$ -) as shown in **Figure 1.9** based on the number of glucose units (6, 7 and 8 for  $\alpha$ -,  $\beta$ -,  $\gamma$ -CD, respectively) in their ring structure, which also determines the cavity size.<sup>21</sup> All three CDs have a truncated cone shape, a hydrophilic interface, a hydrophobic cavity, and the same height. However, they have different cavity diameter thus different cavity

volume, which is related to the number of glucose units, with an increasing trend of 6, 7, and 8 units for  $\alpha$ -,  $\beta$ -, and  $\gamma$ -CD, respectively.

Due to the hollow cavity structure of CDs, the primary application is to create inclusion complexes with a range of guest molecules that exhibit suitable geometry and physicochemical properties. These guest molecules can fit either partially or entirely into the internal hydrophobic cavity of CDs, leaving the hydrophilic outer surface of CDs exposed to the surrounding aqueous environment. The primary driving force behind complex formation is the release of enthalpy-rich water molecules from the cavity. The binding strength relies on the compatibility of the 'host-guest' complex and specific local interactions between surface atoms.<sup>23</sup> Typically,  $\alpha$ -CD can thread along a polymer chain such as polyethylene glycol (PEG) or poly( $\epsilon$ -caprolactone) (PCL) to form inclusion complexes due to its small cavity size, but it is not able to complex with poly(propylene oxide) (PPO).<sup>24</sup> In contrast,  $\gamma$ -CD has a much bigger cavity and thus has the capability to thread onto either a PPO chain or two chains of PEG or PCL simultaneously.<sup>24</sup> Moreover, the big cavity size of  $\gamma$ -CD allows it to accommodate hydrophobic drugs (e.g., doxorubicin)<sup>25</sup> or aromatic compounds (e.g., pyrenes).<sup>26</sup>

Though  $\beta$ -CD has relatively low solubility in water ( $18.5 \text{ g}\cdot\text{L}^{-1}$ ) compared to  $\alpha$ -CD ( $145 \text{ g}\cdot\text{L}^{-1}$ ) and  $\gamma$ -CD ( $232 \text{ g}\cdot\text{L}^{-1}$ ),<sup>27</sup> yet its adequate cavity size provides strong binding for a range of important guest molecules (e.g., responsive molecules, hydrophobic drug molecules). Along with the well-developed modification, scientists have investigated CDs in many different applications, such as responsive hydrogels and for drug delivery.<sup>28</sup>

Selective functionalization of  $\beta$ -CD is important for further modifications to realize different applications. As shown in **Figure 1.10a**, the primary hydroxyl groups at C6 are more reactive than the secondary hydroxy groups at C2 and C3. Thus, mono-tosylated  $\beta$ -CDs at C6 have been exploited frequently as they could easily be transformed into other functional groups, such as

azides, thiols, and amines.<sup>22</sup> Several pathways for the synthesis of C6-mono-tosylated  $\beta$ -CDs have been reported over the years. One common method is to utilize tosyl chloride in aqueous NaOH.<sup>29, 30</sup> Esterification or etherification could also be used to functionalize the hydroxyl groups, however, they display low selectivities.<sup>22</sup>

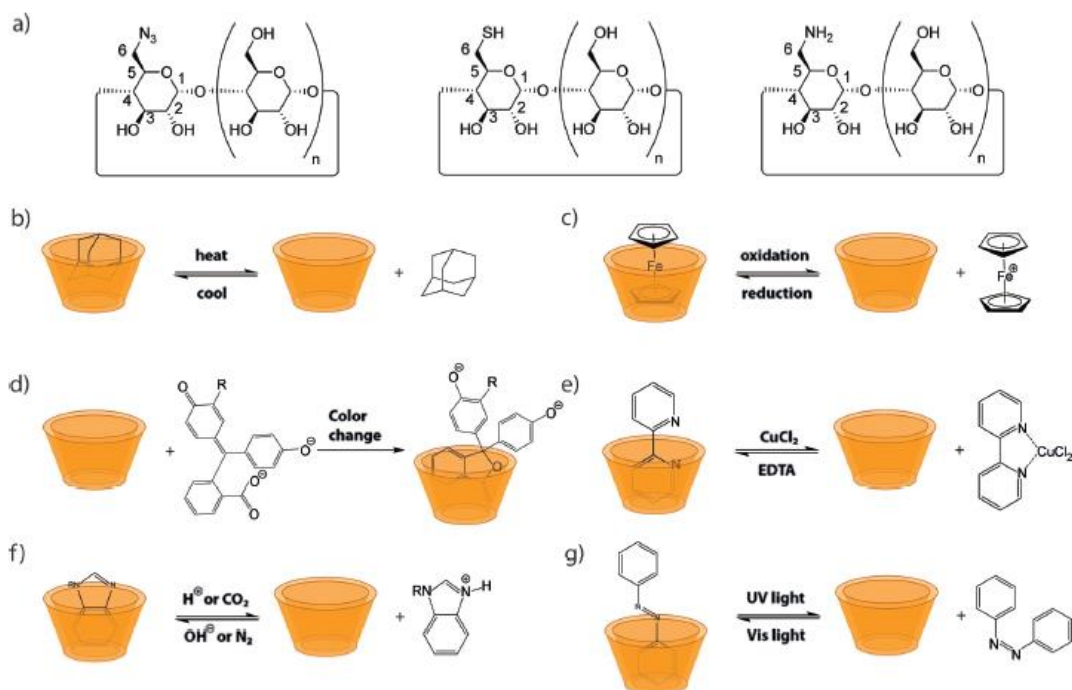


**Figure 1.10.**  $\beta$ -CD structures,  $\beta$ -CD-based host/guest pairs, and their associated response to external fields: (a) Structures of common CD building blocks (azide, thiol, and amine), (b) thermoresponsive adamantyl complex, (c) redox-responsive ferrocene complex, (d) color-changing phenolphthalein complex, (e) metal-ion-responsive bipyridine complex, (f) pH-responsive benzimidazole complexes, and (g) light-responsive azobenzene complexes. Reused with permission.<sup>22</sup>

Several common guests for  $\beta$ -CD are shown in **Figure 1.10**.<sup>22</sup> The most important property of these inclusion complexes is that they are stimuli-responsive, which means the reversible dissociation and association of these complexes upon application of some external stimuli. Already well-established in the literature, Ad fits into  $\beta$ -CD cavity very efficiently ( $\log K=5.04$ ) and can be freed upon heating the solution containing the inclusion complex. Ferrocene (Fc) is another example of a guest molecule that is strongly bound by  $\beta$ -CD under standard conditions but can be dissociated upon oxidation of Fc (**Figure 1.10c**). To gain precise spatial and temporal

control over dissociation, azobenzene<sup>31</sup> is a good guest molecule for forming a complex with  $\beta$ -CD, followed by its induced release as a function of photoisomerization of azobenzene from *trans* to *cis* forms upon exposure to UV light (**Figure 1.10g**). Another important category of guest molecules that form inclusion complexes with  $\beta$ -CDs is hydrophobic drugs that typically lack or exhibit low solubility in water. **Figure 1.11** shows the dynamic equilibrium between free CDs, free drugs, and drug-CD complexes (1:1 and 1:2). It is possible to have the entire drug or only a portion of it entering into the CD cavity to form inclusion complexes.<sup>32</sup>

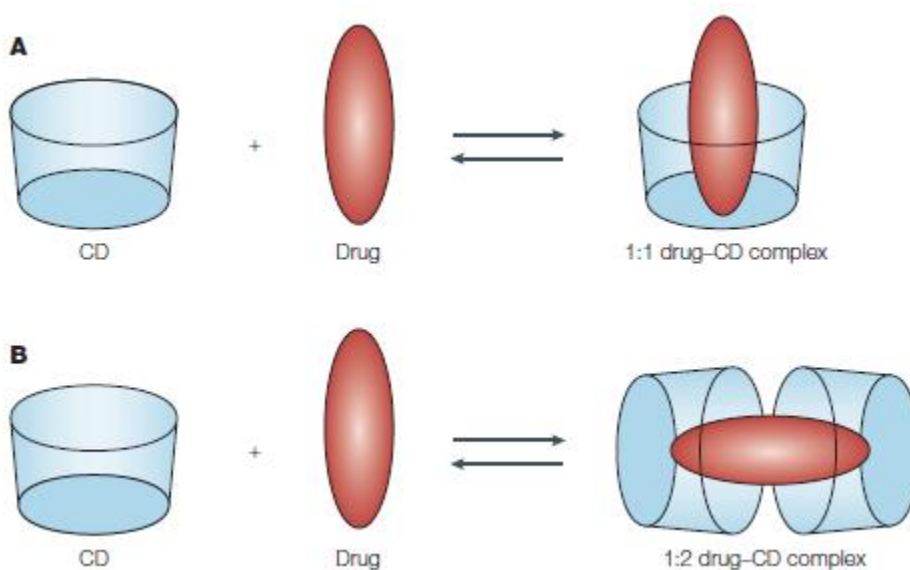


**Figure 1.11.** Schematic illustration of the association of free cyclodextrin (CD) and drug to form drug-CD complexes. Reused with permission.<sup>32</sup>

Though CDs normally will form inclusion complexes with the suitable guest molecules summarized above, there may be multiple factors that contribute to the formation of a CD-based complex in different systems (e.g., solvent). Nevertheless, a favorable net energetic driving force that pulls the guest molecule into CD cavity is necessary to form the inclusion complex.

## 1.2.2 Cyclodextrin-based Supramolecular Materials and Applications

The flexibility of CDs to form a multitude of host-guest-based inclusion complexes has inspired the creation of novel supramolecular materials for various applications, such as biomedical ones.<sup>24</sup>

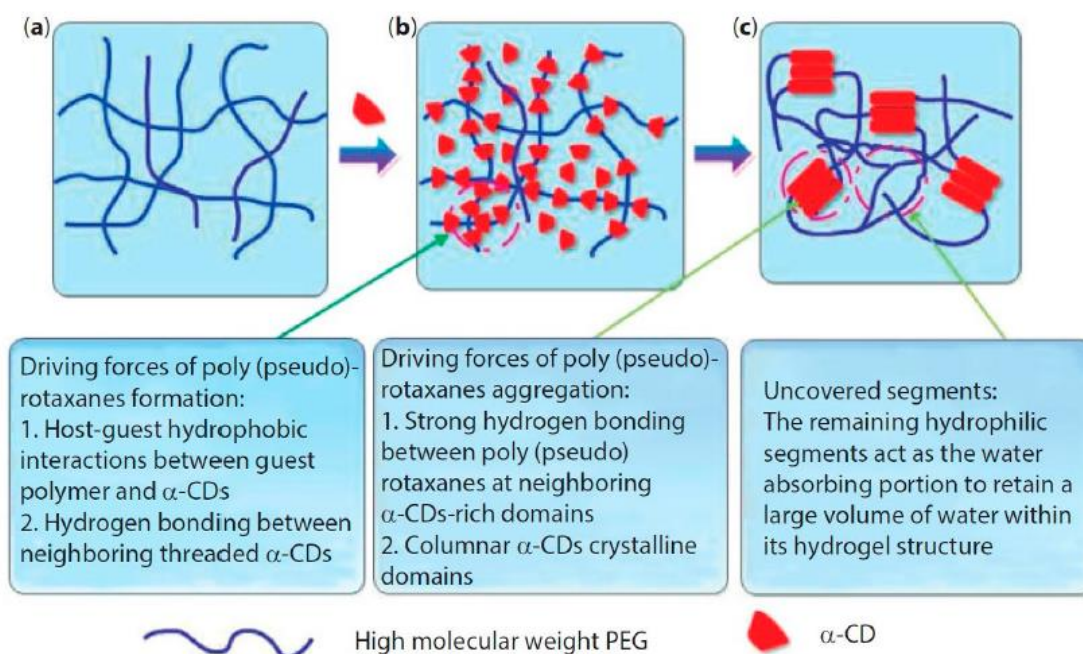


**Figure 1.12.** Formation of poly(pseudo)rotaxane hydrogels from  $\alpha$ -CD and high molecular weight PEG. Reused with permission.<sup>33</sup>

The ability of  $\alpha$ -CDs to thread along polymer chains (e.g., PEG) has led to these smaller CDs being widely investigated in CD-based poly(pseudo)rotaxanes. For example, Kamachi and co-workers pioneered research in this area, where in 1992, they reported the first example of threading several  $\alpha$ -CDs onto a single PEG chain that was terminated with sterically bulky groups.<sup>34</sup> In the two years after this seminal example, they demonstrated how the molecular weight of the PEG can influence the formation of  $\alpha$ -CD/PEG complexes<sup>35</sup> and reported the first supramolecular hydrogel based on  $\alpha$ -CD and high molecular weight PEG in an aqueous environment.<sup>36</sup> Since then,  $\alpha$ -CD-based poly(pseudo)rotaxanes have been incorporated extensively into hydrogels for many applications, such as injectable drug delivery systems that

possess thixotropic and reversible properties. The general formation of the hydrogel is summarized in Figure 1.12.<sup>33</sup>

Despite  $\gamma$ -CD possessing the largest cavity and highest water solubility among the three main CDs, its high cost of purification restricts the large-scale production and consequently limits its utilization in the fabrication of polymeric materials.<sup>37</sup> While not abundant, there have been instances reported over the years. For example, in 2020, Hadizadeh and colleagues developed an injectable hydrogel using  $\gamma$ -CD and PCL-PEG-PCL triblock copolymers at ambient temperature to achieve prolonged insulin release.<sup>38</sup>

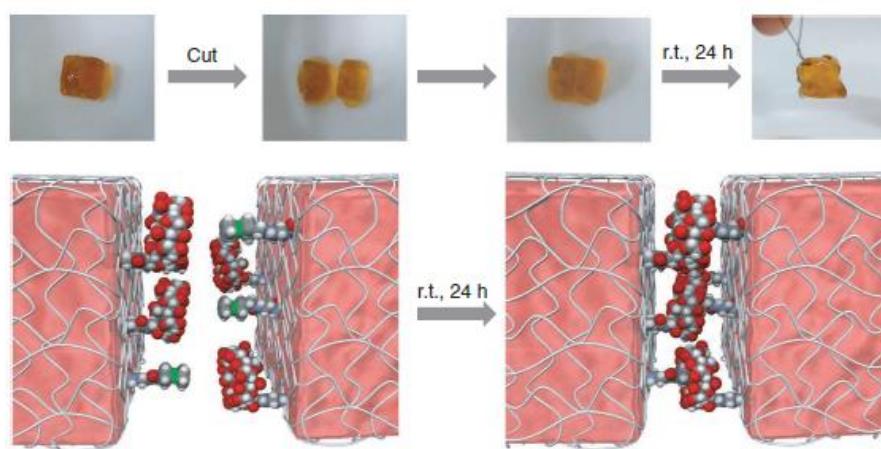


**Figure 1.13.** Self-healing experiments. Reused with permission.<sup>39</sup>

With so many well-documented host-guest pairs involving  $\beta$ -CD, as well as its straightforward modification mentioned in section 1.2.1, numerous polymeric systems have been designed and reported over the years, yielding multifunction materials that may be used to fabricate hydrogels for biomedical applications.<sup>22, 24</sup> As discussed thoroughly in Section 1.1, Ad/ $\beta$ -CD-based host-guest system has been used a lot for shear-thinning hydrogels, and there are other stimuli-responsive hydrogel systems that have been investigated as well by using some of the small-molecule guests mentioned earlier. For example, Harada and co-workers reported the redox-responsive self-healing hydrogels formed from Fc/ $\beta$ -CD polymers in 2011.<sup>39</sup> As illustrated in

**Figure 1.13**, when the self-assembled hydrogels were cut into two pieces, they could “self-heal” within several hours. Further experiments showed that treating the cut surface with an oxidizing agent (NaClO) inhibited the two pieces from re-adhering into one piece as the oxidized ferrocenium was too hydrophilic and could therefore not complex with  $\beta$ -CD anymore; however, treating the cut surface with a reducing agent (glutathione), the two pieces could be re-adhered again. Other stimuli-responsive hydrogels have also been reported, such as those that are pH-responsive<sup>40</sup> or light-responsive.<sup>41</sup>

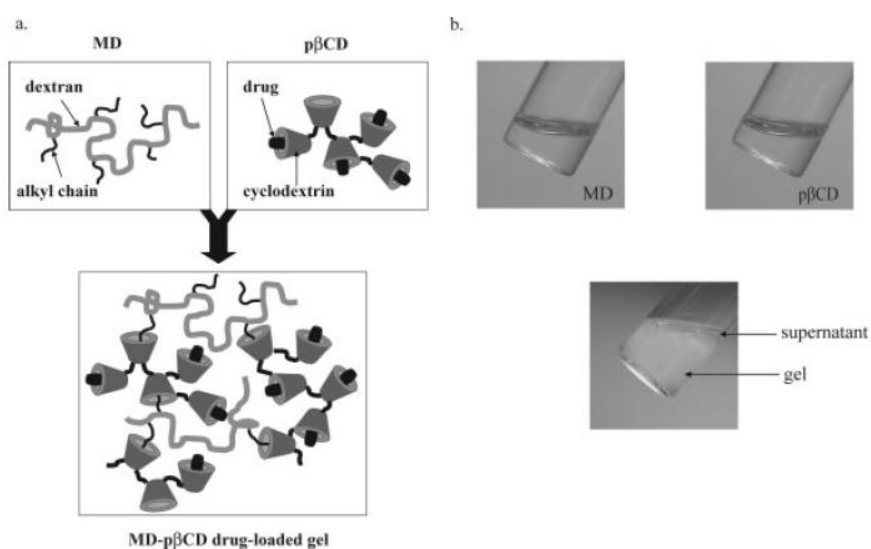


**Figure 1.14.** (a) Schematic representation of the formation of MD-p $\beta$ CD gels. (b) Photographs of the formation of a MD- p $\beta$ CD gel. Reused with permission.<sup>42</sup>

Additionally,  $\beta$ -CD is also used for drug delivery purposes through its incorporation into materials such as hydrogels and nanoparticles. For example, Gref and colleagues reported a hydrogel as shown in **Figure 1.14**, where the drug-loaded  $\beta$ -CD polymer formed gels when mixing with a modified dextran polymer. In this case, two hydrophobic drugs (benzophenone and tamoxifen) were loaded with a 90% loading efficiency. The *in vitro* release studies showed that gradual release was achieved with less than 25% benzophenone and 75% tamoxifen after 6 days of incubation. Along with the low toxicity, the hydrogel system provided a promising way for delivery of drugs.<sup>42</sup>

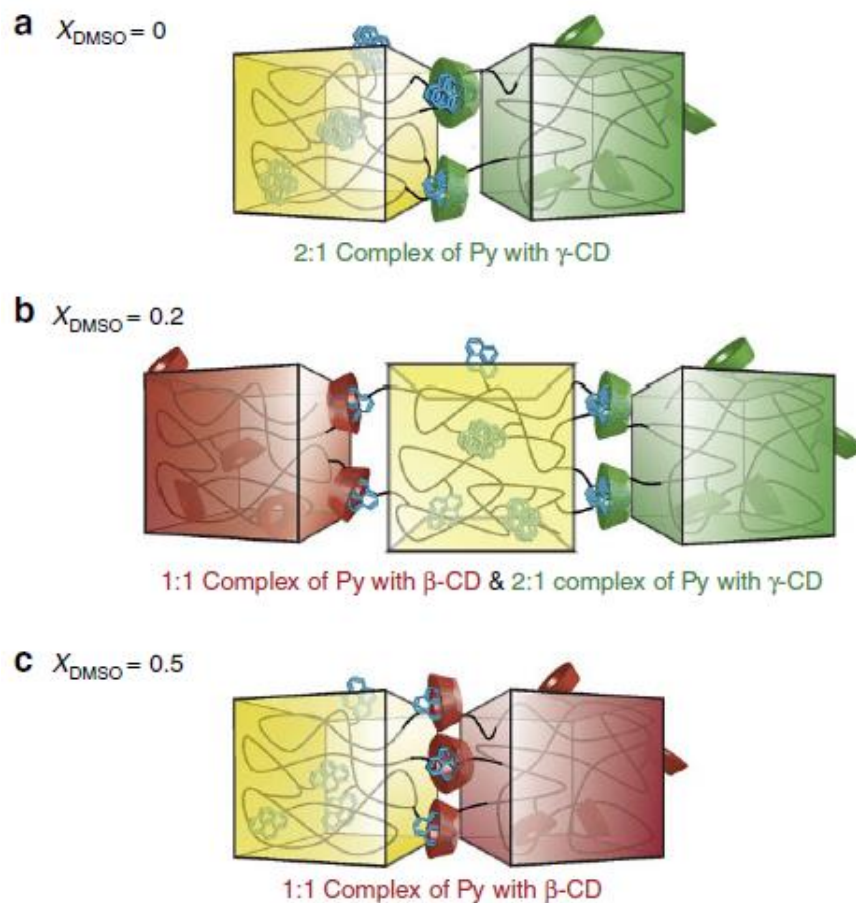


**Figure 1.15.** Conceptual illustrations for selectivity switching of Py gel as a function of  $x_{\text{DMSO}}$ . Reused with permission.<sup>43</sup>

While the majority of CD-based materials showcased above are primarily intended for biomedical applications, there have also been reports of other systems and applications. One notable example was reported by Harada and co-workers in 2012 using the pyrene (Py) gel to discriminate different CD gels ( $\alpha$ -,  $\beta$ -,  $\gamma$ -) by adjusting the solvent system.<sup>43</sup> This macroscopic molecular recognition of different CD gels is based on the fact that Py forms dimers easily in aqueous solutions, but remains in its monomeric state in organic solvents, such as dimethyl sulfoxide (DMSO). As illustrated in **Figure 1.15**, in pure water ( $x_{\text{DMSO}}=0$ ), the Py moieties on the Py gel surface aggregate and form dimers, leading to interactions with only the  $\gamma$ -CD-functionalized gel; at  $x_{\text{DMSO}}=0.5$ , only the  $\beta$ -CD gel interacts with the Py gel as the majority of Py moieties are in their monomer form. While at  $x_{\text{DMSO}}=0.2$ , both  $\beta$ -CD and  $\gamma$ -CD gels have interactions with Py-

functionalized gels. Regardless of the fraction of DMSO in the environment, Py gels have no interactions with  $\alpha$ -CD gels, as the cavity of  $\alpha$ -CD is too small for Py to fit in.

Overall, the diverse molecular recognition properties of CDs have led to numerous polymer/material functions in the past few years, and we believe CD-based supramolecular materials will continue to be investigated yielding more applications in the near future.

## **1.3 Common Controlled Polymerization Methods for Cyclodextrin-based Polymers**

### **1.3.1 Cyclodextrin-based Polymers through ATRP**

Atom transfer radical polymerization (ATRP) is one of the most common controlled radical polymerization methods. It was first reported by Matyjaszewski and co-workers in 1995<sup>44</sup> and has been widely used since then. ATRP proceeds through a reversible activation/deactivation cycle mediated by a transition metal complex, typically copper complexes. The general mechanism is shown in **Figure 1.16**.<sup>45</sup> The initiation starts from that the catalyst abstracts the halogen (X) from the initiator (alkyl halide) to form an activated radical, where monomers (vinyl species) then add to the activated end and propagate. The catalyst alternates between oxidation states, enabling controlled polymer growth by deactivating and reactivating the polymer chain. This mechanism allows for precise control over polymer structure including chain length, architecture, and composition, while maintaining a low polydispersity.

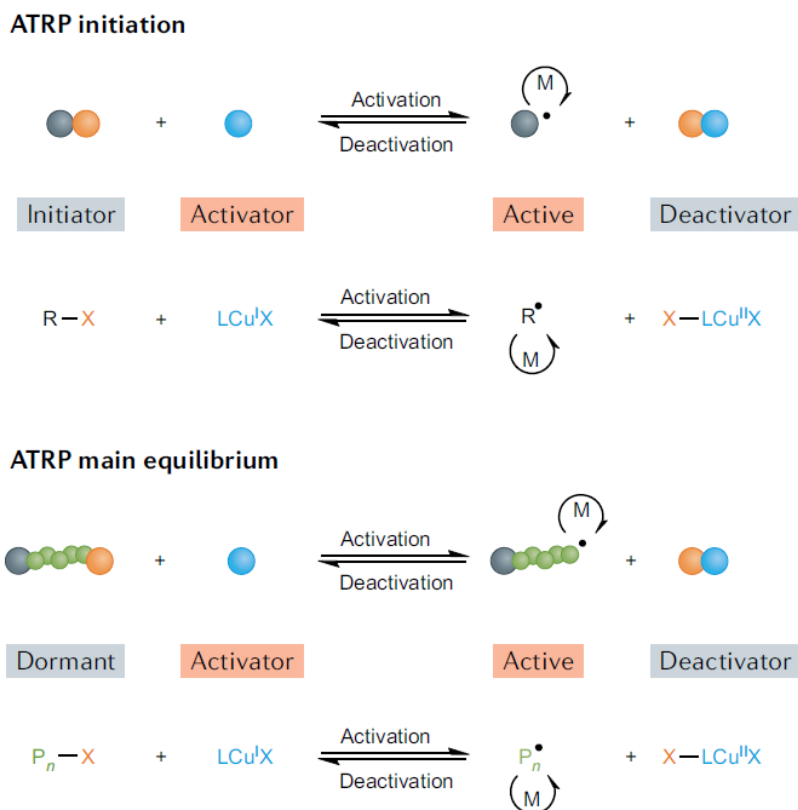


**Figure 1.16.** Mechanism of ATRP. Reused with permission.<sup>45</sup>

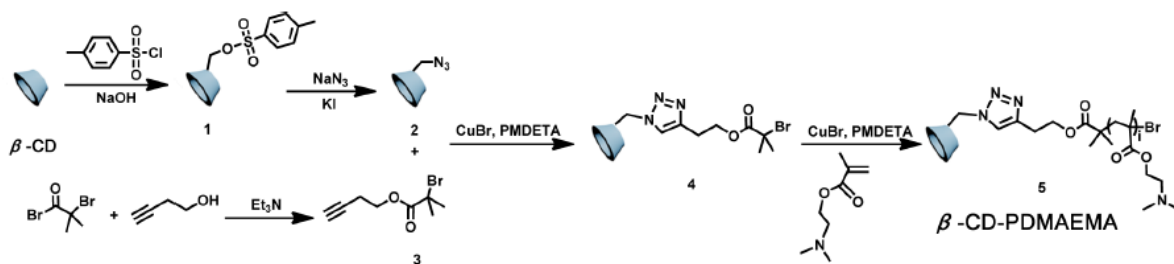


**Figure 1.17.** Synthetic route for  $\beta\text{-CD-PDMAEMA}$ . Reused with permission.<sup>46</sup>

In the context of CD-based polymers, ATRP is used most frequently. CDs can be functionalized as either an initiator or a monomer to participate in the ATRP process. Alternatively, CD can be appended via post-functionalization to a polymer chain synthesized using ATRP. As demonstrated in section 1.2, each CD contains multiple hydroxyl groups which are readily to be functionalized, thus it could be either mono-functionalized or multi-functionalized, and  $\beta\text{-CD}$  is typically the preferred option among various CDs.

While CD is functionalized to be an initiator in ATRP, it could lead to either CD-capped polymers or multi-arm polymers with varying degrees of modification. For example, Yuan and colleagues reported the synthesis of the  $\beta$ -CD-based initiator by CuAAC coupling of mono-azido-CD with but-3-ynyl-2-bromo-2-methylpropanoate, then it was polymerized with 2-(dimethylamino)ethyl methacrylate through ATRP to form the CD-capped polymers (**Figure 1.17**).<sup>46</sup> As for multi-arm polymers, attention should be given to optimize conditions to minimize star-star couplings. The first example was reported in 2001 by Haddleton and co-workers. In this case, all the 21 hydroxyl groups of  $\beta$ -CD were functionalized as shown in **Figure 1.18**, and 21-arm star polymers were successfully achieved with multiple monomers, such as methyl methacrylate (MMA) and styrene.<sup>47</sup> Later, more systems under varied conditions have been reported, including electrochemically mediated ATRP (eATRP),<sup>48</sup> ATRP in aqueous environment,<sup>49</sup> etc.

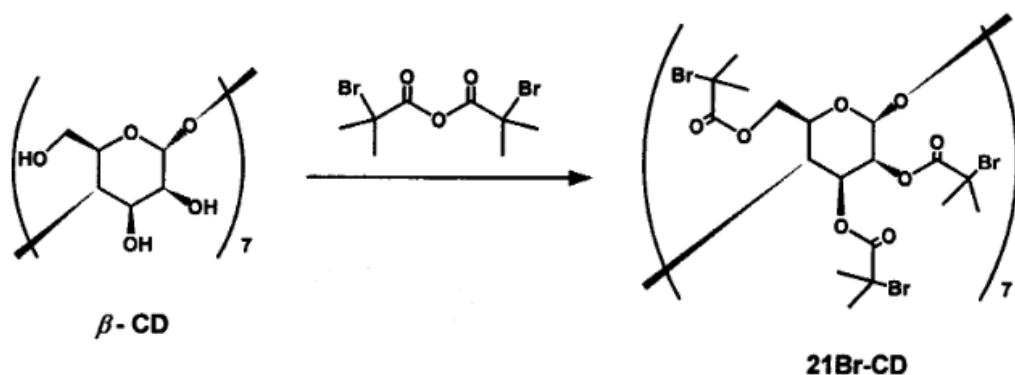


**Figure 1.18.** Synthesis of 21Br-CD. Reused with permission.

In the aforementioned cases, only one CD will be integrated onto the polymer as it functions as the initiation core. To create the CD-pendant polymers, of which each polymer contains multiple CDs, CD will be required to act as a monomer. It is challenging to prepare the mono-vinyl substituted CD monomers and often results in low molecular weight polymers because of steric hindrance accumulation. In 2014, Zhang *et al.* successfully synthesized a hydrophilic diblock copolymer via ATRP from of mono-methacrylate substituted CD from PEG macroinitiator (**Figure 1.19**).<sup>50</sup> An alternative way to make high density of CD on each polymer chain is through post-

modification. For example, Ren and co-workers successfully made the  $\beta$ -CD grafted poly(glycidyl methacrylate) (PGMA) polymers with 92% grafting density via ATRP and “click” reaction.<sup>51</sup>

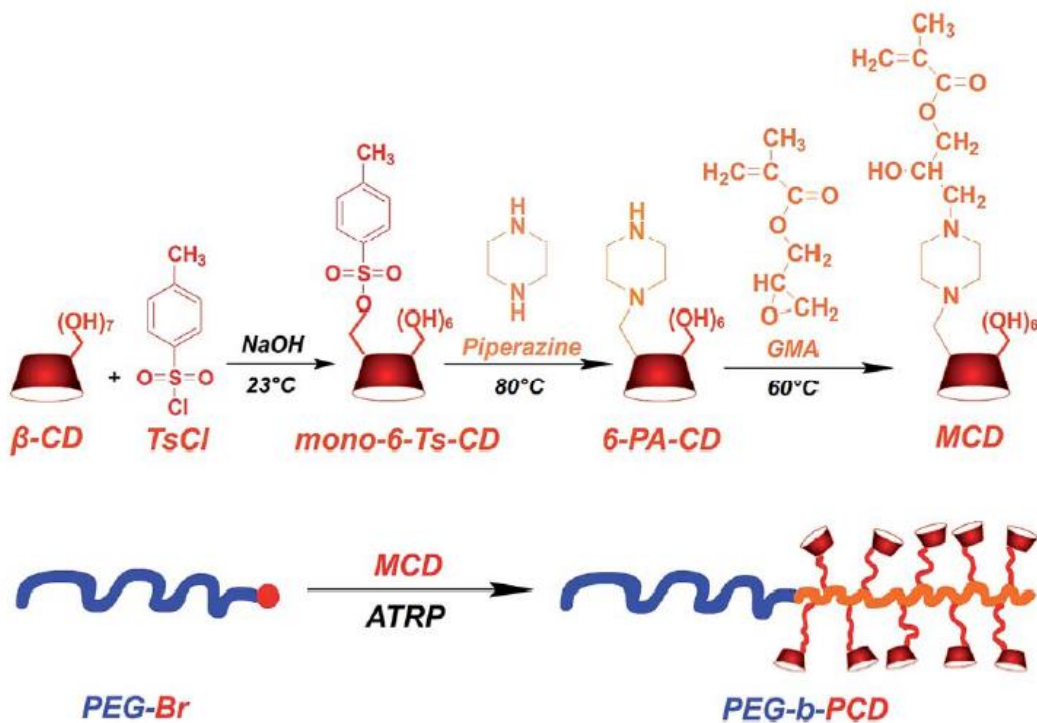


**Figure 1.19.** Synthesis of mono-methyl methacrylate substituted cyclodextrin (MCD) and atom transfer radical polymerization of MCD from PEG–Br initiator. Reused with permission.<sup>50</sup>

With so many pathways to generate CD-based polymers through ATRP, it has been investigated widely by scientists during the past few years. However, there are still some drawbacks needed to be considered by ATRP, such as the polymerization is air-sensitive and normally requires several freeze-pump thaw cycles. Therefore, additional research is needed to explore alternative methods to optimize these conditions.

### 1.3.2 Cyclodextrin-based Polymers through RAFT

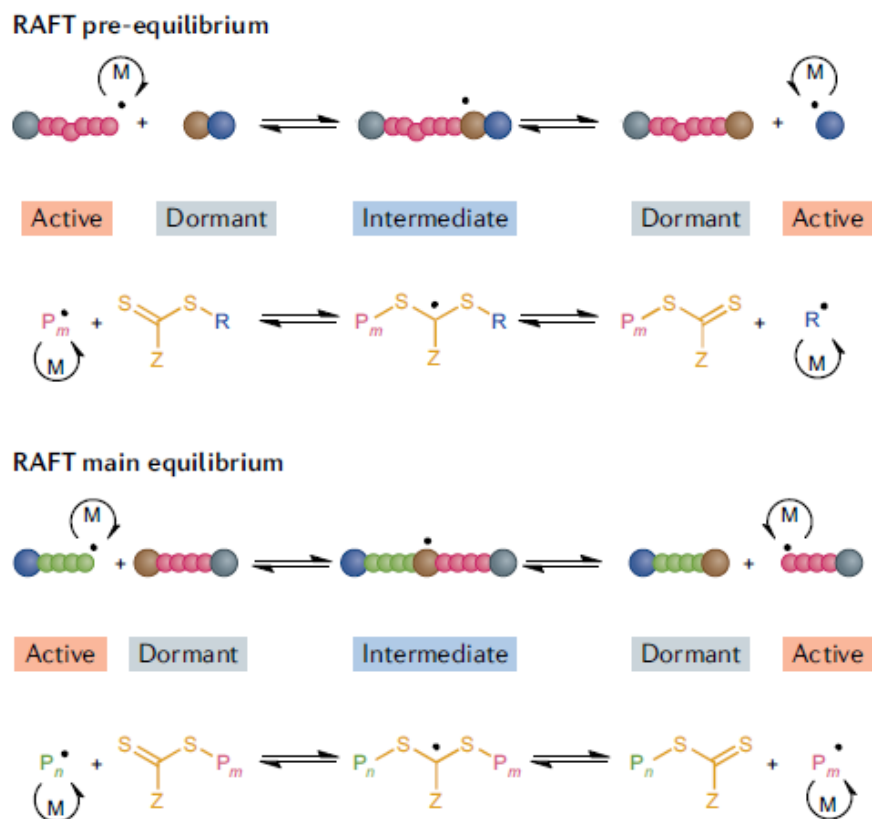


**Figure 1.20.** Mechanism of RAFT. Reused with permission.<sup>45</sup>

Another commonly used controlled radical polymerization method is reversible addition-fragmentation chain-transfer (RAFT) polymerization. Following the chain growth mechanism, RAFT was discovered after ATRP and was first reported in 1998.<sup>52</sup> The general mechanism of RAFT is illustrated in **Figure 1.20**, where an initiator (radical source), chain-transfer agent (CTA) and monomers are required in the polymerization process.<sup>45</sup> The selection of R and Z groups on CTA must be carefully considered in relation to the types of monomers used. Typically, a CTA (thiocarbonylthio or thiocarbonylsulfanyl compound) mediates the polymerization process by reversibly transferring active radical species to control the polymer chain growth. The control allows for the resulting polymers with narrow molecular weight distributions and well-defined architectures.

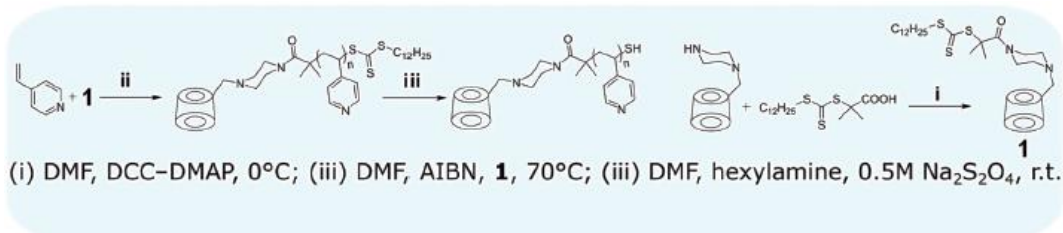


**Figure 1.21.** Introduction of CD end group with CTA agent. Reused with permission.<sup>53</sup>

Similar to ATRP, CD can be conveniently mono-functionalized to serve as a CTA, enabling the production of CD-capped polymers through RAFT. For example, Zeng *et al.* synthesized a CTA containing  $\beta$ -CD and used it in the RAFT polymerization of 4-vinylpyridine as shown in **Figure 1.21**.<sup>53, 54</sup> Though CD can also be multi-functionalized as a CTA to form multi-arm polymers, it is less attractive because steric hindrance around the RAFT agent along with the close proximity of neighboring RAFT agents usually leads to a higher occurrence of termination events. Specifically, as illustrated in **Figure 1.22**, CD can be either part of the Z or R group.<sup>53</sup> RAFT agent will be buried near the CD core when CD is a part of the Z group, while undesired formation of linear macroRAFT agent and star-star coupling happens when CD is a part of the R group. Therefore, the resultant polymers typically have short arm lengths.

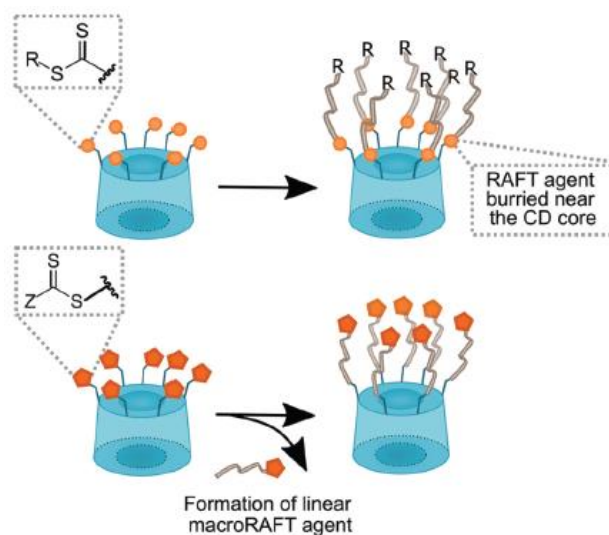


**Figure 1.22.** In a CD-RAFT agent, CD can be either part of the Z or the R group. Reused with permission.<sup>53</sup>



origin of ROMP dates back to the mid-1950s, when researchers began exploring the reactivities of olefins by combining various metals and reagents. The general mechanism of ROMP is shown in **Figure 1.23**.<sup>57</sup> The initiation step begins with the coordination of a cyclic olefin to a metal alkylidene complex, and this leads to a [2+2] cycloaddition, forming a metallacyclobutane intermediate and initiating the growth of a polymer chain. During propagation, the intermediate undergoes cycloreversion, generating a new metal alkylidene. These steps repeat until the polymerization stops, either due to complete consumption of monomers, reaction equilibrium, or the termination of the reaction. The living ROMP reactions can be intentionally quenched by a specialized reagent and ethyl vinyl ether is used most often.

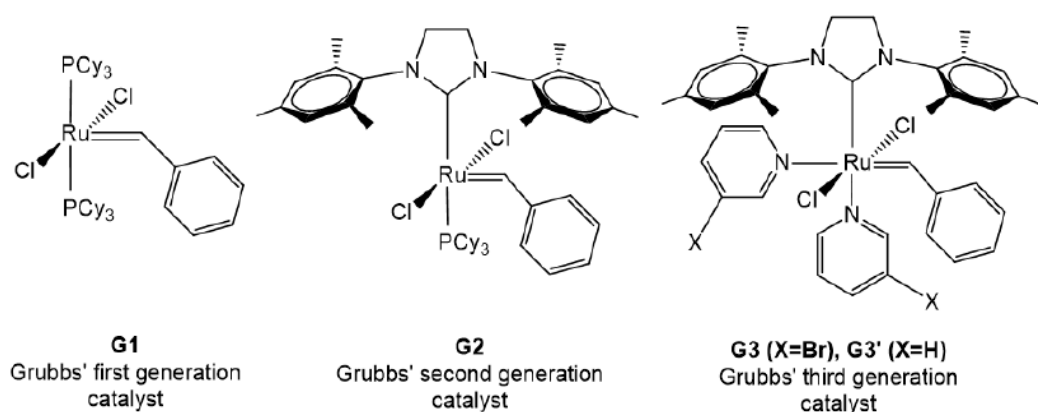


**Figure 1.24.** Grubbs' catalysts. Reused with permission.<sup>58</sup>

ROMP can be catalyzed by a variety of transition metal complexes, including titanium (Ti), tantalum (Ta), tungsten (W), molybdenum (Mo), Ruthenium (Ru) and so on. Among these, Ru complexes exhibit greater tolerance towards polar functional groups due to its low oxophilicity. The Grubbs' catalysts (**Figure 1.24**) stand out as the most renowned catalysts for ROMP as they successfully resolved issues concerning catalyst functional group tolerance, susceptibility to air and moisture, and the degree of polymerization (DP) of macro monomers. Currently, Grubbs' 3<sup>rd</sup> generation catalyst is predominately chosen for its high activity and functional group tolerance.<sup>58</sup>

The driving force for ROMP is that the polymerization process releases the ring strain in the cyclic olefin monomer, accompanied by a reduction in entropy. ROMP commonly employs cyclic olefins with considerable ring strain, including cyclobutene, cyclopentene, cis-cyclooctene, and norbornene. Among these, norbornene and its derivatives are widely preferred due to their high ROMP activity and the ease of incorporating substituents into the ring.<sup>57</sup>

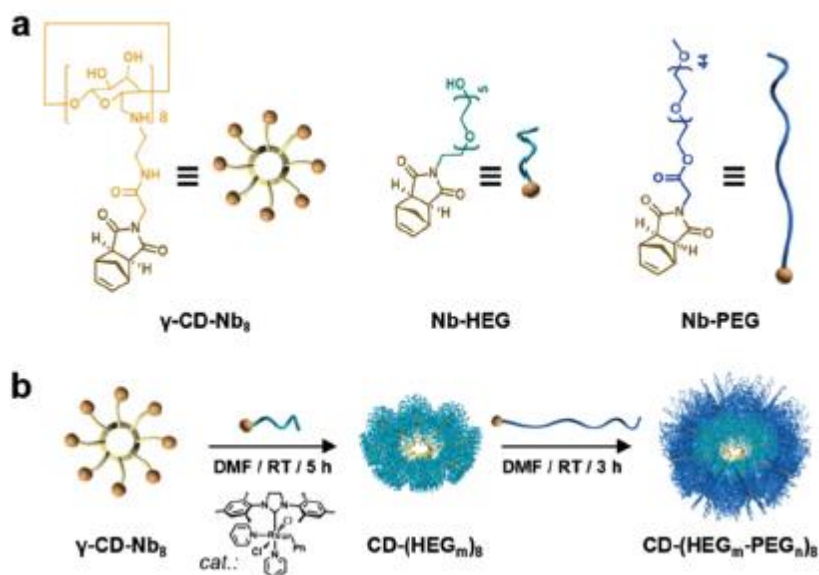


**Figure 1.25.** (a) Chemical structures and corresponding cartoon representations of  $\gamma$ -CD- $\text{Nb}_8$ , Nb-HEG, and Nb-PEG. (b) Core-first/graft-from synthetic strategy for DBASCs ( $\text{CD}-(\text{HEG}_m\text{-PEG}_n)_8$ ). Reused with permission.<sup>59</sup>

While numerous papers have addressed the synthesis of polymers and materials via ROMP for various applications, limited studies are related to CD-based polymers. In 2020, our group reported the synthesis of  $\gamma$ -CD-based star polymers, which is also the first example of macrocycle-based star polymers synthesized by ROMP.<sup>59</sup> As illustrated in **Figure 1.25**,  $\gamma$ -CD was functionalized with eight norbornenes to serve as the multifunctional core initiator, norbornene functionalized hexaethylene glycol (Nb-HEG) and poly(ethylene glycol) (Nb-PEG) were used as monomers to form the star polymers. Another example was reported by Matson and colleagues in 2021 (**Figure 1.26**), where  $\beta$ -CD was mono-functionalized with an azide and all other hydroxyl groups were protected with either acetyl (Ac) or methyl (Me) group.<sup>60</sup> Next, the protected CD was

coupled to the propargyl norbornene ether to yield the monomer, which further polymerized through ROMP and the protecting groups could be removed afterwards to form poly( $\beta$ -CD). The resulted polymers that reacted in acetone had molecular weights more than  $10^5$  g/mol with lower dispersity. However, the authors stated that attempting to directly polymerize the norbornene functionalized  $\beta$ -CD was unsuccessful, indicating that the protection/deprotection steps were necessary to achieve the desired CD-based polymers.

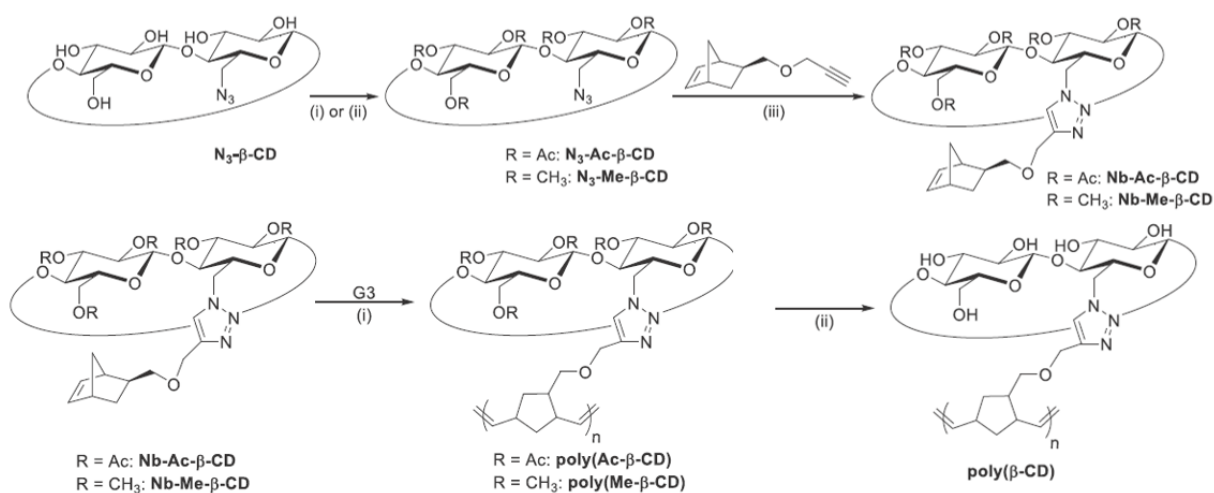


**Figure 1.26.** Synthetic routes of norbornene functionalized monomers and polymers through ROMP. Reused with permission.<sup>60</sup>

Though ROMP offers several advantages over ATRP and RAFT, including more functional group tolerance and reduced susceptibility to oxygen, it has not been utilized extensively to produce CD-based polymers as described in detail in this section. Therefore, there is much room for innovation in ROMP of CD-based polymers.

## 1.4 References

- (1) van Bemmelen, J. M. Das Hydrogel und das krystallinische Hydrat des Kupferoxyds. *Z. ANORG. ALLG. CHEM.* **1894**, 5 (1), 466-483.
- (2) Heidarian, P.; Kouzani, A. Z.; Kaynak, A.; Paulino, M.; Nasri-Nasrabadi, B. Dynamic Hydrogels and Polymers as Inks for Three-Dimensional Printing. *ACS Biomater. Sci. Eng.* **2019**, 5 (6), 2688-2707.

- (3) Uman, S.; Dhand, A.; Burdick, J. A. Recent advances in shear-thinning and self-healing hydrogels for biomedical applications. *J. Appl. Polym. Sci.* **2020**, *137* (25), 48668.
- (4) Ramli, H.; Zainal, N. F. A.; Hess, M.; Chan, C. H. Basic principle and good practices of rheology for polymers for teachers and beginners. *Chem. Teach. Int.* **2022**, *4* (4), 307-326.
- (5) Bertsch, P.; Diba, M.; Mooney, D. J.; Leeuwenburgh, S. C. G. Self-Healing Injectable Hydrogels for Tissue Regeneration. *Chem. Rev.* **2023**, *123* (2), 834-873.
- (6) Schneider, J. P.; Pochan, D. J.; Ozbas, B.; Rajagopal, K.; Pakstis, L.; Kretsinger, J. Responsive hydrogels from the intramolecular folding and self-assembly of a designed peptide. *J. Am. Chem. Soc.* **2002**, *124* (50), 15030-15037.
- (7) Yang, J.-A.; Yeom, J.; Hwang, B. W.; Hoffman, A. S.; Hahn, S. K. In situ-forming injectable hydrogels for regenerative medicine. *Prog. Polym. Sci.* **2014**, *39* (12), 1973-1986.
- (8) Martens, T. P.; Godier, A. F. G.; Parks, J. J.; Wan, L. Q.; Koeckert, M. S.; Eng, G. M.; Hudson, B. I.; Sherman, W.; Vunjak-Novakovic, G. Percutaneous Cell Delivery into the Heart Using Hydrogels Polymerizing in Situ. *Cell Transplant.* **2009**, *18* (3), 297-304.
- (9) Hillel, A. T.; Unterman, S.; Nahas, Z.; Reid, B.; Coburn, J. M.; Axelman, J.; Chae, J. J.; Guo, Q.; Trow, R.; Thomas, A.; et al. Photoactivated Composite Biomaterial for Soft Tissue Restoration in Rodents and in Humans. *Sci. Transl. Med.* **2011**, *3* (93), 93ra67.
- (10) Purcell, B. P.; Lobb, D.; Charati, M. B.; Dorsey, S. M.; Wade, R. J.; Zellars, K. N.; Doviak, H.; Pettaway, S.; Logdon, C. B.; Shuman, J. A.; et al. Injectable and bioresponsive hydrogels for on-demand matrix metalloproteinase inhibition. *Nat. Mater.* **2014**, *13* (6), 653-661.
- (11) Wang, L. L.; Sloand, J. N.; Gaffey, A. C.; Venkataraman, C. M.; Wang, Z.; Trubelja, A.; Hammer, D. A.; Atluri, P.; Burdick, J. A. Injectable, Guest–Host Assembled Polyethylenimine Hydrogel for siRNA Delivery. *Biomacromolecules* **2017**, *18* (1), 77-86.
- (12) Burdick, J. A.; Prestwich, G. D. Hyaluronic Acid Hydrogels for Biomedical Applications. *Adv. Mater.* **2011**, *23* (12), H41-H56.
- (13) Li, Y.; Fan, L.; Liu, S.; Liu, W.; Zhang, H.; Zhou, T.; Wu, D.; Yang, P.; Shen, L.; Chen, J.; et al. The promotion of bone regeneration through positive regulation of angiogenic–osteogenic coupling using microRNA-26a. *Biomaterials* **2013**, *34* (21), 5048-5058.
- (14) Ouyang, L.; Highley, C. B.; Rodell, C. B.; Sun, W.; Burdick, J. A. 3D Printing of Shear-Thinning Hyaluronic Acid Hydrogels with Secondary Cross-Linking. *ACS Biomater. Sci. Eng.* **2016**, *2* (10), 1743-1751.
- (15) Highley, C. B.; Rodell, C. B.; Burdick, J. A. Direct 3D Printing of Shear-Thinning Hydrogels into Self-Healing Hydrogels. *Adv. Mater.* **2015**, *27* (34), 5075-5079.
- (16) Mohamadhoseini, M.; Mohamadnia, Z. Supramolecular self-healing materials via host-guest strategy between cyclodextrin and specific types of guest molecules. *Coord. Chem. Rev.* **2021**, *432*, 213711.
- (17) Pedersen, C. J. Cyclic polyethers and their complexes with metal salts. *J. Am. Chem. Soc.* **1967**, *89* (26), 7017-7036.
- (18) Lou, X.-Y.; Song, N.; Yang, Y.-W. Fluorescence Resonance Energy Transfer Systems in Supramolecular Macrocyclic Chemistry. *Molecules* **2017**, *22* (10), 1640.
- (19) Chen, M. H.; Wang, L. L.; Chung, J. J.; Kim, Y.-H.; Atluri, P.; Burdick, J. A. Methods To Assess Shear-Thinning Hydrogels for Application As Injectable Biomaterials. *ACS Biomater. Sci. Eng.* **2017**, *3* (12), 3146-3160.

- (20) Loebel, C.; Rodell, C. B.; Chen, M. H.; Burdick, J. A. Shear-thinning and self-healing hydrogels as injectable therapeutics and for 3D-printing. *Nat. Protoc.* **2017**, *12* (8), 1521-1541.
- (21) Harada, A.; Takashima, Y.; Nakahata, M. Supramolecular Polymeric Materials via Cyclodextrin–Guest Interactions. *Acc. Chem. Res.* **2014**, *47* (7), 2128-2140.
- (22) Schmidt, B. V. K. J.; Barner-Kowollik, C. Dynamic Macromolecular Material Design—The Versatility of Cyclodextrin-Based Host–Guest Chemistry. *Angew. Chem. Int. Ed.* **2017**, *56* (29), 8350-8369.
- (23) Del Valle, E. M. M. Cyclodextrins and their uses: a review. *Process Biochem.* **2004**, *39* (9), 1033-1046.
- (24) Liu, G.; Yuan, Q.; Hollett, G.; Zhao, W.; Kang, Y.; Wu, J. Cyclodextrin-based host–guest supramolecular hydrogel and its application in biomedical fields. *Polym. Chem.* **2018**, *9* (25), 3436-3449.
- (25) Monnaert, V.; Betbeder, D.; Fenart, L.; Bricout, H.; Lenfant, A. M.; Landry, C.; Cecchelli, R.; Monflier, E.; Tilloy, S. Effects of  $\gamma$ - and Hydroxypropyl- $\gamma$ -cyclodextrins on the Transport of Doxorubicin across an in Vitro Model of Blood-Brain Barrier. *J. Pharmacol. Exp. Ther.* **2004**, *311* (3), 1115-1120.
- (26) Tanhuanpää, K.; Cheng, K. H.; Anttonen, K.; Virtanen, J. A.; Somerharju, P. Characteristics of pyrene phospholipid/ $\gamma$ -cyclodextrin complex. *Biophys. J.* **2001**, *81* (3), 1501-1510.
- (27) Cova, T. F.; Murtinho, D.; Pais, A. A.; Valente, A. J. Combining cellulose and cyclodextrins: Fascinating designs for materials and pharmaceuticals. *Front. Chem.* **2018**, *6*, 271.
- (28) Wankar, J.; Kotla, N. G.; Gera, S.; Rasala, S.; Pandit, A.; Rochev, Y. A. Recent Advances in Host–Guest Self-Assembled Cyclodextrin Carriers: Implications for Responsive Drug Delivery and Biomedical Engineering. *Adv. Funct. Mater.* **2020**, *30* (44), 1909049.
- (29) Petter, R. C.; Salek, J. S.; Sikorski, C. T.; Kumaravel, G.; Lin, F. T. Cooperative binding by aggregated mono-6-(alkylamino)- $\beta$ -cyclodextrins. *J. Am. Chem. Soc.* **1990**, *112* (10), 3860-3868.
- (30) Tripodo, G.; Wischke, C.; Neffe, A. T.; Lendlein, A. Efficient synthesis of pure monotosylated  $\beta$ -cyclodextrin and its dimers. *Carbohydr. Res.* **2013**, *381*, 59-63.
- (31) Rekharsky, M. V.; Inoue, Y. Complexation Thermodynamics of Cyclodextrins. *Chem. Rev.* **1998**, *98* (5), 1875-1918.
- (32) Davis, M. E.; Brewster, M. E. Cyclodextrin-based pharmaceuticals: past, present and future. *Nat. Rev. Drug Discov.* **2004**, *3* (12), 1023-1035.
- (33) Domiński, A.; Konieczny, T.; Kurcok, P.  $\alpha$ -Cyclodextrin-Based Polypseudorotaxane Hydrogels. *Mater.* **2020**, *13* (1), 133.
- (34) Harada, A.; Li, J.; Kamachi, M. The molecular necklace: a rotaxane containing many threaded  $\alpha$ -cyclodextrins. *Nature* **1992**, *356* (6367), 325-327.
- (35) Harada, A.; Li, J.; Kamachi, M. Preparation and properties of inclusion complexes of polyethylene glycol with  $\alpha$ -cyclodextrin. *Macromolecules* **1993**, *26* (21), 5698-5703.
- (36) Li, J.; Harada, A.; Kamachi, M. Sol–gel transition during inclusion complex formation between  $\alpha$ -cyclodextrin and high molecular weight poly (ethylene glycol) s in aqueous solution. *Polym. J.* **1994**, *26* (9), 1019-1026.
- (37) Zhou, J.; Jia, J.; He, J.; Li, J.; Cai, J. Cyclodextrin inclusion complexes and their application in food safety analysis: recent developments and future prospects. *Foods* **2022**, *11* (23), 3871.

- (38) Khodaverdi, E.; Heidari, Z.; Tabassi, S. A. S.; Tafaghodi, M.; Alibolandi, M.; Tekie, F. S. M.; Khameneh, B.; Hadizadeh, F. Injectable supramolecular hydrogel from insulin-loaded triblock PCL-PEG-PCL copolymer and  $\gamma$ -cyclodextrin with sustained-release property. *Aaps Pharmscitech* **2015**, *16*, 140-149.
- (39) Nakahata, M.; Takashima, Y.; Yamaguchi, H.; Harada, A. Redox-responsive self-healing materials formed from host-guest polymers. *Nat. Commun.* **2011**, *2* (1), 511.
- (40) Zheng, Y.; Hashidzume, A.; Harada, A. pH-Responsive Self-Assembly by Molecular Recognition on a Macroscopic Scale. *Macromol. Rapid Commun.* **2013**, *34* (13), 1062-1066.
- (41) Yamaguchi, H.; Kobayashi, Y.; Kobayashi, R.; Takashima, Y.; Hashidzume, A.; Harada, A. Photoswitchable gel assembly based on molecular recognition. *Nat. Commun.* **2012**, *3* (1), 603.
- (42) Daoud-Mahammed, S.; Grossiord, J.; Bergua, T.; Amiel, C.; Couvreur, P.; Gref, R. Self-assembling cyclodextrin based hydrogels for the sustained delivery of hydrophobic drugs. *J. Biomed. Mater. Res. Part A* **2008**, *86* (3), 736-748.
- (43) Zheng, Y.; Hashidzume, A.; Takashima, Y.; Yamaguchi, H.; Harada, A. Switching of macroscopic molecular recognition selectivity using a mixed solvent system. *Nat. Commun.* **2012**, *3* (1), 831.
- (44) Wang, J.-S.; Matyjaszewski, K. Controlled/" living" radical polymerization. atom transfer radical polymerization in the presence of transition-metal complexes. *J. Am. Chem. Soc.* **1995**, *117* (20), 5614-5615.
- (45) Truong, N. P.; Jones, G. R.; Bradford, K. G.; Konkolewicz, D.; Anastasaki, A. A comparison of RAFT and ATRP methods for controlled radical polymerization. *Nat. Rev. Chem.* **2021**, *5* (12), 859-869.
- (46) Liu, B.-w.; Zhou, H.; Zhou, S.-t.; Zhang, H.-j.; Feng, A.-C.; Jian, C.-m.; Hu, J.; Gao, W.-p.; Yuan, J.-y. Synthesis and self-assembly of CO<sub>2</sub>-temperature dual stimuli-responsive triblock copolymers. *Macromolecules* **2014**, *47* (9), 2938-2946.
- (47) Ohno, K.; Wong, B.; Haddleton, D. M. Synthesis of well-defined cyclodextrin-core star polymers. *J. Polym. Sci., Part A: Polym. Chem.* **2001**, *39* (13), 2206-2214.
- (48) Chmielarz, P.; Park, S.; Sobkowiak, A.; Matyjaszewski, K. Synthesis of  $\beta$ -cyclodextrin-based star polymers via a simplified electrochemically mediated ATRP. *Polymer* **2016**, *88*, 36-42.
- (49) Li, J.; Xiao, H.; Kim, Y. S.; Lowe, T. L. Synthesis of water-soluble cationic polymers with star-like structure based on cyclodextrin core via ATRP. *J. Polym. Sci., Part A: Polym. Chem.* **2005**, *43* (24), 6345-6354.
- (50) Zhang, M.; Xiong, Q.; Shen, W.; Zhang, Q. Facile synthesis of well-defined cyclodextrin-pendant polymer via ATRP for nanostructure fabrication. *RSC Adv.* **2014**, *4* (58), 30566-30572.
- (51) Ma, Q.; Yuan, X.; Zhao, Y.; Ren, L. High grafting density of cyclodextrin polymer for fast removal of aromatic compounds from water. *RSC Adv.* **2015**, *5* (59), 47998-48004.
- (52) Chiefari, J.; Chong, Y.; Ercole, F.; Krstina, J.; Jeffery, J.; Le, T. P.; Mayadunne, R. T.; Meijs, G. F.; Moad, C. L.; Moad, G. Living free-radical polymerization by reversible addition-fragmentation chain transfer: the RAFT process. *Macromolecules* **1998**, *31* (16), 5559.
- (53) Przybyla, M. A.; Yilmaz, G.; Becer, C. R. Natural cyclodextrins and their derivatives for polymer synthesis. *Polym. Chem.* **2020**, *11* (48), 7582-7602.

- (54) Zeng, J.; Shi, K.; Zhang, Y.; Sun, X.; Zhang, B. Construction and micellization of a noncovalent double hydrophilic block copolymer. *Chem. Commun.* **2008**, (32), 3753-3755.
- (55) Asman, S.; Mohamad, S.; Muhamad Sarih, N. Effects of RAFT agent on the selective approach of molecularly imprinted polymers. *Polymers* **2015**, 7 (3), 484-503.
- (56) Yhaya, F.; Binauld, S.; Kim, Y.; Stenzel, M. H. Shell Cross-linking of Cyclodextrin-Based Micelles via Supramolecular Chemistry for the Delivery of Drugs. *Macromol. Rapid Commun.* **2012**, 33 (21), 1868-1874.
- (57) Bielawski, C. W.; Grubbs, R. H. Living ring-opening metathesis polymerization. *Prog. Polym. Sci.* **2007**, 32 (1), 1-29.
- (58) Choinopoulos, I. Grubbs' and Schrock's catalysts, ring opening metathesis polymerization and molecular brushes—synthesis, characterization, properties and applications. *Polymers* **2019**, 11 (2), 298.
- (59) Li, R.; Li, X.; Zhang, Y.; Delawder, A. O.; Colley, N. D.; Whiting, E. A.; Barnes, J. C. Diblock brush-arm star copolymers via a core-first/graft-from approach using  $\gamma$ -cyclodextrin and ROMP: a modular platform for drug delivery. *Polym. Chem.* **2020**, 11 (2), 541-550.
- (60) Alaboalirat, M.; Matson, J. B. Poly ( $\beta$ -Cyclodextrin) Prepared by Ring-Opening Metathesis Polymerization Enables Creation of Supramolecular Polymeric Networks. *ACS Macro Lett.* **2021**, 10 (12), 1460-1466.

# Chapter 2: Saltwater-Induced Rapid

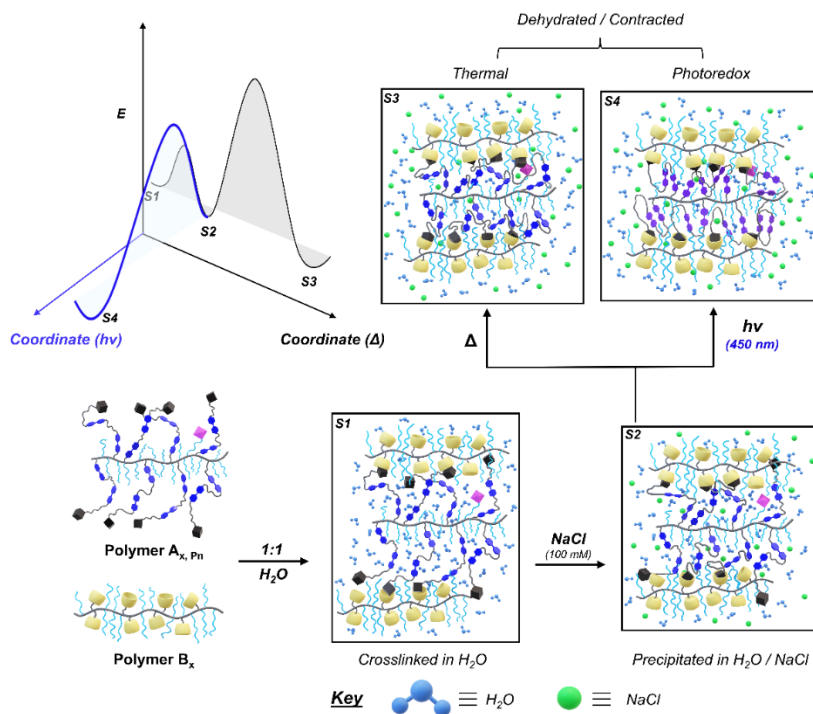
## Gelation of Photoredox-Responsive

### Mucomimetic Hydrogels

This chapter is based on work described in the following publication:

**Zhang, Y.;** Li, R.; Trick, T. C.; Nosiglia, M. A.; Palmquist, M. S.; Wong, M. L.; Dorsainvil, J. M.; Tran, S. L.; Danielson, M. K.; Barnes, J. C. Saltwater-Induced Rapid Gelation of Photoredox-Responsive Mucomimetic Hydrogels. *Adv. Mater.* **2023**, 2307356.

J.C.B. conceived the idea for the project, J.C.B., Y.Z. and R.L. designed the monomers and polymers. Y.Z., R.L., T.C.T., M.L.W. and J.M.D. carried out the synthesis of the monomers, Y.Z. synthesized the polymers and hydrogels. Y.Z., R.L., T.C.T. and M.K.D. characterized the monomers and polymers. Y.Z. and M.A.N. carried out rheological experiments. Y.Z., M.S.P. and M.A.N. performed lap-shear experiments. Y.Z. and S.L.T. prepared figures for the manuscript. J.C.B. and Y.Z. co-wrote the manuscript and Supplementary Information documents, and all authors contributed to the refinement of each document.



## 2.1 Abstract

Shear-thinning hydrogels represent an important class of injectable soft materials that are often used in a wide range of biomedical applications. Creation of new shear-thinning materials often requires that factors such as viscosity, injection rate/force, and needle gauge be evaluated to achieve efficient delivery, while simultaneously protecting potentially sensitive cargo. Here, a new approach to establishing shear-thinning hydrogels is reported where a host–guest cross-linked network initially remains soluble in deionized water but is kinetically trapped as a viscous hydrogel once exposed to saltwater. The shear-thinning properties of the hydrogel is then “switched on” in response to heating or exposure to visible light. These hydrogels consist of polynorbornene-based bottlebrush copolymers with porphyrin- and oligoviologen-containing side chains that are cross-linked through the reversible formation of  $\beta$ -cyclodextrin–adamantane inclusion complexes. The resultant viscous hydrogels display broad adhesive properties across polar and nonpolar substrates, mimicking that of natural mucous and thus making it easier to distribute onto a wide range of surfaces. Additional control over the hydrogel's mechanical properties (storage/loss moduli) and performance (adhesion) is achieved post-injection using a low-energy (blue light) photoinduced electron-transfer process. This work envisions these injectable copolymers and multimodal hydrogels can serve as versatile next-generation biomaterials capable of light-based mechanical manipulation post-injection.

## 2.2 Introduction

Shear-thinning hydrogels<sup>1</sup> are a type of dynamic soft material that exhibit a decrease in viscosity when subjected to shear stress, meaning they become thinner and more fluid-like when agitated or injected but become thicker and more solid-like when at rest (a.k.a., self-healing). This property makes them ideal for a variety of applications,<sup>2, 3</sup> including drug delivery, tissue engineering, bioprinting, cosmetics, etc. The dynamic nature of shear-thinning hydrogels arises from

exchangeable covalent or non-covalent bonds, the latter of which typically involve reversible through-space interactions, such as hydrogen bonding,<sup>4, 5</sup> electrostatics,<sup>6, 7</sup> or the formation of host–guest complexes.<sup>8-11</sup> An elegant example of such gelation employing host–guest complexes was reported<sup>12</sup> previously by Burdick and co-workers who used  $\beta$ -cyclodextrin ( $\beta$ -CD) and adamantane (Ad)-functionalized hyaluronic acid (HA) to establish dynamic crosslinks and thus soft hydrogels which were used for the delivery of cells and other biologically relevant molecules. Given the ease of synthesis and scalability of these types of host–guest networks, this approach, in principle, should be generally applicable to many different classes of polymers for the purpose of high-throughput production of dynamic biomaterials with novel properties and potential use in clinical applications. However, before proceeding with bioengineering applications, the ‘injectability’ of new shear-thinning hydrogels must be evaluated.<sup>13</sup> This assessment includes identifying an appropriate viscosity and storage/loss moduli for a particular hydrogel composition, as well as other factors like the injection force, which is dictated by the length and gauge of the needle and the rate of injection. Thus, optimization of not only the composition and mechanical properties of the material must be considered, but also iteration of the physical parameters associated with the injection method is required before a consistent delivery and retention of the shear-thinning hydrogel can be achieved.

Mucin glycoproteins are an example of a dynamic, stimuli-responsive hydrogel<sup>14, 15</sup> found in nature which serves an important role in the body’s defense against dust, debris, and foreign pathogens. Typically, these glycoproteins—whose backbone are made of long peptide chains derived from proline, threonine, and/or serine amino acid residues and can reach molecular weights between 200–500 kDa—are the main component in mucus-based hydrogels<sup>16, 17</sup> that comprise mostly water (93–97% w/v). However, most of the glycoprotein dry mass arises from the N- and O-linked oligosaccharides (made from glucose, galactose, mannose, etc.) that forms highly glycosylated side chains resembling a bottlebrush-like architecture (**Figure 2.1a**, green) that exhibit

noncovalent interactions, such as hydrogen bonding and electrostatic repulsion. Moreover, cysteine-rich domains at the termini of these natural bottlebrush polymers lead to dynamic covalent cross-linking through disulfide linkages (**Figure 2.1a**, yellow) which produces an extended biopolymer network. It is precisely these design components that make mucous-based hydrogels very soft and adaptable to a variety of surfaces. Additionally, the physicochemical properties of mucus-based hydrogels depend on a variety of external factors,<sup>17</sup> including pH, ionic strength, charge, and the number of disulfide cross-links. One astonishing example<sup>18</sup> of a mucin-derived hydrogel that forms rapidly in a high ionic strength environment has been observed when hagfish respond to a predator by releasing tightly bound protein threads and mucin glycoproteins. This rapid, stimuli-responsive event is facilitated by a high ionic strength environment that is critical to the mechanism of release and formation of protective slime. In contrast, synthetic polyelectrolyte gels<sup>19</sup> typically undergo deswelling in high ionic strength media on account of electrostatic screening that occurs between the polymer-bound charges.<sup>20</sup>

Synthetic stimuli-responsive hydrogels<sup>21</sup> can also be programmed to undergo changes in their structure, properties, and functions in response to external stimuli. These stimuli can be physical: such as changes in temperature<sup>19</sup> or the application of shearing forces or a magnetic field,<sup>22</sup> or chemical: such as a change in pH,<sup>23</sup> or the presence of a redox agent<sup>24</sup> or a reactive biomolecule.<sup>25</sup> Light<sup>26</sup> may also be used to remotely trigger a physical response in hydrogels, such as the photothermal-based precipitation of an embedded thermoresponsive polymer<sup>27</sup> or the isomerization of a photoresponsive building block such as azobenzene<sup>28-30</sup> or spiropyran.<sup>31, 32</sup> It can also be used to elicit a chemical response: such as the disconnection of photolabile covalent bonds<sup>33, 34</sup> or driving a photoredox-based self-assembly process.<sup>35-38</sup> The prospects of combining bottlebrush architectures and host–guest noncovalent interactions, such as the Ad/ $\beta$ -CD complex (**Figure 2.1b**), with light-responsive functionality into a single hydrogel platform represents a powerful approach to building scalable, adaptive, and bioinspired materials whose injectability is

operationally simpler overall and its shear-thinning properties can be controlled spatiotemporally post-injection.<sup>11</sup>

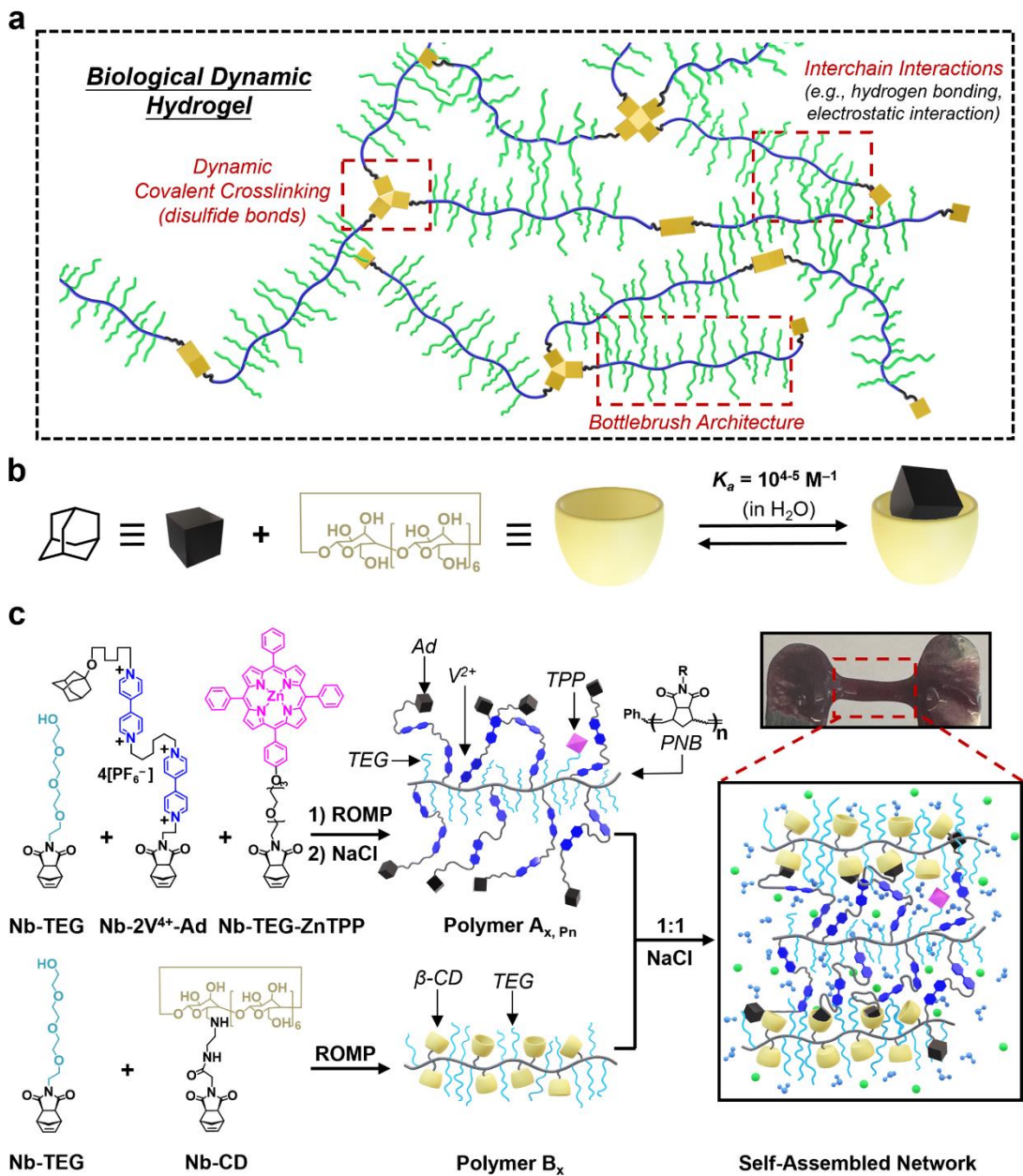


**Figure 2.1.** Self-assembly of natural and synthetic hydrogels comprising bottlebrush polymers. (a) Graphical representation of mucin proteins cross-linked by disulfide linkages (yellow). Oligosaccharide side chains (green) appended to the polypeptide backbone (blue) give a bottlebrush-like architecture, which aids hydrogel network formation. (b) Example of dynamic host–guest molecular recognition between  $\beta$ -cyclodextrin ( $\beta$ -CD, host; yellow) and adamantane (Ad, guest; black). In  $H_2O$ , the equilibrium affinity constant ( $K_a$ ) is on the order of  $10^{4-5} M^{-1}$ . (c) This work: Ring-opening metathesis polymerization (ROMP) of norbornene-based functional monomers in DMF yielded a set of bottlebrush supramolecular copolymers that, after dialysis, self-assembled 1:1 in saltwater (but not deionized  $H_2O$ ) to afford a photoresponsive mucomimetic hydrogel with broad adhesive properties. *Note:* For copolymers  $A_{x, Pn}$  and  $B_x$ , the x and n values are summarized in Table 1 with detailed information on monomer units.

Inspired by the dynamic and versatile bottlebrush architectures of mucous-based hydrogels, we describe here a novel stimuli-responsive hydrogel that is both saltwater- and photoredox-responsive (i.e., blue light) and which exhibits broad adhesive properties on multiple materials with polar and non-polar surfaces, analogous to natural mucous-based hydrogels. The hydrogel consists of two norbornene (Nb)-based bottlebrush copolymers ( $A_{x, Pn}$  and  $B_x$ ) bearing Ad and  $\beta$ -CD groups as sidechains (respectively) that self-assemble into soluble host–guest-cross-linked networks upon mixing in  $H_2O$ , but which do not form a kinetically trapped viscous hydrogel (**Figure 2.1c**) until the ionic strength of the solution is raised above at least  $20 \times 10^{-3} M$  NaCl. The lack of gelation in deionized  $H_2O$  results from the Ad group being tethered to a polynorbornene (PNB) backbone via polar oligoviologen dimer linkers bearing four positive charges per repeat subunit. This unique gelation mechanism is akin to the “salting out” of proteins and yet was not dependent on the concentration of polymer in the pre-gel solution. The implication of this feature is that the cross-linked network could be readily ejected from the syringe as a soluble aqueous solution prior to rapid gelation in saltwater without having to optimize any parameters associated with the injection method. Moreover, a zinc-based tetraphenyl porphyrin photocatalyst was introduced as a side chain in the “guest” copolymer containing Ad groups so it could serve as a photocatalyst capable of transferring an electron to the electron-deficient oligoviologen side chains upon absorption of visible light, the latter of which resulted in contraction and stiffening of the self-assembled network by way of a novel viologen-based radical molecular recognition mechanism. A library of structural analogues was synthesized to identify the correct ratio of host–guest pairs as it pertains to gelation, and the corresponding viscous hydrogels ( $G'' > G'$ ) were fabricated and

tested on polar and nonpolar surfaces to evaluate their broad adhesive properties pre/post heat curing and in response to blue light. Notably, heat curing and photoactivation of the mucomimetic hydrogels “switched on” elastic ( $G' > G''$ ) and shear-thinning properties and increased its adhesive strength, as H<sub>2</sub>O was removed from the hydrogel either through direct evaporation or through the photoinduced contraction mechanism, respectively, ultimately leading to an increase in host–guest cross-linking. We believe this fundamentally new approach to mechanical manipulation of these versatile and scalable mucomimetic hydrogels post-injection opens the door to such applications as 3D (bio)printing and manufacturing, 4D tissue culture, therapeutic delivery, and regenerative medicine.

## 2.3 Results and Discussion

### 2.3.1 Molecular Design of Photoredox-Responsive Viscous Hydrogels

Previously, we have shown that visible light can be used in a novel photoredox mechanism<sup>35-38</sup> to control the network structure and therefore the macroscopic properties (e.g., size, stiffness) of covalently cross-linked hydrogels. This level of control was achieved by introducing a photocatalyst—specifically, a zinc-based tetraphenyl porphyrin (ZnTPP)—into the gel network, which was cross-linked by styrenated oligoviologens. Upon irradiation with blue or red light, the porphyrin transferred an electron to the viologen subunits in the cross-linker via a photoinduced electron transfer (PET) process (i.e.,  $V^{2+}$  to  $V^{\bullet+}$ ). The corresponding viologen radical cations underwent intra- and intermolecular stacking as the result of radical–radical based molecular recognition between two unpaired electrons. Moreover, photoreduction led to a loss of half of the positive charges in the oligoviologen cross-linker, which decreased the electrostatic repulsion and expelled the corresponding counteranions.

Building off this work, a photoredox-responsive hydrogel was designed (**Figure 2.1c**), where the method of cross-linking relied on noncovalent host–guest complexes formed between Ad and  $\beta$ -

CD groups as side chains of two separate PNB-based statistical copolymers (**Table 2.1**) with the general formula: poly( $2V^{4+}Ad_m\text{-TEG}_{2-4m}\text{-ZnTPP}_n$ )<sub>stat</sub> (**A<sub>x, P<sub>n</sub></sub>**) and poly( $CD_m\text{-TEG}_{2-4m}$ )<sub>stat</sub> (**B<sub>x</sub>**). On account of the functional-group tolerant nature of Grubbs' catalysts, each copolymer was synthesized using ring-opening metathesis polymerization (ROMP)<sup>39, 40</sup> of Nb-based monomers. Copolymer **A<sub>x, P<sub>n</sub></sub>** was designed with polar, dicationic viologen subunits linking the Ad group to the polymerizable Nb group (**Nb-2V<sup>4+</sup>-Ad**) as well as with a photocatalyst-based monomer, **Nb-TEG-ZnTPP**, where the subscripted *n* refers to 0, 1, 2, or 4 porphyrin repeat units on average per copolymer chain. Copolymer **B<sub>x</sub>** was designed with β-CD and tetraethylene glycol (TEG) functionalized monomers (**Nb-CD** and **Nb-TEG**, respectively) to serve as the "host" copolymer. It is important to note that the **Nb-TEG** monomer was necessary to improve the H<sub>2</sub>O solubility of copolymer **B<sub>x</sub>**, while also functioning as a spacer subunit in between the larger CD macrocycles without negatively impacting the CD's ability to form host–guest complexes. The 30:90 ratio of CD:TEG subunits was selected after extensive screening of reaction conditions and stoichiometries to provide the necessary amount of host macrocycles required to form a hydrogel and to maintain the copolymer's solubility in H<sub>2</sub>O, respectively. This optimization process began by first determining the maximum number of CD subunits that could be polymerized into copolymer **B<sub>x</sub>**, as **Nb-CD** proved to be more challenging to polymerize than **Nb-2V<sup>4+</sup>-Ad** to make the complimentary copolymer **A<sub>x, P<sub>n</sub></sub>**. Based on <sup>1</sup>H NMR analyses of aliquots taken from quenched ROMP reactions (see Section 2.4.3, **Figure 2.6**), it was clear that 30 CD subunits was the upper bound for the average number of macrocycles that can be incorporated per chain. For example, the olefin proton resonances associated with the **Nb-CD** monomer remained in the <sup>1</sup>H NMR spectra following attempts to polymerize 35 and 40 CD subunits into copolymers **B<sub>5</sub>** and **B<sub>6-8</sub>**, respectively, regardless of the amount of TEG present. Next, the range of TEG:CD ratios was investigated for copolymer **B<sub>x</sub>** (**Table 2.1**), when only 20 and 30 CD repeat subunits were present (**B<sub>1</sub>** and **B<sub>2</sub>-B<sub>4</sub>**, respectively). Although all these polymerizations went to completion, rheological characterization of the 1:1 mixture of **B<sub>x</sub>** with the corresponding **A<sub>x, P<sub>1</sub></sub>** copolymer in saltwater

revealed changes in the storage and loss moduli pre- and post-heating. Specifically, copolymers bearing only 20 CD subunits (**B<sub>1</sub>**) did not gel efficiently, while copolymers bearing 30 CD subunits and four times as many TEG repeat subunits (**B<sub>4</sub>**) could not achieve efficient cross-linking after heat curing, as evidenced by much lower storage/loss moduli (**Table 2.2**). The latter result we hypothesize is because of steric crowding when too many TEG side chains are present, thus preventing efficient formation of the host–guest inclusion complexes between Ad-CD functional groups. The results of this screening demonstrated that copolymers **B<sub>2</sub>** and **B<sub>3</sub>** were the most optimal in terms of the polymerization and gel formation. Copolymer **B<sub>3</sub>** was selected to move forward with direct comparisons to other control copolymers (**C<sub>x, P1</sub>** and **D<sub>P1</sub>**, **Tables 2.1** and **2.2**) since it maintained good solubility at higher concentrations in H<sub>2</sub>O.

<i>Monomer</i>	<i>Monomer Units of Statistical Copolymers</i>							
	<b>A<sub>1, P1</sub></b>	<b>A<sub>2, P1</sub></b>	<b>A<sub>3, P0</sub></b>	<b>A<sub>3, P1</sub></b>	<b>A<sub>3, P2</sub></b>	<b>A<sub>3, P4</sub></b>	<b>A<sub>4, P1</sub></b>	<b>A<sub>5, P1</sub></b>
Nb-2V-Ad·4PF <sub>6</sub> ( <b>8</b> )	20	30	30	30	30	30	30	35
Nb-TEG ( <b>19</b> )	60	60	90	90	90	90	120	105
Nb-TEG-ZnTPP ( <b>22</b> )	1	1	0	1	2	4	1	1
<i>Monomer</i>	<b>B<sub>1</sub></b>	<b>B<sub>2</sub></b>	<b>B<sub>3</sub></b>	<b>B<sub>4</sub></b>	<b>B<sub>5</sub></b>	<b>C<sub>1, P1</sub></b>	<b>C<sub>2, P1</sub></b>	<b>D<sub>P1</sub></b>
Nb-CD ( <b>16</b> )	20	30	30	30	35	—	—	—
Nb-Hexyl-Ad ( <b>23</b> )	—	—	—	—	—	30	—	—
Nb-TEG-Ad ( <b>26</b> )	—	—	—	—	—	—	30	—
Nb-2V-Me·4PF <sub>6</sub> ( <b>10</b> )	—	—	—	—	—	—	—	30
Nb-TEG ( <b>19</b> )	60	60	90	120	105	90	90	90
Nb-TEG-ZnTPP ( <b>22</b> )	—	—	—	—	—	1	1	1

**Table 2.1.** Summary of statistical copolymers synthesized in this investigation. Note, the **C<sub>1, P1</sub>**, **C<sub>2, P1</sub>**, and **D<sub>P1</sub>** are control copolymers lacking oligoviologen side chains (**C<sub>1, P1</sub>** and **C<sub>2, P1</sub>**) or Ad groups (**D<sub>P1</sub>**).

### 2.3.2 Saltwater-Induced Mechanism of Gelation

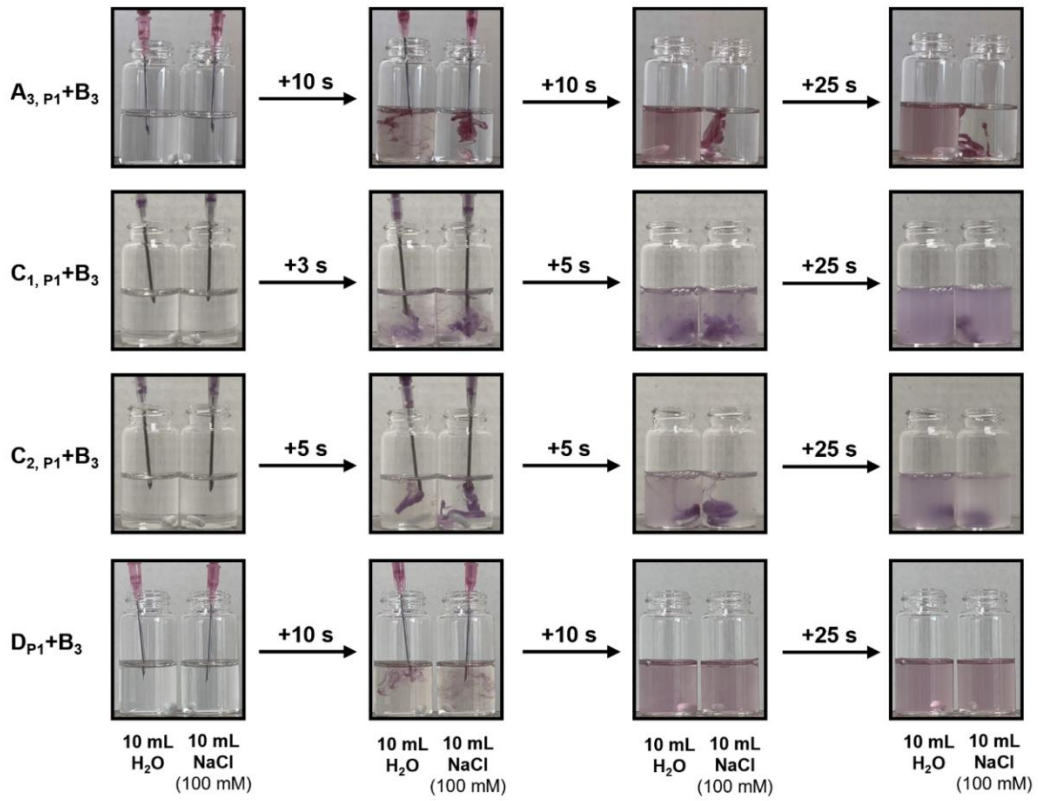
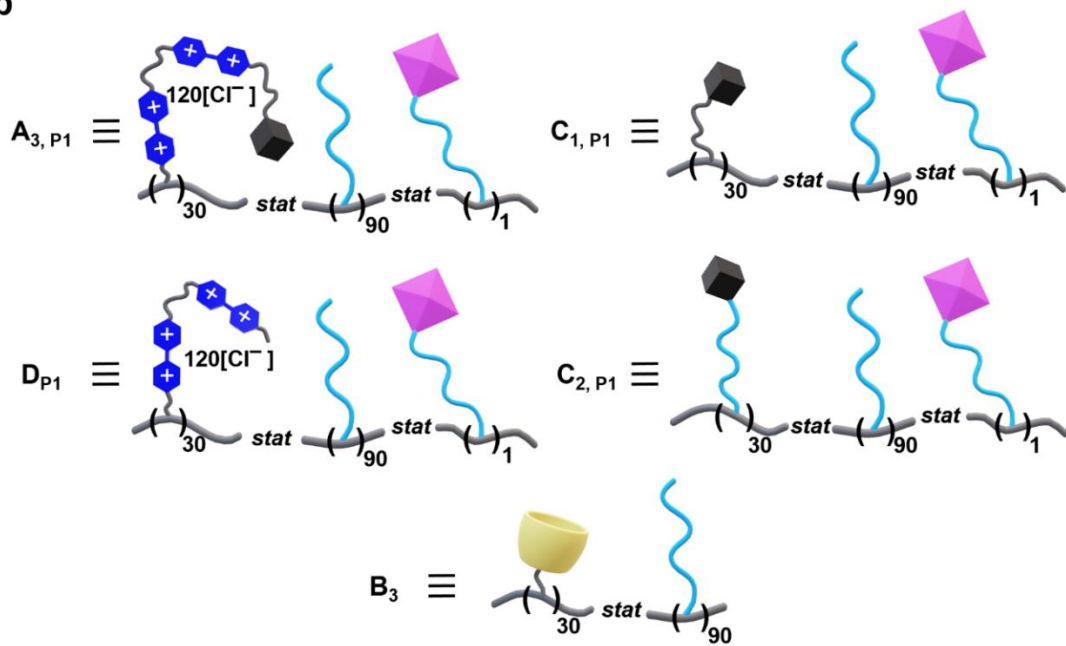
The unique two-part mechanism of gelation (**Figure 2.2**) entails the formation of a soluble polymer network upon mixing copolymers  $A_{3, P1}$  and  $B_3$  in  $H_2O$  at  $50 \text{ mg}\cdot\text{mL}^{-1}$ . At this stage, crosslinking occurs in solution as a function of host–guest complex formation between the Ad/CD side chain groups, as expected. However, no hydrogel formed until the soluble  $A_{3, P1}+B_3$  copolymer network was added via syringe (**Figure 2.2a**) to a saltwater solution containing 100 mM NaCl. Rapid gelation resulted as soon as the  $A_{3, P1}+B_3$  pre-gel solution was injected into saltwater, and the hydrogel adopted a filamentous morphology that adhered to the stainless-steel syringe needle, the glass walls of the vial, and the “non-stick” Teflon stir bar. By comparison, when the  $A_{3, P1}+B_3$  pre-gel solution was injected into deionized  $H_2O$ , the copolymer mixture dissolved, but no hydrogel formation was observed. Crosslinking in deionized  $H_2O$  without gelation was confirmed by both diffusion-ordered spectroscopy (DOSY, see Section 2.4.3, **Figures 2.7-2.9**) and isothermal titration calorimetry (ITC, **Figure 2.10**). We hypothesize the polar oligoviologen side chains of the ‘guest’ copolymer makes the  $A_{3, P1}+B_3$  network more hydrophilic and therefore more soluble in  $H_2O$ . When exposed to a high ionic strength solution, the  $A_{3, P1}+B_3$  network rapidly formed a hydrogel. This type of salt-responsive phenomenon has been observed previously<sup>41</sup> by Tang and co-workers for PNB-based copolymers bearing non-viologen cationic side chains. Their results demonstrated that higher ionic strength solutions decreased electrostatic repulsion between the cationic side chains of bottlebrush polymers, which resulted in a conformational change from an extended polymer structure to a collapsed and therefore precipitated state. It should be noted, though, that the precipitate in the former case produced an emulsion instead of a hydrogel, whereas the PNBs described here were crosslinked non-covalently through the formation of host–guest complexes, which allowed the network structure to persist even after being exposed to a high ionic strength solution. Thus, the  $A_{3, P1}+B_3$  pre-gel solution (**Figure 2.2a** and **Figure 2.3, S1**) was kinetically trapped as a viscous hydrogel (**Figure 2.3, S2**) instead of as

a precipitated emulsion that was observed previously. Moreover, the  $\mathbf{A}_{3, P1} + \mathbf{B}_3$  hydrogels could be converted back to their water-soluble form by removing the saltwater and replacing it with deionized  $\text{H}_2\text{O}$ . This level of reversible gelation is quite distinct from most other host-guest crosslinked and shear-thinning hydrogels reported in the literature. For example, a typical shear-thinning hydrogel will form in deionized  $\text{H}_2\text{O}$  at high enough concentrations as well as in saltwater. When loading a syringe with this material, parameters such as viscosity, composition, concentration, the length and gauge of the needle, and the rate of injection must be determined in advance to ensure proper flow. However, the  $\mathbf{A}_{3, P1} + \mathbf{B}_3$  polymer mixture reported here remains completely soluble in  $\text{H}_2\text{O}$  and is therefore readily injectable with practically any syringe setup. Conversely, formation of a viscous hydrogel occurs rapidly (i.e., kinetic trapping) upon contact with a high ionic strength solution (e.g., cell culture media, *in vivo* conditions, etc.). It is important to note that changing the salt from NaCl to LiCl also produced cohesive hydrogels from 50–100 mM (see Section 2.4.4, **Figure 2.25a-b**), whereas with KCl, the solution surrounding the hydrogels appeared more colored at 50 mM (see Section 2.4.4, **Figure 2.25c**), meaning more of  $\mathbf{A}_{3, P1}$  was freed.

To confirm our hypothesis for the two-part gelation mechanism, three additional copolymers were synthesized (illustrated in **Figure 2.2b**): poly(HexylAd<sub>30</sub>-TEG<sub>90</sub>-ZnTPP)<sub>stat</sub> ( $\mathbf{C}_{1, P1}$ ), poly(TEGAd<sub>30</sub>-TEG<sub>90</sub>-ZnTPP)<sub>stat</sub> ( $\mathbf{C}_{2, P1}$ ), and poly(2V<sup>4+</sup>Me<sub>30</sub>-TEG<sub>90</sub>-ZnTPP)<sub>stat</sub> ( $\mathbf{D}_{P1}$ ). Copolymers  $\mathbf{C}_{1, P1}$  and  $\mathbf{C}_{2, P1}$  were designed to mimic copolymer  $\mathbf{A}_{3, P1}$  except the oligoviologen subunits were replaced by a non-polar hexamethylene aliphatic tether and a polar TEG linker, respectively. Copolymer  $\mathbf{D}_{P1}$  was also designed to mimic  $\mathbf{A}_{3, P1}$  except the Ad group was replaced by a methyl group. Preparation of the  $\mathbf{C}_{1, P1} + \mathbf{B}_3$  copolymer mixture in a syringe at  $50 \text{ mg} \cdot \text{mL}^{-1}$  in deionized  $\text{H}_2\text{O}$  proved cumbersome to load and inject into vials containing deionized  $\text{H}_2\text{O}$  or saltwater given its propensity to immediately form a gelatinous emulsion in the syringe. Nevertheless, care was taken to add the two copolymers  $\mathbf{C}_{1, P1}$  and  $\mathbf{B}_3$  to the syringe with as little mixing as possible (to

maintain injectability), followed by injecting the 1:1 mixture into H<sub>2</sub>O and saltwater (**Figure 2.2a**, second row) through a 16 G needle (vs the smaller 18 G needle used for **A<sub>3, P1</sub>+B<sub>3</sub>**). A murky precipitate formed in both solutions, however, the gelation was more pronounced in the 100 mM NaCl solution, as evidenced by the solution becoming less colored and containing a higher concentration of non-gel precipitates. At lower concentrations (i.e.,  $\leq 30 \text{ mg}\cdot\text{mL}^{-1}$ ), the **C<sub>1, P1</sub>+B<sub>3</sub>** mixture could be loaded 1:1 into the syringe without as much initial gelation, making it easier to eject from the syringe into each solution. Even still, the injected solution remained murky with some hydrogel observed at the bottom of the vial.

The issues encountered with the **C<sub>1, P1</sub>+B<sub>3</sub>** copolymer mixture led us to pursue a more polar copolymer that would better mimic **A<sub>3, P1</sub>**, while still lacking the positive charges associated with the oligoviologen side chains. To this end, copolymer **C<sub>2, P1</sub>** was synthesized with polar TEG linkers tethering the Ad groups to the PNB backbone (**Figure 2.2b**). Initial attempts to mix this copolymer 1:1 with **B<sub>3</sub>** at room temperature also proved difficult because **C<sub>2, P1</sub>** precipitated out of H<sub>2</sub>O above its lower critical solution temperature (LCST). In fact, **C<sub>2, P1</sub>** copolymer solutions had to be cooled to 4 °C (below the LCST) to fully dissolve in either H<sub>2</sub>O or saltwater. Thus, to carry out the control experiment, **C<sub>2, P1</sub>** and **B<sub>3</sub>** were kept in separate vials at 4 °C before being loaded into a syringe at a concentration of 50 mg·mL<sup>-1</sup> and immediately injected into the vials filled with either H<sub>2</sub>O or aqueous 100 mM NaCl. The results from this control experiment (third row of **Figure 2.2a**) demonstrate that upon injection of the **C<sub>2, P1</sub>+B<sub>3</sub>** copolymer mixture, uniform hydrogels were formed initially, but quickly became unstable, as evidenced by the clear-to-murky visible transition that occurred after only ~25 sec. Both of these control experiments demonstrate the necessity for the positively charged oligoviologen side chains, which helped solubilize the **A<sub>3, P1</sub>+B<sub>3</sub>** copolymer mixture in H<sub>2</sub>O without any hydrogel formation, while also serving as the reason for rapid gelation (or kinetic trapping, **Figure 2.3**, S2) upon addition to a saltwater solution.

**a****b**

**Figure 2.2.** Demonstration of saltwater-induced gelation and illustration of copolymer architectures. (a) Comparison of copolymer mixtures  $A_{3, P1+B3}$ ,  $C_{1, P1+B3}$ ,  $C_{2, P1+B3}$  and  $D_{P1+B3}$  which were injected\* separately into 10 mL deionized H<sub>2</sub>O and 100×10<sup>-3</sup> M NaCl solutions at 50 mg·mL<sup>-1</sup>. Screenshots are chosen from timepoints: before injection, during injection, immediately after injection and a while after injection. (b) Cartoon structures of statistical copolymers ( $A_{3, P1}$ ) poly(2V<sup>4+</sup>Ad<sub>30</sub>-TEG<sub>90</sub>-ZnTPP)<sub>stat</sub>, ( $B_3$ ) poly(CD<sub>30</sub>-TEG<sub>90</sub>)<sub>stat</sub>, ( $C_{1, P1}$ ) poly(HexylAd<sub>30</sub>-TEG<sub>90</sub>-ZnTPP)<sub>stat</sub>, ( $C_{2, P1}$ ) poly(TEGAd<sub>30</sub>-TEG<sub>90</sub>-ZnTPP)<sub>stat</sub>, and ( $D_{P1}$ ) poly(2V<sup>4+</sup>Me<sub>30</sub>-TEG<sub>90</sub>-ZnTPP)<sub>stat</sub>. \*Note: 18 G needle gauge was used for  $A_{3, P1+B3}$  and  $D_{P1+B3}$ , while 16 G needle gauge was used for  $C_{1, P1+B3}$  and  $C_{2, P1+B3}$ . Additionally,  $C_{2, P1+B3}$  were maintained at 4 °C in solution until injected.

An additional four-week degradation experiment (see Section 2.4.3, **Figure 2.18-2.19**) was carried out using UV-vis absorption spectroscopy to quantify the stability of host–guest-crosslinked products for copolymer mixtures  $C_{1, P1+B3}$  vs  $A_{3, P1+B3}$  in solution – both at 30 mg·mL<sup>-1</sup> in 100 mL of an aqueous 100 mM NaCl solution. Aliquots were taken intermittently and assessed by UV-vis. Copolymer mixture  $C_{1, P1+B3}$  in contrast to  $A_{3, P1+B3}$  demonstrated absorption at 430 nm immediately after injection into the saltwater solution (note, the porphyrin side chain absorbs strongly in the visible region). Conversely, copolymer mixture  $A_{3, P1+B3}$  demonstrated little to no solution-phase absorption at 430 nm over the entire four-week experiment. The results of this stability study confirmed that  $A_{3, P1+B3}$  copolymer mixture maintained its heterogeneous hydrogel form over extended durations and the  $C_{1, P1+B3}$  copolymer mixture took longer for smaller precipitates to aggregate and fall out of solution. Lastly, the gelation mechanism was evaluated in the absence of Ad groups (i.e.,  $D_{P1+B3}$  copolymer mixture), and hence no host–guest interactions were possible. Not surprisingly, both copolymers dissolved (fourth row of **Figure 2.2a**) in deionized H<sub>2</sub>O and in saltwater without hydrogel formation in either case.

### 2.3.3 Modulating Rheological Properties as a Function of Host-Guest Crosslinking and Water Content

To further investigate the host–guest crosslinking dynamics in the copolymer network, the  $A_{3, P1+B3}$  hydrogels were heated from 25 to 80 °C on the rheometer stage, then held there for 10 min, followed by cooling it back to 25 °C and holding for an additional 10 min prior to testing. All the  $A_{3, P1+B3}$  hydrogels post-heating exhibited (**Figure 2.3b**) shear-thinning properties in response to

higher strain as well as a large increase in both  $G'$  and  $G''$ . Also, the  $A_{3, P1}+B_3$  hydrogels demonstrated more elastic-like properties (i.e.,  $G' > G''$ ) after heating versus the more viscous behavior ( $G'' > G'$ ) that was observed for hydrogels freshly prepared in saltwater (black vs blue data traces in **Figure 2.3b**, respectively). Moreover, the frequency sweep data for the pre-heated samples (**Figure 2.3c**) shows higher  $G'$  and  $G''$  values at higher angular frequencies, as would be expected for a shear-thinning material, however, no formal crossover point occurs in the frequency range tested during the experiment. Nevertheless, we hypothesize the change in behavior pre-/post-heating is directly related to the efficiency by which the CD hosts of copolymer  $B_3$  can form inclusion complexes with the Ad guests of copolymer  $A_{3, P1}$ . Because the gelation step occurred rapidly upon addition of copolymers  $A_{3, P1}$  and  $B_3$  to saltwater, we speculate that not all the CD and Ad groups were initially able to participate in host–guest-based crosslinking (i.e., kinetically trapped). However, after heating at 80 °C for 10 min, the hydrogels lost some  $H_2O$  through evaporation and became even more viscous, which we suspect resulted from the formation of more Ad/CD inclusion complexes and thus greater crosslinking. This proposed mechanism (**Figure 2.3a**) is supported by the rheological data shown in **Figure 2.3b–c**, where the pre-heated  $A_{3, P1}+B_3$  hydrogels demonstrated viscous behavior and the post-heated samples exhibited more elastic-like properties. As the percent strain was increased during the rheological characterization experiments, a crossover point occurred where the storage modulus ( $G'$ ) fell below the loss modulus ( $G''$ ), clearly indicating shear-thinning properties post-heating.

To further support the proposed kinetic trapping mechanism, the rheological properties were evaluated for the series of  $A_{x, P1}+B_x$  hydrogels described in section 2.3.1 and listed in **Table 2.2** (see Section 2.4.4, **Figure 2.26**). Because the  $A_{1, P1}+B_1$  copolymer mixture had less host-guest crosslinking before heating – a function of having the fewest (20) available crosslinking sites per copolymer – it exhibited the lowest initial values for  $G'$  and  $G''$  out of all the as-injected hydrogels. Conversely, the  $A_{4, P1}+B_4$  mixture was functionalized with 30 Ad/CD crosslinking sites, yet both

copolymers possessed more TEG repeat subunits (120/copolymer) than any other copolymer mixture in the series. These additional TEG side chains would be expected to create a larger steric/kinetic barrier that could offset the increased number of crosslinking host–guest complexes. For the  $\mathbf{A}_{5, P1}+\mathbf{B}_5$  copolymers, the polymerization did not go to full completion and the errors, particularly for the post-heated samples, is large. Both the  $\mathbf{A}_{3, P1}+\mathbf{B}_3$  and  $\mathbf{A}_{2, P1}+\mathbf{B}_2$  copolymer mixtures gave the best performance in terms of storage/loss moduli, before and after heating, meaning that an optimal balance between the number of crosslinking sites (30) and number of TEG side chains per copolymer (90 and 60, respectively) was achieved.

Before investigating their photoredox-based responsiveness (*vide infra*), the rheological properties of  $\mathbf{A}_{3, Pn}+\mathbf{B}_3$  hydrogels were evaluated (see Section 2.4.4, **Figure 2.27**, **Table 2.7**) as a function of the average number of porphyrin-based side chains ( $n = 0, 1, 2, \text{ or } 4$ ) present in copolymer  $\mathbf{A}_{3, Pn}$ . It was hypothesized that the physical properties of the hydrogels could be modulated by the number of porphyrin subunits in the network, as it has been shown previously that small- molecule TPPs can self-assemble into stacks in solution,<sup>42-44</sup> which, in the context of a polymer network, may contribute to additional crosslinking between  $\mathbf{A}_{3, Pn}$  copolymers. All the  $\mathbf{A}_{3, Pn}+\mathbf{B}_3$  hydrogels that were investigate exhibited viscous-like properties prior to heating (i.e.,  $G'' > G'$  when initially mixed in saltwater), even at higher oscillatory strain. However, as more porphyrin side chains were introduced into copolymer  $\mathbf{A}_{3, Pn}$ , the storage modulus ( $G'$ ) of the  $\mathbf{A}_{3, Pn}+\mathbf{B}_3$  hydrogels increased more than the corresponding loss modulus ( $G''$ ). This change resulted in a decreasing differential between the two moduli and supports the hypothesis that the porphyrin side chains can participate some in crosslinking through stacking,<sup>45</sup> thus increasing the overall viscosity of the photoredox-responsive hydrogels.

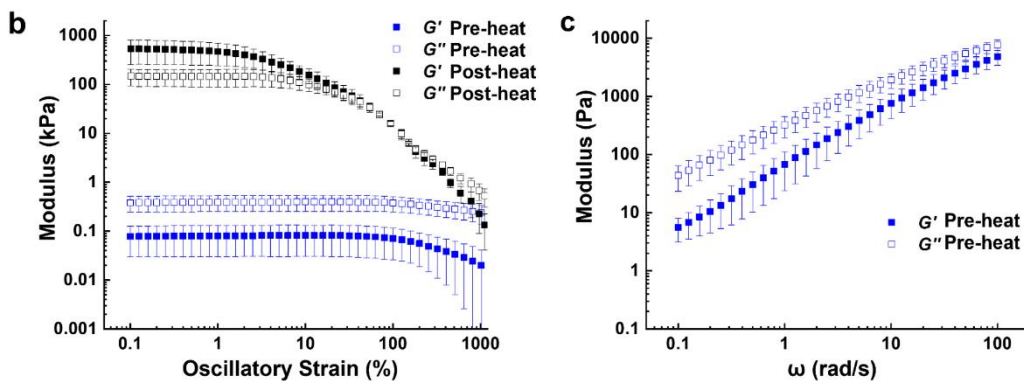
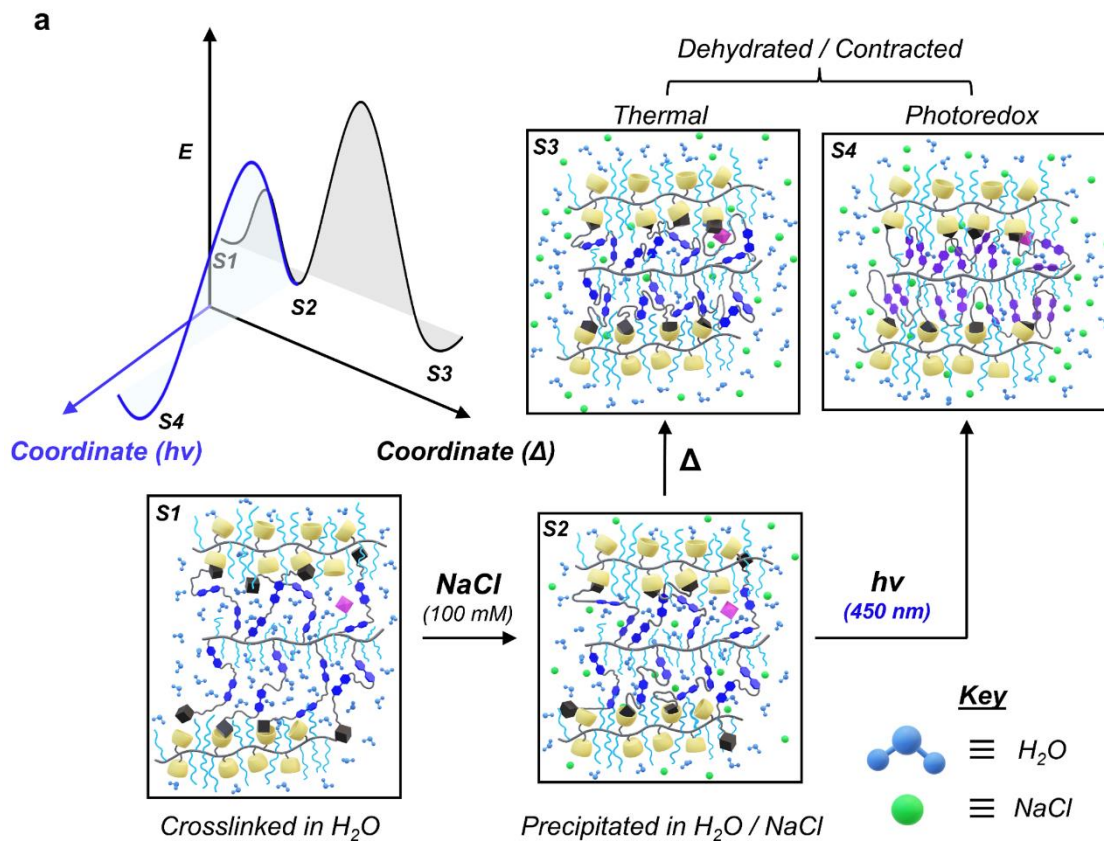


**Figure 2.3.** Modulating rheological properties. (a) General reaction coordinate diagram showing the different material states (S1-S4): upon mixing (S1), addition to saltwater (S2), and exposure to heat (S3) or light (S4). The cartoon diagram illustrates the mechanism of water loss in response to addition to saltwater and in response to heating or visible-light irradiation. (b) Rheology strain sweep experiments at 25 °C at a frequency of 1 rad·s<sup>-1</sup>. (c) Rheology frequency sweep experiments at 25 °C at 1% strain. The hydrogels were prepared in an aqueous 100×10<sup>-3</sup> M NaCl solution at a concentration of 50 mg·mL<sup>-1</sup>. All hydrogel samples were tested in triplicate pre- and post-heating\*. \*Note: Hydrogel samples tested immediately after mixing was labeled as “Pre-heat”. Then, each hydrogel sample was heated to 80 °C and held at this temperature for 10 min, followed by cooling the sample back to 25 °C, where it was held for an additional 10 min and tested again. This latter state was labeled as “Post-heat”.

Next, the rheological properties of the control hydrogels,  $\mathbf{C}_{1, P1+B3}$  and  $\mathbf{C}_{2, P1+B3}$ , were evaluated. The  $\mathbf{C}_{1, P1+B3}$  hydrogel exhibited the highest  $G'$  and  $G''$  prior to being heated than any of the other gels (**Table 2.2**, see Section 2.4.4, **Figure 2.30**), indicating it was much stiffer in its kinetically trapped state. Moreover, as it was found to be much stiffer, the strain sweep experiment prior to heating displayed a drop at higher strain values. After heating, the  $\mathbf{C}_{1, P1+B3}$  hydrogel exhibited a much lower storage and loss moduli relative to the other hydrogels in the series, which likely occurred because of it not holding onto  $\text{H}_2\text{O}$  as much, which may be largely excluded due to the non-polar aliphatic linkers present in the copolymer's side chains. This early occlusion of  $\text{H}_2\text{O}$  meant that heating would not be expected to increase the extent of host-guest crosslinking compared to the more polar  $\mathbf{A}_{3, P1+B3}$  hydrogels. Moreover, after heating, the  $\mathbf{C}_{1, P1+B3}$  hydrogel became sticky (see Section 2.4.4, **Figure 2.28c**), which may explain the results from the lap-shear tests (**Table 2.3**), where oven drying for 24 h of the  $\mathbf{C}_{1, P1+B3}$  mixture in between two pieces of metal yielded the largest shear stress values of the series of hydrogels on glass, metal, and high-density polyethylene (HDPE).

Lastly, the other control hydrogel,  $\mathbf{C}_{2, P1+B3}$ , bearing polar TEG linkers between the Ad groups and the PNB backbone was assessed by strain and frequency sweep rheology to determine its mechanical properties pre-/post-heating. Given the similarity of structures and overall polarity, it was not surprising to see this control hydrogel  $\mathbf{C}_{2, P1+B3}$  yield  $G'$  and  $G''$  values comparable to the  $\mathbf{A}_{3, P1+B3}$  hydrogels (**Table 2.2**, see Section 2.4.4, **Figure 2.30**). The post-heating rheological data seems to suggest that even though the  $\mathbf{C}_{2, P1}$  copolymer has more polar TEG side chains, it still may not absorb as much  $\text{H}_2\text{O}$  as the  $\mathbf{A}_{3, P1}$  copolymer on account of the viologen subunits' higher polarity and greater propensity to absorb  $\text{H}_2\text{O}$ . This interpretation is based on the relative increase in  $G'$  observed for the  $\mathbf{A}_{3, P1+B3}$  hydrogels vs that which was measured for the  $\mathbf{C}_{2, P1+B3}$  hydrogels (i.e., 5875x vs 2810x increase, respectively). However, it is important to note once again that the

process for performing rheological tests on the  $C_{2,P1}$  copolymer requires it to be kept at 4 °C until mixed with polymer  $B_3$  so the mixture is as homogeneous as possible.

Hydrogel	Pre-heat			Post-heat		
	$G'$ (kPa)	$G''$ (kPa)	Tan ( $\delta$ )	$G'$ (kPa)	$G''$ (kPa)	Tan ( $\delta$ )
$A_{1,P1}+B_1$	0.017±0.005	0.114±0.028	6.7	178±98	51±22	0.29
$A_{2,P1}+B_2$	0.065±0.016	0.308±0.066	4.7	580±351	186±87	0.32
$A_{3,P1}+B_3$	0.080±0.050	0.390±0.140	4.9	470±227	145±57	0.31
$A_{4,P1}+B_4$	0.056±0.004	0.249±0.019	4.4	91±53	41±17	0.45
$A_{5,P1}+B_5$	0.049±0.018	0.201±0.057	4.1	227±232	79±82	0.35
$C_{1,P1}+B_3$	0.418±0.107	0.718±0.177	1.7	31±5	17±3	0.55
$C_{2,P1}+B_3$	0.111±0.015	0.529±0.037	4.8	312±239	89±53	0.29

**Table 2.2.** Oscillatory shear rheology testing summary for  $A_{x,P1}+B_x$  hydrogel and  $C_{x,P1}+B_3$  control materials in aqueous  $100 \times 10^{-3}$  M NaCl solutions.

### 2.3.4 Versatile Adhesive Properties of the Viscous Hydrogels

The investigation of the two-part gelation mechanism (i.e., host–guest crosslinking followed by saltwater-induced gelation and kinetic trapping, **Figures 2.2-2.3**) revealed the versatile nature of the  $A_{3,P1}+B_3$  hydrogel's affinity for different surfaces, such as on the glass vial, the stainless-steel syringe, and the non-stick Teflon coated stir bar. Motivated by these observations, we then turned to lap-shear tests to evaluate the adhesive properties of the hydrogels on different substrates such as glass slides, a stainless-steel metal ruler, sheets of HDPE, and store-bought ham, the latter of which was chosen to simulate organic tissue. A dual-syringe method (see Section 2.4.4, **Figure 2.35a**) was used to apply the polymer samples onto the substrates. One syringe contained 0.5 mL of a 200 mM NaCl solution while the other contained an equimolar mixture of copolymers  $A_{3,P1}$  and  $B_3$  (15 mg in total) dissolved in 0.5 mL deionized  $H_2O$ . The plunger of each syringe was suppressed simultaneously to mix both solutions and to apply the hydrogels onto the different substrates. Once deposited onto each surface, another identical substrate was placed on top,

sandwiching the hydrogel in between (**Figure 2.4a**). Next, the glass, metal, and HDPE samples were clamped using a standard binder clip and left to dry in air for 24 h. For the ham sample, a small weight (122.7 g) was set on top to keep the ham in place during the curing process instead of a binder clip, which cut through the soft substrate. The lap-shear tests were then conducted to measure the adhesive strength of the hydrogels in between each substrate. The shear stress (MPa) vs. extension (mm) plots are shown in **Figure 2.4b**, where three replicates were performed for each substrate but only the median data trace is overlaid for comparison. The **A<sub>3</sub>, P<sub>1</sub>+B<sub>3</sub>** hydrogels adhered to the glass, metal, and HDPE with a maximum stress ranging from 0.15–0.30 MPa, whereas the store-bought ham used to mimic human tissue barely showed any adhesion, an outcome which may be well suited for coatings on medical devices. The latter statement is well supported by SEM data obtained for thin films comprising the **A<sub>3</sub>, P<sub>1</sub>+B<sub>3</sub>** hydrogels, which showed (see Section 2.4.4, **Figures 2.31-2.34**) cohesive and homogeneous films.

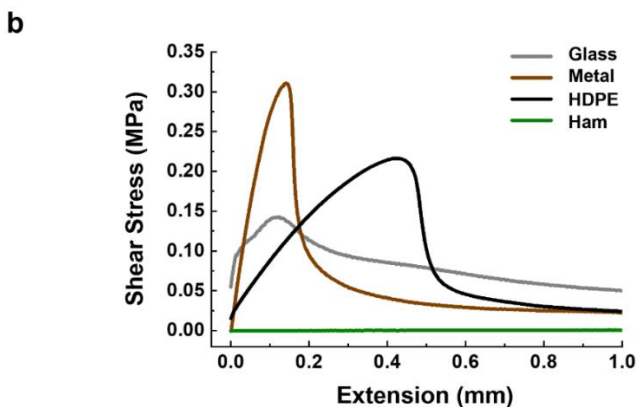
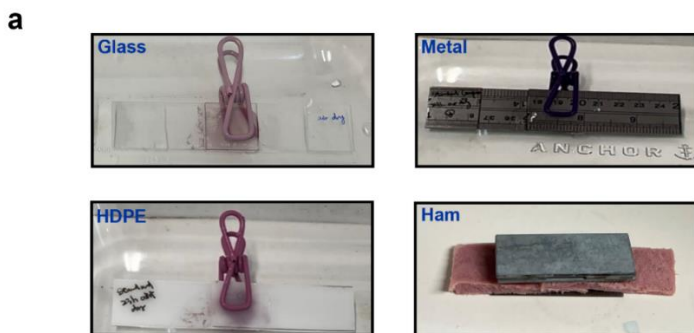


**Figure 2.4.** Lap-shear adhesion testing for  $A_3, P_1+B_3$  hydrogels on different substrates. (a) Pictures of copolymer mixtures applied to different surfaces in aqueous  $100 \times 10^{-3}$  M NaCl solutions. (b) Representative lap-shear adhesion tests of  $A_3, P_1+B_3$  hydrogels on different surfaces including glass, metal, high density polyethylene (HDPE), and ham after 24 h air dry. *Note:* All samples tested were prepared at a concentration of  $30 \text{ mg} \cdot \text{mL}^{-1}$ .

Since the hydrogels behaved differently before and after heating, as evidenced by the rheological data shown in Figure 2.3b–c, the adhesive strength of the  $A_3, P_1+B_3$  hydrogels was then tested on HDPE using the following different curing protocols: (i) 24 h air dry, (ii) 12 h air dry followed by 12 h oven dry at  $80^\circ\text{C}$ , and (iii) 24 h oven dry at  $80^\circ\text{C}$  (see Section 2.4.4, Figure 2.43). The adhesive strength (Table 2.3) for the 24 h air dried samples (0.18–0.24 MPa) was lower than that which was observed for the samples that were oven dried. However, the 24 h oven dried samples exhibited lower adhesive strength (0.70–0.87 MPa) than the hydrogels that were cured using the 12 h air and 12 h oven dry protocol (0.84–0.96 MPa) (see Section 2.4.4, Figure 2.43). To rationalize this different behavior, we hypothesize the hydrogels that were oven dried for 24 h underwent nearly complete dehydration, which resulted in the samples becoming more brittle than those which were air and oven dried over a combined 24 h period. This is an important aspect as the copolymers operate through dynamic host–guest inclusion complexes, which may be affected by the lack of solvent present in the hydrogels. Moreover, the underlying HDPE sheets also may have been affected by the oven-based curing protocols, which could have softened the plastic and potentially contributed to a reduction in the observed adhesive strength. Nevertheless, it is clear that the adhesive strength increased 3–4 times for the oven-dried samples relative to those that were only air dried for 24 h. To confirm the ubiquitous nature of these results,  $A_3, P_1+B_3$  hydrogels were also tested on glass and metal substrates (Table 2.3, see Section 2.4.4, Figure 2.38a and 2.40). Similar to HDPE, the hydrogels that were heat cured for 24 h demonstrated stronger adhesive properties than those that were air dried (glass: 1.12 vs 0.17 MPa; metal: 2.0–3.3 vs 0.23–0.31 MPa), which is further evidence of the affinity that the viscous hydrogels have for both polar and non-polar surfaces (see Section 2.4.3, Figure 2.23 for water-contact angle measurements that characterized the polarity of each surface). To put these lap-shear adhesive

results into context, positively charged catechol-based polymers reported elsewhere in the literature have been shown<sup>46</sup> to adhere to different surfaces such as glass and aluminum metal to similar effect after drying at 55 °C for 24 h (i.e., 1.5–2.4 MPa vs 1.1–3.3 MPa for **A**<sub>3, P1</sub>+**B**<sub>3</sub>). Lastly, attempts to switch the solvent to a 90% MeOH, 10% H<sub>2</sub>O mixture (containing 100 mM NaCl) to induce faster evaporation and therefore better crosslinking were ineffective, as it appeared to have affected the formation of the host–guest complexes, which resulted in only partial formation of hydrogels that did not adhere very well to the non-polar HDPE, as well as other surfaces, as the hydrogels that were formed using only saltwater (see Section 2.4.4, **Figures 2.38c, 2.41 and 2.44**).

<b>Substrate</b>	<b>Shear Stress (MPa)</b>					
	<b>A<sub>3, P1</sub>+B<sub>3</sub> Hydrogel</b>			<b>C<sub>1, P1</sub>+B<sub>3</sub> Emulsion</b>		
	<i>i</i> <sup>a</sup>	<i>ii</i> <sup>a</sup>	<i>iii</i> <sup>a</sup>	<i>i</i> <sup>a</sup>	<i>ii</i> <sup>a</sup>	<i>iii</i> <sup>a</sup>
Glass <sup>b</sup>	0.14–0.17	0.66	1.12	0.24	1.65	1.55
Metal <sup>c</sup>	0.23–0.31	0.42–0.51	2.0–3.3	0.43–0.52	1.98–3.7	4.98–8.5
HDPE <sup>d</sup>	0.18–0.24	0.84–0.96	0.70–0.87	0.14–0.20	0.59–0.76	0.56–0.85

**Table 2.3.** Lap-shear adhesion testing summary for **A**<sub>3, P1</sub>+**B**<sub>3</sub> hydrogel and **C**<sub>1, P1</sub>+**B**<sub>3</sub> emulsion in aqueous 100×10<sup>-3</sup> M NaCl solutions. *Note:* <sup>a</sup>Curing protocol: (*i*) 24 h air dry, (*ii*) 12 h air dry followed by 12 h oven dry at 80 °C, and (*iii*) 24 h oven dry at 80 °C. <sup>b</sup>Microscope slide (VWR brand 25 x 75 x 0.9 mm). <sup>c</sup>Stainless steel ruler (28 x 75 x 0.9 mm). <sup>d</sup>High density polyethylene (25 x 75 x 1.6 mm).

Because copolymers **A**<sub>3, P1</sub> and **B**<sub>3</sub> consisted mostly of oligoethylene glycol side chains and the PNB backbone, each of which may have contributed to the copolymers' overall adhesive properties, two additional PNB-based copolymers were synthesized: poly(TEG<sub>120</sub>-ZnTPP)<sub>stat</sub> (**E**<sub>P1</sub>) and poly(Me<sub>120</sub>-ZnTPP)<sub>stat</sub> (**F**<sub>P1</sub>). The TEG-based copolymer was first dissolved in either H<sub>2</sub>O or an aqueous 100 mM NaCl solution and then deposited via a syringe onto glass surfaces, followed by curing (i.e., 24 h air dried, 12 h air and 12 h oven dried, or 24 h oven dried). Then, lap-shear adhesion tests were performed on the cured samples of copolymer **E**<sub>P1</sub>. The sample in deionized

H<sub>2</sub>O demonstrated (see Section 2.4.4, **Figure 2.37b**) minimal adhesion (0.24 MPa) between the two glass surfaces after drying by oven for 24 h, however, the sample prepared in saltwater that was oven dried for 24 h exhibited (see Section 2.4.4, **Figure 2.37c**) stronger adhesive properties (1.0 MPa). For the saltwater samples cured by shorter oven drying times, little (0.1 MPa) to no adhesion was observed. Next, the contribution of the PNB backbone was evaluated by dissolving copolymer **F<sub>P1</sub>** in CH<sub>2</sub>Cl<sub>2</sub> instead of H<sub>2</sub>O or saltwater because it was hydrophobic and therefore not soluble in polar solvents, followed by depositing it between two glass slides and curing it using the same protocols as those used for copolymer **E<sub>P1</sub>**. It is important to note that the use of a volatile organic solvent made it difficult to obtain consistent deposition of the material as the copolymer solution would run off the slides when pressed together. Nevertheless, some adhesion was observed, the strength of which ranged from 0.28–0.54 MPa.

To better understand the role oligoviologen side chains played in adhesion, copolymer **C<sub>1, P1</sub>** (bearing no oligoviologen side chains, **Fig. 2.2b**) was mixed with copolymer **B<sub>3</sub>** in saltwater via the dual-syringe method. This mixture did not completely form hydrogels, however, but rather yielded an emulsion. Moreover, when applied to an HDPE substrate, the **C<sub>1, P1</sub>+B<sub>3</sub>** emulsion did not adhere as readily as the **A<sub>3, P1</sub>+B<sub>3</sub>** hydrogels, which resulted in more material runoff when the second HDPE sheet was added on top prior to clamping. This behavioral difference yielded lap-shear data (**Table 2.3**, see Section 2.4.4, **Figure 2.45**) that exhibited slightly lower adhesion strength on average for all three curing protocols when compared to the **A<sub>3, P1</sub>+B<sub>3</sub>** hydrogels (**Table 2.3**, see Section 2.4.4, **Figure 2.43**). Even with this difference, the samples that were oven dried yielded adhesive strengths in the range of 0.56–0.85 MPa vs the air-dried samples, which maxed out at 0.14–0.2 MPa. Consistent with earlier experiments, the **C<sub>1, P1</sub>+B<sub>3</sub>** emulsions were also evaluated in lap-shear adhesion tests involving the more polar glass and non-polar metal substrates. Some runoff was encountered during the deposition onto these surfaces, however, far less sample was lost when compared to deposition onto the non-polar HDPE substrate. This

difference allowed for easier deposition of the  $C_{1, P1}+B_3$  sample, but still not nearly as efficiently as the  $A_{3, P1}+B_3$  hydrogels. Next, the deposited  $C_{1, P1}+B_3$  emulsions were clamped and cured for 24 h in an oven at 80 °C and the corresponding adhesive strengths were measured (**Table 2.3**, see Section 2.4.4, **Figures 2.39 and 2.42**; glass: 1.55 MPa; metal: 4.98–8.5 MPa, respectively) and found to be comparable to the  $A_{3, P1}+B_3$  hydrogels. With that said, it is important to reiterate the difficulty associated with depositing the  $C_{1, P1}+B_3$  emulsion onto different substrates (particularly non-polar surfaces) relative to the process involved with depositing the stickier  $A_{3, P1}+B_3$  hydrogels on polar and non-polar surfaces.

### 2.3.5 Photoredox-based Control Over the Mechanical Properties Using Visible Light

Although the oligoviologen side chains proved critical to the gelation mechanism of the hydrogels (**Figures 2.2 and 2.3a**), they are also well known<sup>47</sup> to be excellent electron acceptors and are compatible with a wide-range of visible-light-based photoredox catalysts, such as tetraphenyl porphyrins.<sup>35</sup> Therefore, we next sought to control the photoredox-responsive properties and performance of the viscous hydrogels using a PET mechanism (**Figure 2.5a**). Accordingly, porphyrin side chains were designed and incorporated into copolymer  $A_{3, Pn}$ , where in these experiments  $n = 1$ . Having the photoredox catalyst (ZnTPP) tethered to the PNB backbone allowed it to be in close proximity to the oligoviologen side chains, meaning fast electron transfer could occur while providing multiple electrons per PNB chain because an excess of sacrificial reductant (triethanolamine, TEOA) was included in the hydrogel solution and used to regenerate the photocatalyst. This PET process allowed multiple oligoviologen side chains to be reduced (i.e.,  $V^{2+}$  to  $V^{\bullet+}$ ) in response to blue light (450 nm) and for radical-radical-based spin pairing and molecular recognition to occur ( $V^{\bullet+}-V^{\bullet+}$ , **Figure 2.5a**) while also decreasing the overall electrostatic repulsion and halving the number of chloride anions ( $Cl^-$ ), the latter of which left as the corresponding TEOA•Cl salt.

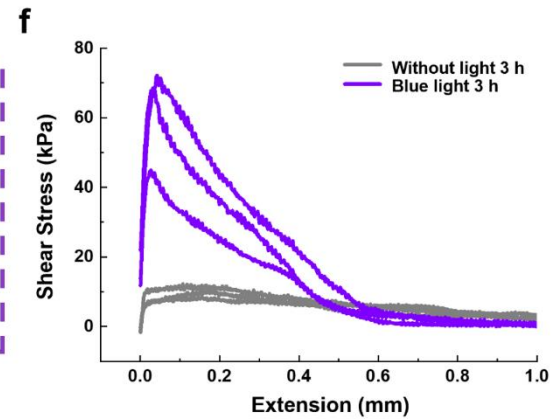
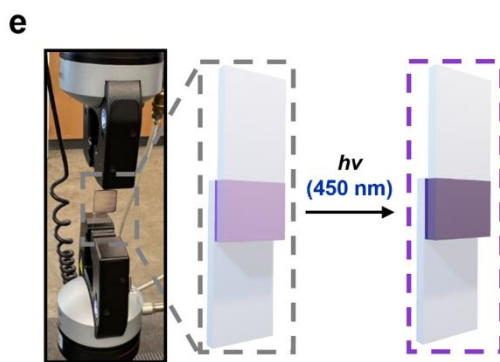
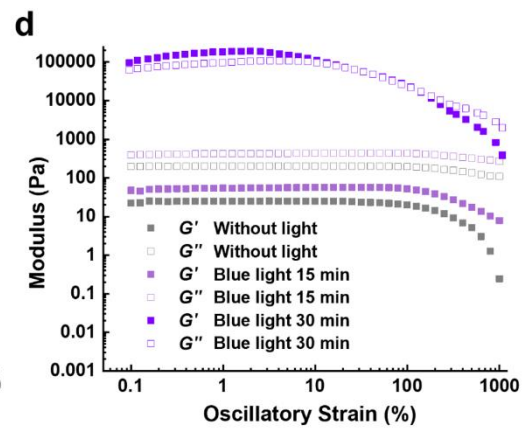
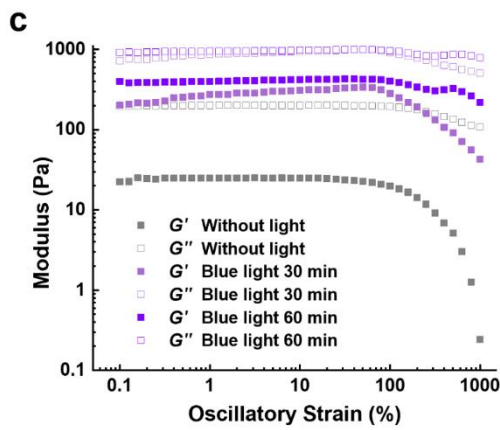
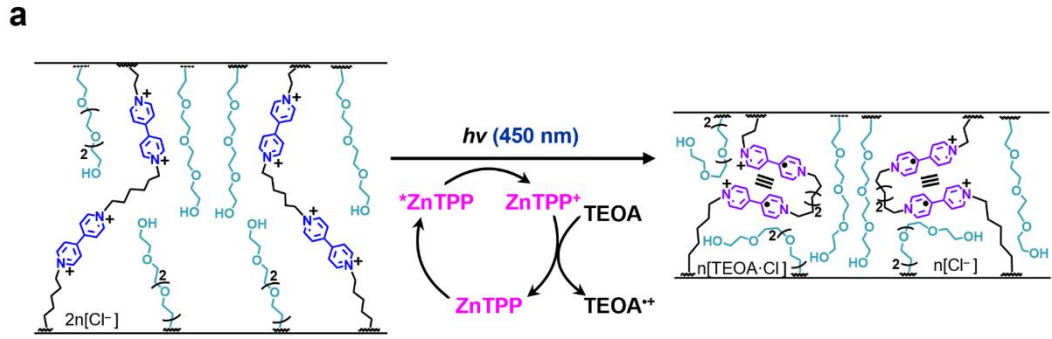


**Figure 2.5.** Photoredox-based control over mechanical properties. (a) Chemical structures of hydrogel network components and corresponding proposed self-assembled structures after reduction of the oligoviologen subunits via the integrated zinc-tetraphenyl porphyrin (**ZnTPP**) photoredox catalyst and sacrificial reductant (**TEOA**, triethanolamine). (b) Images of photoreduction process before and after irradiation, as well as after rheological assessment. (c) Oscillatory shear rheology strain sweep data for three hydrogels ( $50 \text{ mg}\cdot\text{mL}^{-1}$ ) at  $25 \text{ }^\circ\text{C}$  and  $1.0 \text{ rad}\cdot\text{s}^{-1}$ . Hydrogels were tested without light irradiation (gray), 30 min blue light irradiation (light purple), and 60 min blue light irradiation (purple). (d) Oscillatory shear rheology strain sweep data for one hydrogel ( $50 \text{ mg}\cdot\text{mL}^{-1}$ ) at  $25 \text{ }^\circ\text{C}$  and  $1.0 \text{ rad}\cdot\text{s}^{-1}$ . The hydrogel was tested in sequence without light irradiation (gray), then 15 (light purple) and 30 min (purple) blue light irradiation. (e) Experimental setup and illustration of photoreduction process for lap-shear adhesion tests. (f) Lap-shear adhesion stress (kPa) vs extension (mm) for **A<sub>3</sub>, P<sub>1</sub>+B<sub>3</sub>** hydrogels ( $30 \text{ mg}\cdot\text{mL}^{-1}$ ) on glass with 3 h air dry (without light, gray) and 3 h blue light irradiation (purple). *Note:* All hydrogels tested for rheology (c, d) and lap-shear adhesion (f) were prepared in an aqueous  $3\times 10^{-3} \text{ M}$  TEOA/ $100 \times 10^{-3} \text{ M}$  NaCl solution.

The change in mechanical properties that occurred during the visible-light-based photoredox process was quantified (**Figure 2.5b-c**) using oscillatory shear rheology. The **A<sub>3</sub>, P<sub>1</sub>+B<sub>3</sub>** hydrogels were prepared in an aqueous  $100\times 10^{-3} \text{ M}$  NaCl solution containing  $3\times 10^{-3} \text{ M}$  TEOA and were deposited onto the rheometer stage. Next, the storage ( $G'$ ) and loss ( $G''$ ) moduli were measured for the **A<sub>3</sub>, P<sub>1</sub>+B<sub>3</sub>** hydrogels in three separate experiments: (i) prior to irradiation (**Figure 2.5c**, gray) and after 30 min (ii) and 60 min (iii) of blue light irradiation (**Figure 2.5c**, purple), all while the stage was maintained at  $25 \text{ }^\circ\text{C}$  and the intensity of a single light source was  $23.9 \text{ W}\cdot\text{m}^{-2}$  at a distance of 0.2 m. Without irradiation, the hydrogels were softer, where  $G'$  at 1% strain was 25 Pa and  $G''$  was 201 Pa, indicative of viscous-like properties. After the hydrogel sample was irradiated with blue light for 30 min, there was an obvious increase in both moduli (274 and 875 Pa, respectively, at 1% strain), as well as a decrease in  $\tan \delta$  (8.0 to 3.2), meaning the hydrogels became stiffer as a function of the photoreduction process. Raising the irradiation time to 60 min caused the outside layer of the hydrogel to become darker (**Figure 2.5b**) and an increase of  $G'$  to 400 Pa was observed while  $G''$  exhibited only a marginal increase to 952 Pa. Moreover, it is important to note that at higher percent strain ( $\geq 80\%$ ), the non-irradiated and 30 min-irradiated hydrogel samples showed (**Figure 2.5c**) a substantial drop in  $G'$ , however, the sample irradiated for 60 min maintained a more robust storage modulus, even up to 1000% strain.

To further confirm the hydrogel's ability to contract and stiffen in response to visible light, another photoredox experiment was conducted (**Figure 2.5d**) using a freshly prepared **A<sub>3</sub>, P<sub>1</sub>+B<sub>3</sub>** hydrogel,

which was irradiated with blue light at the same distance (0.2 m) and intensity ( $23.9 \text{ W}\cdot\text{m}^{-2}$ ) for 0, 15, and 30 min. After each irradiation period, the rheometer's geometry was lowered back down to establish complete contact with the hydrogel to measure the change in the storage and loss moduli as a function of photoirradiation times on the same hydrogel. Under these experimental conditions, the hydrogel became stiffer (i.e.,  $G'$  increased from 25 to 54 Pa at 1% strain) after 15 min of blue light irradiation. Moreover, the distance between the geometry and the stage was lowered from 1.0 to 0.75 mm because the hydrogel contracted in the  $Z$  direction while being irradiated with blue light. Next, the hydrogel was irradiated for an additional 15 min (i.e., 30 min in total at this point) and the geometry was lowered again to 0.5 mm to re-establish complete contact with the hydrogel. This second photoirradiation experiment resulted in a steep increase in  $G'$  (54 to 184,306 Pa at 1% strain) and also showed  $G'$  moving higher than  $G''$ . The significant increase in the storage modulus is reminiscent of the heat curing experiments (**Figure 2.3b**) in that irradiation with blue light caused the hydrogels to become stiffer and therefore more viscous. We hypothesize that the photo-induced contraction combined with the agitation of the hydrogel by the instrument's geometry resulted in the loss of  $\text{H}_2\text{O}$  through some evaporation as well as loss of a portion of the  $\text{H}_2\text{O}$ :TEOA solution as it was squeezed out of the hydrogel during photoreduction (**S4 in Figure 2.3a**). Likewise, heating at  $80 \text{ }^\circ\text{C}$  on the rheometer stage caused direct evaporation of  $\text{H}_2\text{O}$  and stiffening of the hydrogel via loss of  $\text{H}_2\text{O}$  and an increase in the extent of host-guest crosslinking. Moreover, at higher percent strain, the material exhibited shear-thinning properties, as evidenced by the crossover point between  $G'$  and  $G''$ , which, again, was also observed for the samples that were heated on the rheometer stage. Essentially, application of either external stimulus resulted in the 'switching on' of elastic ( $G' > G''$ ) and shear-thinning properties via stimuli-induced dehydration mechanisms (**Figure 2.3a**, S3 and S4).

To evaluate the adhesive performance of the  $\mathbf{A}_3, \mathbf{P}_1 + \mathbf{B}_3$  hydrogels in response to blue light, lap-shear adhesion tests were carried out using glass slides, the latter of which were amenable to

maximum light penetration (light source was at 0.25 m distance and  $15.3 \text{ W}\cdot\text{m}^{-2}$  intensity). Two sets of three  $\mathbf{A}_{3, \text{P1}}+\mathbf{B}_3$  hydrogels were applied to the glass substrates using the dual-syringe method (see Section 2.4.4, **Figure 2.35a**), where the  $\mathbf{A}_{3, \text{P1}}$  and  $\mathbf{B}_3$  copolymers were once again dissolved in an  $\text{H}_2\text{O}:\text{TEOA}$  solution and mixed with an aqueous saltwater solution containing  $3\times 10^{-3} \text{ M}$  TEOA. One set of hydrogel samples was air dried for 3 h in the dark (i.e., samples were covered with aluminum foil) and the other set of hydrogels was subjected to blue light irradiation for 3 h (**Figure 2.5e**). The results from the lap-shear adhesion tests (**Figure 2.5f**) showed on average a six-fold increase in the shear stress, ranging from 8.3–12.2 kPa for the non-irradiated set of hydrogels and up to 44.2–77.2 kPa for the photoreduced hydrogels. The results from these photoirradiation and lap-shear experiments provide an alternative method to heat-curing protocols for the purpose of increasing the strength of hydrogel-based adhesives.

## 2.4 Materials and Methods

### 2.4.1 Experimental Methods

All reagents were purchased from commercial suppliers and used without further purification unless stated otherwise. All reactions were performed under nitrogen ( $\text{N}_2$ ) or argon (Ar) gas unless otherwise stated. Column chromatography was carried out with silica gel (Sorbtech, 0.040–0.063 mm). Polymerization of all polymers was performed under an inert atmosphere of UHP  $\text{N}_2$  in a glovebox using a modified Grubbs' 3<sup>rd</sup> generation catalyst that was prepared according to a previous reported protocol.<sup>48</sup> All nuclear magnetic resonance (NMR) spectra were recorded on Varian Inova-500 spectrometer at 25 °C, with working frequencies of 500 ( $^1\text{H}$ ) and 125 ( $^{13}\text{C}$ ) MHz. Chemical shifts are reported in ppm relative to the signals corresponding to the residual non-deuterated solvents:  $\text{CDCl}_3$ :  $\delta_{\text{H}} = 7.26 \text{ ppm}$  and  $\delta_{\text{C}} = 77.16 \text{ ppm}$ ;  $(\text{CD}_3)_2\text{SO}$ :  $\delta_{\text{H}} = 2.50 \text{ ppm}$  and  $\delta_{\text{C}} = 39.52 \text{ ppm}$ ;  $\text{CD}_2\text{Cl}_2$ :  $\delta_{\text{H}} = 5.32 \text{ ppm}$  and  $\delta_{\text{C}} = 53.84 \text{ ppm}$ ;  $\text{D}_2\text{O}$ :  $\delta_{\text{H}} = 4.79 \text{ ppm}$ . High-resolution mass spectrometry (HRMS) data was recorded on a Bruker maXis 4G UHR-TOF mass

spectrometer. Matrix assisted laser desorption/ionization time-of-flight mass spectrometry (MALDI-TOF-MS) was recorded on a Bruker Solaris 12T FT-MS, samples were prepared using 2,5-dihydroxybenzoic or  $\alpha$ -cyano-4-hydroxycinnamic acid matrices. Ultraviolet-visible-near-infrared (UV-vis-NIR) absorbance spectra were recorded on Agilent Cary 5000 spectrophotometer with a PbSmart NIR detector. Isothermal titration calorimetry was performed on a VP-ITC (MicroCalorimeter Malvern Panalytical, Malvern, U.K.) at 25 °C. Size exclusion chromatography (SEC) analyses were performed on an Agilent 1260 Infinity setup with three PSS NOVEMA MAX Lux analytical 100 Å columns in tandem and 0.025 M Na<sub>2</sub>SO<sub>4</sub> in H<sub>2</sub>O mobile phase run at 23 °C with 1.0 mL·min<sup>-1</sup> flow rate, or with two Shodex GPC KD-806M columns in sequence and 0.025 M LiBr in DMF mobile phase run at 60 °C at 1.0 mL·min<sup>-1</sup>. The differential refractive index (dRI) of each compound was monitored using a Wyatt Optilab T-rEX detector and the light scattering (LS) of each compound was monitored using Wyatt Dawn Heleos-II detector. Isothermal titration calorimetry (ITC) was performed on a VP-ITC MicroCalorimeter at 25 °C. The related titration parameters are as follows: 25 °C, 5.0 µL/injection, 25 injections, 8.5 s injection duration, 300 s delay between injections, and 2 s filter period. All the photochemical reduction experiments of oligoviologen-based hydrogels were accomplished using one Hampton Bay desk lamp with an ABI LED aquarium light bulb (450 nm / 12 Watt / 740 lumens). The distance between the light bulb and the sample on rheometer stage was 0.2 m, while the light intensity was 23.9 W·m<sup>-2</sup>. The distance between the light bulb and the glass slides with hydrogels for lap shear tests was 0.25 m, while the light intensity was 15.3 W·m<sup>-2</sup>. Contact angle images were acquired through the use of a Samsung Note 10+ as camera with a Xenvo 15x macro lens attachment. Images were captured at 1 s after dropping 7.5 µL of solution onto the substrate. All images were analyzed in ImageJ and all contact angles ( $\Theta_E$ ) are reported. Scanning electron microscopy (SEM) was conducted using a Thermofisher Quattro S ESEM apparatus with a high-stability Schottky field emission gun electron source providing electron resolution of 0.7 nm at 30 keV, 1.4 nm at 1 keV.

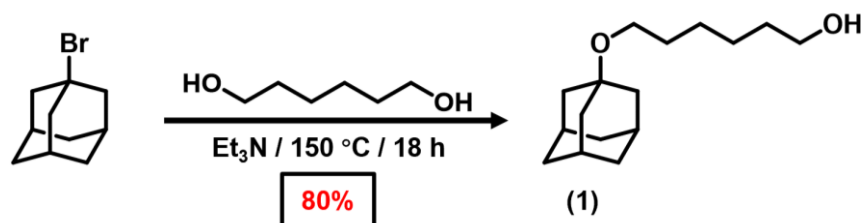
Rheological data was obtained on a TA HR-20 Rheometer using a 20 mm plain geometry. All samples tested were between 80–100 mg of mixed supramolecular gel smoothed over the stage to cover the geometry. Testing was conducted at a constant gap of 500  $\mu\text{m}$  as a constant axial force could not be maintained in many samples. Strain sweep tests ranged from 0.1–1000 % strain, and angular frequency was kept constant at 1  $\text{rad}\cdot\text{s}^{-1}$  throughout the test. Frequency sweeps ranged from 0.1–1000  $\text{rad}\cdot\text{s}^{-1}$  with a constant strain of 1%. Temperature dependent rheology was performed at a constant strain of 1% and a constant frequency of 1  $\text{rad}\cdot\text{s}^{-1}$  ranging from 25–80  $^{\circ}\text{C}$ , with a temperature increasing rate at 3  $^{\circ}\text{C} / \text{min}$  (around 18 min for the entire process). Samples were cured by heating at 80  $^{\circ}\text{C}$  for 10 min, then cooled to 25  $^{\circ}\text{C}$  for 10 min. Strain and frequency sweeps were then repeated after curing. Strain sweeps were performed before frequency sweeps in each run before and after heating unless otherwise stated. Rheological data of photoreduction experiments was obtained on a TA HR-20 Rheometer using an 8 mm plain geometry.

Substrates for lap-shear adhesion tests were constructed from glass microscope slides (VWR brand 25 x 75 x 0.9 mm), stainless steel ruler segments (28 x 75 x 0.9 mm), and HDPE (25 x 75 x 1.6 mm). To align the slides and eliminate any torsion forces on the surface during lap-shear testing, glass slides and steel ruler segments were cut into tabs (25 x 25 x 0.9 mm for glass slides and 28 x 25 x 0.9 mm for steel ruler) and superglued onto the ends of the substrates. Lap-shear samples on each surface (glass, stainless steel, HDPE, ham) were analyzed using an Instron 68TM-30 Load Frame universal testing apparatus to determine the adhesive strength. Each sample's cross-sectional area of adhesion was measured prior to testing. The HDPE, steel, and glass samples were gripped at 60 psi within the load frame using Instron 2712-041 series pneumatic side action tensile grips with rubber jaw faces and a 1 kN limit. The ham samples were gripped at 15 psi to avoid damage to the tissue. The samples were tested under tension at a rate

of 1 mm·min<sup>-1</sup>. Samples that exceeded 1 kN of force were stopped and retested using 30 kN limit wedge grips.

## 2.4.2 Synthetic Methods

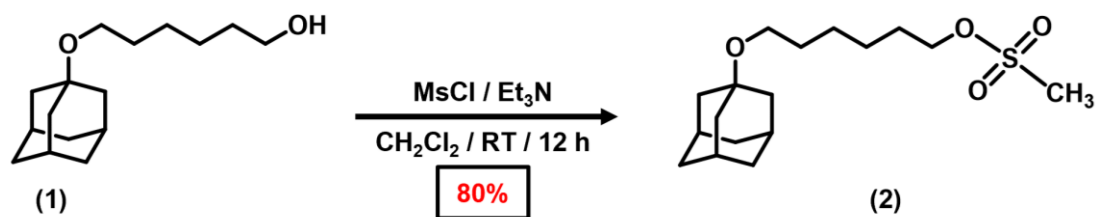
### Synthesis of Ad-Hexyl-OH (1)



### Scheme 2.1. Synthesis of Ad-Hexyl-OH.

1-Bromoadamantane (2.15 g, 10 mmol, 1 equiv.) and 1,6-Hexanediol (23.6 g, 200 mmol, 20 equiv.) were added into a round bottom flask. The reaction mixture was heated to 150 °C and refluxed for 18 h. After completion of the reaction, the crude mixture was dissolved in CH<sub>2</sub>Cl<sub>2</sub> (150 mL), washed with 1 M HCl (30 mL) three times, and then washed with brine solution (30 mL). The organic layer was dried over Na<sub>2</sub>SO<sub>4</sub> and concentrated. The compound was further purified by flash column chromatography (silica gel, 100:1 CH<sub>2</sub>Cl<sub>2</sub>: MeOH) to yield the desired compound **1** as a colorless oil (2.02 g, 80% yield). <sup>1</sup>H NMR (500 MHz, CDCl<sub>3</sub>): δ<sub>H</sub> 3.62 (t, *J* = 6.6 Hz, 2H); 3.38 (t, *J* = 6.7 Hz, 2H); 2.12 (s, 3H); 1.73 (d, *J* = 2.8 Hz, 5H); 1.66 – 1.48 (m, 12H); 1.40 – 1.32 (m, 4H). <sup>13</sup>C NMR (125 MHz, CDCl<sub>3</sub>): δ<sub>C</sub> 71.89, 63.05, 59.77, 41.73, 36.66, 32.86, 30.79, 30.64, 26.20, 25.73. MALDI-TOF: theoretical mass of C<sub>16</sub>H<sub>28</sub>O<sub>2</sub>, 252.21; found: 275.39 for [M+Na]<sup>+</sup>.

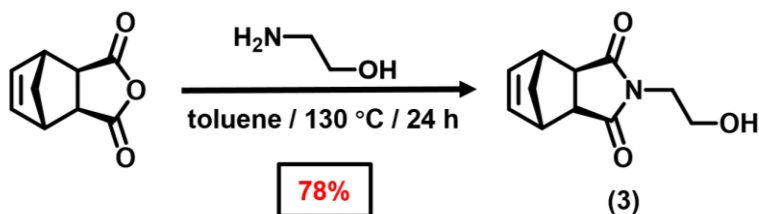
### Synthesis of Ad-Hexyl-OMs (2)



**Scheme 2.2.** Synthesis of Ad-Hexyl-OMs.

Compound **1** (2.02 g, 8 mmol, 1 equiv.) and  $\text{Et}_3\text{N}$  (1.22 g, 1.7 mL, 12 mmol, 1.5 equiv.) were dissolved in  $\text{CH}_2\text{Cl}_2$  (30 mL) and cooled to 0 °C. Methanesulfonyl chloride (MsCl, 1.15 g, 0.8 mL, 10 mmol, 1.25 equiv.) was then added to the solution. The reaction mixture was stirred at room temperature for 12 h. Next, the reaction mixture was washed with 1M HCl, saturated  $\text{NaHCO}_3$  solution and brine (30 mL each). The compound was further purified by flash column chromatography (silica gel, pure  $\text{CH}_2\text{Cl}_2$ ) to yield the desired compound **2** as a colorless oil (2.13 g, 80% yield).  $^1\text{H}$  NMR (500 MHz,  $\text{CDCl}_3$ ):  $\delta_{\text{H}}$  4.22 (t,  $J = 6.6$  Hz, 2H); 3.39 (t,  $J = 6.6$  Hz, 2H); 3.00 (s, 3H); 2.13 (s, 3H); 1.78 – 1.71 (m, 8H); 1.67 – 1.49 (m, 8H); 1.45 – 1.34 (m, 4H).  $^{13}\text{C}$  NMR (125 MHz,  $\text{CDCl}_3$ ):  $\delta_{\text{C}}$  71.90, 70.24, 59.59, 41.78, 37.54, 36.68, 30.67, 30.64, 29.25, 25.91, 25.47. MALDI-TOF: theoretical mass of  $\text{C}_{17}\text{H}_{30}\text{O}_4\text{S}$ , 330.19; found: 353.23 for  $[\text{M}+\text{Na}]^+$ .

**Synthesis of Nb-Ethyl-OH (3)**

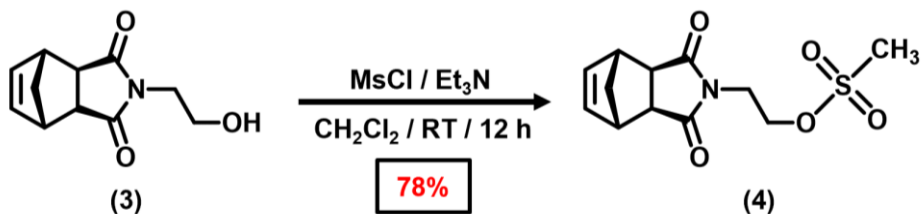


**Scheme 2.3.** Synthesis of Nb-Ethyl-OH.

Based on literature,<sup>49</sup> *cis*-5-Norbornene-*exo*-2,3-dicarboxylic acid (10.01 g, 60.98 mmol, 1 equiv.), ethanolamine (5.55 g, 5.50 mL, 91.09 mmol, 1.5 equiv.), and  $\text{Et}_3\text{N}$  (1.23 g, 1.70 mL, 12.20 mmol, 0.2 equiv.) were dissolved in 150 mL of toluene and heated to reflux at 130 °C with a Dean Stark

trap for 24 h. The organic solvent was removed, the crude material was redissolved in CH<sub>2</sub>Cl<sub>2</sub>, washed with 1 M HCl (2 x 50 mL) and with brine (50 mL). The organic layer was collected, dried by Na<sub>2</sub>SO<sub>4</sub>, and concentrated by rotary evaporation to yield the desired product **3** as a white solid (9.85 g, 78% yield). <sup>1</sup>H NMR (500 MHz, CDCl<sub>3</sub>): δ<sub>H</sub> 6.29 (t, *J* = 1.8 Hz, 2H); 3.79 – 3.76 (m, 2H); 3.72 – 3.69 (m, 2H); 3.30 – 3.27 (m, 2H); 2.72 (d, *J* = 1.3 Hz, 2H); 2.03 (s, 1H); 1.54 – 1.50 (m, 1H); 1.35 (d, *J* = 9.9 Hz, 1H). <sup>13</sup>C NMR (125 MHz, CDCl<sub>3</sub>): δ<sub>C</sub> 178.88, 137.97, 60.71, 48.05, 45.44, 42.94, 41.51.

### Synthesis of Nb-Ethyl-OMs (**4**)

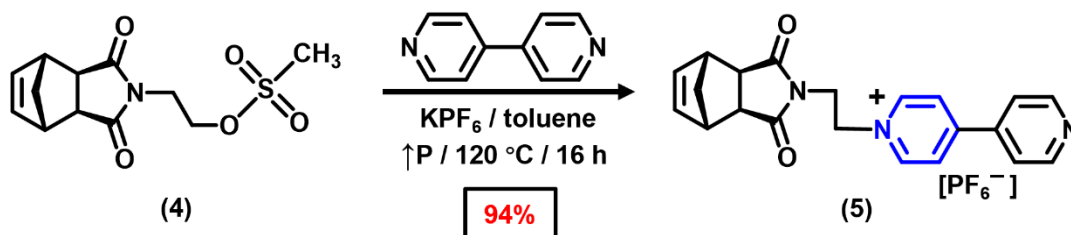


#### Scheme 2.4. Synthesis of Nb-Ethyl-OMs.

Compound **3** (5.54 g, 26.74 mmol, 1 equiv.) and Et<sub>3</sub>N (4.07 g, 5.60 mL, 40.17 mmol, 1.5 equiv.) were dissolved in 85 mL of CH<sub>2</sub>Cl<sub>2</sub>. The solution was allowed to cool to 0 °C. MsCl (4.74 g, 3.20 mL, 40.63 mmol, 1.5 equiv.) was slowly added to the cooled reaction mixture. The resulting solution was slowly warmed to room temperature and stirred for 12 h. After completion, the reaction mixture was washed in a separatory funnel with 1 M CH<sub>3</sub>COOH (3 x 100 mL), saturated NaHCO<sub>3</sub> (2 x 100 mL), and brine (2 x 100 mL). The organic layers were collected, dried with Na<sub>2</sub>SO<sub>4</sub>, and concentrated by rotary evaporation. The product was purified by flash column chromatography (silica gel, 0–3% MeOH in CH<sub>2</sub>Cl<sub>2</sub>) to yield the desired compound **4** as a pale-yellow solid (5.92 g, 78% yield). <sup>1</sup>H NMR (500 MHz, CDCl<sub>3</sub>): δ<sub>H</sub> 6.28 (t, *J* = 1.7 Hz, 2H); 4.38 (t, *J* = 5.3 Hz, 2H); 3.82 (t, *J* = 5.3 Hz, 2H); 3.28 – 3.25 (m, 2H); 3.00 (s, 3H); 2.72 (d, *J* = 1.1 Hz, 2H); 2.02 (s, 1H); 1.54 – 1.50 (m, 1H); 1.27 (d, *J* = 9.9 Hz, 1H). <sup>13</sup>C NMR (125 MHz, CDCl<sub>3</sub>): δ<sub>C</sub> 177.83,

137.89, 65.02, 48.02, 45.29, 42.92, 38.00, 37.82. MALDI-TOF: theoretical mass of  $C_{12}H_{15}NO_5S$ , 285.07; found: 286.08 for  $[M+H]^+$ , 308.07 for  $[M+Na]^+$ .

### Synthesis of Nb-1V•1PF<sub>6</sub> (5)

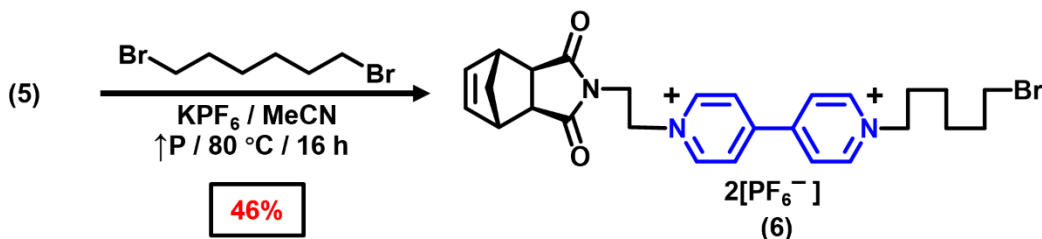


### Scheme 2.5. Synthesis of Nb-1V•1PF<sub>6</sub>.

Compound **4** (1.00 g, 3.50 mmol, 1 equiv.), 4,4'-bipyridine (10.95 g, 70.12 mmol, 20 equiv.), and KPF<sub>6</sub> (3.23 g, 17.54 mmol, 5 equiv.) were dissolved in 30 mL of toluene in a high-pressure flask equipped with a stir bar. The flask was heated at 120 °C for 16 h. After completion, the reaction mixture was allowed to cool to room temperature and concentrated by rotary evaporation. The crude product was redissolved in MeCN and transferred into 50 mL centrifuge tubes (~ 5 mL per tube) and diluted to 45 mL with Et<sub>2</sub>O. The tubes were centrifuged at 4500 rpm for 20 min. The supernatant was decanted away, the solid was re-dissolved in a minimal amount of MeCN and diluted to 45 mL with Et<sub>2</sub>O. The previous two steps were repeated three times. The resulting product was converted to **5** by dissolving in H<sub>2</sub>O followed by the addition of excess KPF<sub>6</sub>. The product precipitate was collected by centrifugation. The supernatant was decanted away and the solid was re-washed with H<sub>2</sub>O by centrifugation three times before drying under vacuum to yield the desired product **5** as a pale brown solid (1.61 g, 94% yield). <sup>1</sup>H NMR (500 MHz, (CD<sub>3</sub>)<sub>2</sub>SO): δ<sub>H</sub> 9.28 (d, *J* = 6.9 Hz, 2H); 8.88 (dd, *J* = 4.5, 1.7 Hz, 2H); 8.64 (d, *J* = 6.9 Hz, 2H); 8.06 (dd, *J* = 4.5, 1.7 Hz, 2H); 6.28 (t, *J* = 1.7 Hz, 2H); 4.82 – 4.77 (m, 2H); 4.05 – 4.01 (m, 2H); 3.03 (s, 2H); 2.67 (s, 2H); 1.35 (d, *J* = 9.8 Hz, 1H); 1.15 (d, *J* = 9.7 Hz, 1H). <sup>13</sup>C NMR (125 MHz, (CD<sub>3</sub>)<sub>2</sub>SO): δ<sub>C</sub> 177.41, 152.73, 151.07, 145.95, 140.53, 137.61, 125.16, 121.86, 58.62, 47.39, 44.39, 42.66,

38.79. MALDI-TOF: theoretical mass of  $C_{21}H_{20}F_6N_3O_2P$ , 346.16 for  $[M-PF_6]^+$ ; found: 346.21 for  $[M-PF_6]^+$ .

### Synthesis of Nb-1V•2PF<sub>6</sub> (6)

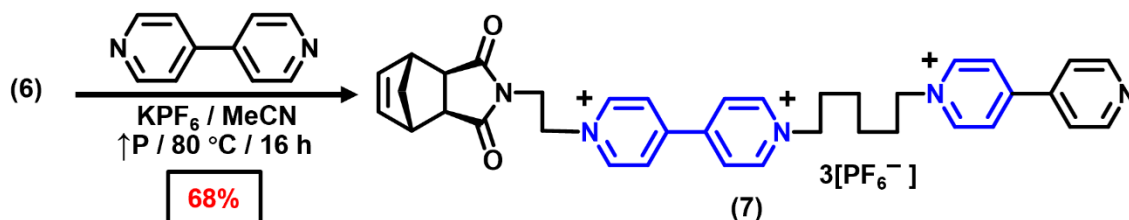


### Scheme 2.6. Synthesis of Nb-1V•2PF<sub>6</sub>.

Compound **5** (0.60 g, 1.23 mmol, 1 equiv.), dibromohexane (9.04 g, 5.70 mL, 37.05 mmol, 30 equiv.), and KPF<sub>6</sub> (1.15 g, 6.24 mmol, 5 equiv.) were dissolved in 20 mL of dry MeCN in a high-pressure flask equipped with a stir bar. The flask was heated at 80 °C and the reaction ran for 16 h. After completion, the reaction mixture was allowed to cool to room temperature. The crude product was transferred into 50 mL centrifuge tubes (~ 5 mL per tube) and diluted to 45 mL with Et<sub>2</sub>O. The tubes were centrifuged at 4500 rpm for 20 min. The supernatant was decanted away and the solid was re-dissolved in a minimal amount of MeCN and diluted to 45 mL with Et<sub>2</sub>O. The previous two steps were repeated three times. The resulting product was converted to **6** by dissolving in H<sub>2</sub>O followed by the addition of excess KPF<sub>6</sub>. The product precipitate was collected by centrifugation. The supernatant was decanted and the solid was re-washed with H<sub>2</sub>O by centrifugation three times before drying under vacuum to yield the desired product **6** as a pale brown solid (0.45 g, 46% yield). <sup>1</sup>H NMR (500 MHz, (CD<sub>3</sub>)<sub>2</sub>SO): δ<sub>H</sub> 9.44 (d, *J* = 6.8 Hz, 2H); 9.38 (d, *J* = 6.8 Hz, 2H); 8.79 (dd, *J* = 9.2, 6.9 Hz, 4H); 6.28 (s, 2H); 4.89 – 4.83 (m, 2H); 4.68 (t, *J* = 7.4 Hz, 2H); 4.08 – 4.04 (m, 2H); 3.54 (t, *J* = 6.7 Hz, 2H); 3.03 (s, 2H); 2.66 (s, 2H); 1.99 (dt, *J* = 15.1, 7.6 Hz, 2H); 1.81 (dd, *J* = 14.4, 7.0 Hz, 2H); 1.45 (dt, *J* = 14.6, 7.2 Hz, 2H); 1.39 – 1.31 (m, 3H); 1.16 (d, *J* = 9.7 Hz, 1H). <sup>13</sup>C NMR (125 MHz, (CD<sub>3</sub>)<sub>2</sub>SO): δ<sub>C</sub> 177.42, 148.96, 148.16, 146.50,

145.84, 137.63, 126.58, 126.34, 60.88, 59.23, 47.41, 44.38, 42.69, 38.83, 34.99, 31.89, 30.53, 26.90, 24.51. MALDI-TOF: theoretical mass of  $C_{27}H_{32}BrF_{12}N_3O_2P_2$ , 509.17 for  $[M-2PF_6]^{++}$ ; found: 509.33 for  $[M-2PF_6]^{++}$ .

### Synthesis of Nb-2V•3PF<sub>6</sub> (7)

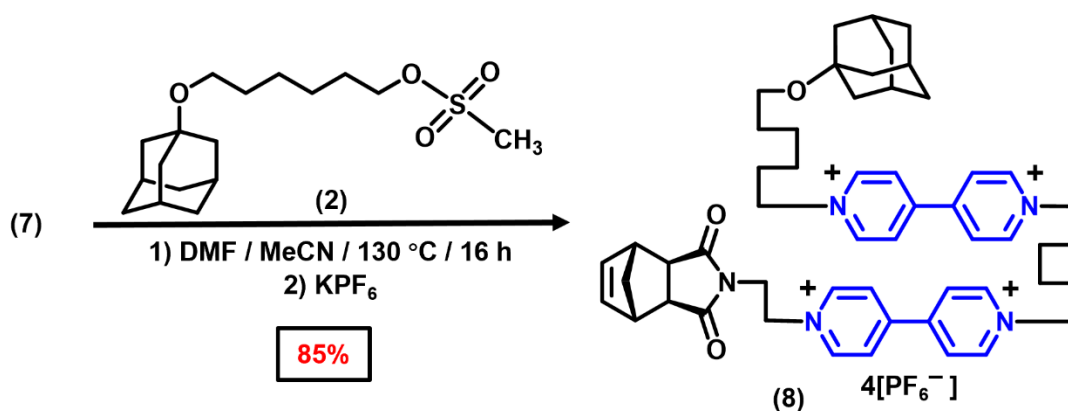


### Scheme 2.7. Synthesis of Nb-2V•3PF<sub>6</sub>.

Compound **6** (0.53 g, 0.67 mmol, 1 equiv.), 4,4'-bipyridine (3.13 g, 20.03 mmol, 30 equiv.), and KPF<sub>6</sub> (0.62 g, 3.33 mmol, 5 equiv.) were dissolved in 20 mL of MeCN in a high-pressure flask equipped with a stir bar. The flask was heated at 80 °C and the reaction ran for 16 h. After completion, the reaction mixture was allowed to cool to room temperature. The crude product was transferred into 50 mL centrifuge tubes (~ 5 mL per tube) and diluted to 45 mL with Et<sub>2</sub>O. The tubes were centrifuged at 4500 rpm for 20 min. The supernatant was decanted away and the solid was re-dissolved in a minimal amount of MeCN and diluted to 45 mL with Et<sub>2</sub>O. The previous two steps were repeated three times. The resulting product was converted to **7** by dissolving in H<sub>2</sub>O followed by the addition of excess KPF<sub>6</sub>. The product precipitate was collected by centrifugation. The supernatant was decanted and the solid was re-washed with H<sub>2</sub>O by centrifugation three times before drying under vacuum to yield the desired product **7** as a brown solid (0.43 g, 68% yield). <sup>1</sup>H NMR (500 MHz, (CD<sub>3</sub>)<sub>2</sub>SO):  $\delta_H$  9.46 (t,  $J = 6.1$  Hz, 2H); 9.36 (d,  $J = 7.0$  Hz, 2H); 9.21 (d,  $J = 7.0$  Hz, 2H); 8.89 (dd,  $J = 4.5, 1.7$  Hz, 2H); 8.83 – 8.77 (m, 4H); 8.64 (d,  $J = 6.9$  Hz, 2H); 8.04 (dd,  $J = 4.5, 1.7$  Hz, 2H); 6.30 – 6.27 (m, 2H); 4.89 – 4.84 (m, 2H); 4.65 (dt,  $J = 23.1, 7.4$  Hz, 4H); 4.09 – 4.04 (m, 2H); 3.02 (s, 2H); 2.67 (t,  $J = 3.6$  Hz, 2H); 1.98 (d,  $J = 6.7$  Hz, 4H); 1.37 (dd,  $J =$

12.4, 8.7 Hz, 5H); 1.16 (d,  $J = 9.7$  Hz, 1H).  $^{13}\text{C}$  NMR (125 MHz,  $(\text{CD}_3)_2\text{SO}$ ):  $\delta_{\text{C}}$  177.45, 152.39, 150.99, 148.92, 148.22, 146.52, 145.82, 145.27, 140.87, 137.63, 126.57, 126.34, 125.40, 121.91, 60.84, 60.32, 59.26, 47.42, 44.39, 42.70, 38.85, 30.48, 30.41, 24.91. MALDI-TOF: theoretical mass of  $\text{C}_{37}\text{H}_{40}\text{F}_{18}\text{N}_5\text{O}_2\text{P}_3$ , 731.28 for  $[\text{M}-2\text{PF}_6]^{++}$ ; found: 731.65 for  $[\text{M}-2\text{PF}_6]^{++}$ .

### Synthesis of Nb-2V-Ad•4PF<sub>6</sub> (8)

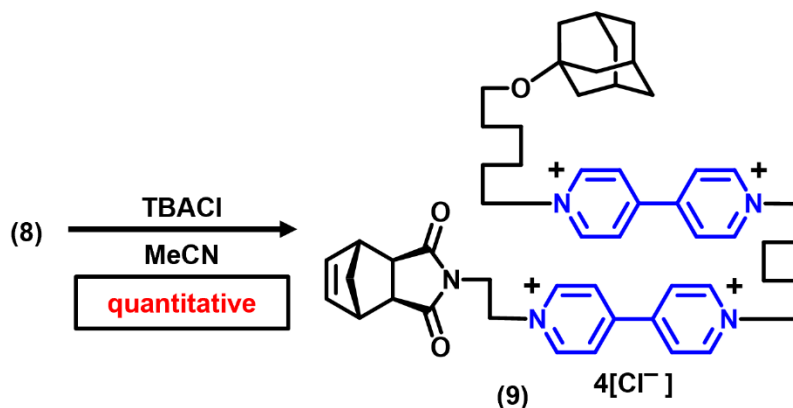


#### Scheme 2.8. Synthesis of Nb-2V-Ad•4PF<sub>6</sub>.

Compound **7** (376.3 mg, 0.37 mmol, 1 equiv.) and **2** (365.2 mg, 1.1 mmol, 3 equiv.) were dissolved in 3 mL solvent (2 mL MeCN + 1 mL DMF) in a tube equipped with a stir bar. The tube was heated at 130 °C and the reaction ran for 16 h. After completion, the reaction mixture was allowed to cool to room temperature. The crude product was then dissolved in 5 mL MeCN, transferred into a 50 mL centrifuge tube, and diluted to 45 mL with Et<sub>2</sub>O. The tube was centrifuged at 4500 rpm for 20 min. The supernatant was decanted away and the solid was re-dissolved in a minimal amount of MeCN and diluted to 45 mL with Et<sub>2</sub>O. The previous two steps were repeated three times. The resulting product was converted to **8** by dissolving in H<sub>2</sub>O followed by the addition of excess KPF<sub>6</sub>. The product precipitate was collected by centrifugation. The supernatant was decanted and the solid was re-washed with H<sub>2</sub>O by centrifugation three times before drying under vacuum to yield the desired product **8** as a brown solid (400 mg, 85% yield).  $^1\text{H}$  NMR (500 MHz,  $(\text{CD}_3)_2\text{SO}$ ):  $\delta_{\text{H}}$  9.45 (d,  $J = 6.1$  Hz, 2H); 9.40 – 9.33 (m, 6H); 8.84 – 8.73 (m, 8H); 6.28 (s, 2H); 4.87 (s, 2H); 4.68

(s, 6H); 4.06 (s, 2H); 3.03 (s, 2H); 2.67 (s, 2H); 2.07 (s, 3H); 2.00 (s, 6H); 1.64 (s, 6H); 1.56 (dd,  $J = 27.4, 12.0$  Hz, 7H); 1.37 (d,  $J = 30.6$  Hz, 12H); 1.17 (d,  $J = 9.5$  Hz, 1H).  $^{13}\text{C}$  NMR  $\delta_{\text{C}}$  177.42, 148.88, 148.66, 148.51, 148.21, 146.51, 145.73, 137.62, 126.54, 126.32, 70.93, 60.98, 60.80, 59.25, 58.68, 47.40, 44.38, 42.68, 41.20, 40.11, 39.94, 39.78, 39.61, 38.85, 35.95, 30.73, 30.51, 29.89, 29.82, 25.32, 25.28, 24.97. MALDI-TOF: theoretical mass of  $\text{C}_{53}\text{H}_{67}\text{F}_{24}\text{N}_5\text{O}_3\text{P}_4$ , 966.50 for  $[\text{M}-3\text{PF}_6]^+$ ; found: 967.10 for  $[\text{M}-3\text{PF}_6]^+$ .

### Synthesis of Nb-2V-Ad•4Cl (9)

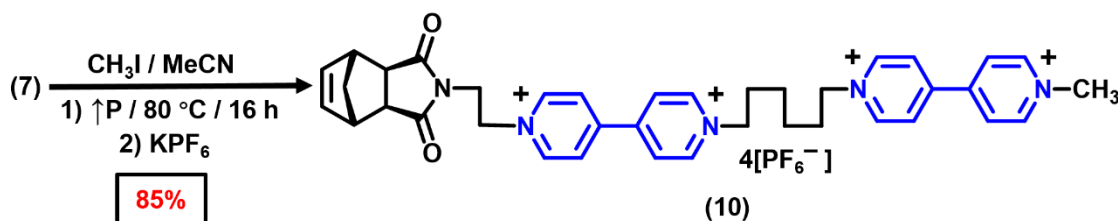


### Scheme 2.9. Synthesis of Nb-2V-Ad•4Cl.

Compound **8** (50 mg, 0.036 mmol, 1 equiv.) was dissolved in 1 mL MeCN in a centrifuge tube. Tetrabutylammonium chloride (TBACl, 240 mg, 0.864 mmol, 24 equiv.) was dissolved in a minimal amount of MeCN and added dropwise to the centrifuge tube. The product precipitate was collected by centrifugation. The supernatant was decanted and the solid was re-washed with MeCN by centrifugation five times before drying under vacuum to yield the desired product **9** as a brown solid.  $^1\text{H}$  NMR (500 MHz,  $\text{D}_2\text{O}$ ):  $\delta_{\text{H}}$  9.23 (d,  $J = 6.1$  Hz, 2H), 9.15 (d,  $J = 5.0$  Hz, 6H), 8.62 – 8.55 (m, 8H), 6.34 (s, 2H), 4.98 (s, 2H), 4.24 (s, 2H), 3.18 (s, 2H), 2.87 (s, 2H), 2.11 (m, 9H), 1.71 (s, 6H), 1.61 (d,  $J = 11.9$  Hz, 4H), 1.54 (d,  $J = 14.3$  Hz, 12H), 1.40 (s, 4H), 1.14 (d,  $J = 10.0$  Hz, 1H).  $^{13}\text{C}$  NMR (125 MHz,  $\text{D}_2\text{O}$ ):  $\delta_{\text{C}}$  180.76, 150.99, 149.93, 149.83, 149.68, 146.01, 145.45, 137.64, 127.11, 127.01, 126.89, 126.85, 74.07, 62.17, 61.96, 61.93, 59.55, 59.50, 47.85, 44.88,

42.26, 40.62, 39.12, 35.58, 30.41, 30.39, 30.34, 30.22, 28.97, 24.86, 24.68. (Note: Compound **9** from the counter anion exchange process is not used for any polymerizations, it is only used in ITC and as a reference monomer peak while running analytical GPC using H<sub>2</sub>O as mobile phase.)

### Synthesis of Nb-2V-Me•4PF<sub>6</sub> (**10**)

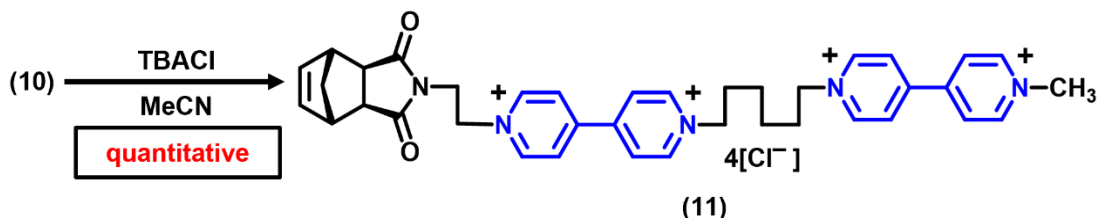


#### Scheme 2.10. Synthesis of Nb-2V-Me•4PF<sub>6</sub>.

Compound **7** (600 mg, 0.59 mmol, 1 equiv.) and iodomethane (83.56 mg, 0.32 mL, 5.9 mmol, 10 equiv.) were dissolved in 15 mL of MeCN in a high-pressure flask equipped with a stir bar. The flask was heated at 80 °C and the reaction ran for 16 h. After completion, the reaction mixture was allowed to cool to room temperature. The crude product was transferred into 50 mL centrifuge tubes (~ 5 mL per tube) and diluted to 45 mL with Et<sub>2</sub>O. The tubes were centrifuged at 4500 rpm for 20 min. The supernatant was decanted away and the solid was re-dissolved in a minimal amount of MeCN and diluted to 45 mL with Et<sub>2</sub>O. The previous two steps were repeated three times. The resulting product was converted to **10** by dissolving in H<sub>2</sub>O followed by the addition of excess KPF<sub>6</sub>. The product precipitate was collected by centrifugation. The supernatant was decanted and the solid was re-washed with H<sub>2</sub>O by centrifugation three times before drying under vacuum to yield the desired product **10** as a yellow solid (548 mg, 90% yield). <sup>1</sup>H NMR (500 MHz, (CD<sub>3</sub>)<sub>2</sub>SO): δ<sub>H</sub> 9.45 (d, *J* = 6.7 Hz, 2H); 9.36 (t, *J* = 6.3 Hz, 4H); 9.28 (d, *J* = 6.6 Hz, 2H); 8.83 – 8.72 (m, 8H); 6.28 (s, 2H); 4.86 (s, 2H); 4.68 (s, 4H); 4.44 (s, 3H); 4.06 (s, 2H); 3.02 (s, 2H); 2.67 (s, 2H); 2.00 (s, 4H); 1.42 – 1.33 (m, 5H); 1.17 (d, *J* = 9.8 Hz, 1H). <sup>13</sup>C NMR (125 MHz, (CD<sub>3</sub>)<sub>2</sub>SO): δ<sub>C</sub> 177.49, 148.96, 148.69, 148.28, 148.20, 146.65, 146.53, 145.83, 145.75, 137.66, 126.61, 126.55, 126.38, 126.10, 60.83, 59.29, 48.10, 47.44, 44.42, 42.72, 39.94, 39.78, 38.88, 30.53,

24.97. MALDI-TOF: theoretical mass of  $C_{38}H_{43}F_{24}N_5O_2P_4$ , 746.31 for  $[M-3PF_6]^+$ ; found: 746.75 for  $[M-3PF_6]^+$ .

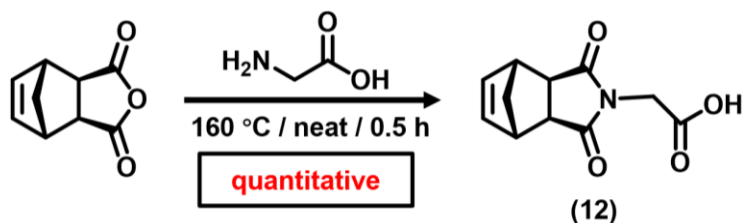
### Synthesis of Nb-2V-Me•4Cl (11)



### Scheme 2.11. Synthesis of Nb-2V-Me•4Cl.

Compound **10** (50 mg, 0.042 mmol, 1 equiv.) was dissolved in 1 mL MeCN in a centrifuge tube. TBACl (280 mg, 1.008 mmol, 24 equiv.) was dissolved in a minimal amount of MeCN and added dropwise to the centrifuge tube. The product precipitate was collected by centrifugation. The supernatant was decanted and the solid was re-washed with MeCN by centrifugation five times before drying under vacuum to yield the desired product **11** as a brown solid. <sup>1</sup>H NMR (500 MHz, D<sub>2</sub>O):  $\delta_H$  9.23 (d,  $J = 6.8$  Hz, 2H), 9.15 – 9.12 (m, 4H), 9.07 (d,  $J = 6.4$  Hz, 2H), 8.61 – 8.52 (m, 8H), 6.34 (s, 2H), 4.95 (m, 2H), 4.52 (s, 3H), 4.26 – 4.22 (m, 2H), 3.18 (s, 2H), 2.87 (s, 2H), 2.13 (s, 4H), 1.53 (s, 5H), 1.14 (d,  $J = 10.1$  Hz, 1H). <sup>13</sup>C NMR (125 MHz, D<sub>2</sub>O):  $\delta_C$  180.77, 151.03, 150.06, 149.75, 149.68, 146.26, 146.00, 145.46, 145.36, 137.66, 127.15, 127.04, 126.95, 126.61, 61.97, 61.90, 59.49, 48.31, 47.86, 44.89, 42.29, 39.12, 30.36, 24.82. (Note: Compound **11** from the counter anion exchange process is not used for any polymerizations, it is only used as a reference monomer peak while running analytical GPC using H<sub>2</sub>O as mobile phase.)

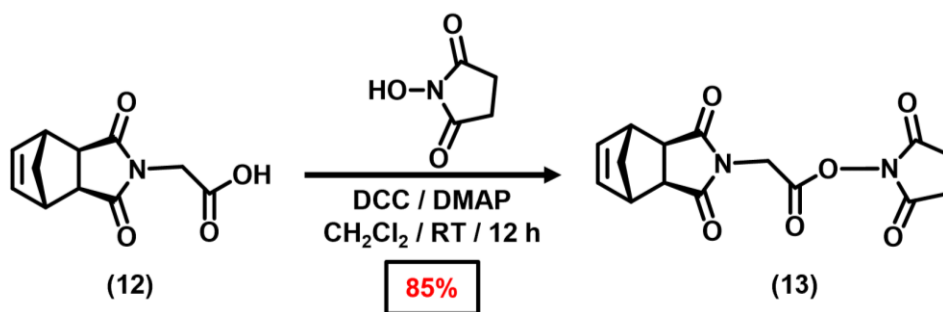
### Synthesis of Nb-Gly (12)



**Scheme 2.12.** Synthesis of **Nb-Gly**.

Compound **12** was synthesized according to a previous literature procedure.<sup>50</sup> *Cis*-5-Norbornene-*exo*-2,3-dicarboxylic anhydride (5.288g, 0.032 mol, 1 equiv.) and glycine (2.418 g, 0.032 mmol, 1 equiv.) were added to a 14/20 neck, 50 mL round-bottom flask and heated to 160 °C for 30 min (melt). After completion, the crude reaction mixture was allowed to cool to room temperature to yield the desired compound **12** as a white solid without further purification (7.12 g, quantitative). <sup>1</sup>H NMR (500 MHz, CDCl<sub>3</sub>):  $\delta_H$  6.30 (s, 2H); 4.27 (s, 2H); 3.31 (s, 2H); 2.76 (s, 2H); 1.60 (d,  $J = 10.0$  Hz, 1H); 1.50 (d,  $J = 9.9$  Hz, 1H). <sup>13</sup>C NMR (125 MHz, CDCl<sub>3</sub>):  $\delta_C$  177.38, 171.95, 138.11, 48.16, 45.55, 42.97, 39.27.

**Synthesis of Nb-NHS (13)**

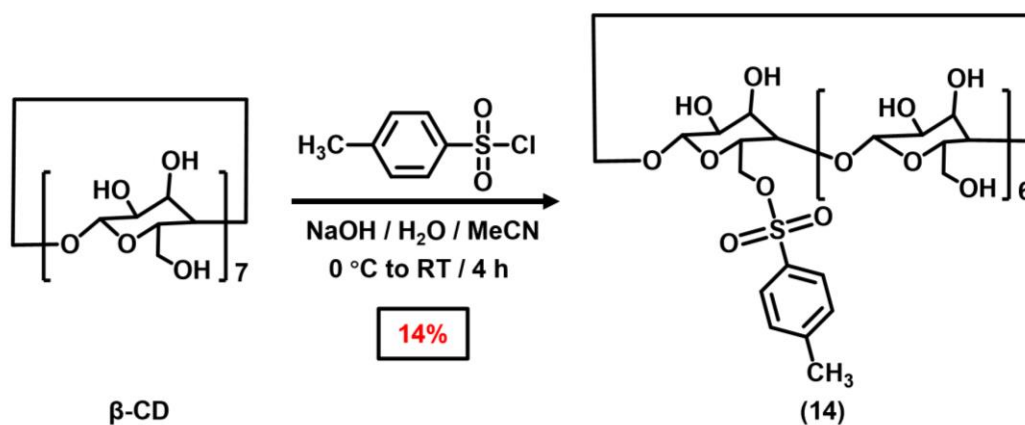


**Scheme 2.13.** Synthesis of **Nb-NHS**.

Based on a literature procedure,<sup>50</sup> a mixture of dicyclohexylcarbodiimide (DCC, 8.11 g, 39.31 mmol, 1.3 equiv.) and **12** (6.689 g, 30.24 mmol, 1 equiv.) was dissolved in CH<sub>2</sub>Cl<sub>2</sub> (anhydrous, 105 mL) and stirred at room temperature for 15 min until a precipitate formed. *N*-hydroxysuccinimide (NHS, 6.96 g, 60.48 mmol, 2 equiv.) was added to the precipitated solution

and stirred at room temperature for 12 h. After filtration of DCU, the crude product was recrystallized with adequate amount of hot EtOAc to dissolve and cooled down in fridge to yield the product **13** as a white solid (8.18 g, 85 % yield).  $^1\text{H}$  NMR (500 MHz,  $\text{CDCl}_3$ ):  $\delta_{\text{H}}$  6.30 (t,  $J = 1.8$  Hz, 2H); 4.57 (s, 2H); 3.39 – 3.26 (m, 2H); 2.83 (s, 4H); 2.78 (d,  $J = 1.1$  Hz, 2H); 1.61 (s, 2H); 1.56 (d,  $J = 10.0$  Hz, 1H), 1.51 (d,  $J = 10.1$  Hz, 1H).  $^{13}\text{C}$  NMR (125 MHz,  $\text{CDCl}_3$ ):  $\delta_{\text{C}}$  176.46, 168.26, 163.26, 138.12, 48.16, 45.62, 43.00, 37.27, 25.67.

### Synthesis of CD-OTs (**14**)

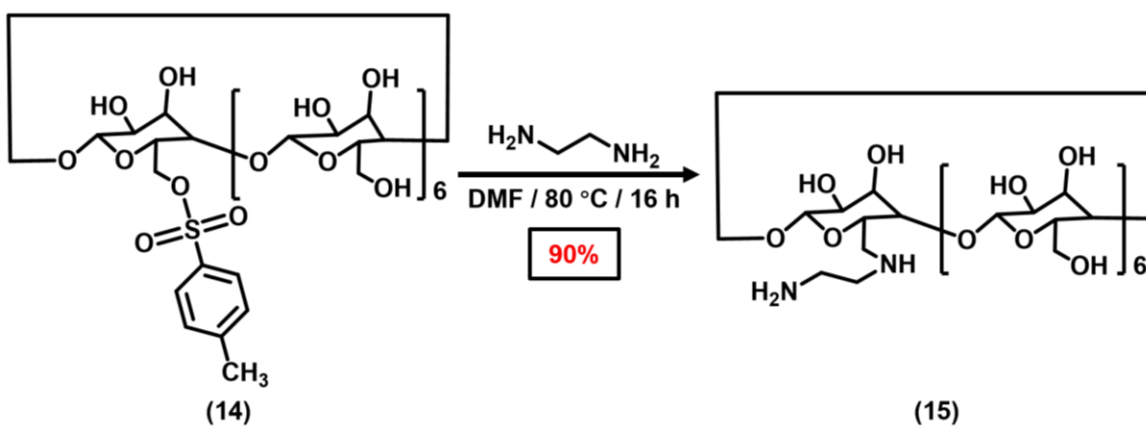


#### Scheme 2.14. Synthesis of CD-OTs.

Based on a reported preparation,<sup>51, 52</sup> a solution of NaOH (2.12 g, 52.9 mmol, 3 equiv.) in  $\text{H}_2\text{O}$  (8 mL) was added dropwise to a solution of purified  $\beta$ -cyclodextrin ( $\beta\text{-CD}$ , 20.0 g, 17.62 mmol, 1 equiv.) in  $\text{H}_2\text{O}$  (110 mL) and stirred for 1 h. A solution *p*-toluenesulfonyl chloride (TsCl, 3.70 g, 19.4 mmol, 1.1 equiv.) in MeCN (15 mL) was added dropwise and the reaction was stirred at room temperature for 3 h. After completion, the unwanted precipitate was filtered, and the pH of the filtrate was adjusted to 7 using 1 M HCl to yield a white solid. Hot  $\text{H}_2\text{O}$  (200 mL) was added and the resulting solution was stirred at 90  $^\circ\text{C}$  until the white solid dissolved, and the solution was cooled to 0–4 $^\circ\text{C}$  overnight. The resulting solid was collected by filtration and washed with cold  $\text{H}_2\text{O}$  to yield the desired compound **14** as a white solid (3.18 g, 14% yield).  $^1\text{H}$  NMR (500 MHz,

(CD<sub>3</sub>)<sub>2</sub>SO):  $\delta_H$  7.75 (d,  $J = 8.3$  Hz, 2H); 7.43 (d,  $J = 8.3$  Hz, 2H); 5.84 – 5.61 (m, 14 H); 4.87 – 4.74 (m, 7H); 4.60 – 4.11 (m, 9H); 3.78 – 3.52 (m, 25 H); 3.52 – 3.16 (m, 14H, overlap with H<sub>2</sub>O), 2.42 (s, 3H). <sup>13</sup>C NMR (125 MHz, (CD<sub>3</sub>)<sub>2</sub>SO):  $\delta_C$  144.65, 133.29, 129.90, 128.06, 79.91, 38.82, 36.85, 33.55, 27.97, 21.79. ESI-MS: theoretical mass of C<sub>49</sub>H<sub>76</sub>O<sub>37</sub>S, 1288.38; found, 1289.38 for [M+H]<sup>+</sup>, 1311.36 for [M+Na]<sup>+</sup>, 667.18 for [M+2Na]<sup>2+</sup>.

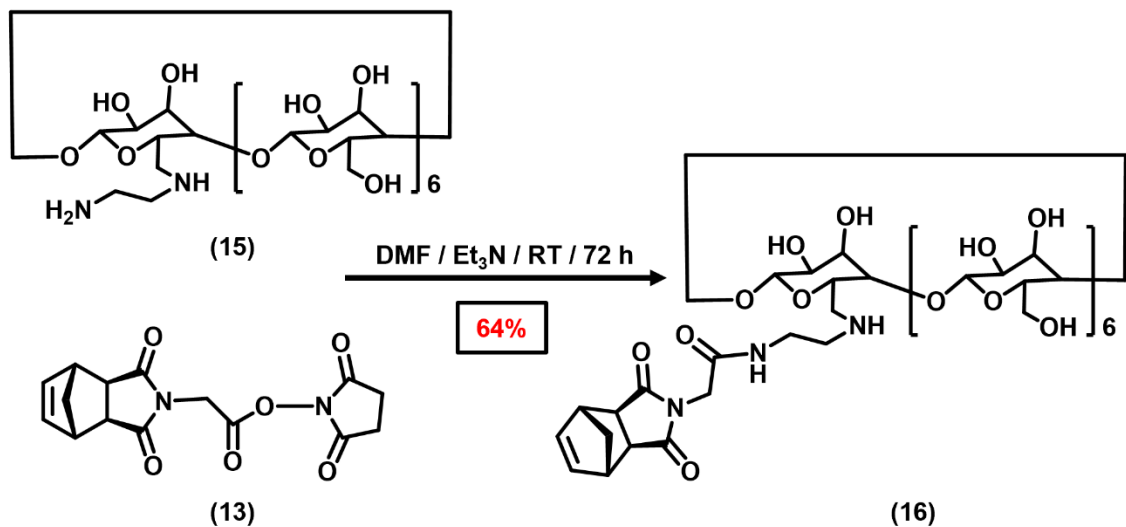
### Synthesis of CD-NH<sub>2</sub> (15)



#### Scheme 2.15. Synthesis of CD-NH<sub>2</sub>.

Compound **14** (1.00 g, 0.78 mmol, 1 equiv.) and ethylenediamine (excess, 9.00 g, 10 mL, 150 mmol, ~100 equiv.) were dissolved in DMF (anhydrous, 10 mL) and heated to 80 °C for 16 h. After completion, the organic solvent and excess ethylenediamine were removed by rotary evaporator. The crude material was re-dissolved in a minimal amount of DMF, and added dropwise to Me<sub>2</sub>CO (500 mL), The solid was filtered and washed with cold Me<sub>2</sub>CO to yield the desired compound **15** as a white powder (0.82 g, 90% yield). <sup>1</sup>H NMR (500 MHz, D<sub>2</sub>O):  $\delta_H$  5.04 (s, 7H); 3.97 – 3.79 (m, 28H); 3.65 – 3.50 (m, 14H); 2.87 – 2.67 (m, 4H). <sup>13</sup>C NMR (125 MHz, (CD<sub>3</sub>)<sub>2</sub>SO):  $\delta_C$  101.94, 81.53, 73.05, 72.41, 72.03, 60.99, 59.95. ESI-MS: theoretical mass of C<sub>44</sub>H<sub>76</sub>N<sub>2</sub>O<sub>34</sub>, 1176.43; found, 1177.43 for [M+H]<sup>+</sup>, 589.21 for [M+2H]<sup>2+</sup>.

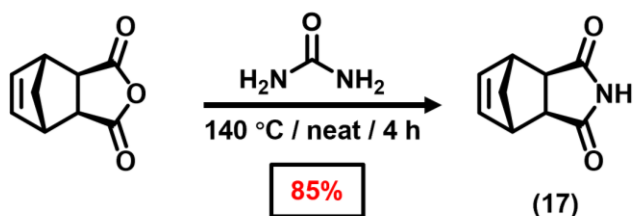
### Synthesis of Nb-CD (16)



**Scheme 2.16.** Synthesis of **Nb-CD**.

Compound **13** (100 mg, 0.314 mmol, 1.05 equiv.) and **15** (352 mg, 0.299 mmol, 1 equiv.) were dissolved in DMF (anhydrous, 15 mL).  $\text{Et}_3\text{N}$  (0.045 g, 0.06 mL, 0.448 mmol, 1.5 equiv.) was added slowly and the resulting solution was stirred at room temperature for 72 h. After completion, the organic solvent and excess  $\text{Et}_3\text{N}$  were removed by rotary evaporator. The crude material was re-dissolved in a minimal amount of DMF and precipitated by the addition of  $\text{Me}_2\text{CO}$ . The solution and precipitate were transferred to a 50 mL centrifuge tube and was centrifuged at 4500 rpm and  $-10^\circ\text{C}$  for 45 min. The  $\text{Me}_2\text{CO}$  was carefully decanted away from the precipitate, the precipitate was re-dissolved in DMF and diluted to 50 mL with  $\text{Me}_2\text{CO}$ , and the mixture was centrifuged at 4500 rpm and  $-10^\circ\text{C}$  for 45 min. The previous two steps were repeated two more times to yield the desired compound **16** as a white powder (265 mg, 64% yield).  $^1\text{H}$  NMR (500 MHz,  $(\text{CD}_3)_2\text{SO}$ ):  $\delta_{\text{H}}$  8.11 (s, 1H); 6.31 (s, 2H); 5.84 – 5.69 (m, 14H); 4.88 – 4.79 (m, 7H); 4.45 (s, 6H); 3.97 (s, 2H); 3.71 – 3.26 (m, 42H, overlap with  $\text{H}_2\text{O}$ ); 3.11 (s, 2H); 2.70 (s, 2H); 1.76 (d,  $J = 9.2$  Hz, 1H); 1.30 (d,  $J = 9.4$  Hz, 1H).  $^{13}\text{C}$  NMR (125 MHz,  $(\text{CD}_3)_2\text{SO}$ ):  $\delta_{\text{C}}$  177.15, 177.10, 165.78, 137.80, 101.97, 83.18, 81.55, 73.06, 72.44, 72.01, 59.90, 48.47, 47.36, 44.67, 44.65, 42.48. ESI-MS: theoretical mass of  $\text{C}_{55}\text{H}_{85}\text{N}_3\text{O}_{37}$ , 1379.49; found, 1380.49 for  $[M+\text{H}]^+$ , 701.74 for  $[M+\text{Na}+\text{H}]^{2+}$ .

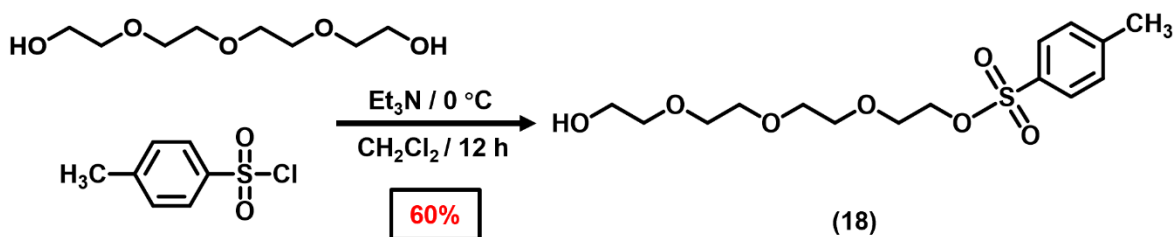
### Synthesis of Nb-DCI (17)



### Scheme 2.17. Synthesis of Nb-DCI.

Compound **17** was synthesized according to a previous literature procedure.<sup>50</sup> *cis*-5-Norbornene-*exo*-2,3-dicarboxylic anhydride (4.00 g, 24.40 mmol, 1 equiv.) and urea (2.932 g, 48.80 mmol, 2 equiv.) were added to a 14/20 neck, 25 mL round-bottom flask and heated to 140 °C for 4 h (melt). After completion of the reaction, H<sub>2</sub>O (10 mL) was added, and the solution was heated until a homogeneous solution formed. The resulting solution was allowed to cool to room temperature and crystals were collected via filtration and washed several times with H<sub>2</sub>O to yield the desired product **17** as a white, crystalline solid (3.40 g, 85% yield). <sup>1</sup>H NMR (500 MHz, CDCl<sub>3</sub>): δ<sub>H</sub> 6.28 (t, *J* = 1.7 Hz, 2H); 3.29 (m, 2H); 2.74 (m, 2H); 1.57 (d, *J* = 9.9 Hz, 1H); 1.46 (d, *J* = 10.0 Hz, 1H). <sup>13</sup>C NMR (125 MHz, CDCl<sub>3</sub>): δ<sub>C</sub> 178.26, 137.90, 49.32, 45.31, 43.06.

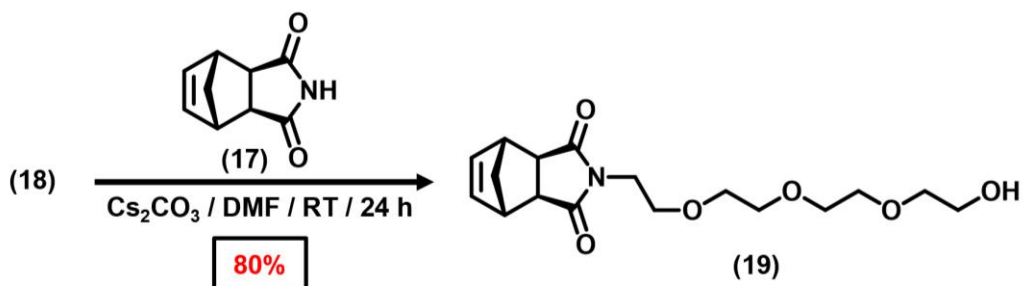
### Synthesis of TEG-OTs (18)



**Scheme 2.18.** Synthesis of TEG-OTs.

Tetraethylene glycol (39.375 g, 202.73 mmol, 4 equiv.) and Et<sub>3</sub>N (10.157 g, 14 mL, 100.38 mmol, 2 equiv.) were dissolved in CH<sub>2</sub>Cl<sub>2</sub> (250 mL) and cooled to 0 °C. A solution of TsCl (9.00 g, 47.20 mmol, 1 equiv.) in CH<sub>2</sub>Cl<sub>2</sub> (50 mL) was added. The resulting solution was stirred overnight. Then, the reaction mixture was washed with saturated K<sub>2</sub>CO<sub>3</sub> solution, brine, and 1M HCl (125 mL each). The organic layer was dried over Na<sub>2</sub>SO<sub>4</sub> and concentrated. The compound was further purified by flash column chromatography (silica gel, 100:1 CH<sub>2</sub>Cl<sub>2</sub>: MeOH) to yield the desired compound **18** as a colorless oil (10.88 g, 60% yield). <sup>1</sup>H NMR (500 MHz, CDCl<sub>3</sub>): δ<sub>H</sub> 7.78 (d, *J* = 8.5 Hz, 2H); 7.33 (d, *J* = 8.5 Hz, 2H); 4.16 – 4.13 (m, 2H); 3.71 – 3.57 (m, 14H); 2.52 (s, 1H); 2.43 (s, 3H). <sup>13</sup>C NMR (125 MHz, CDCl<sub>3</sub>): δ<sub>C</sub> 144.93, 133.00, 129.92, 128.06, 72.55, 70.81, 70.73, 70.54, 70.39, 69.35, 68.78, 21.75. MALDI-TOF: theoretical mass of C<sub>15</sub>H<sub>24</sub>O<sub>7</sub>S, 348.12; found: 349.19 for [M+H]<sup>+</sup>.

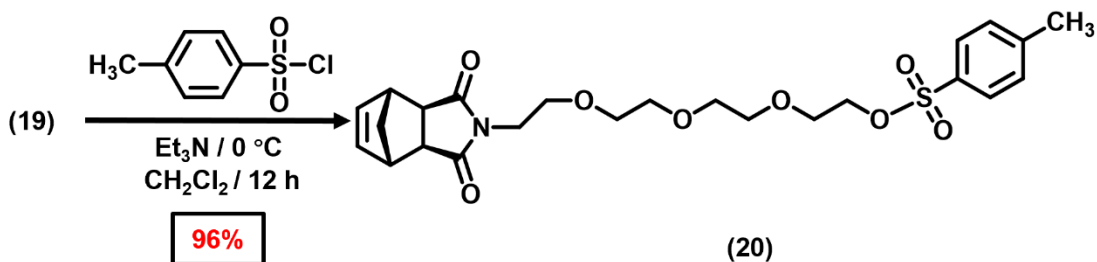
**Synthesis of Nb-TEG (19)**



**Scheme 2.19.** Synthesis of **Nb-TEG**.

Compound **17** (3.01 g, 18.44 mmol, 1.1 equiv.) and  $\text{Cs}_2\text{CO}_3$  (7.30 g, 83.09 mmol, 5 equiv.) were dissolved in DMF (anhydrous, 60 mL) and the solution was stirred at room temperature for 1 h. A solution of **18** (5.84g, 16.76 mmol, 1 equiv.) in DMF (anhydrous, 20 mL) was added and stirred at room temperature for an additional 24 h. After completion, the reaction mixture was filtered and the DMF was removed. The crude was re-dissolved in  $\text{CH}_2\text{Cl}_2$  (100 mL), washed with  $\text{H}_2\text{O}$  (30 mL), and dried over  $\text{Na}_2\text{SO}_4$ . The compound was further purified by flash column chromatography (silica gel, 100:1  $\text{CH}_2\text{Cl}_2$ : MeOH) to yield the desired product **19** as a colorless oil (4.14 g, 72% yield).  $^1\text{H}$  NMR (500 MHz,  $\text{CDCl}_3$ ):  $\delta_{\text{H}}$  6.28 – 6.25 (m, 2H); 3.72 – 3.55 (m, 16H); 3.25 (s, 2H); 2.67 (s, 2H); 2.52 (s, 1H); 1.47 (d,  $J=10.0$  Hz, 1H); 1.34 (d,  $J=10.0$  Hz, 1H).  $^{13}\text{C}$  NMR (125 MHz,  $\text{CDCl}_3$ ):  $\delta_{\text{C}}$  178.20, 137.93, 72.63, 70.76, 70.65, 70.45, 69.97, 67.07, 61.86, 47.93, 45.36, 42.84, 37.86. MALDI-TOF: theoretical mass of  $\text{C}_{17}\text{H}_{25}\text{NO}_6$ , 339.17; found: 340.35 for  $[M+\text{H}]^+$ , 362.22 for  $[M+\text{Na}]^+$ .

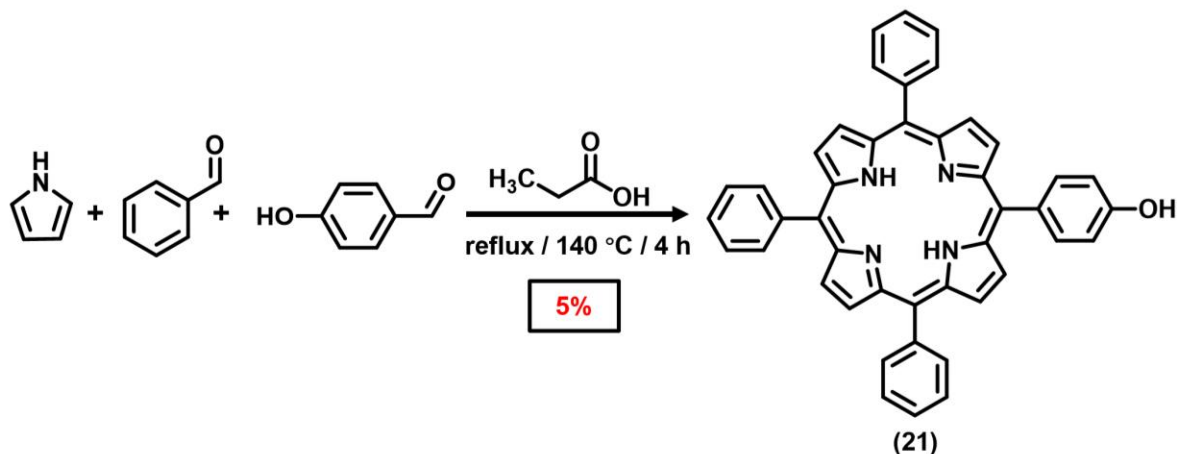
**Synthesis of Nb-TEG-OTs (20)**



**Scheme 2.20.** Synthesis of **Nb-TEG-OTs**.

Compound **19** (720 mg, 2.12 mmol, 1 equiv.) and  $\text{Et}_3\text{N}$  (430 mg, 0.6 mL, 4.24 mmol, 2 equiv.) were dissolved in  $\text{CH}_2\text{Cl}_2$  (15 mL) and cooled to  $0 \text{ }^\circ\text{C}$ . A solution of  $\text{TsCl}$  (809.8 mg, 4.24 mmol, 2 equiv.) in  $\text{CH}_2\text{Cl}_2$  (10 mL) was added, and the resulting solution was stirred overnight. Then, the reaction mixture was washed with  $\text{H}_2\text{O}$  and brine (10 mL each), and the organic layer was dried over  $\text{Na}_2\text{SO}_4$  and concentrated. The compound was further purified by flash column chromatography (silica gel, 100:1  $\text{CH}_2\text{Cl}_2$ : MeOH) to yield the desired compound **20** as a colorless oil (1.03 g, 96% yield).  $^1\text{H}$  NMR (500 MHz,  $\text{CDCl}_3$ ):  $\delta_{\text{H}}$  7.78 (d,  $J = 8.1$  Hz, 2H); 7.33 (d,  $J = 7.9$  Hz, 2H); 6.27 (s, 2H); 4.16 – 4.12 (m, 2H); 3.69 – 3.51 (m, 14H); 3.25 (s, 2H); 2.66 (s, 2H); 2.44 (s, 3H); 1.46 (d,  $J = 9.9$  Hz, 1H); 1.34 (d,  $J = 9.8$  Hz, 1H).  $^{13}\text{C}$  NMR (125 MHz,  $\text{CDCl}_3$ ):  $\delta_{\text{C}}$  178.11, 144.89, 137.94, 133.14, 129.93, 128.09, 70.84, 70.70, 70.66, 69.98, 69.35, 68.80, 67.03, 47.94, 45.39, 42.83, 37.85, 21.76. MALDI-TOF: theoretical mass of  $\text{C}_{24}\text{H}_{31}\text{NO}_8\text{S}$ , 493.18; found: 494.30 for  $[\text{M}+\text{H}]^+$ , 516.30 for  $[\text{M}+\text{Na}]^+$ .

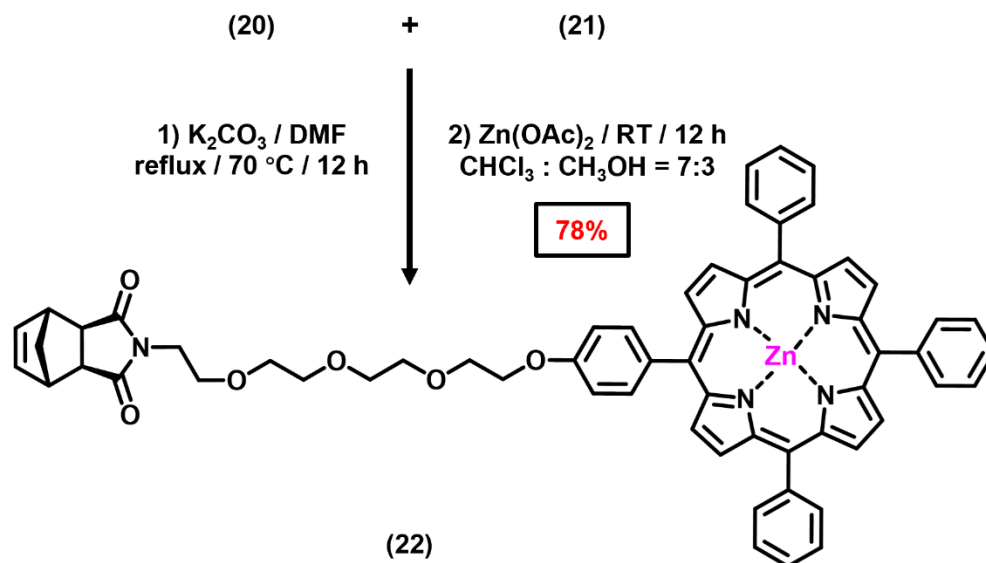
**Synthesis of TPP-OH (21)**



**Scheme 2.21.** Synthesis of **TPP-OH**.

Compound **21** was synthesized according to a previously reported literature procedure.<sup>35</sup> Benzaldehyde (8.60 g, 81 mmol, 3 equiv.) and 4-hydroxybenzaldehyde (3.30 g, 27 mmol, 1 equiv.) were dissolved in propionic acid (180 mL). This solution was heated to reflux at 140 °C for 30 min. Pyrrole (7.25 g, 108 mmol, 4 equiv.) was added dropwise to the solution under N<sub>2</sub>. The reaction mixture was refluxed for 4 h and then allowed to cool to room temperature. Then, about half the volume of the reaction mixture was removed under reduced pressure and MeOH (250 mL) was added into the concentrated solution. The dark blue solution was stored overnight at 4 °C. After filtration, the purple precipitate was collected and washed with cold MeOH. Crude product was dried under vacuum and subsequently purified by column chromatography using Hexanes: CH<sub>2</sub>Cl<sub>2</sub> (1:1 → 0:1) as the eluent to yield the desired product **21** as a purple solid (0.85 g, 5% yield). <sup>1</sup>H NMR (500 MHz, CD<sub>2</sub>Cl<sub>2</sub>): δ<sub>H</sub> 8.86 (m, 8H); 8.22 (m, 6H); 8.08 (m, 2H); 7.77 (m, 9H); 7.20 (m, 2H); -2.78 (s, 2H). <sup>13</sup>C NMR (125 MHz, CD<sub>2</sub>Cl<sub>2</sub>): δ<sub>C</sub> 155.54, 142.33, 142.31, 135.85, 134.87, 134.70, 127.84, 126.82, 120.23, 120.15, 113.82. MALDI-TOF: theoretical mass of C<sub>44</sub>H<sub>30</sub>N<sub>4</sub>O, 630.24; found: 631.53 for [M+H]<sup>+</sup>.

### Synthesis of Nb-TEG-ZnTPP (22)

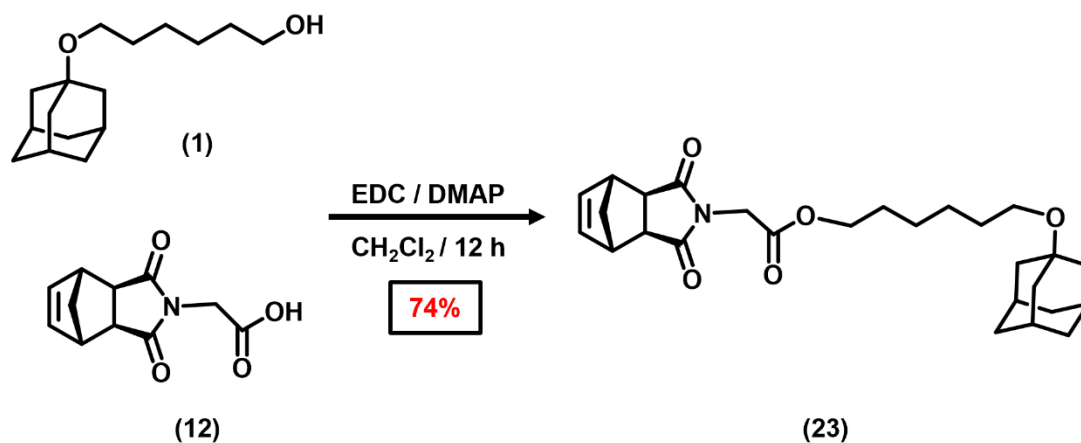


**Scheme 2.22.** Synthesis of **Nb-TEG-ZnTPP**.

Compound **21** (0.334 g, 0.53 mmol, 1 equiv.), **20** (0.392 g, 0.8 mmol, 1.5 equiv.), and  $\text{K}_2\text{CO}_3$  (0.732 g, 5.3 mmol, 10 equiv.) were dissolved in 15 mL dry DMF and refluxed at 70 °C under  $\text{N}_2$  for 12 h. The mixture was then filtered, and the solvent was removed by rotary evaporation to give a purple residue, which was dissolved in  $\text{CHCl}_3$  (50 mL) and washed with brine (3 × 50 mL) and then  $\text{H}_2\text{O}$  (2 × 50 mL). The combined organic phases were dried over anhydrous  $\text{Na}_2\text{SO}_4$ , filtered, concentrated by rotary evaporation, and purified by column chromatography using EtOAc as the eluent. The product collected from the previous column (0.2638 g, 0.28 mmol, 1 equiv.) and  $\text{Zn}(\text{OAc})_2$  (0.6146 g, 2.8 mmol, 10 equiv.) were dissolved in a (7:3)  $\text{CHCl}_3$  : MeOH mixture (15 mL) and stirred overnight in the dark. The reaction mixture was diluted with  $\text{CHCl}_3$  (50 mL) and washed with  $\text{H}_2\text{O}$  (3 × 50 mL). The combined organic phases were dried over anhydrous  $\text{Na}_2\text{SO}_4$ , concentrated by rotary evaporation to yield the desired product **22** as a purple solid (418 mg, 78% yield).  $^1\text{H}$  NMR (500 MHz,  $\text{CD}_2\text{Cl}_2$ ):  $\delta_{\text{H}}$  9.00 – 8.93 (m, 8H); 8.22 (m, 6H); 8.11 (m, 2H); 7.77 (m, 8H); 7.27 (m, 2H); 6.20 (m, 2H); 4.30 (m, 2H); 3.87 (m, 2H); 3.65 – 3.45 (m, 12H); 3.02 (s, 2H); 2.42 (s, 2H); 1.36 (d,  $J$  = 10 Hz, 2H); 1.18 (d,  $J$  = 10 Hz, 2H).  $^{13}\text{C}$  NMR (125 MHz,  $\text{CD}_2\text{Cl}_2$ ):  $\delta_{\text{C}}$  177.76, 158.64, 150.63, 150.27, 150.20, 142.91, 137.78, 135.51, 135.31, 134.52, 132.06, 131.93,

131.89, 127.53, 126.63, 121.11, 112.80, 70.78, 70.59, 70.45, 69.97, 69.86, 67.86, 66.78, 47.65, 45.24, 42.56, 37.71. MALDI-TOF: theoretical mass of  $C_{61}H_{51}N_5O_6Zn$ , 1013.31; found, 1013.19 for  $[M]^+$ .

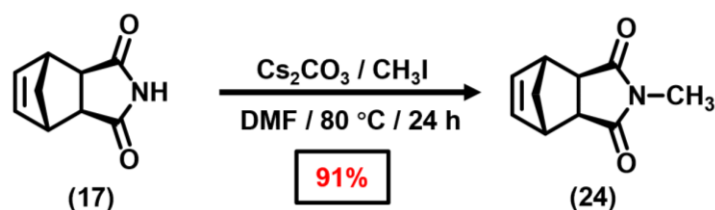
### Synthesis of Nb-Hexyl-Ad (23)



### Scheme 2.23. Synthesis of Nb-Hexyl-Ad.

Compound 1 (0.227 g, 0.9 mmol, 1 equiv.) and compound 12 (0.4 g, 1.8 mmol, 2 equiv.) were dissolved in dry  $CH_2Cl_2$  (10 mL) and cooled to 0 °C. Then, EDC·HCl (0.5176 g, 2.7 mmol, 3 equiv.) and DMAP (0.0033 g, 0.27 mmol, 0.2 equiv.) were added into the solution, which was stirred overnight at room temperature for 12 h. After completion, the reaction mixture was washed with  $H_2O$  and brine (10 mL each), and the organic layer was dried over  $Na_2SO_4$  and concentrated. The compound was further purified by flash column chromatography (silica gel, 100:1  $CH_2Cl_2$ : MeOH) to yield the desired compound 23 as a white solid (0.302 g, 74% yield).  $^1H$  NMR (500 MHz,  $CDCl_3$ ):  $\delta_H$  6.31 (s, 2H); 4.22 (s, 2H); 4.13 (t,  $J = 6.7$  Hz, 2H); 3.38 (t,  $J = 6.6$  Hz, 2H); 3.32 (s, 2H); 2.75 (s, 2H); 2.14 (s, 3H); 1.74 (d,  $J = 2.4$  Hz, 6H); 1.66 – 1.57 (m, 9H); 1.52 (dd,  $J = 10.2, 8.5$  Hz, 3H); 1.37 – 1.33 (m, 4H).  $^{13}C$  NMR (125 MHz,  $CDCl_3$ ):  $\delta_C$  177.28, 167.08, 138.13, 71.85, 66.17, 59.66, 48.16, 45.59, 43.01, 41.76, 39.59, 36.69, 30.70, 30.66, 28.58, 26.03, 25.79. MALDI-TOF: theoretical mass of  $C_{27}H_{37}NO_5$ , 455.27; found: 478.11 for  $[M+Na]^+$ .

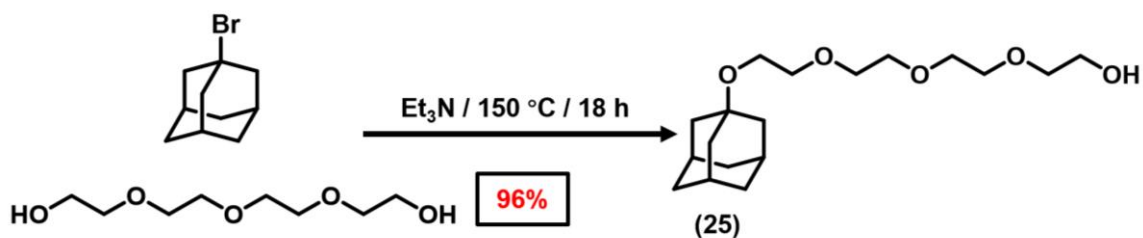
### Synthesis of Nb-Me (24)



### Scheme 2.24. Synthesis of Nb-Me.

The compound was synthesized using the procedure from literature.<sup>50</sup> Compound **17** (0.2 g, 1.23 mmol, 1 equiv.) and  $\text{Cs}_2\text{CO}_3$  (0.802 g, 2.46 mmol, 2 equiv.) were dissolved in DMF and stirred for 30 min. Iodomethane (0.524 g, 0.23 mL, 3.69 mmol, 3 equiv.) was added and the resulting mixture was heated to  $80\text{ }^\circ\text{C}$  for 24 h. After completion of the reaction, the resulting unwanted precipitate was filtered, and the organic solvent was removed. The residual organic material was re-dissolved in  $\text{CH}_2\text{Cl}_2$ , washed with  $\text{H}_2\text{O}$ , and dried over  $\text{Na}_2\text{SO}_4$  to yield the desired compound **24** as a white solid (198 mg, 91% yield).  $^1\text{H}$  NMR (500 MHz,  $\text{CDCl}_3$ ):  $\delta_{\text{H}}$  6.27 – 6.25 (m, 2H); 3.26 – 3.24 (m, 2H); 2.95 (s, 3H); 2.68 (s, 2H); 1.52 – 1.48 (m, 1H); 1.21 – 1.16 (m, 1H).  $^{13}\text{C}$  NMR (125 MHz,  $\text{CDCl}_3$ ):  $\delta_{\text{C}}$  178.26, 137.86, 48.07, 45.25, 43.03, 24.73. ESI-MS: theoretical mass of  $\text{C}_{10}\text{H}_{11}\text{NO}_2$ , 177.08; found: 178.09 for  $[\text{M}+\text{H}]^+$ .

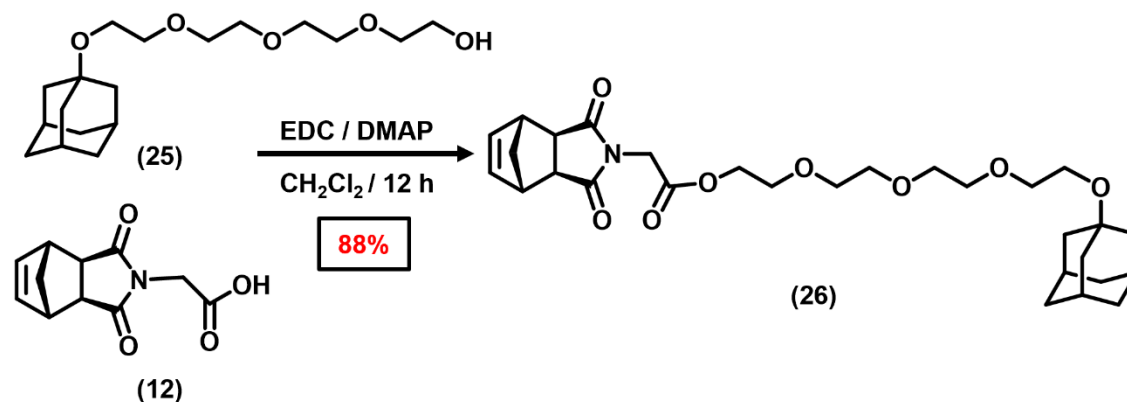
### Synthesis of Ad-TEG-OH (25)



**Scheme 2.25.** Synthesis of **Ad-TEG-OH**.

1-Bromoadamantane (2.00 g, 9.3 mmol, 1 equiv.), tetraethylene glycol (45 g, 40 mL, excess equiv.), and Et<sub>3</sub>N (2.18 g, 3.88 mL, 27.9 mmol, 3 equiv.) were added into a round bottom flask. The reaction mixture was heated to 150 °C and refluxed for 18 h. After completion of the reaction, the crude mixture was dissolved in CH<sub>2</sub>Cl<sub>2</sub> (100 mL), washed with 1 M HCl (30 mL) two times, and then washed with brine solution (30 mL). The organic layer was dried over Na<sub>2</sub>SO<sub>4</sub> and concentrated to yield the desired compound **25** as a dark brown oil (2.96 g, 96% yield). <sup>1</sup>H NMR (500 MHz, CDCl<sub>3</sub>): δ<sub>H</sub> 3.72 (s, 2H); 3.66 (m, 8H); 3.61 – 3.56 (m, 6H); 2.80 (s, 1H); 2.13 (s, 3H); 1.74 (s, 6H); 1.60 (q, *J* = 12.2, 6H). <sup>13</sup>C NMR (125 MHz, CDCl<sub>3</sub>): δ<sub>C</sub> 72.58, 72.31, 71.24, 70.59, 70.55, 70.52, 70.29, 61.68, 61.67, 59.22, 45.35, 41.40, 36.41, 36.06, 30.46. ESI-MS: theoretical mass of C<sub>18</sub>H<sub>32</sub>O<sub>5</sub>, 328.22; found: 329.0 for [M+H]<sup>+</sup>, 350.9 for [M+Na]<sup>+</sup>, 175.7 for [M+Na]<sup>2+</sup>.

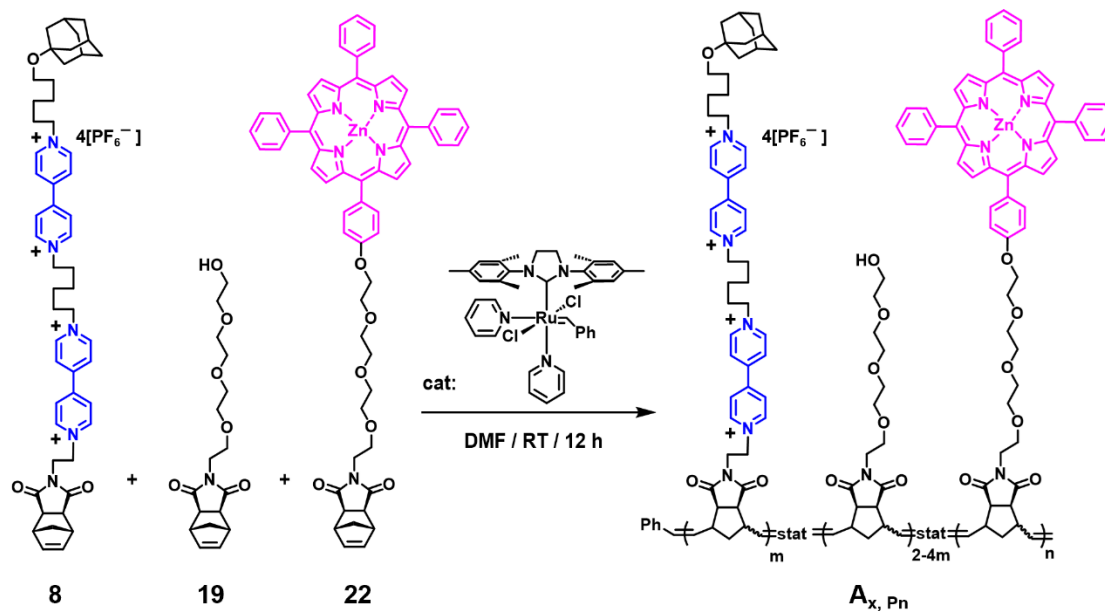
**Synthesis of Nb-TEG-Ad (26)**



**Scheme 2.26.** Synthesis of **Nb-TEG-Ad**.

Compound **25** (0.256 g, 0.78 mmol, 1 equiv.) and compound **12** (0.345 g, 1.56 mmol, 2 equiv.) were dissolved in dry  $\text{CH}_2\text{Cl}_2$  (10 mL) and cooled to 0 °C. Then, EDC·HCl (0.449 g, 2.34 mmol, 3 equiv.) and DMAP (0.0286 g, 0.234 mmol, 0.3 equiv.) were added into the solution, which was stirred overnight at room temperature for 12 h. After completion, the reaction mixture was concentrated by rotary evaporation, and then further purified by flash column chromatography (silica gel, 100:1  $\text{CH}_2\text{Cl}_2$ : MeOH) to yield the desired compound **26** as a pale-yellow oil (0.364 g, 88% yield).  $^1\text{H}$  NMR (500 MHz,  $\text{CDCl}_3$ ):  $\delta_{\text{H}}$  6.30 (t,  $J = 1.7$  Hz, 2H), 4.29 (dd,  $J = 5.5, 4.0$  Hz, 2H), 4.26 (s, 2H), 3.69 (dd,  $J = 5.5, 4.0$  Hz, 2H), 3.67 – 3.63 (m, 8H), 3.58 (dd,  $J = 6.2, 3.5$  Hz, 4H), 3.33 – 3.30 (m, 2H), 2.75 (d,  $J = 0.9$  Hz, 2H), 2.13 (s, 3H), 1.73 (d,  $J = 2.8$  Hz, 6H), 1.60 (q,  $J = 12.2$  Hz, 7H), 1.52 (dd,  $J = 8.7, 1.3$  Hz, 1H).  $^{13}\text{C}$  NMR (125 MHz,  $\text{CDCl}_3$ ):  $\delta_{\text{C}}$  177.08, 166.94, 137.97, 72.23, 71.26, 70.65, 70.63, 70.58, 70.55, 68.76, 64.90, 59.23, 48.00, 45.42, 42.85, 41.46, 39.40, 36.44, 30.48. ESI-MS: theoretical mass of  $\text{C}_{29}\text{H}_{41}\text{NO}_8$ , 531.28; found: 554.3 for  $[\text{M}+\text{Na}]^+$ .

**Synthesis of Statistical Copolymers  $\text{A}_{x, \text{Pn}}$ :  $\text{poly}(2\text{V}^{4+}\text{Ad}_m\text{-TEG}_{2-4m}\text{-ZnTPP}_n)_{\text{stat}}$**



**Scheme 2.27.** Synthesis of statistical copolymers  $A_{x, P_n}$ :  $\text{poly}(2V^{4+}Ad_m\text{-TEG}_{2-4m}\text{-ZnTPP}_n)_{\text{stat}}$ .

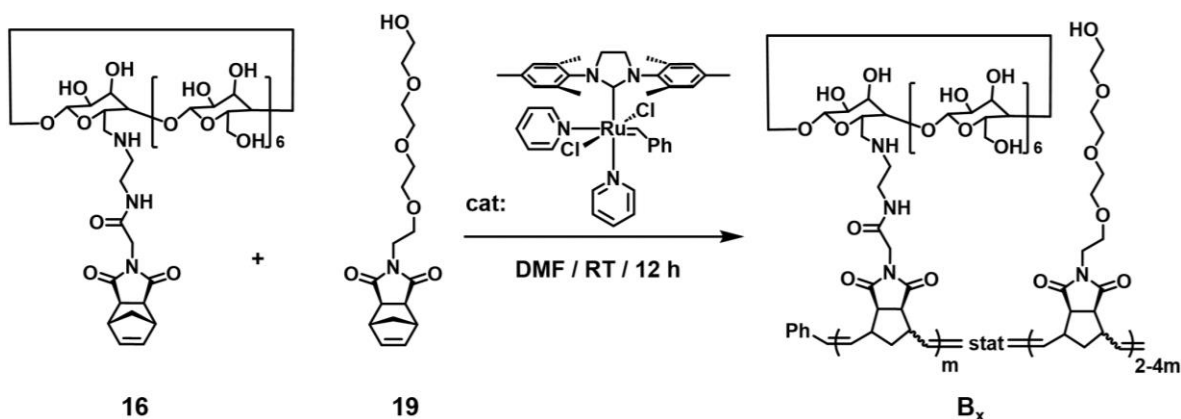
<i>Monomer</i>	<i>Monomer Units of Statistical Copolymers</i>							
	$A_{1, P1}$	$A_{2, P1}$	$A_{3, P0}$	$A_{3, P1}$	$A_{3, P2}$	$A_{3, P4}$	$A_{4, P1}$	$A_{5, P1}$
Nb-2V-Ad-4PF <sub>6</sub> ( <b>8</b> )	20	30	30	30	30	30	30	35
Nb-TEG ( <b>19</b> )	60	60	90	90	90	90	120	105
Nb-TEG-ZnTPP ( <b>22</b> )	1	1	0	1	2	4	1	1

**Table 2.4.** Summary of monomer ratios for different statistical copolymers  $A_{x, P_n}$ .

A series of statistical copolymers  $A_{x, P_n}$  were synthesized through a similar procedure. **Table 2.4** summarized the ratio of monomers incorporated into each specific copolymer. All copolymers  $A_{x, P_n}$  were synthesized on the same scale, dialyzed and dried using the same method. Detailed procedure was shown below using statistical copolymer  $\text{poly}(2V^{4+}Ad_{30}\text{-TEG}_{90}\text{-ZnTPP})$  ( $A_{3, P1}$ ) as an example: A solution of modified G3 was freshly prepared in DMF. G3 (0.0595 mL, 0.86 mg, 1.19  $\mu\text{mol}$ , 1 equiv.) was added to a solution of **8** (50.1 mg, 35.7  $\mu\text{mol}$ , 30 equiv.), **19** (36.4 mg, 107.2  $\mu\text{mol}$ , 90 equiv.), and **22** (1.21 mg, 1.19  $\mu\text{mol}$ , 1 equiv.) in 1.370 mL DMF to give G3:**8** ratio of 1:30 and a 0.025 M concentration of **8**. The resulting solution was stirred for 12 h at room

temperature. After the polymerization went to completion, the reaction was quenched by addition of EVE. Then, the reaction mixture was transferred to dialysis tubing (RC dialysis tubing, 1 kDa molecular weight cut-off, 38 mm flat-width) and was placed in a beaker with 500 mL H<sub>2</sub>O to remove the excess EVE and DMF. The dialysis continued for 12 h with H<sub>2</sub>O and was then switched to 500 mL saturated NaCl solution to do counter anion exchange from PF<sub>6</sub><sup>-</sup> to Cl<sup>-</sup> for 6 h. After that, the solution in the beaker was switched back to 500 mL H<sub>2</sub>O, followed by changing the H<sub>2</sub>O every 12 h for a total of two more times. After dialysis, copolymer **A**<sub>3, P1</sub> was lyophilized for 24 h to yield a purple solid (62.7 mg, 87% yield).

### Synthesis of Statistical Copolymers **B**<sub>x</sub>: poly(CD<sub>m</sub>-TEG<sub>2-4m</sub>)<sub>stat</sub>



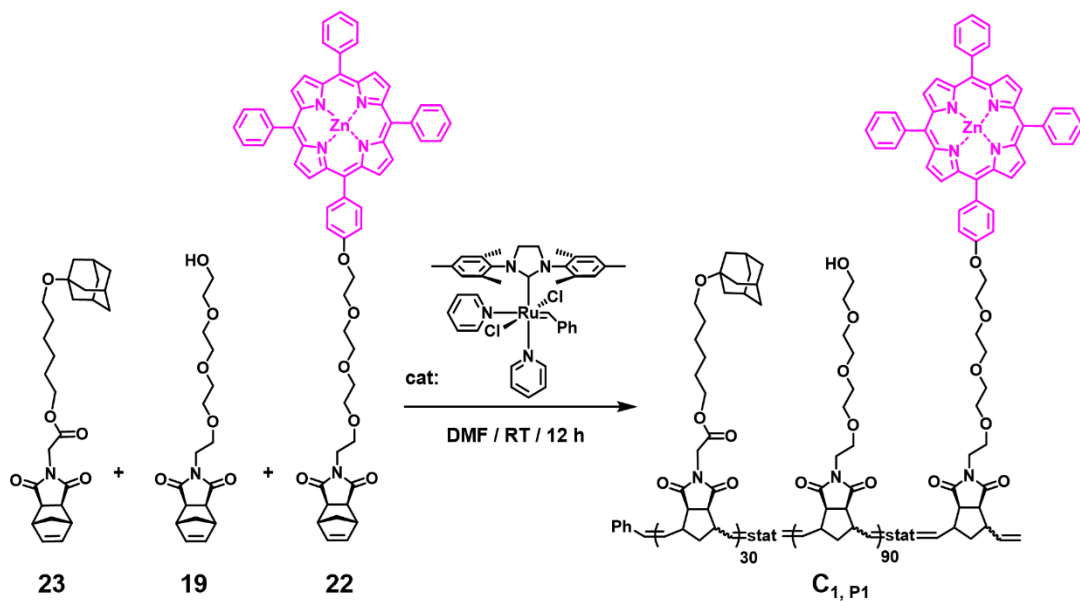
**Scheme 2.28.** Synthesis of statistical copolymers **B**<sub>x</sub>: poly(CD<sub>m</sub>-TEG<sub>2-4m</sub>)<sub>stat</sub>.

Monomer	Monomer Units of Statistical Copolymers							
	<b>B</b> <sub>1</sub>	<b>B</b> <sub>2</sub>	<b>B</b> <sub>3</sub>	<b>B</b> <sub>4</sub>	<b>B</b> <sub>5</sub>	<b>B</b> <sub>6</sub>	<b>B</b> <sub>7</sub>	<b>B</b> <sub>8</sub>
Nb-CD ( <b>16</b> )	20	30	30	30	35	40	40	40
Nb-TEG ( <b>19</b> )	60	60	90	120	105	80	120	160

**Table 2.5.** Summary of monomer ratios for different statistical copolymers **B**<sub>x</sub>.

A series of statistical copolymers **B<sub>x</sub>** were synthesized through a similar procedure. **Table 2.5** summarized the ratio of monomers incorporated into each specific copolymer. All copolymers **B<sub>x</sub>** were synthesized on the same scale, dialyzed and dried using the same method. Detailed procedure was shown below using statistical copolymer poly(CD<sub>30</sub>-TEG<sub>90</sub>) (**B<sub>3</sub>**) as an example: A solution of modified Grubbs 3rd generation catalyst (G3) was freshly prepared in DMF. G3 (0.0479 mL, 0.69 mg, 0.96 μmol, 1 equiv.) was added to a solution of **16** (39.7 mg, 28.8 μmol, 30 equiv.) and **19** (29.3 mg, 86.3 μmol, 90 equiv.) in 1.103 mL DMF to give G3:**16** ratio of 1:30 (the concentration of **16** in solution was 0.025 M). The resulting solution was stirred for 12 h at room temperature. After the polymerization went to completion, the reaction was quenched by addition of ethyl vinyl ether (EVE). Then, the reaction mixture was transferred to dialysis tubing (RC dialysis tubing, 1 kDa molecular weight cut-off, 38 mm flat-width), and was placed in a beaker with 500 mL H<sub>2</sub>O to remove the excess EVE and DMF. The dialysis continued for 24 h and the H<sub>2</sub>O was changed every 12 h. After dialysis, copolymer **B<sub>3</sub>** was lyophilized for 24 h to yield a pale-yellow solid (51.5 mg, 75% yield). *Note:* For copolymers **B<sub>6</sub>**, **B<sub>7</sub>** and **B<sub>8</sub>**, there were obvious signals showing reaction couldn't go to completion from NMR (**Figure 2.6**), so no dialysis and further characterizations performed.

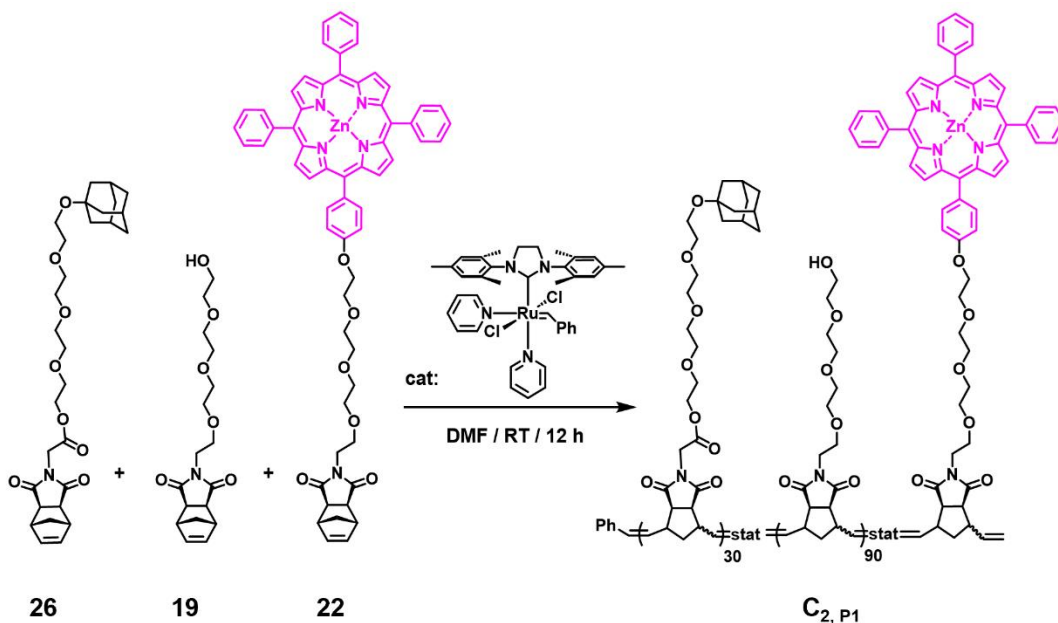
#### **Synthesis of Statistical Copolymer C<sub>1, P1</sub>: poly(HexylAd<sub>30</sub>-TEG<sub>90</sub>-ZnTPP)<sub>stat</sub>**



**Scheme 2.29.** Synthesis of statistical copolymer  $\text{C}_{1, P1}$ : **poly(HexylAd<sub>30</sub>-TEG<sub>90</sub>-ZnTPP)<sub>stat</sub>**.

A solution of modified G3 was freshly prepared in DMF. G3 (0.0956 mL, 1.39 mg, 1.91  $\mu\text{mol}$ , 1 equiv.) was added to a solution of **23** (26.1 mg, 57.3  $\mu\text{mol}$ , 30 equiv.), **19** (58.4 mg, 172  $\mu\text{mol}$ , 90 equiv.), and **22** (1.94 mg, 1.91  $\mu\text{mol}$ , 1 equiv.) in 2.199 mL DMF to give G3:**23** ratio of 1:30 and a 0.025 M concentration of **23**. The resulting solution was stirred for 12 h at room temperature. After the polymerization went to completion, the reaction was quenched by addition of EVE. Then, the reaction mixture was transferred to dialysis tubing (RC dialysis tubing, 1 kDa molecular weight cut-off, 38 mm flat-width) and was placed in a beaker with 500 mL H<sub>2</sub>O to remove the excess EVE and DMF. The dialysis continued for 24 h and the H<sub>2</sub>O was changed every 12 h. After dialysis, copolymer  $\text{C}_{1, P1}$  was lyophilized for 24 h to yield a pale-purple solid (79.5 mg, 90% yield).

### Synthesis of Statistical Copolymer $\text{C}_{2, P1}$ : **poly(TEGAd<sub>30</sub>-TEG<sub>90</sub>-ZnTPP)<sub>stat</sub>**

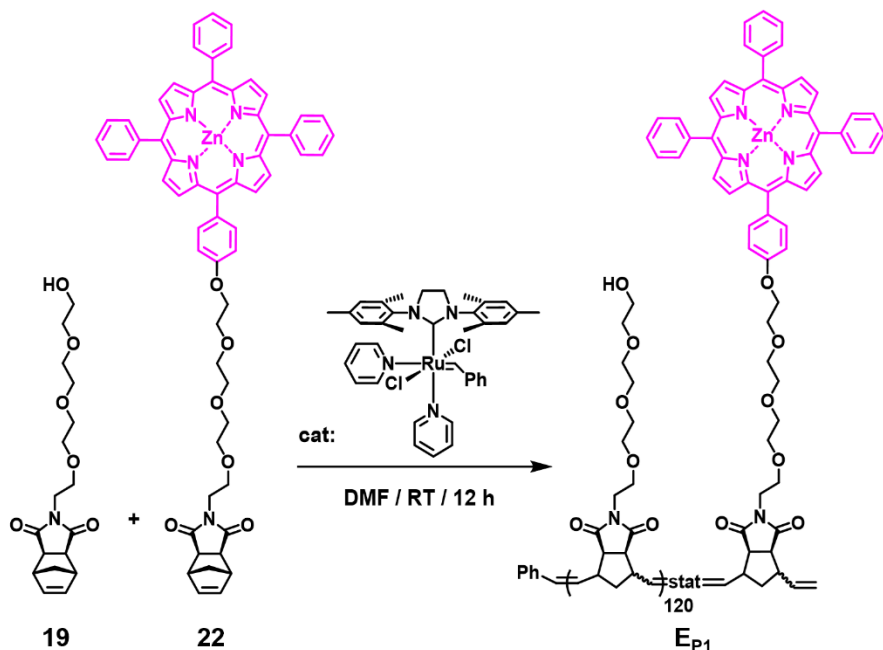


**Scheme 2.30.** Synthesis of statistical copolymer  $\text{C}_{2, P1}$ : **poly(TEGAd<sub>30</sub>-TEG<sub>90</sub>-ZnTPP)<sub>stat</sub>**.

A solution of modified G3 was freshly prepared in DMF. G3 (0.0797 mL, 1.15 mg, 1.59  $\mu\text{mol}$ , 1 equiv.) was added to a solution of **26** (25.4 mg, 47.8  $\mu\text{mol}$ , 30 equiv.), **19** (48.7 mg, 143  $\mu\text{mol}$ , 90 equiv.), and **22** (1.62 mg, 1.59  $\mu\text{mol}$ , 1 equiv.) in 1.833 mL DMF to give G3:**26** ratio of 1:30 and a 0.025 M concentration of **26**. The resulting solution was stirred for 12 h at room temperature. After the polymerization went to completion, the reaction was quenched by addition of EVE. Then, the reaction mixture was transferred to dialysis tubing (RC dialysis tubing, 1 kDa molecular weight cut-off, 38 mm flat-width) and was placed in a beaker with 500 mL H<sub>2</sub>O to remove the excess EVE and DMF. The dialysis continued for 24 h at 4 °C and the H<sub>2</sub>O was changed every 12 h. After dialysis, copolymer  $\text{C}_{2, P1}$  was lyophilized for 24 h to yield a pale-purple solid (58.8 mg, 80% yield).

**Synthesis of Statistical Copolymer  $\text{D}_{P1}$ : poly(2V<sup>4+</sup>Me<sub>30</sub>-TEG<sub>90</sub>-ZnTPP)<sub>stat</sub>**

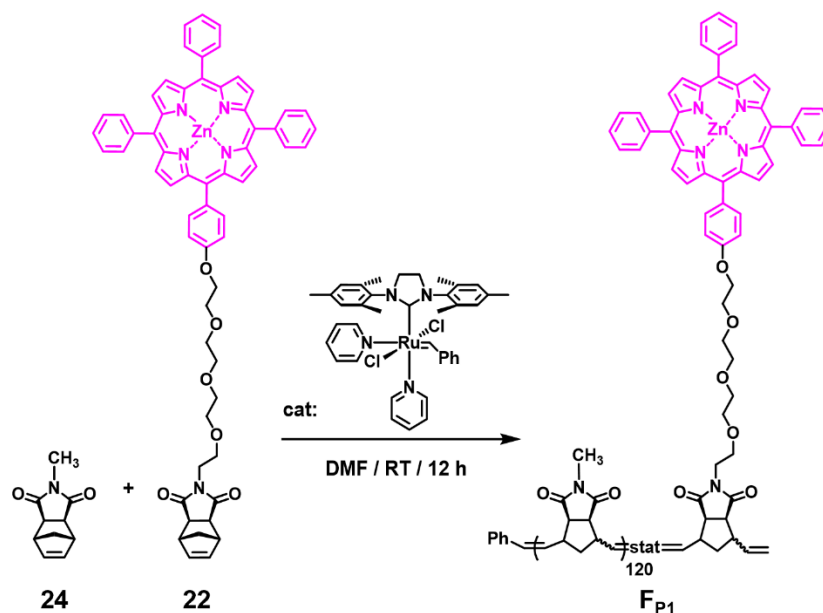




**Scheme 2.32.** Synthesis of statistical copolymer  $E_{P1}$ :  $\text{poly}(\text{TEG}_{120}\text{-ZnTPP})_{\text{stat}}$ .

A solution of modified G3 was freshly prepared in DMF. G3 (0.0669 mL, 0.97 mg, 1.34  $\mu\text{mol}$ , 1 equiv.) was added to a solution of **19** (54.5 mg, 160.6  $\mu\text{mol}$ , 120 equiv.) and **22** (1.36 mg, 1.34  $\mu\text{mol}$ , 1 equiv.) in 3.15 mL DMF to give G3:**19** ratio of 1:120 and a 0.05 M concentration of **22**. The resulting solution was stirred for 12 h at room temperature. After the polymerization went to completion, the reaction was quenched by addition of EVE. Then, the reaction mixture was transferred to dialysis tubing (RC dialysis tubing, 1 kDa molecular weight cut-off, 38 mm flat-width) and was placed in a beaker with 500 mL  $\text{H}_2\text{O}$  to remove the excess EVE and DMF. The dialysis was continued for 24 h and the  $\text{H}_2\text{O}$  was changed every 12 h. After dialysis, copolymer  $E_{P1}$  was dried under vacuum to yield as a purple solid (43.3 mg, 76% yield).

### Synthesis of Statistical Copolymer $F_{P1}$ : $\text{poly}(\text{Me}_{120}\text{-ZnTPP})_{\text{stat}}$



**Scheme 2.33.** Synthesis of statistical copolymer **F<sub>P1</sub>**: **poly(Me<sub>120</sub>-ZnTPP)<sub>stat.</sub>**

A solution of modified G3 was freshly prepared in DMF. G3 (0.119 mL, 1.72 mg, 2.37  $\mu\text{mol}$ , 1 equiv.) was added to a solution of **24** (50.5 mg, 285.0  $\mu\text{mol}$ , 120 equiv.) and **22** (2.41 mg, 2.37  $\mu\text{mol}$ , 1 equiv.) in 5.58 mL DMF to give G3:**24** ratio of 1:120 and a 0.05 M concentration of **24**. The resulting solution was stirred for 12 h at room temperature. After the polymerization went to completion, the reaction was quenched by addition of EVE. Then, the reaction mixture was transferred to dialysis tubing (RC dialysis tubing, 1 kDa molecular weight cut-off, 38 mm flat-width) and was placed in a beaker with 500 mL  $\text{CH}_2\text{Cl}_2$  to remove the excess EVE and DMF. The dialysis continued for 24 h and the  $\text{CH}_2\text{Cl}_2$  was changed every 12 h. After dialysis, copolymer **F<sub>P1</sub>** was dried under vacuum to yield as a dark brown solid (45.6 mg, 83% yield).

### 2.4.3 Spectroscopic Characterization of Novel Compounds

#### Nuclear Magnetic Resonance (<sup>1</sup>H NMR) Characterization

The completion of polymerization for each statistical copolymer was characterized by  $^1\text{H}$  NMR spectroscopy. Specifically, the peak close to 6.3 ppm from Nb-based monomers disappeared over the course of the polymerization. As mentioned in Section 2.3.1, all polymerizations were completed successfully, except for copolymers **B**<sub>6</sub>-**B**<sub>8</sub> as illustrated in **Figure 2.6**.

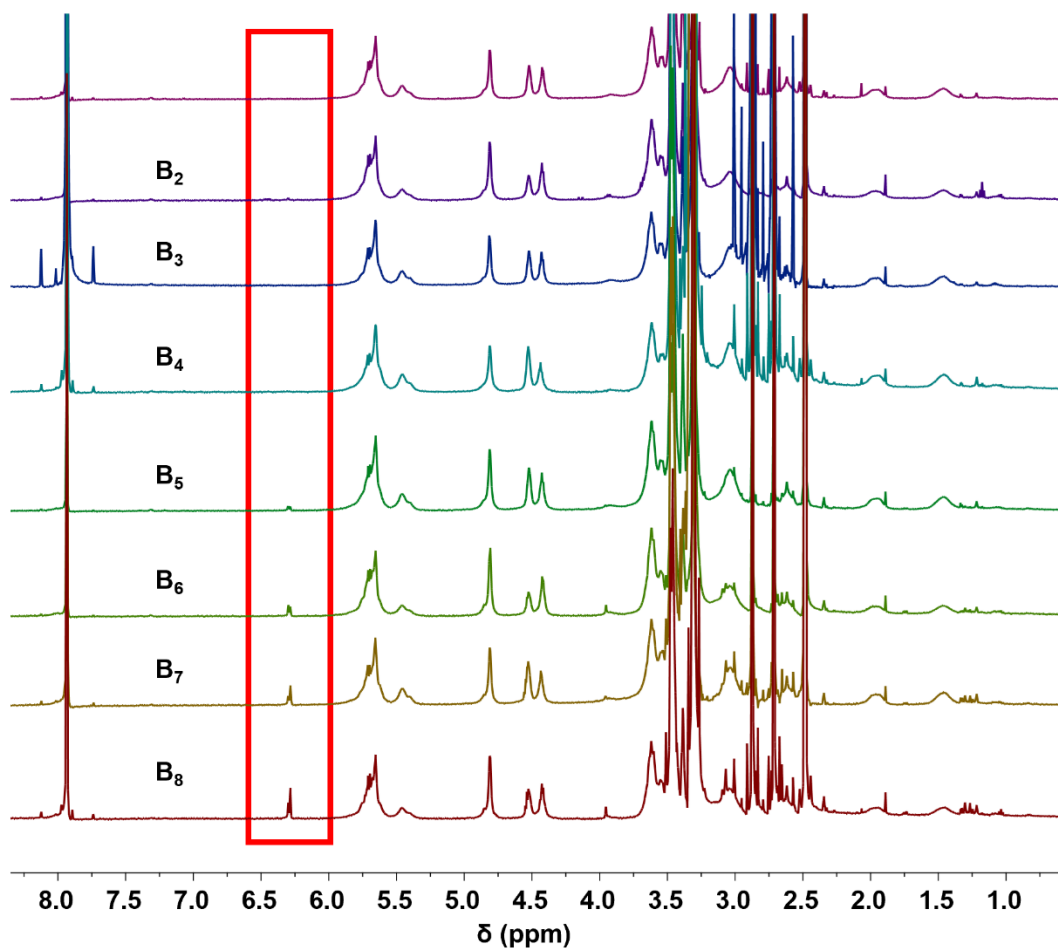


**Figure 2.6.**  $^1\text{H}$  NMR (500 MHz, 25 °C,  $(\text{CD}_3)_2\text{SO}$ ) spectra of statistical copolymers **B**<sub>x</sub>. The red box highlights the comparison of conversion to polymer between different statistical copolymers **B**<sub>x</sub>.

### DOSY NMR Characterization

DOSY NMR characterization was carried out for copolymers **A**<sub>3, P1</sub>, **B**<sub>3</sub>, and copolymer mixture **A**<sub>3, P1</sub>+**B**<sub>3</sub> to confirm the cross-linking of Ad and  $\beta$ -CD in deionized H<sub>2</sub>O (**Figure 2.7-2.9**).



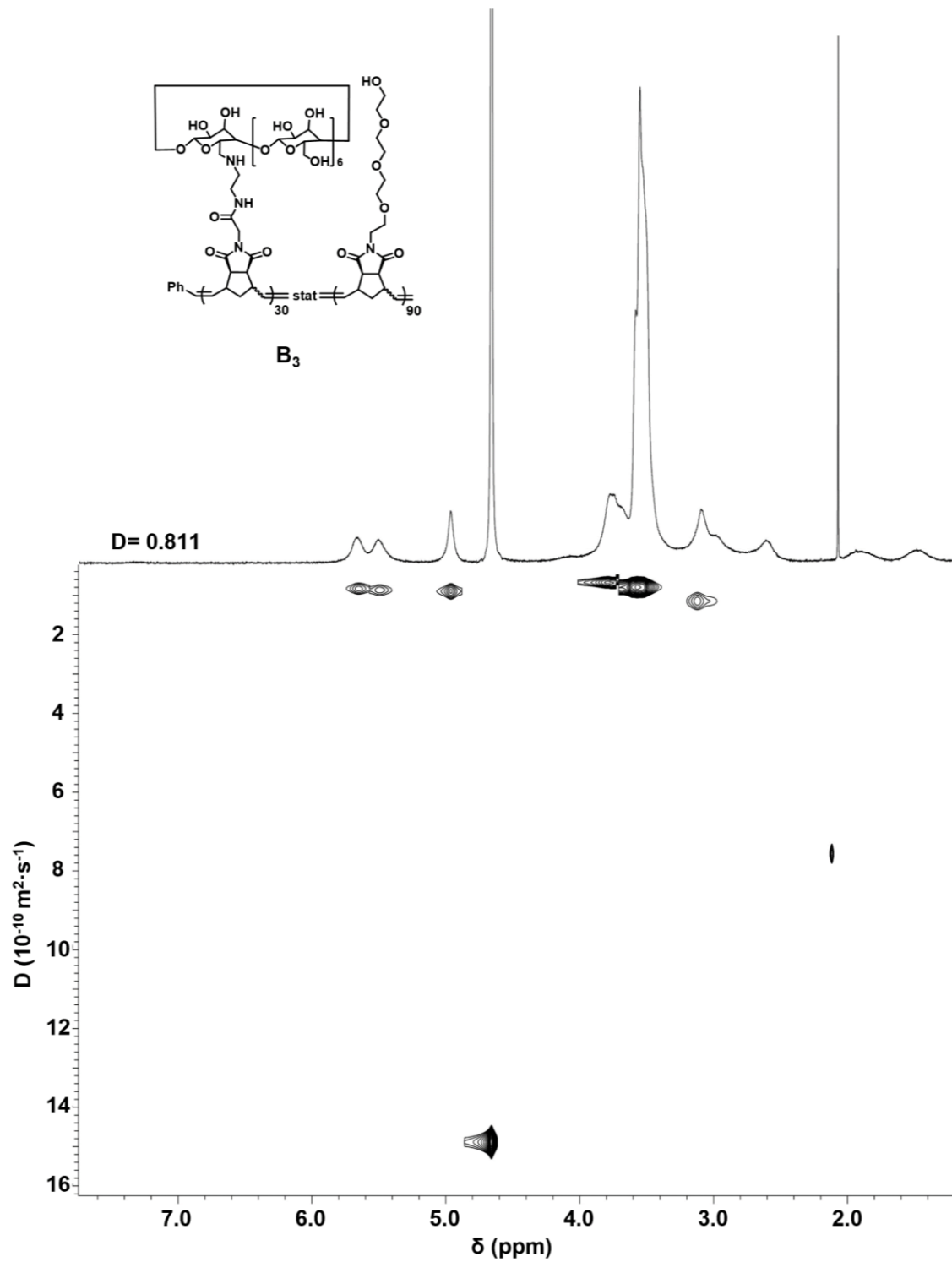


**Figure 2.8.** DOSY NMR ( $\text{D}_2\text{O}$ ,  $25^\circ\text{C}$ ) of statistical copolymer **B<sub>3</sub>**.

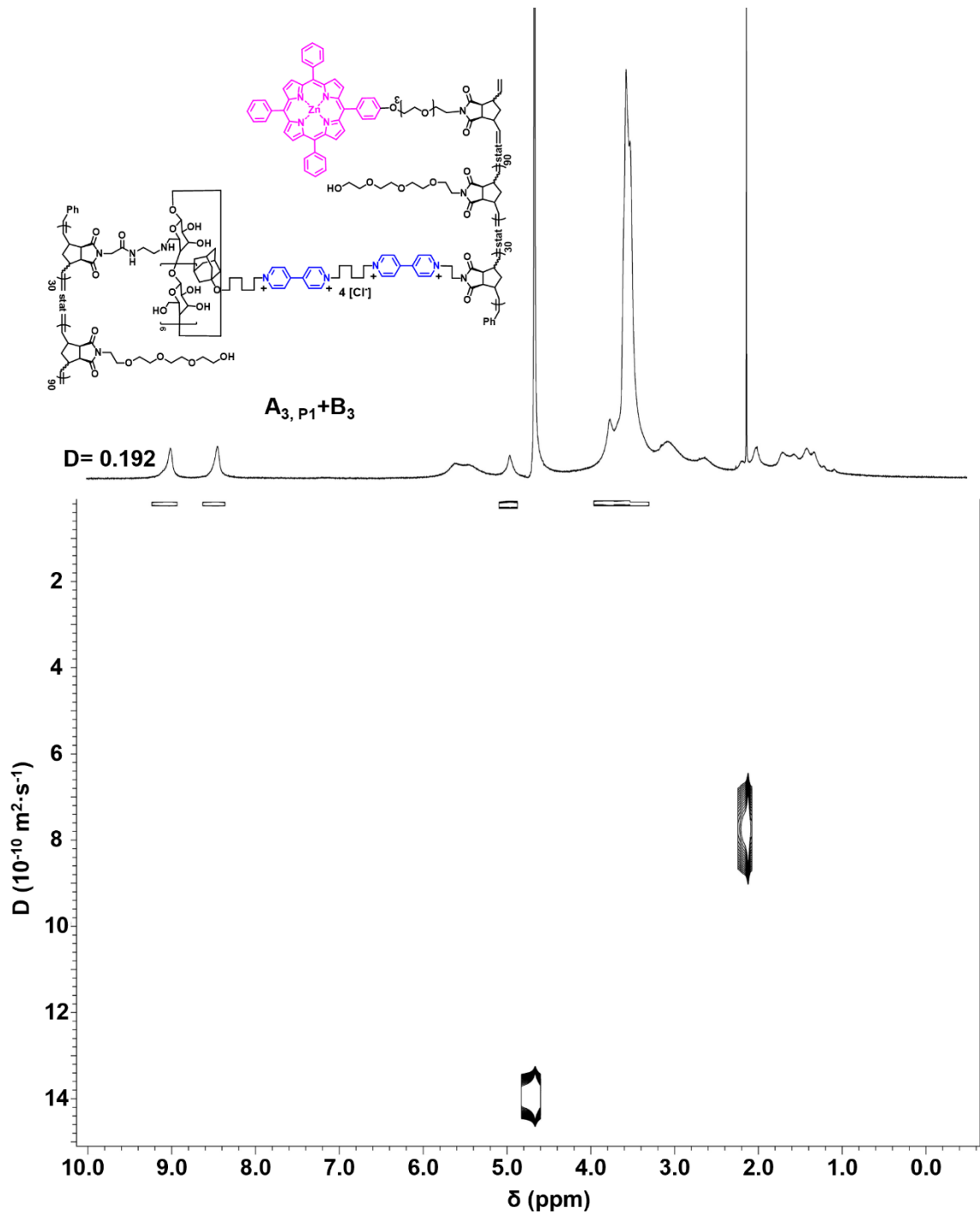
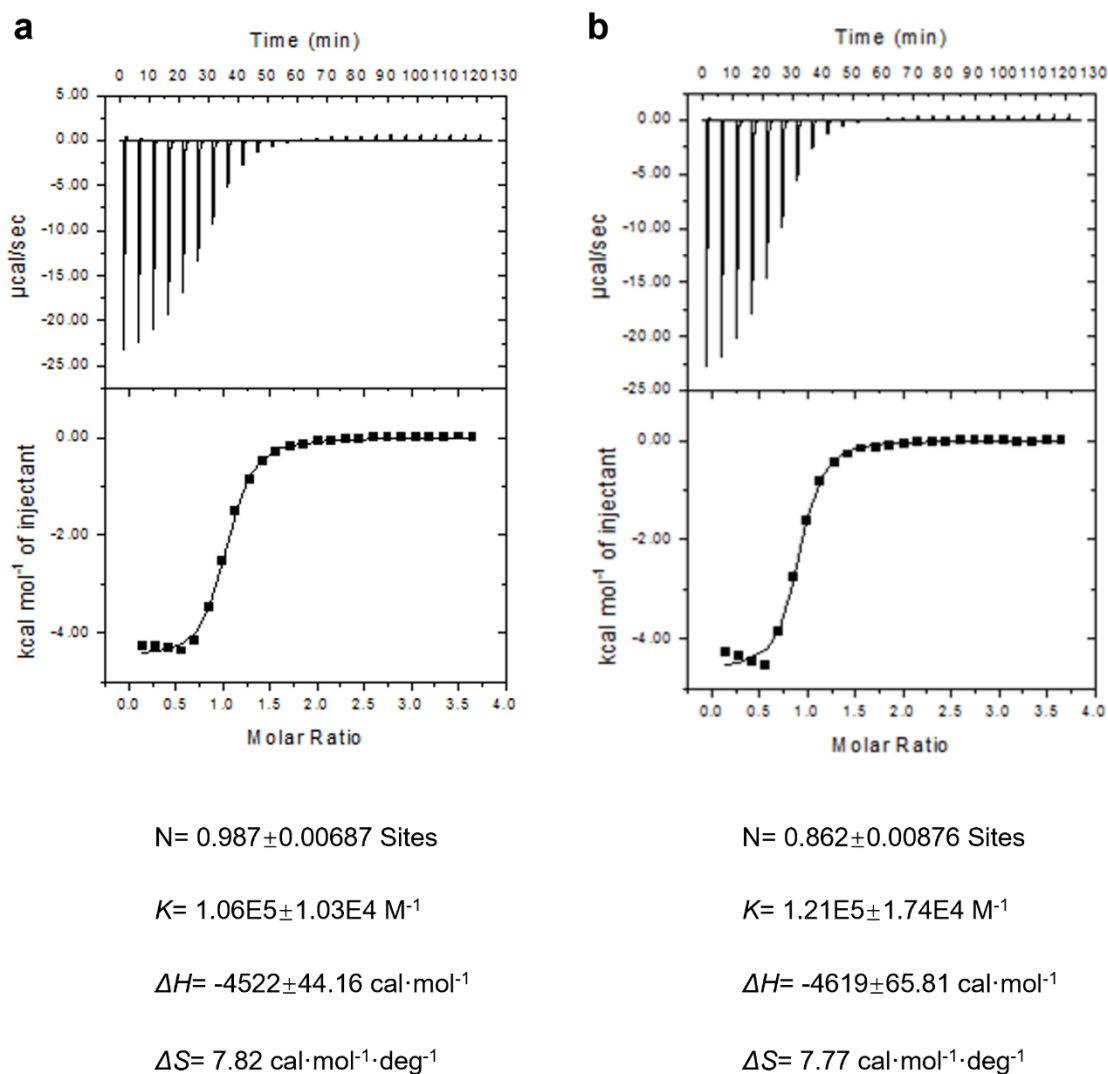


Figure 2.9. DOSY NMR (D<sub>2</sub>O, 25°C) of copolymer complex **A<sub>3</sub>, P<sub>1</sub>+B<sub>3</sub>**.

### Isothermal Titration Calorimetry (ITC) Characterization

Solutions of **9** in a 250  $\mu\text{L}$  syringe were titrated into the sample cell, containing a 1.4 mL  $\beta\text{-CD}$  solution. Titrations were made in 5  $\mu\text{L}$  aliquots with 25 total injections and at a stirring speed of 480 rpm. The concentration of the  $\beta\text{-CD}$  and **9** solutions were 0.5 and 20 mM, respectively. The solutions were prepared in either pure  $\text{H}_2\text{O}$  or 100 mM NaCl solution. All titrations were carried out at 25  $^\circ\text{C}$ .



**Figure 2.10.** ITC of  $\beta\text{-CD}$  and **9** in (a)  $\text{H}_2\text{O}$ , (b) 100 mM NaCl solution.

### Gel Permeation Chromatography (GPC) Characterization

All the data (**Figure 2.11-2.13**) was collected using three PSS NOVEMA MAX Lux analytical 100 Å columns in tandem and H<sub>2</sub>O mobile phase (0.025 M Na<sub>2</sub>SO<sub>4</sub>) running at 23 °C with 1.0 mL·min<sup>-1</sup> flow rate. (Note: No GPC trace of monomer **22** (Nb-TEG-ZnTPP) was overlaid on the graphs below as it is not soluble in H<sub>2</sub>O)

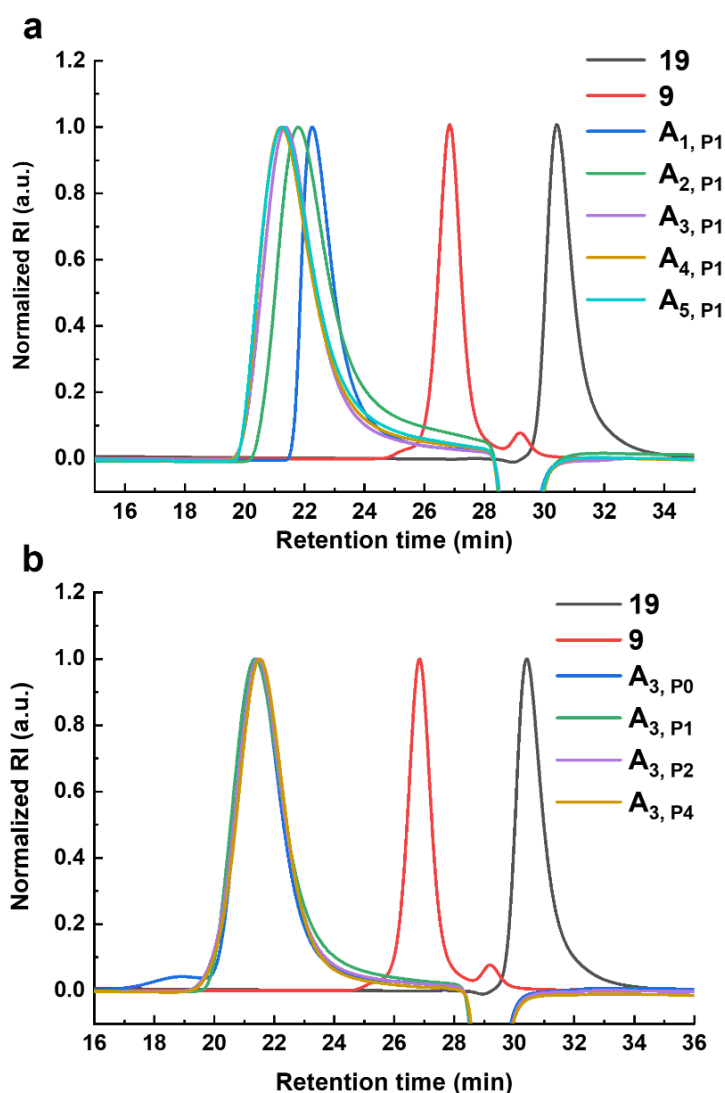


**Figure 2.11.** GPC traces of (a) **19**, **9** and statistical copolymers **A<sub>1</sub>, P<sub>1</sub>**, **A<sub>2</sub>, P<sub>1</sub>**, **A<sub>3</sub>, P<sub>1</sub>**, **A<sub>4</sub>, P<sub>1</sub>**, and **A<sub>5</sub>, P<sub>1</sub>** (similar components with different units of monomers incorporated and increasing molecular weight theoretically). (b) **19**, **9** and statistical copolymer **A<sub>3</sub>, P<sub>0</sub>**, **A<sub>3</sub>, P<sub>1</sub>**, **A<sub>3</sub>, P<sub>2</sub>**, and **A<sub>3</sub>, P<sub>4</sub>** (copolymers with similar molecular weight theoretically but with different amounts of porphyrin incorporated per chain).

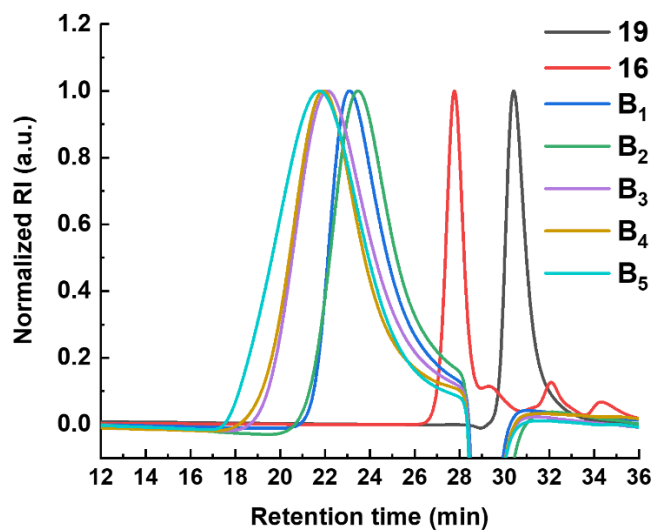


**Figure 2.12.** GPC traces of **19**, **16** and statistical copolymers **B<sub>1</sub>**, **B<sub>2</sub>**, **B<sub>3</sub>**, **B<sub>4</sub>**, and **B<sub>5</sub>** (similar components with different units of monomers incorporated and increasing molecular weight theoretically).

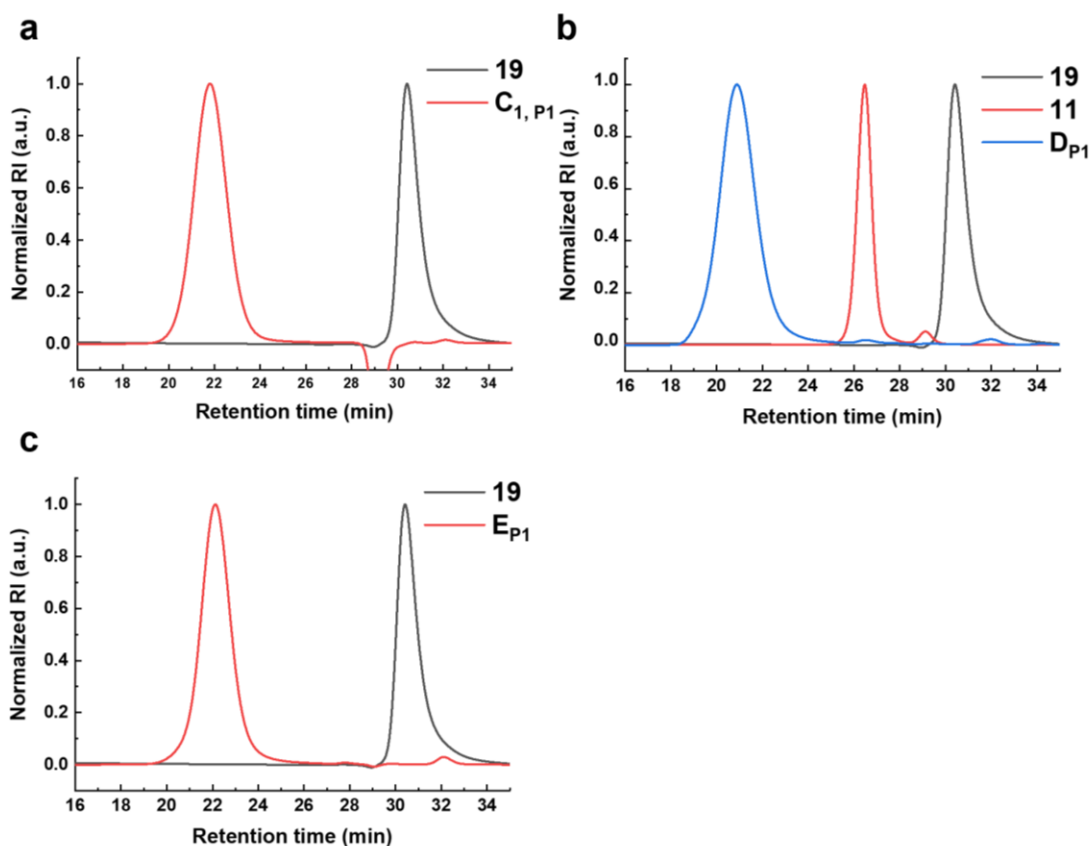


**Figure 2.13.** GPC traces of (a) **19** and statistical copolymer **C<sub>1,P1</sub>**. (b) **19**, **11** and statistical copolymer **D<sub>P1</sub>**. (c) **19** and statistical copolymer **E<sub>P1</sub>**.

Statistical copolymer  $C_{2,P1}$  is not very soluble in  $H_2O$  at room temperature (**Figure 2.14**), so we were not able to collect data for it on the PSS NOVEMA MAX Lux analytical 100 Å columns in tandem using  $H_2O$  mobile phase (0.025 M  $Na_2SO_4$ ). Thus, we have collected data for  $C_{2,P1}$  by using two Shodex GPC KD-806M columns in sequence in DMF mobile phase (0.025 M LiBr) running at 60 °C at 1.0 mL·min<sup>-1</sup>. Data was collected again for statistical copolymer  $C_{1,P1}$  on this column (DMF mobile phase) as a reference since  $C_{1,P1}$  and  $C_{2,P1}$  have similar molecular weight theoretically (**Figure 2.15**).

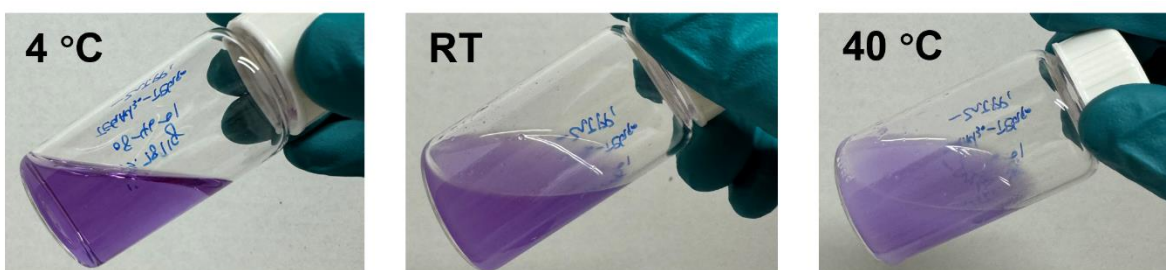


**Figure 2.14.** Solubility illustration for statistical copolymer  $C_{2,P1}$ .

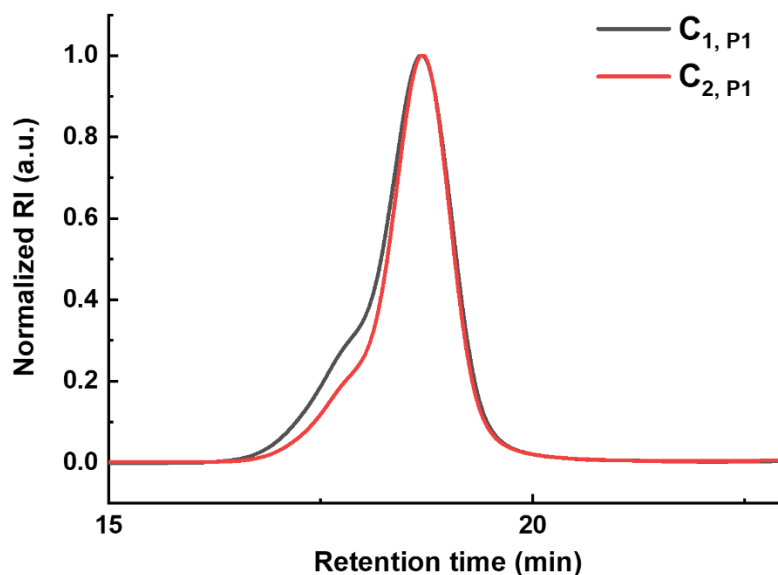


**Figure 2.15.** GPC traces of statistical copolymers  $C_{1,P1}$  and  $C_{2,P1}$ .

To calculate the  $dn/dc$  values of the different copolymers, known concentrations (0.1, 0.3, 0.5, 0.7, 0.9 mg·mL<sup>-1</sup>) of statistical copolymers  $A_{3,P1}$ ,  $B_3$ ,  $C_{1,P1}$  and  $D_{P1}$  in the same buffer (0.025 M

Na<sub>2</sub>SO<sub>4</sub> in H<sub>2</sub>O) were prepared. The samples were directly injected into the Optilab (U)T-rEX detector using a syringe pump (flow rate 0.33 mL·min<sup>-1</sup>). The dRI signal was measured for each injection, and the slope of the dRI-concentration describes the dn/dc value of the polymer.

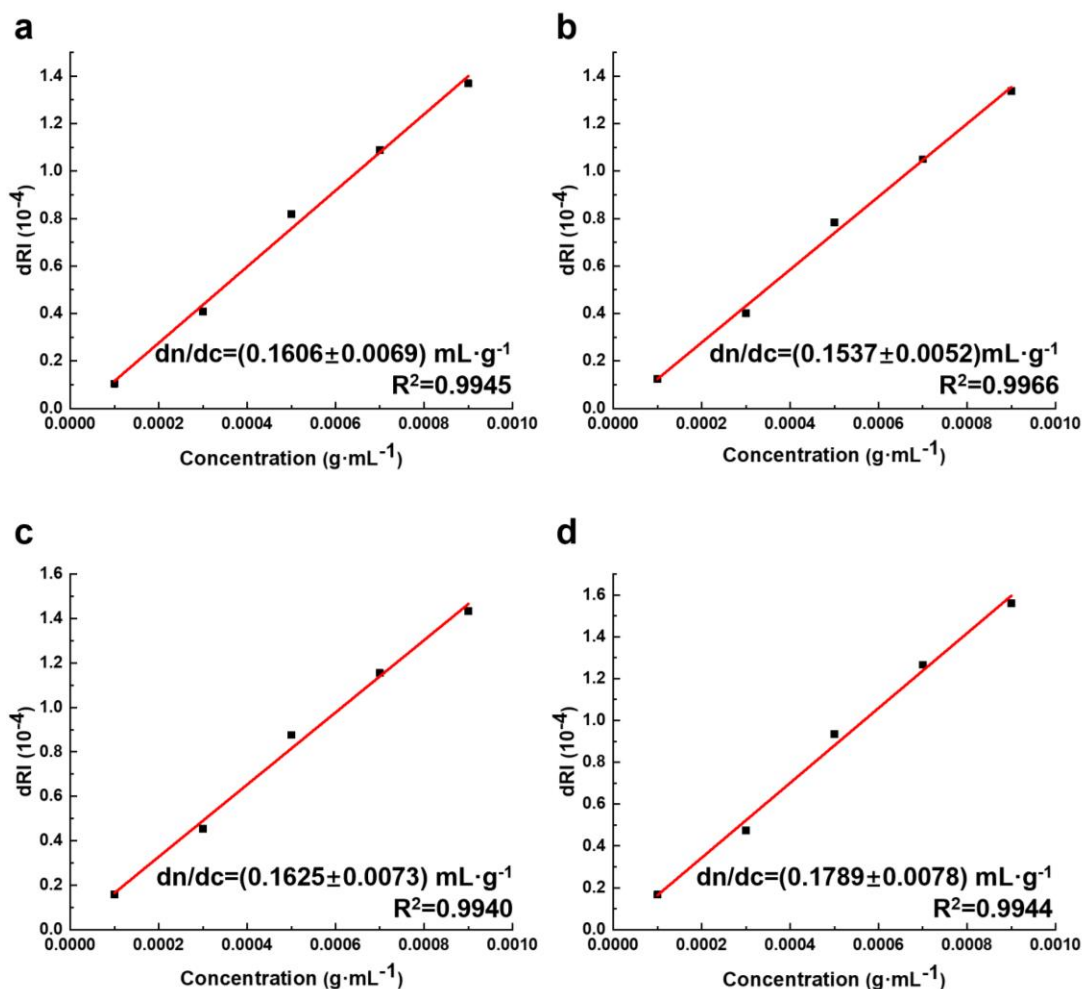


**Figure 2.16.** Plots of dRI vs. Concentration to determine dn/dc of statistical copolymers (a) A<sub>3</sub>, P<sub>1</sub>, (b) B<sub>3</sub>, (c) C<sub>1</sub>, P<sub>1</sub>, and (d) D<sub>P1</sub>.

The dn/dc value of copolymer C<sub>2</sub>, P<sub>1</sub> is calculated using the same method described above by preparing known concentrations (0.1, 0.3, 0.5, 0.7, 0.9 mg·mL<sup>-1</sup>) in 0.025 M LiBr in DMF.

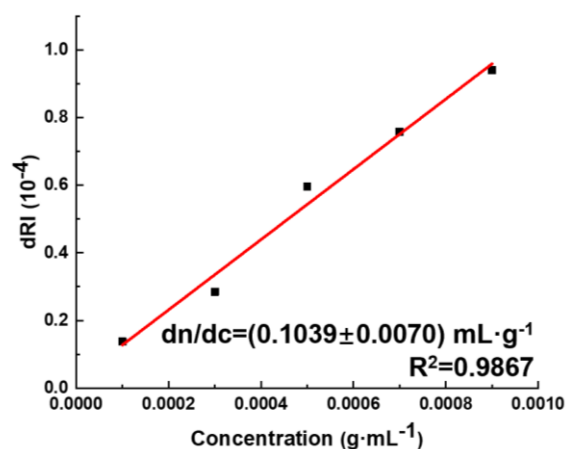


**Figure 2.17.** Plot of dRI vs. Concentration to determine  $dn/dc$  of statistical copolymer  $C_{2,P1}$ .

The molecular weight and dispersity of different statistical copolymers  $A_{3,P1}$ ,  $B_3$ ,  $C_{1,P1}$  and  $D_{P1}$  are summarized in **Table 2.6** and were determined using the GPC traces and  $dn/dc$  values. (Note: Light scattering data showed that  $M_w$  and  $M_n$  were an order of magnitude higher for  $C_{2,P1}$ , it was probably due to porphyrin fluorescence that gave false signals. However, we had MW for  $C_{1,P1}$  in  $H_2O$ , and it matched the peak of  $C_{2,P1}$  in DMF.)

Polymer	Molecular Weight (kDa)			$D_{GPC}$
	$M_{n,theo}$	$M_{n,GPC}$	$M_{w,GPC}$	
$A_{3,P1}$	60.48	44.87	58.07	1.294
$B_3$	71.95	36.57	38.47	1.052
$C_{1,P1}$	45.21	89.80	93.49	1.041
$D_{P1}$	53.87	41.88	43.19	1.031

**Table 2.6.** Molecular weight and dispersity data for the different statistical copolymers described in this report.

### UV-vis of Degradation Experiment

A pre-mixed solution of 15 mg  $A_{3, P1+B3}$  in 0.5 mL  $H_2O$  and a pre-mixed solution of 15 mg  $C_{1, P1+B3}$  in 0.5 mL  $H_2O$  were added to 100 mM NaCl solution (100 mL) separately. After the full injection of copolymer mixture into the bottle, 1 mL aliquots of the supernatant were taken to test the UV-vis absorbance at different time points. The detection by UV-vis spectroscopy is based on the absorbance of the porphyrin molecule (430 nm) integrated in the copolymer complex.

The purpose of this experiment is to show the stability of copolymer complex  $A_{3, P1+B3}$  compared to  $C_{1, P1+B3}$  under dilute conditions. As the process of forming the  $A_{3, P1+B3}$  hydrogel is concentration independent, there should be hardly any absorbance of porphyrin at 430 nm detected (**Figure S45**). Copolymer complex  $C_{1, P1+B3}$  will be partially dissolved in solution (with the peak showing up at 430 nm), followed by gradual precipitation (with the peak disappearing at 430 nm) but has some degradation, as evidenced by the emergence of an absorbance peak occurring at 634 nm (**Figure S46**). **Figure S47** shows the comparison summary of the two copolymer mixtures at absorbance of 430 and 634 nm at different time points.

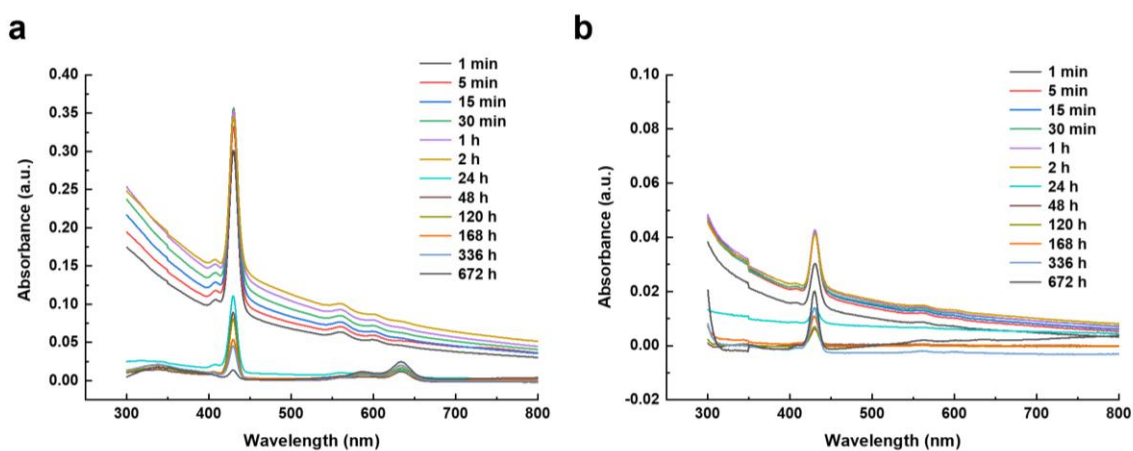


**Figure 2.18.** UV-vis absorbance of the supernatant at different time points from copolymer mixture (a)  $A_{3, P1+B3}$ , (b)  $C_{1, P1+B3}$ .

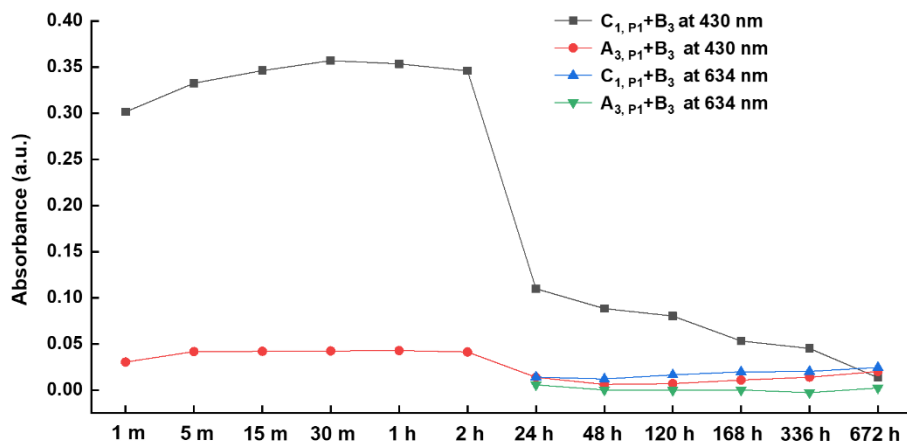


**Figure 2.19.** Comparison of UV-vis absorbance at 430 and 634 nm of the supernatant from copolymer mixture  $A_{3,P1}+B_3$  and  $C_{1,P1}+B_3$  at different time points.

### Contact Angle Measurements

Contact angle measurements were performed on three different substrates: metal (steel ruler), glass, and high density polyethylene (HDPE).  $H_2O$ , copolymer  $A_{3,P1}$  in  $H_2O$  ( $45.7 \text{ mg}\cdot\text{mL}^{-1}$ ,  $0.023 \text{ mol}\cdot\text{L}^{-1}$ ), copolymer  $B_3$  in  $H_2O$  ( $54.3 \text{ mg}\cdot\text{mL}^{-1}$ ,  $0.023 \text{ mol}\cdot\text{L}^{-1}$ ), copolymer  $C_{1,P1}$  in  $H_2O$  ( $34.2 \text{ mg}\cdot\text{mL}^{-1}$ ,  $0.023 \text{ mol}\cdot\text{L}^{-1}$ ), and copolymer mixture  $A_{3,P1}+B_3$  in  $H_2O$  ( $50 \text{ mg}\cdot\text{mL}^{-1}$ ,  $0.023 \text{ mol}\cdot\text{L}^{-1}$ ) were tested. Each solution ( $7.5 \mu\text{L}$ ) was deposited onto each substrate three separate times to calculate the average. No saltwater solutions were used because a gel would form and give inaccurate contact angle measurements.



**Figure 2.20.** Representative picture of  $H_2O$  droplets on different surfaces: (a) metal, (b) glass, (c) HDPE.



**Figure 2.21.** Representative picture of copolymer  $A_{3,P1}$  on different surfaces: (a) metal, (b) glass, (c) HDPE.

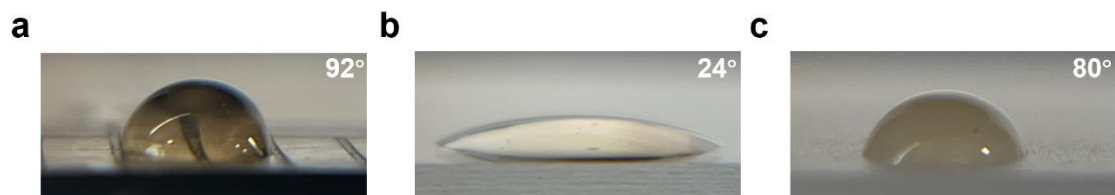


**Figure 2.22.** Representative picture of copolymer  $B_3$  on different surfaces: (a) metal, (b) glass, (c) HDPE.

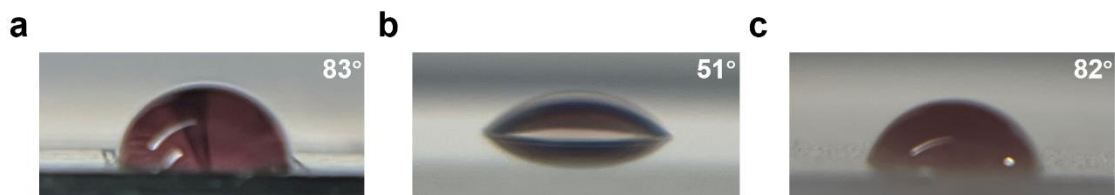


**Figure 2.23.** Representative picture of copolymer mixture  $A_{3,P1}+B_3$  on different surfaces: (a) metal, (b) glass, (c) HDPE.

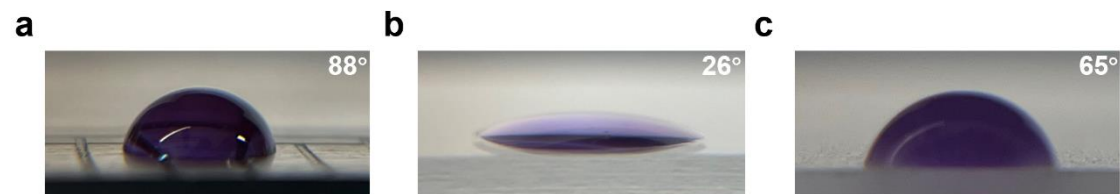


**Figure 2.24.** Representative picture of copolymer  $C_{1,P1}$  on different surfaces: (a) metal, (b) glass, (c) HDPE.

## 2.4.4 Evaluation of Hydrogel Properties

### Different Salt Concentration Tests with $A_{3,P1}+B_3$ Copolymer Complex

As the  $A_{3,P1}+B_3$  copolymer complex completely formed gels in 100 mM NaCl solutions, the gelation process of  $A_{3,P1}+B_3$  was further tested with different NaCl concentrations (**Figure 2.25a**). 25 mg·mL<sup>-1</sup> for  $A_{3,P1}+B_3$  was used for this test as it was easier to see the differences compared to higher complex concentrations. Similar experiments were also performed with LiCl (**Figure**

**2.25b**) and KCl (**Figure 2.25c**). For all three salts,  $A_{3, P1}+B_3$  stayed in solution at 10 mM, became viscous at 15 mM, started to gel at 20 mM, and formed gels completely at 100 mM. However, there were differences for the gelation of  $A_{3, P1}+B_3$  at 50 mM among the three salts: in LiCl  $A_{3, P1}+B_3$  formed gels better than NaCl, and KCl last, as illustrated by the remaining solution colors (formed gels better had less purple in the solution).

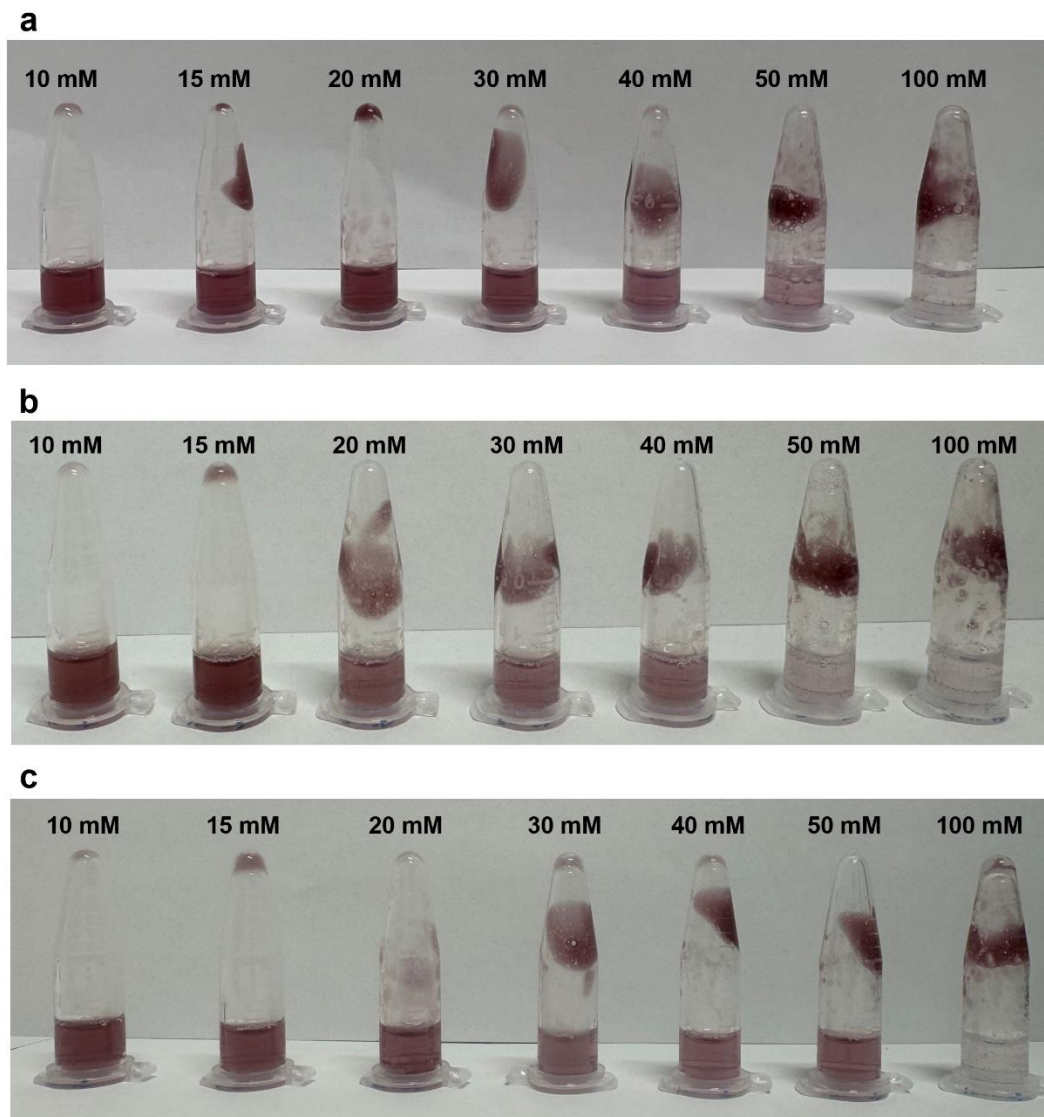


**Figure 2.25.**  $A_{3, P1}$  and  $B_3$  mixed at  $25 \text{ mg}\cdot\text{mL}^{-1}$  in different concentrations of (a) NaCl solutions, (b) LiCl solutions, (c) KCl solutions.

### Rheology of Hydrogels

Initial Screening: The guest copolymer **A<sub>3, P1</sub>** and host copolymer **B<sub>3</sub>** were dissolved separately in buffered solutions. The solution of guest copolymer **A<sub>3, P1</sub>** was then added into the solution of host copolymer **B<sub>3</sub>** to form the hydrogel to be tested. The amount of hydrogel was between 80–100 mg (pre-weighed dry mass before dissolving in any buffered solutions) for each run. The hydrogels were first tested at different concentrations in PBS: 25, 50 and 75 mg·mL<sup>-1</sup>, among which the 50 mg·mL<sup>-1</sup> hydrogel concentration was the only one that showed obvious shear-thinning properties (i.e., G'/G'' crossover) for strain sweep tests at both 15 °C and 25 °C after heat curing at 80 °C. To simplify the salt solution, the 50 mg·mL<sup>-1</sup> gel concentration was selected to do the rheology screening for different NaCl solutions at 50, 100 and 200 mM. It is important to note that the 100 mM NaCl solution was chosen as the standard solution for all tests at this point, as shear-thinning properties were evident for strain sweep tests at both 15 and 25 °C after heat curing at 80 °C. After these initial screening tests were conducted, all hydrogels moving forward were assessed at 25 °C, before and after heat curing at 80 °C.

Tests (three replicates for each) for a series of **A<sub>x, Pn</sub>+B<sub>x</sub>** hydrogels: The best condition of 50 mg·mL<sup>-1</sup> in 100 mM NaCl solution was used to do the experiments for different **A<sub>x, Pn</sub>+B<sub>x</sub>** hydrogels. All tests were conducted at 25 °C before and after heat curing at 80 °C. The same hydrogel test was repeated three times. (*Note: all the polymerizations for the copolymers used to form hydrogels and do rheology went to completion, one exception was copolymer **B<sub>5</sub>** that the polymerization was almost complete, and we still did three replicates for **A<sub>5, P1</sub>+B<sub>5</sub>**.)*

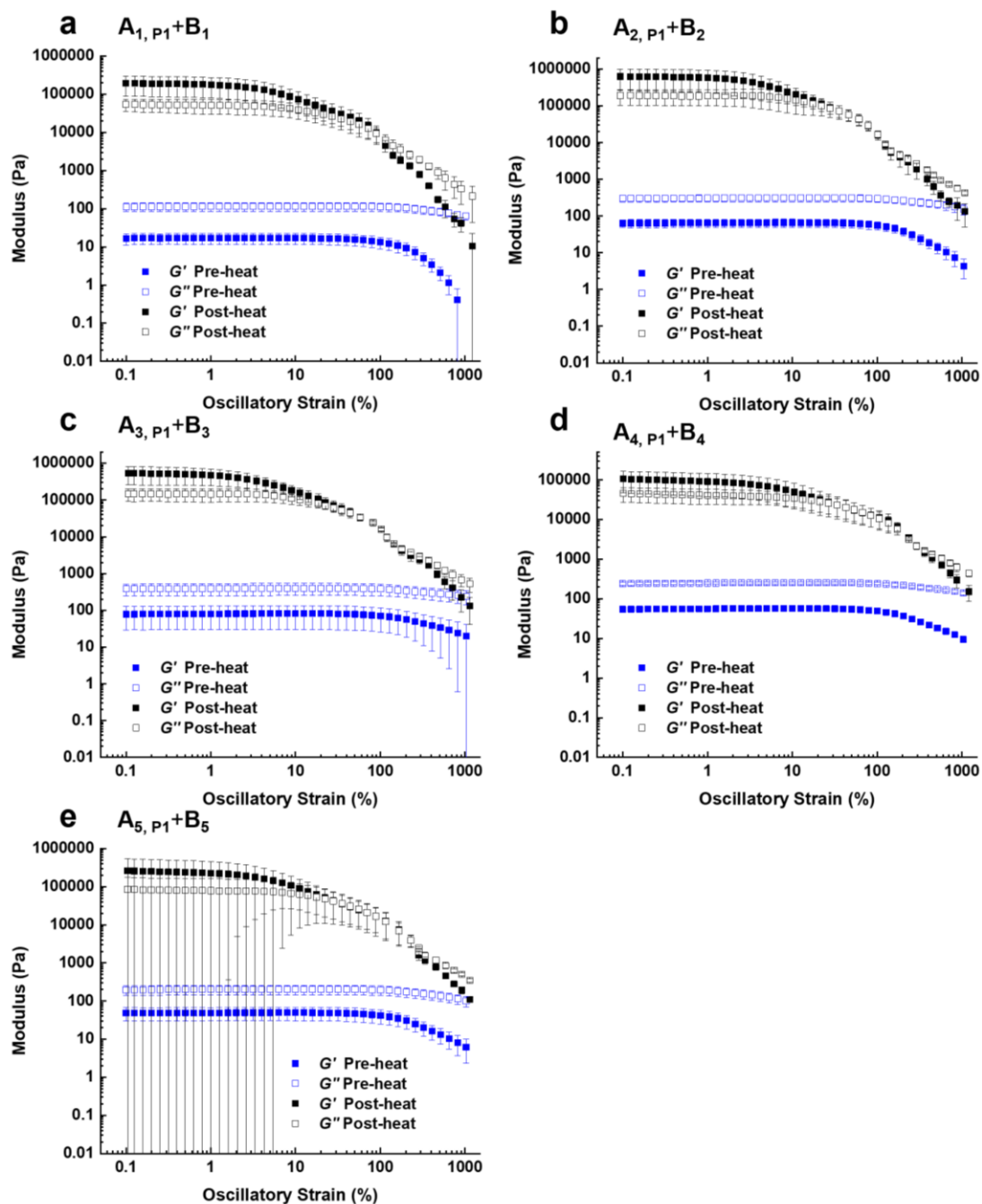


**Figure 2.26.** Oscillatory strain rheology (performed at  $1 \text{ rad}\cdot\text{s}^{-1}$ ) data (average) at  $50 \text{ mg}\cdot\text{mL}^{-1}$  in  $100 \text{ mM}$  NaCl at  $25 \text{ }^\circ\text{C}$  for  $A_n, P1+B_n$  ( $n=1, 2, 3, 4$  and  $5$ ) hydrogels. (a)  $A_{1, P1+B_1}$ , (b)  $A_{2, P1+B_2}$ , (c)  $A_{3, P1+B_3}$ , (d)  $A_{4, P1+B_4}$ , (e)  $A_{5, P1+B_5}$ . (Note: The reason why hydrogel  $A_{5, P1+B_5}$  has a big error bar after heating is that polymerization of  $B_5$  could not go to full completion and each batch of polymer  $B_5$  was not exact same.)

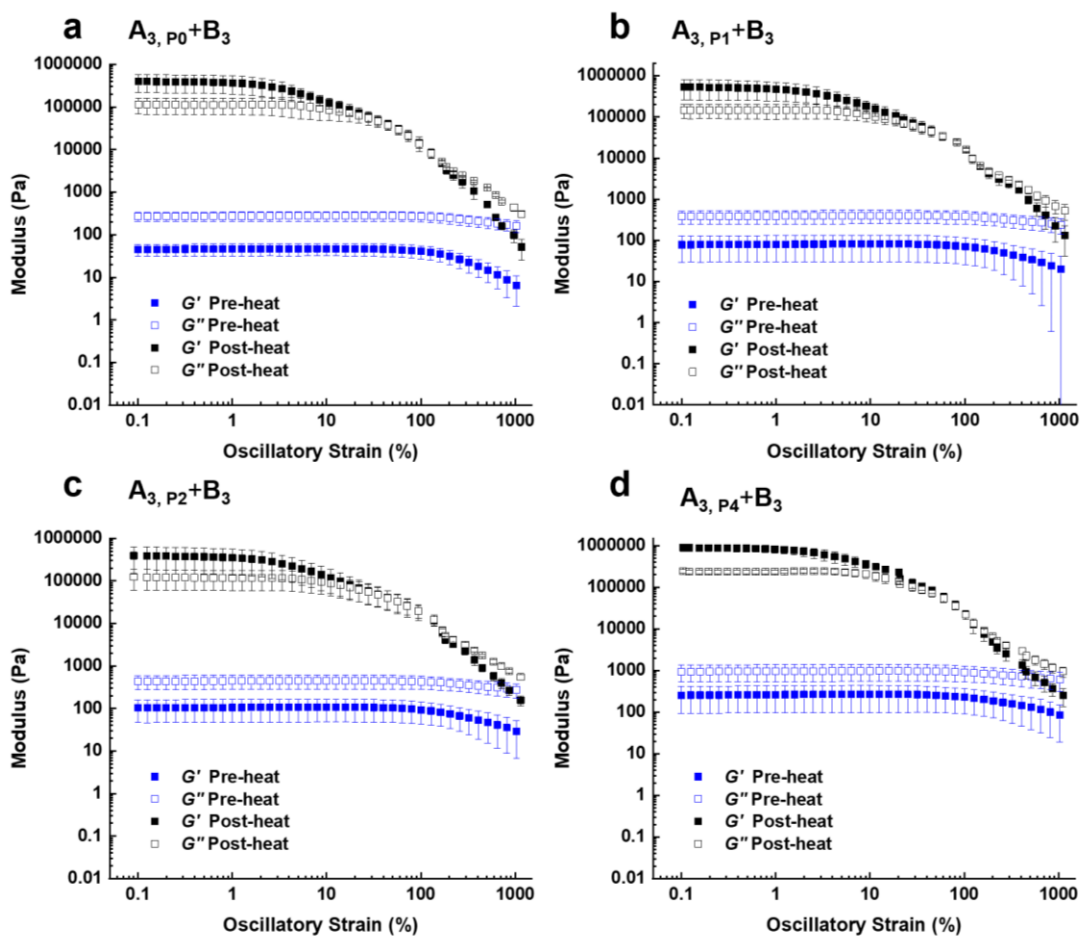


**Figure 2.27.** Oscillatory strain rheology (performed at  $1 \text{ rad}\cdot\text{s}^{-1}$ ) data (average) at  $50 \text{ mg}\cdot\text{mL}^{-1}$  in  $100 \text{ mM}$  NaCl at  $25 \text{ }^\circ\text{C}$  for  $\text{A}_3, \text{P}_n+\text{B}_3$  ( $n=0, 1, 2$  and  $4$ ) hydrogels. (a)  $\text{A}_3, \text{P}_0+\text{B}_3$ , (b)  $\text{A}_3, \text{P}_1+\text{B}_3$ , (c)  $\text{A}_3, \text{P}_2+\text{B}_3$ , (d)  $\text{A}_3, \text{P}_4+\text{B}_3$ .

Hydrogel	Pre-heat			Post-heat		
	$G'$ (kPa)	$G''$ (kPa)	Tan ( $\delta$ )	$G'$ (kPa)	$G''$ (kPa)	Tan ( $\delta$ )
$\text{A}_3, \text{P}_0+\text{B}_3$	$0.046\pm 0.014$	$0.275\pm 0.068$	6.0	$368\pm 169$	$113\pm 47$	0.31
$\text{A}_3, \text{P}_1+\text{B}_3$	$0.080\pm 0.050$	$0.390\pm 0.140$	4.9	$470\pm 227$	$145\pm 57$	0.31
$\text{A}_3, \text{P}_2+\text{B}_3$	$0.105\pm 0.058$	$0.443\pm 0.162$	4.2	$348\pm 209$	$117\pm 58$	0.34
$\text{A}_3, \text{P}_4+\text{B}_3$	$0.262\pm 0.166$	$0.964\pm 0.425$	3.7	$830\pm 159$	$237\pm 25$	0.29

**Table 2.7.** Summary of storage and loss moduli for different  $\text{A}_3, \text{P}_n+\text{B}_3$  ( $n=0, 1, 2$  and  $4$ ) hydrogels, where different units of porphyrin were incorporated per chain. (Data was collected from **Figure 2.27** at 1% strain.)

**C<sub>1, P1</sub>+B<sub>3</sub>**: Rheology tests were performed on **C<sub>1, P1</sub>+B<sub>3</sub>** hydrogels at 50 mg·mL<sup>-1</sup> in 100 mM NaCl solution. Same procedure was used as described for **A<sub>x, Pn</sub>+B<sub>x</sub>** hydrogels. Each run contained around 100 mg **C<sub>1, P1</sub>+B<sub>3</sub>** hydrogels. However, **C<sub>1, P1</sub>+B<sub>3</sub>** was not as soft material as **A+B** hydrogels (a big piece and not sticky before test, **Figure 2.28**), and to avoid the axial force being too high, gap was adjusted to fit each sample (1100 μm, 1100 μm and 950 μm for three runs, separately).



**Figure 2.28.** Pictures of **C<sub>1, P1</sub>+B<sub>3</sub>** for rheology tests. **a)** as prepared on stage, **b)** before the test covering the gap, **c)** after test.

**C<sub>2, P1</sub>+B<sub>3</sub>**: Rheology tests were performed on **C<sub>2, P1</sub>+B<sub>3</sub>** hydrogels at 50 mg·mL<sup>-1</sup> in 100 mM NaCl solution. Same procedure was used as described for **A<sub>x, Pn</sub>+B<sub>x</sub>** hydrogels. Each run contained around 100 mg **C<sub>2, P1</sub>+B<sub>3</sub>** hydrogels. However, as illustrated in **Figure 2.14**, copolymer **C<sub>2, P1</sub>** is not soluble in H<sub>2</sub>O at room temperature, so copolymer **C<sub>2, P1</sub>** was dissolved in 100 mM NaCl solution at 4 °C and kept at this temperature until mixed with copolymer **B<sub>3</sub>** (still dissolved in 100 mM NaCl solution at room temperature) to form hydrogels for tests. **C<sub>2, P1</sub>+B<sub>3</sub>** hydrogels were soft materials (also sticky) similar as **A+B** hydrogels, so the gap was able to be maintained at 500 μm for each run. Pictures were taken for the tests and shown in **Figure 2.29**.



**Figure 2.29.** Pictures of  $C_{2, P1+B3}$  for rheology tests. **a)** as prepared on stage, **b)** before the test covering the gap, **c)** after test.

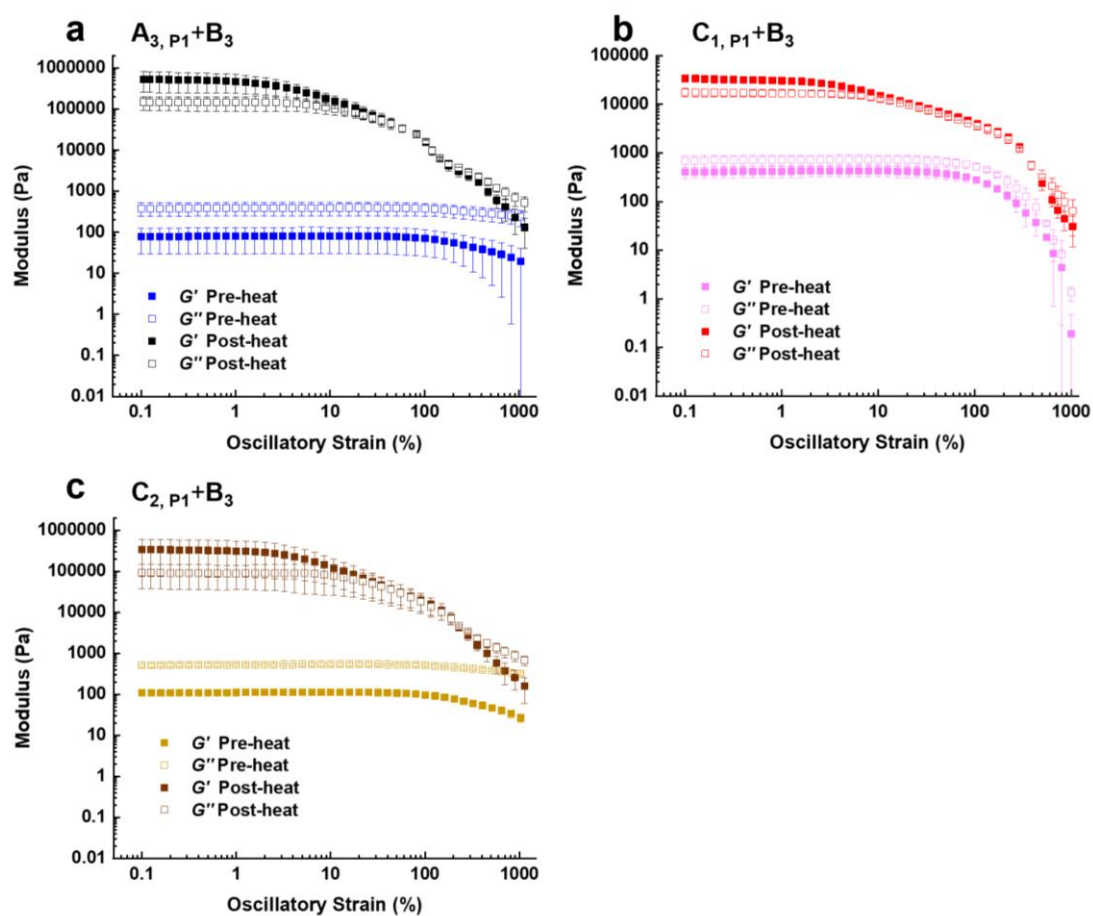


**Figure 2.30.** Oscillatory strain rheology (performed at  $1 \text{ rad}\cdot\text{s}^{-1}$ ) data (average) at  $50 \text{ mg}\cdot\text{mL}^{-1}$  in  $100 \text{ mM}$  NaCl at  $25 \text{ }^\circ\text{C}$  for hydrogels. (a)  $A_{3, P1+B3}$ , (b)  $C_{1, P1+B3}$ , (c)  $C_{2, P1+B3}$ .

## Scanning Electron Microscopy (SEM) Imaging

To better understand the  $\mathbf{A}_{3, P1}+\mathbf{B}_3$  hydrogels formation only in salt solution not in  $\text{H}_2\text{O}$ , scanning electron microscopy (SEM) experiments were performed. Three different samples of  $\mathbf{A}_{3, P1}+\mathbf{B}_3$  were prepared for SEM: 1)  $\mathbf{A}_{3, P1}+\mathbf{B}_3$  dissolved in  $\text{H}_2\text{O}$  at  $50 \text{ mg}\cdot\text{mL}^{-1}$  and dropped onto clean gold wafer by pipette; 2)  $\mathbf{A}_{3, P1}$  and  $\mathbf{B}_3$  were dissolved separately in 100 mM NaCl solution, and  $\mathbf{A}_{3, P1}$  was dropped onto clean gold wafer using pipette followed by dropping  $\mathbf{B}_3$  to form fresh hydrogels with a concentration of  $50 \text{ mg}\cdot\text{mL}^{-1}$ , excess NaCl solution was also on gold wafer; 3) pre-made hydrogels of  $\mathbf{A}_{3, P1}+\mathbf{B}_3$  with a concentration of  $50 \text{ mg}\cdot\text{mL}^{-1}$  were attached to the gold wafer using a pipette. All three samples were air dried overnight, and the samples were then loaded into the SEM chamber. The sample chamber was evacuated using the HiVac setting, and images were recorded at 1000x, 5000x, 10000x, and 35000x magnification.

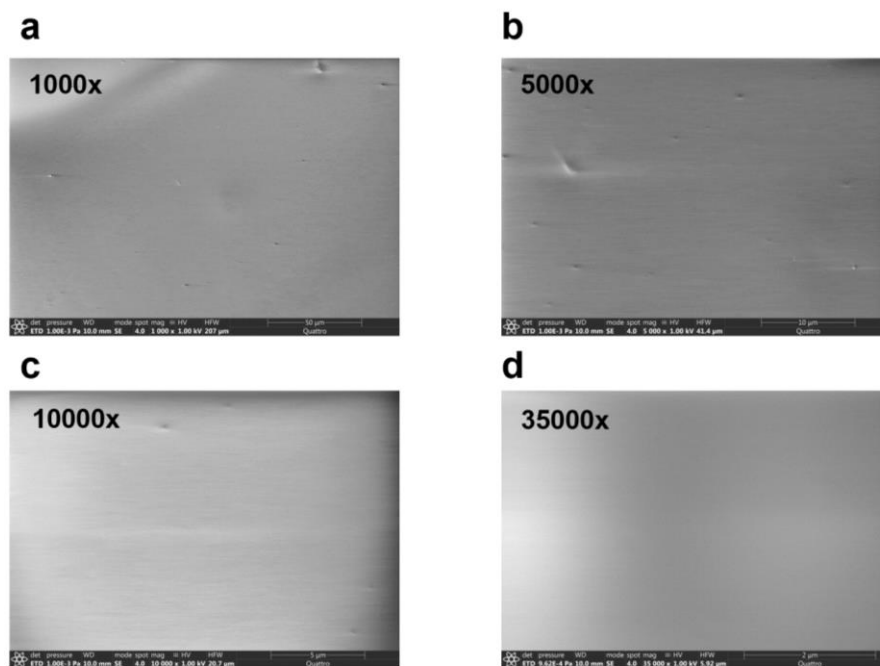


**Figure 2.31.** SEM images of  $\mathbf{A}_{3, P1}+\mathbf{B}_3$  in  $\text{H}_2\text{O}$  after air dried overnight. (a) 1000x, (b) 5000x, (c)10000x, (d) 10000x.

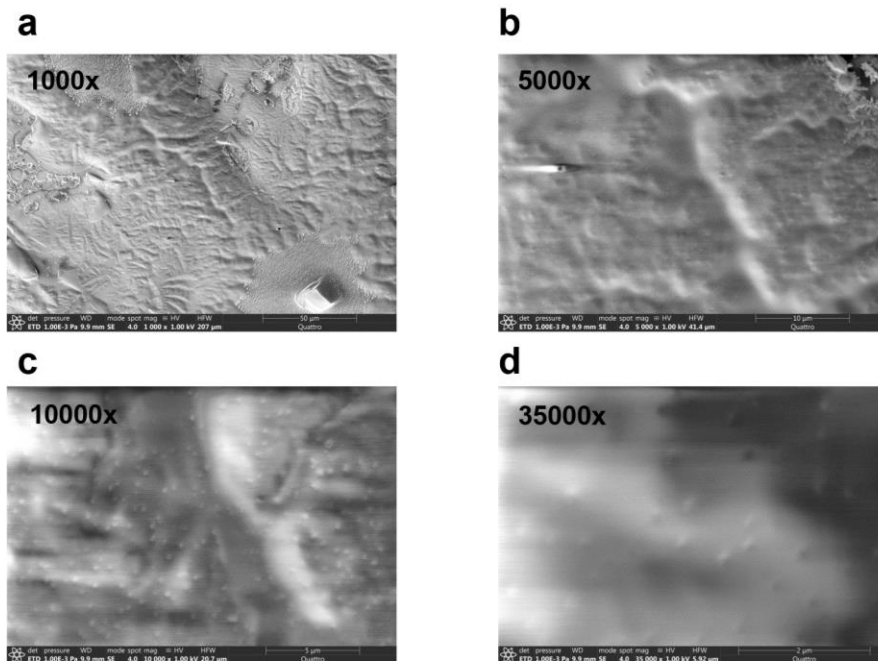


**Figure 2.32.** SEM images of  $A_3, P_1+B_3$  hydrogel (fresh) in 100 mM NaCl solution after air dried overnight. Region 1: (a) 1000x, (b) 5000x, (c) 10000x, (d) 10000x.

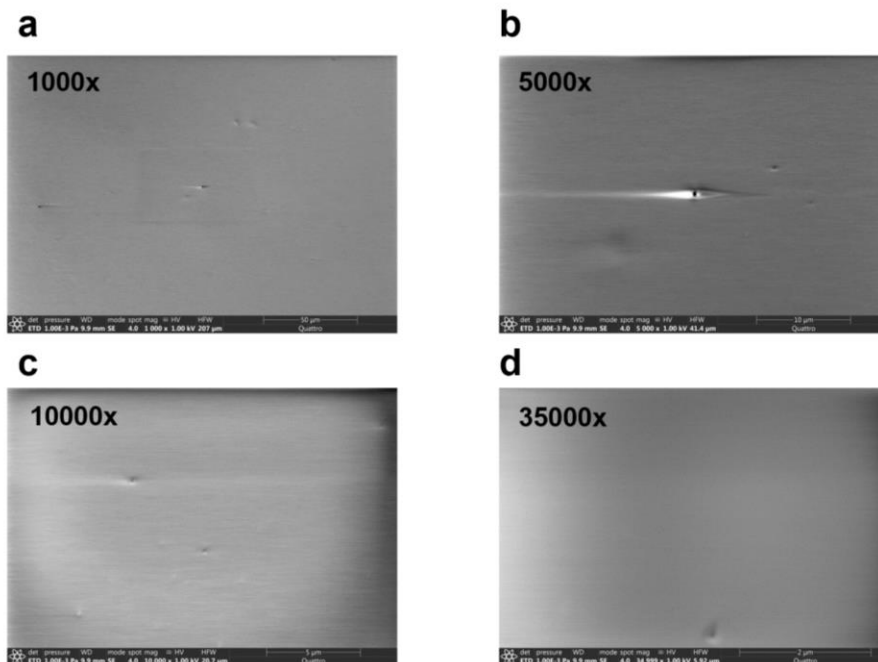


**Figure 2.33.** SEM images of  $A_3, P_1+B_3$  hydrogel (fresh) in 100 mM NaCl solution after air dried overnight. Region 2: (a) 1000x, (b) 5000x, (c) 10000x, (d) 10000x.

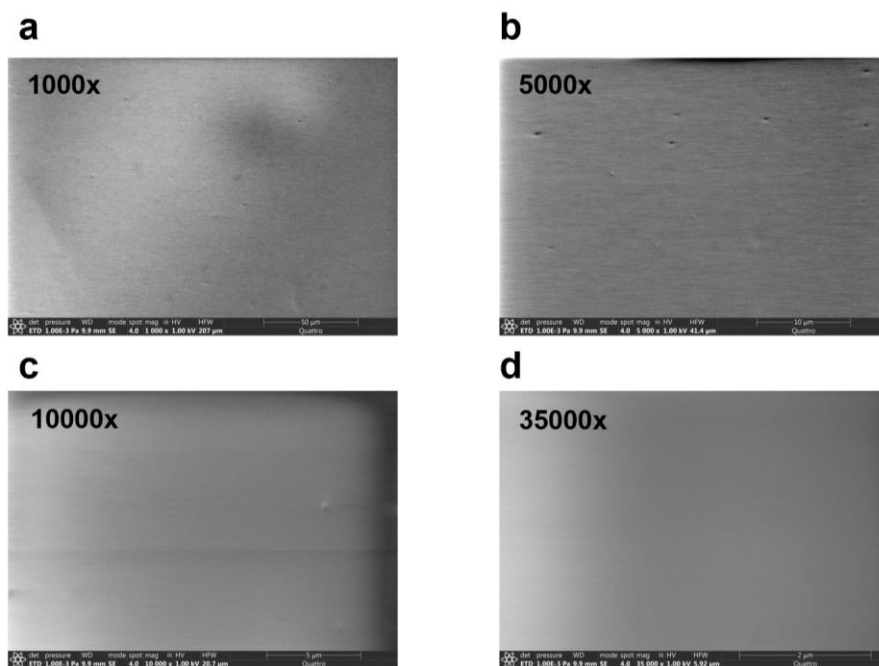


**Figure 2.34.** SEM images of  $A_3, P_1+B_3$  hydrogel (pre-made) in 100 mM NaCl solution after air dried overnight. (a) 1000x, (b) 5000x, (c)10000x, (d) 10000x.

### Lap-Shear Adhesion Test

All the hydrogel materials were applied onto the substrate (HDPE, stainless steel, glass, ham) through a dual-syringe method (**Figure 2.35a**), where one syringe contained an aqueous 100 mM NaCl solution (0.5 mL), and the other syringe contained the copolymer mixture ( $A_3, P_1+B_3$ ) aqueous solution (0.5 mL). Each sample contained 15 mg of  $A_3, P_1+B_3$  when applying to a substrate (some small amount was lost during the application process). After sandwiching the two substrates around the gel materials, the samples with glass, stainless steel, and HDPE as substrates were clamped with plastic clamps, while the sample with ham as the substrate, which was too soft for a clamp, was held together with a metal weight (122.7 g), as illustrated in **Figure 2.35**.

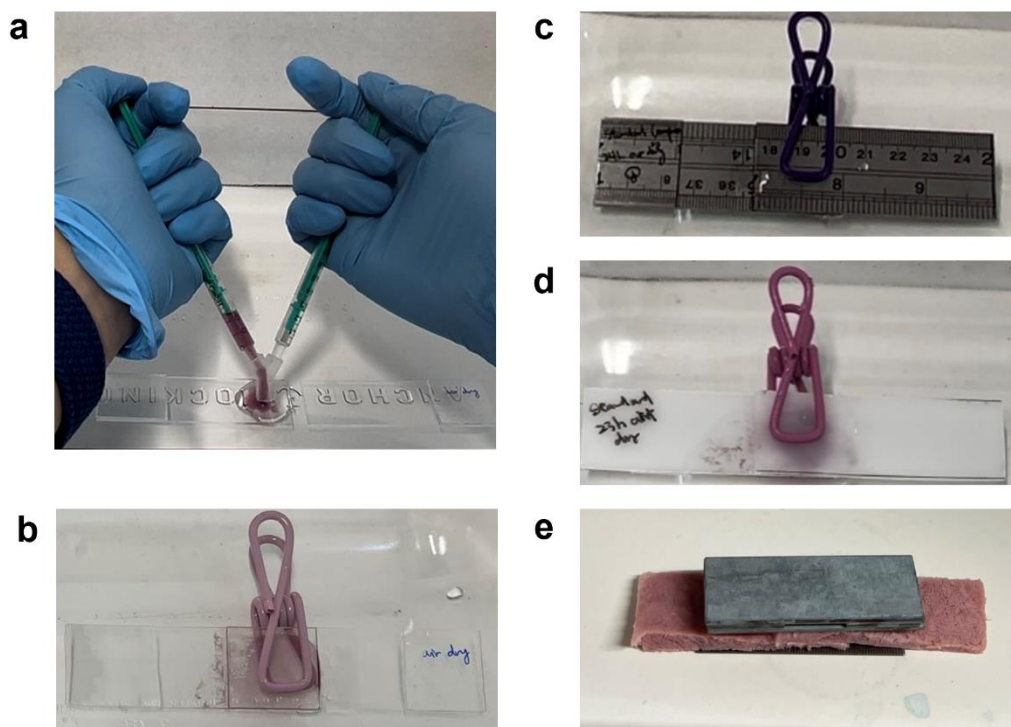


**Figure 2.35.** Pictures of (a) the dual syringe method and different surfaces investigated with hydrogel materials: (b) glass, (c) steel ruler, (d) HDPE, (e) ham.

Different curing protocols were applied to the samples before the lap-shear adhesion tests, including **1)** 24 h air dry, **2)** 12 h air dry followed by 12 h oven dry at 80 °C, and **3)** 24 h oven dry at 80 °C, as summarized in **Table 2.8** to simplify the graphs in the following sections. The numbers **(1, 2, 3)** are the code assigned to each curing protocol. The curing protocols were chosen to control the evaporation rate of H<sub>2</sub>O, which affected the adhesive strength. Heating at 80 °C sped up the drying process.

<b>1</b>	<b>24 h air dry</b>
<b>2</b>	<b>12 h air dry, 12 h oven dry at 80 °C</b>
<b>3</b>	<b>24 h oven dry at 80 °C</b>

**Table 2.8.** Summary of curing protocols for lap-shear adhesion tests.

As the H<sub>2</sub>O amount in the copolymer mixture and the evaporation speed of H<sub>2</sub>O affect the adhesive strength, we also performed the solubility test for copolymer **A<sub>3, P1</sub>** (30 mg·mL<sup>-1</sup>) and **C<sub>1, P1</sub>** (30 mg·mL<sup>-1</sup>) to better understand the adhesive strength. As shown in **Figure 2.36**, copolymer **C<sub>1, P1</sub>** precipitated out after heating at 80 °C for 10 min, while copolymer **A<sub>3, P1</sub>** stayed soluble in H<sub>2</sub>O.

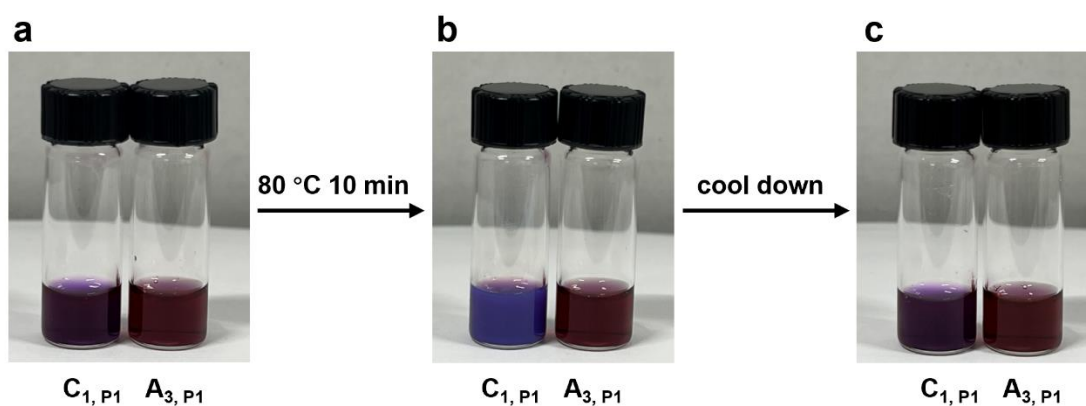


**Figure 2.36.** Solubility test of copolymer **A<sub>3, P1</sub>** and **C<sub>1, P1</sub>** in H<sub>2</sub>O (a) at room temperature, (b) after heating at 80 °C for 10 min, (c) cooled back to room temperature.

**Lap-Shear Adhesion Test on Glass:** A 100 mM NaCl solution, statistical copolymer **E<sub>P1</sub>**, and statistical copolymer **F<sub>P1</sub>** were used to start adhesion tests on glass (**Figure S86**) to show that a single polymer (i.e., not the self-assembled complex, in flowing solution form) could not provide significant adhesion. All the copolymers in the flowing solution form were applied to the substrates via a syringe (15 mg in 1 mL solvent). Next, hydrogels **A<sub>3, P1</sub>+B<sub>3</sub>** (**Figure S87**) and **C<sub>1, P1</sub>+B<sub>3</sub>** emulsions (**Figure S88**) were tested with different solution conditions on glass, involving a majority of organic solvent (CH<sub>3</sub>OH) to investigate faster curing times and with and without salt present. The **C<sub>1, P1</sub>+B<sub>3</sub>** emulsions were applied to the substrates with a similar dual-syringe method, while **B<sub>3</sub>** and **C<sub>1, P1</sub>** (15 mg for **C<sub>1, P1</sub>+B<sub>3</sub>**) were dissolved separately in 0.5 mL 100 mM NaCl aqueous solution in each syringe. It should be noted, however, that performing these experiments on glass made it difficult to reproduce each run. This is because the glass would fail

under stress at different time points during the lap shear experiments. When the adhesion became stronger, the strain limit relied on the quality of glass slide.

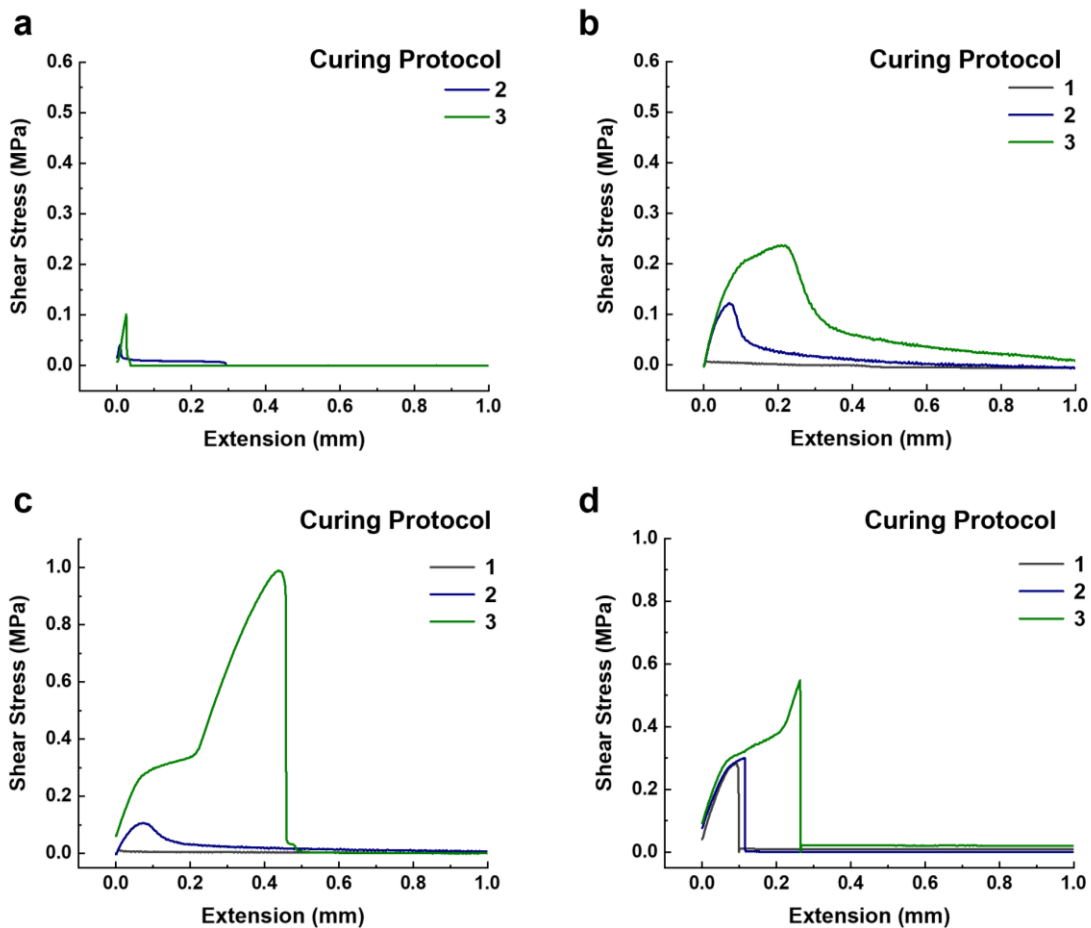


**Figure 2.37.** Lap-shear adhesion test on glass: (a) aqueous 100 mM NaCl solution, (b) statistical copolymer  $E_{P1}$  in  $H_2O$ , (c) statistical copolymer  $E_{P1}$  in aqueous 100 mM NaCl solution, and (d) statistical copolymer  $F_{P1}$  in  $CH_2Cl_2$ .

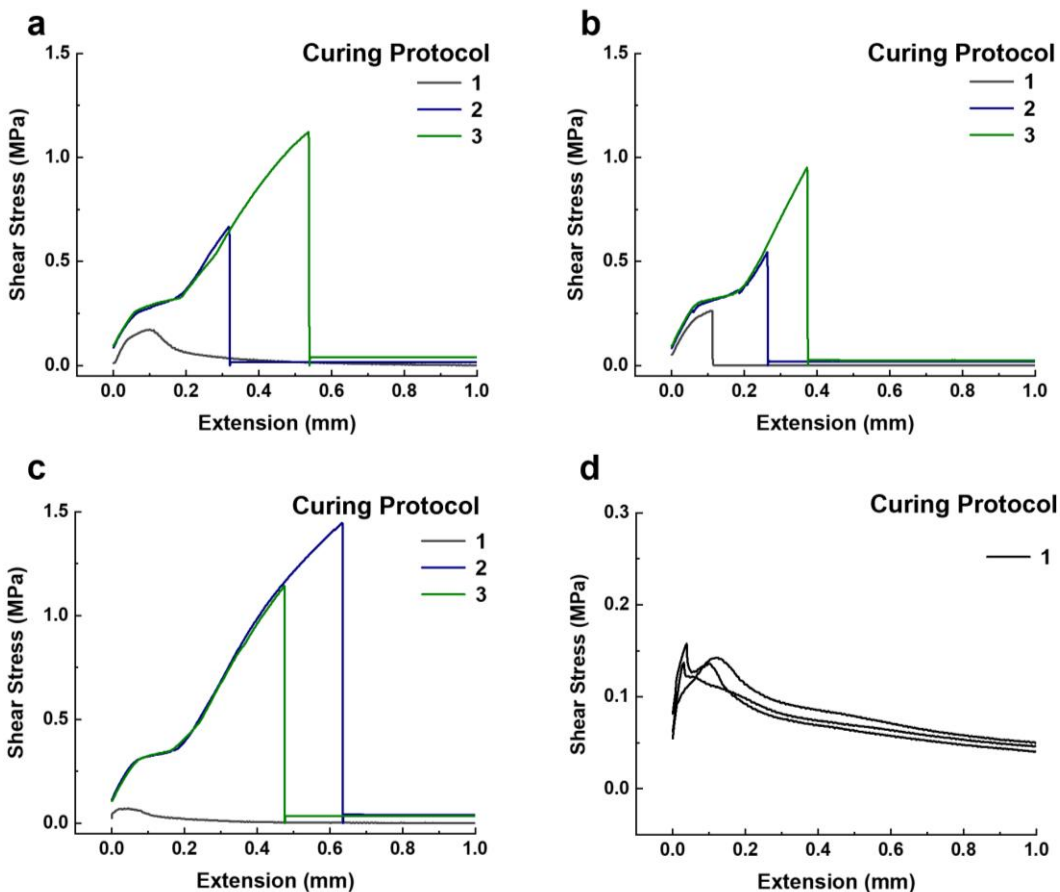


**Figure 2.38.** Lap-shear adhesion test on glass: (a)  $A_{3, P_1+B_3}$  hydrogels in aqueous 100 mM NaCl solution, (b)  $A_{3, P_1+B_3}$  copolymer mixture in 90%  $CH_3OH$  and 10%  $H_2O$ , and (c)  $A_{3, P_1+B_3}$  hydrogels in 100 mM NaCl in 90%  $CH_3OH$  and 10%  $H_2O$ , (d) three replicates of  $A_{3, P_1+B_3}$  hydrogels in aqueous 100 mM NaCl solution with curing protocol 1.

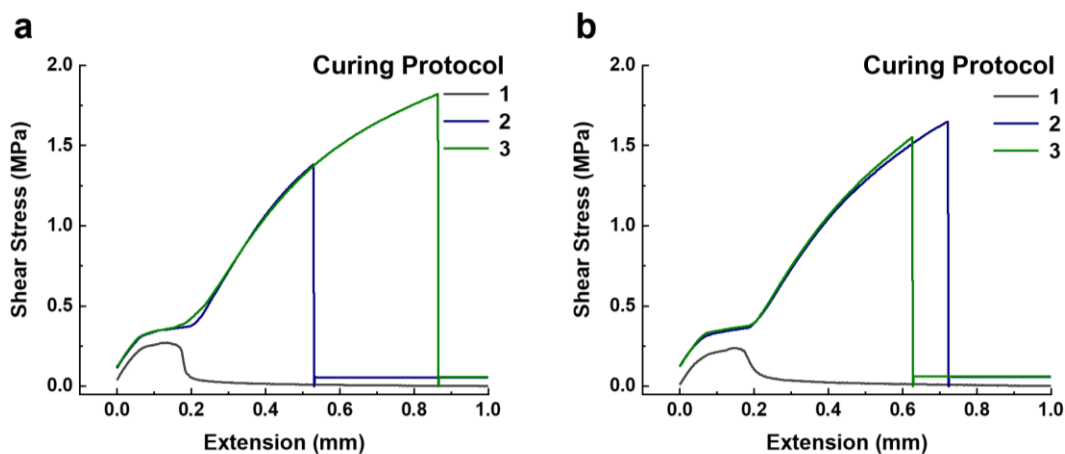


**Figure 2.39.** Lap-shear adhesion test on glass: (a)  $C_{1, P_1+B_3}$  emulsion in  $H_2O$ , (b)  $C_{1, P_1+B_3}$  emulsion in aqueous 100 mM NaCl solution.

**Lap-Shear Adhesion Test on Metal (Steel Ruler):** All the copolymer samples on the metal substrate were first tested using Instron 2712-041 series pneumatic side action tensile grips with rubber jaw faces and a 1 kN limit. Samples that exceeded 1 kN of force were stopped and retested using 30 kN limit wedge grips. Each sample was tested in triplicate for each curing protocol (1, 2, 3).

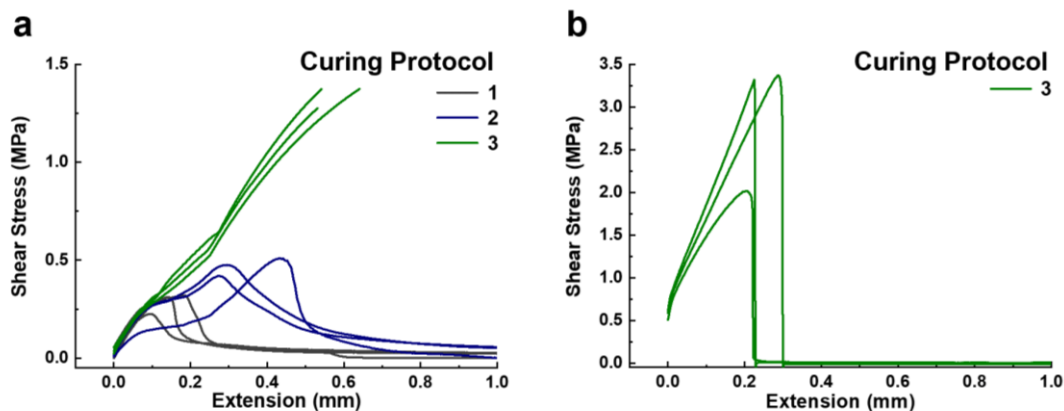


**Figure 2.40.** Lap-shear adhesion test of  $A_3, P_1+B_3$  hydrogels in aqueous 100 mM NaCl solution on metal: (a) pneumatic grips, and (b) wedge grips.

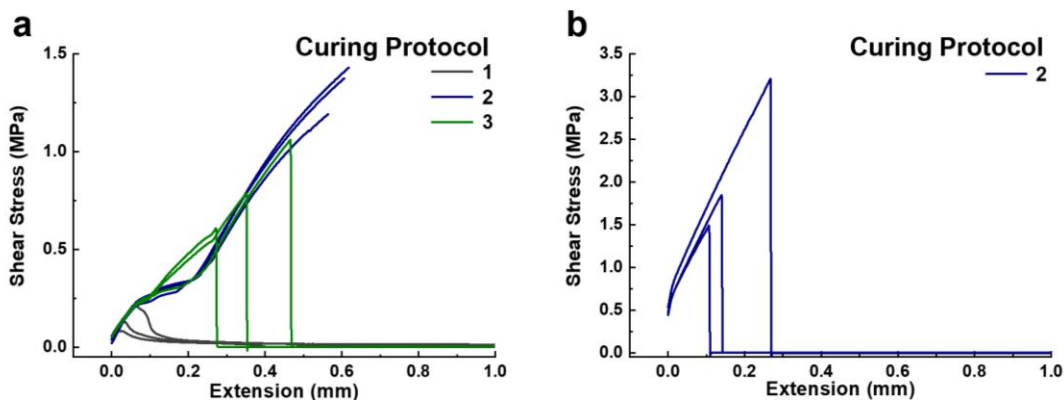


**Figure 2.41.** Lap-shear adhesion test of  $A_3, P_1+B_3$  hydrogels in 100 mM NaCl in 90%  $CH_3OH$  and 10%  $H_2O$  on metal: (a) pneumatic grips, and (b) wedge grips.

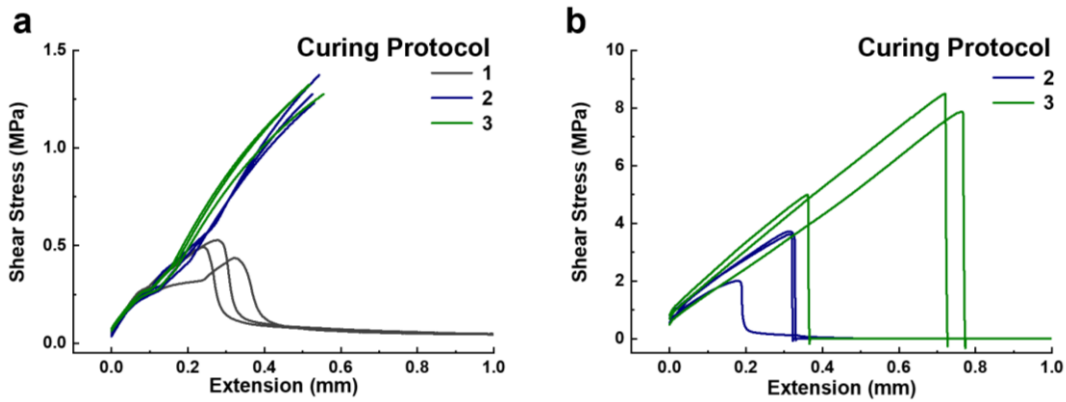


**Figure 2.42.** Lap-shear adhesion test of  $C_{1,P1}+B_3$  emulsion in aqueous 100 mM NaCl solution on metal: (a) pneumatic grips, and (b) wedge grips.

**Lap-Shear Adhesion Test on High Density Polyethylene (HDPE):** Each sample was tested in triplicate for each curing protocol (1, 2, 3).

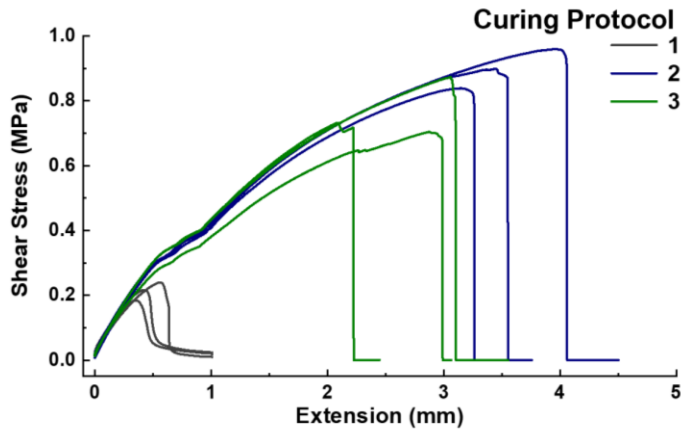


**Figure 2.43.** Lap-shear adhesion test of  $A_{3,P1}+B_3$  hydrogels in aqueous 100 mM NaCl solution on HDPE.

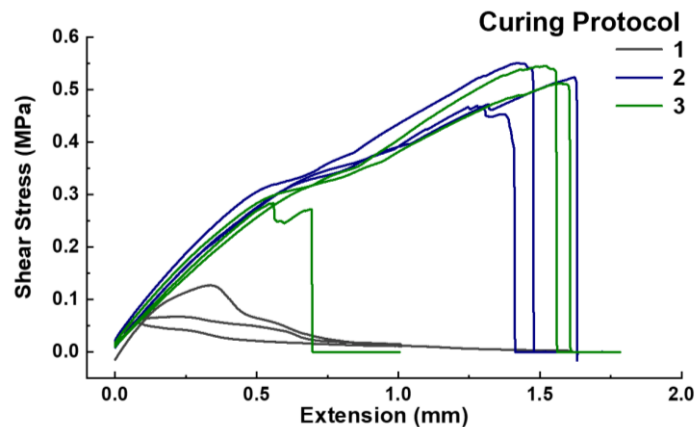


**Figure 2.44.** Lap-shear adhesion test of  $A_{3, P1+B3}$  hydrogels in 100 mM NaCl in 90%  $CH_3OH$  and 10%  $H_2O$  on HDPE.

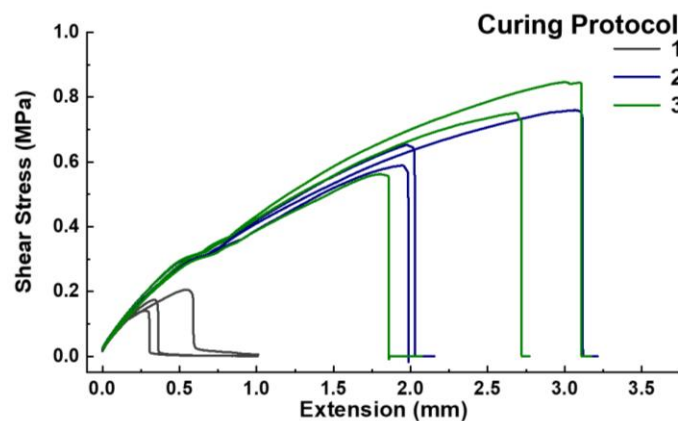


**Figure 2.45.** Lap-shear adhesion test of  $C_{1, P1+B3}$  emulsion in aqueous 100 mM NaCl solution on HDPE.

**Lap-Shear Adhesion Test on Store-Bought Ham:** The  $A_{3, P1+B3}$  hydrogels were tested as an adhesive on ham to mimic organic tissue. To imitate conditions that would be used for organic tissue, no heating was performed. The sample was cured using protocol **1** with triplicate.

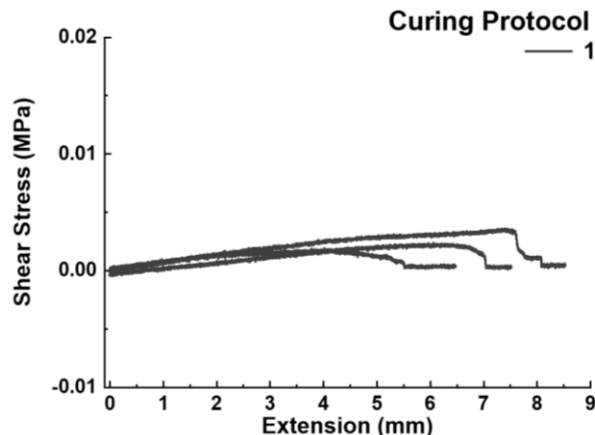


**Figure 2.46.** Lap-shear adhesion test of  $A_{3, P1}+B_3$  hydrogels in aqueous 100 mM NaCl solution on ham.

## 2.5 Conclusions

The design, synthesis, and visible light-based control over the gelation, mechanical properties, and adhesive performance of a mucomimetic photoredox-responsive hydrogel was described. The hydrogels were prepared by mixing two PNB-based bottlebrush copolymers ( $A_{x, Pn}$  and  $B_x$ ), each of which was synthesized through ROMP of functional Nb-based monomers terminated by  $\beta$ -CD and Ad groups, respectively. Formation of host–guest inclusion complexes between the ‘host’  $\beta$ -CD and ‘guest’ Ad groups in  $H_2O$  resulted in soluble polymer networks that only formed a kinetically trapped viscous hydrogel once the copolymer mixture was exposed to a high ionic strength solution. The rapid, saltwater-induced gelation mechanism resulted from copolymer  $A_{x, Pn}$  having multiple polar, dicationic viologen subunits whose positive charges were screened in saline environments, effectively ‘salting out’ the  $A_{x, Pn}+B_x$  copolymer network. This two-part mechanism of network formation followed by rapid gelation is distinct from most injectable and shear-thinning hydrogels in that the host–guest crosslinked network remained soluble in  $H_2O$  and could easily be administered by syringe to any surface or location without any concern for clogging the needle or the rate of injection (i.e., injectability). Rheological evaluation of these self-assembled hydrogels revealed viscous behavior ( $G'' > G'$ ) in the post-injected state, but also

elastic behavior ( $G' > G''$ ) and shear-thinning properties that were 'switched on' after heating the hydrogels at 80 °C for 10 min. A similar level of control over the hydrogel's mechanical properties was demonstrated in response to blue light through the incorporation of a zinc-based tetraphenyl porphyrin monomer into the backbone of the 'guest' copolymer ( $\mathbf{A}_{3, P1}$ ). The incorporated porphyrin functioned as a visible-light-absorbing photocatalyst that could transfer electrons to the oligoviologen side chains. This reduction process converted all viologen subunits to their corresponding radical cations (i.e.,  $V^{2+}$  to  $V^{\bullet+}$ ) and resulted in contraction and stiffening of the hydrogel as a function of viologen radical-based self-assembly, a decrease in electrostatic repulsion, and a loss of the corresponding charge-screening anions, all of which led to higher crosslinking as  $H_2O$  was emitted. The change in the hydrogel's mechanical properties as a function of this photoredox process was monitored by rheology. Both moduli increased as  $\tan \delta$  decreased after irradiation with blue light. Moreover, after repeated rheological tests on the same photo-irradiated sample, both elastic ( $G' > G''$ ) and shear-thinning properties were 'switched on'. In addition to understanding the gelation and photoredox-responsive mechanisms, the viscous hydrogel also exhibited broad adhesive properties on polar and non-polar surfaces, such as glass, metal, and HDPE, but not on a tissue mimic such as ham. The corresponding adhesive performance of the hydrogels was tested through lap-shear experiments, where a dramatic increase in adhesive strength was observed in samples that were either heat- or photo-cured. Taken together, these experiments demonstrated how the mechanical properties (storage/loss moduli), physical behavior (shear-thinning), and performance (adhesive strength) of a kinetically trapped mucomimetic hydrogel can be tuned using either heat or a low-energy source of visible light. We envision this dynamic mucomimetic photoredox-responsive hydrogel platform may be useful in potential biomedical applications, such as in 3D (bio)printing and manufacturing, 4D tissue culture, drug delivery, and regenerative medicine.

## 2.6 References

- (1) Zhang, Y. S.; Khademhosseini, A. Advances in engineering hydrogels. *Science* **2017**, 356 (6337), eaaf3627.
- (2) Uman, S.; Dhand, A.; Burdick, J. A. Recent advances in shear-thinning and self-healing hydrogels for biomedical applications. *J. Appli. Polym. Sci.* **2020**, 137 (25), 48668.
- (3) Loebel, C.; Rodell, C. B.; Chen, M. H.; Burdick, J. A. Shear-thinning and self-healing hydrogels as injectable therapeutics and for 3D-printing. *Nat. Protoc.* **2017**, 12 (8), 1521-1541.
- (4) Zhang, G.; Chen, Y.; Deng, Y.; Ngai, T.; Wang, C. Dynamic Supramolecular Hydrogels: Regulating Hydrogel Properties through Self-Complementary Quadruple Hydrogen Bonds and Thermo-Switch. *ACS Macro Lett.* **2017**, 6 (7), 641-646.
- (5) Ren, P.; Li, J.; Zhao, L.; Wang, A.; Wang, M.; Li, J.; Jian, H.; Li, X.; Yan, X.; Bai, S. Dipeptide Self-assembled Hydrogels with Shear-Thinning and Instantaneous Self-healing Properties Determined by Peptide Sequences. *ACS Appl. Mater. Interfaces* **2020**, 12 (19), 21433-21440.
- (6) Zhu, Y.; Luo, Q.; Zhang, H.; Cai, Q.; Li, X.; Shen, Z.; Zhu, W. A shear-thinning electrostatic hydrogel with antibacterial activity by nanoengineering of polyelectrolytes. *Biomater. Sci.* **2020**, 8 (5), 1394-1404.
- (7) Appel, E. A.; Tibbitt, M. W.; Greer, J. M.; Fenton, O. S.; Kreuels, K.; Anderson, D. G.; Langer, R. Exploiting Electrostatic Interactions in Polymer-Nanoparticle Hydrogels. *ACS Macro Lett.* **2015**, 4 (8), 848-852.
- (8) Mantooth, S. M.; Munoz-Robles, B. G.; Webber, M. J. Dynamic Hydrogels from Host-Guest Supramolecular Interactions. *Macromol. Biosci.* **2019**, 19 (1), 1800281.
- (9) Lee, H. J.; Le, P. T.; Kwon, H. J.; Park, K. D. Supramolecular assembly of tetronic-adamantane and poly( $\beta$ -cyclodextrin) as injectable shear-thinning hydrogels. *J. Mater. Chem. B* **2019**, 7 (21), 3374-3382.
- (10) Zou, L.; Braegelman, A. S.; Webber, M. J. Dynamic Supramolecular Hydrogels Spanning an Unprecedented Range of Host-Guest Affinity. *ACS Appl. Mater. Interfaces* **2019**, 11 (6), 5695-5700.
- (11) Rosales, A. M.; Rodell, C. B.; Chen, M. H.; Morrow, M. G.; Anseth, K. S.; Burdick, J. A. Reversible Control of Network Properties in Azobenzene-Containing Hyaluronic Acid-Based Hydrogels. *Bioconjug. Chem.* **2018**, 29 (4), 905-913.
- (12) Rodell, C. B.; Kaminski, A. L.; Burdick, J. A. Rational Design of Network Properties in Guest-Host Assembled and Shear-Thinning Hyaluronic Acid Hydrogels. *Biomacromolecules* **2013**, 14 (11), 4125-4134.
- (13) Chen, M. H.; Wang, L. L.; Chung, J. J.; Kim, Y.-H.; Atluri, P.; Burdick, J. A. Methods To Assess Shear-Thinning Hydrogels for Application As Injectable Biomaterials. *ACS Biomater. Sci. Eng.* **2017**, 3 (12), 3146-3160.
- (14) Thornton, D. J.; Sheehan, J. K. From Mucins to Mucus. *Proc. Am. Thorac. Soc.* **2004**, 1 (1), 54-61.
- (15) Werlang, C.; Cárcarmo-Oyarce, G.; Ribbeck, K. Engineering mucus to study and influence the microbiome. *Nat. Rev. Mater.* **2019**, 4 (2), 134-145.

- (16) Bansil, R.; Turner, B. S. Mucin structure, aggregation, physiological functions and biomedical applications. *Curr. Opin. Colloid Interface Sci.* **2006**, *11* (2), 164-170.
- (17) Bej, R.; Haag, R. Mucus-Inspired Dynamic Hydrogels: Synthesis and Future Perspectives. *J. Am. Chem. Soc.* **2022**, *144* (44), 20137-20152.
- (18) Boni, L. J.; Zurfluh, R.; Baumgartner, M. E.; Windhab, E. J.; Fischer, P.; Kuster, S.; Ruhs, P. A. Effect of ionic strength and seawater cations on hagfish slime formation. *Sci. Rep.* **2018**, *8* (1), 9867.
- (19) Zhang, K.; Xue, K.; Loh, X. J. Thermo-Responsive Hydrogels: From Recent Progress to Biomedical Applications. *Gels* **2021**, *7* (3), 77.
- (20) Košovan, P.; Richter, T.; Holm, C. Modeling of Polyelectrolyte Gels in Equilibrium with Salt Solutions. *Macromol.* **2015**, *48* (20), 7698-7708.
- (21) Li, Z.; Zhou, Y.; Li, T.; Zhang, J.; Tian, H. Stimuli-responsive hydrogels: Fabrication and biomedical applications. *VIEW* **2022**, *3* (2), 20200112.
- (22) Li, Z.; Li, Y.; Chen, C.; Cheng, Y. Magnetic-responsive hydrogels: From strategic design to biomedical applications. *J. Controlled Release* **2021**, *335*, 541-556.
- (23) De, S. K.; Aluru, N. R.; Johnson, B.; Crone, W. C.; Beebe, D. J.; Moore, J. Equilibrium swelling and kinetics of pH-responsive hydrogels: models, experiments, and simulations. *J. Microelectromechanical Sys.* **2002**, *11* (5), 544-555.
- (24) Kilic Boz, R.; Aydin, D.; Kocak, S.; Golba, B.; Sanyal, R.; Sanyal, A. Redox-Responsive Hydrogels for Tunable and "On-Demand" Release of Biomacromolecules. *Bioconjug. Chem.* **2022**, *33* (5), 839-847.
- (25) Sharifzadeh, G.; Hosseinkhani, H. Biomolecule-Responsive Hydrogels in Medicine. *Adv. Healthc. Mater.* **2017**, *6* (24), 1700801.
- (26) Li, L.; Scheiger, J. M.; Levkin, P. A. Design and Applications of Photoresponsive Hydrogels. *Adv. Mater.* **2019**, *31* (26), 1807333.
- (27) Tang, L.; Wang, L.; Yang, X.; Feng, Y.; Li, Y.; Feng, W. Poly(N-isopropylacrylamide)-based smart hydrogels: Design, properties and applications. *Prog. Mater. Sci.* **2021**, *115*, 100702.
- (28) Zhao, Y.-L.; Stoddart, J. F. Azobenzene-Based Light-Responsive Hydrogel System. *Langmuir* **2009**, *25* (15), 8442-8446.
- (29) Accardo, Joseph V.; Kalow, J. A. Reversibly tuning hydrogel stiffness through photocontrolled dynamic covalent crosslinks. *Chem. Sci.* **2018**, *9* (27), 5987-5993.
- (30) Rosales, A. M.; Mabry, K. M.; Nehls, E. M.; Anseth, K. S. Photoresponsive Elastic Properties of Azobenzene-Containing Poly(ethylene-glycol)-Based Hydrogels. *Biomacromolecules* **2015**, *16* (3), 798-806.
- (31) Li, C.; Iscen, A.; Palmer, L. C.; Schatz, G. C.; Stupp, S. I. Light-Driven Expansion of Spiropyran Hydrogels. *J. Am. Chem. Soc.* **2020**, *142* (18), 8447-8453.
- (32) Li, C.; Xiong, Q.; Clemons, T. D.; Sai, H.; Yang, Y.; Hussain Sangji, M.; Iscen, A.; Palmer, L. C.; Schatz, G. C.; Stupp, S. I. Role of supramolecular polymers in photo-actuation of spiropyran hydrogels. *Chem. Sci.* **2023**, *14* (22), 6095-6104.
- (33) Griffin, D. R.; Kasko, A. M. Photodegradable Macromers and Hydrogels for Live Cell Encapsulation and Release. *J. Am. Chem. Soc.* **2012**, *134* (31), 13103-13107.

- (34) Fairbanks, B. D.; Singh, S. P.; Bowman, C. N.; Anseth, K. S. Photodegradable, Photoadaptable Hydrogels via Radical-Mediated Disulfide Fragmentation Reaction. *Macromol.* **2011**, *44* (8), 2444-2450.
- (35) Amir, F.; Li, X.; Gruschka, M. C.; Colley, N. D.; Li, L.; Li, R.; Linder, H. R.; Sell, S. A.; Barnes, J. C. Dynamic, multimodal hydrogel actuators using porphyrin-based visible light photoredox catalysis in a thermoresponsive polymer network. *Chem. Sci.* **2020**, *11* (40), 10910-10920, 10.1039/D0SC04287K.
- (36) Amir, F.; Liles, K. P.; Delawder, A. O.; Colley, N. D.; Palmquist, M. S.; Linder, H. R.; Sell, S. A.; Barnes, J. C. Reversible Hydrogel Photopatterning: Spatial and Temporal Control over Gel Mechanical Properties Using Visible Light Photoredox Catalysis. *ACS Appl. Mater. Interfaces* **2019**, *11* (27), 24627-24638.
- (37) Greene, A. F.; Danielson, M. K.; Delawder, A. O.; Liles, K. P.; Li, X.; Natraj, A.; Wellen, A.; Barnes, J. C. Redox-Responsive Artificial Molecular Muscles: Reversible Radical-Based Self-Assembly for Actuating Hydrogels. *Chem. Mater.* **2017**, *29* (21), 9498-9508.
- (38) Liles, K. P.; Greene, A. F.; Danielson, M. K.; Colley, N. D.; Wellen, A.; Fisher, J. M.; Barnes, J. C. Photoredox-Based Actuation of an Artificial Molecular Muscle. *Macromol. Rapid Commun.* **2018**, *39* (17), 1700781.
- (39) Sutthasupa, S.; Shiotsuki, M.; Sanda, F. Recent advances in ring-opening metathesis polymerization, and application to synthesis of functional materials. *Polym. J.* **2010**, *42* (12), 905-915.
- (40) Bielawski, C. W.; Grubbs, R. H. Living ring-opening metathesis polymerization. *Prog. Polym. Sci.* **2007**, *32* (1), 1-29.
- (41) Yao, K.; Chen, Y.; Zhang, J.; Bunyard, C.; Tang, C. Cationic salt-responsive bottle-brush polymers. *Macromol. Rapid Commun.* **2013**, *34* (8), 645-651.
- (42) Siggel, U.; Bindig, U.; Endisch, C.; Komatsu, T.; Tsuchida, E.; Voigt, J.; Fuhrhop, J.-H. Photophysical and photochemical properties of porphyrin aggregates. *Ber. Bunsenges. Phys. Chem.* **1996**, *100* (12), 2070-2075.
- (43) Maiti, N. C.; Mazumdar, S.; Periasamy, N. J- and H-Aggregates of Porphyrin-Surfactant Complexes: Time-Resolved Fluorescence and Other Spectroscopic Studies. *J. Phys. Chem. B* **1998**, *102* (9), 1528-1538.
- (44) Micali, N.; Villari, V.; Castriciano, M. A.; Romeo, A.; Monsù Scolaro, L. From Fractal to Nanorod Porphyrin J-Aggregates. Concentration-Induced Tuning of the Aggregate Size. *J. Phys. Chem. B* **2006**, *110* (16), 8289-8295.
- (45) Weyandt, E.; Leanza, L.; Capelli, R.; Pavan, G. M.; Vantomme, G.; Meijer, E. W. Controlling the length of porphyrin supramolecular polymers via coupled equilibria and dilution-induced supramolecular polymerization. *Nat. Commun.* **2022**, *13* (1), 248.
- (46) White, J. D.; Wilker, J. J. Underwater Bonding with Charged Polymer Mimics of Marine Mussel Adhesive Proteins. *Macromol.* **2011**, *44* (13), 5085-5088.
- (47) Kathiresan, M.; Ambrose, B.; Angulakshmi, N.; Mathew, D. E.; Sujatha, D.; Stephan, A. M. Viologens: a versatile organic molecule for energy storage applications. *J. Mater. Chem. A* **2021**, *9* (48), 27215-27233.
- (48) Love, J. A.; Morgan, J. P.; Trnka, T. M.; Grubbs, R. H. A practical and highly active ruthenium-based catalyst that effects the cross metathesis of acrylonitrile. *Angew. Chem.* **2002**, *114* (21), 4207-4209.

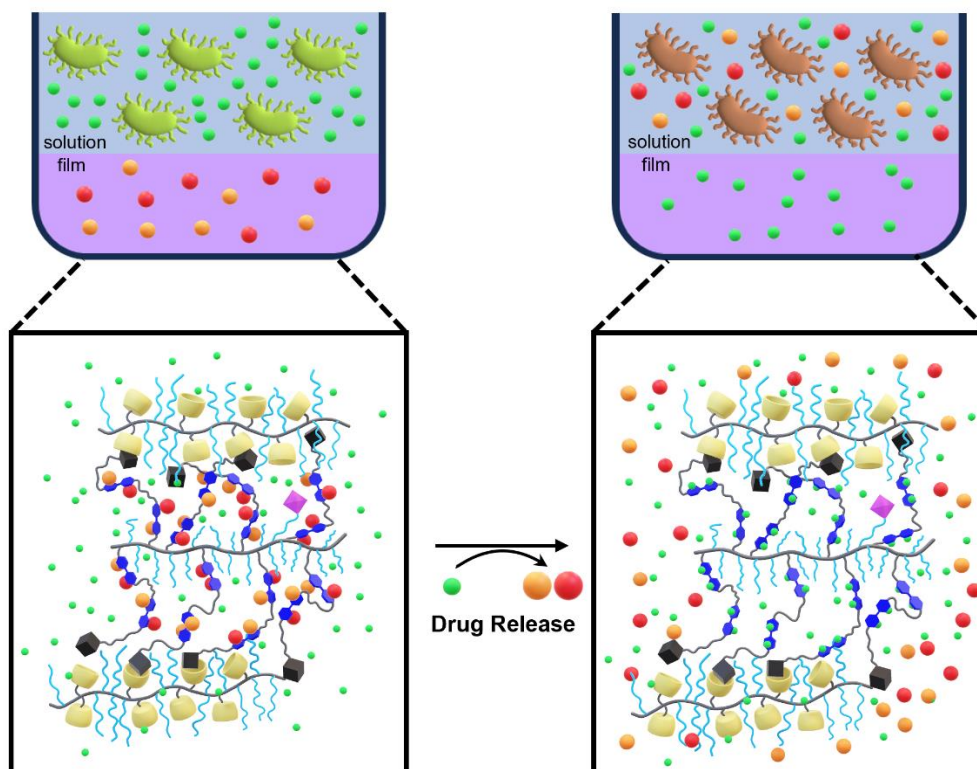
- (49) Matson, J. B.; Grubbs, R. H. Synthesis of Fluorine-18 Functionalized Nanoparticles for use as in vivo Molecular Imaging Agents. *J. Am. Chem. Soc.* **2008**, *130* (21), 6731-6733.
- (50) Li, R.; Li, X.; Zhang, Y.; Delawder, A. O.; Colley, N. D.; Whiting, E. A.; Barnes, J. C. Diblock brush-arm star copolymers via a core-first/graft-from approach using  $\gamma$ -cyclodextrin and ROMP: a modular platform for drug delivery. *Polym. Chem.* **2020**, *11* (2), 541-550.
- (51) Petter, R. C.; Salek, J. S.; Sikorski, C. T.; Kumaravel, G.; Lin, F. T. Cooperative binding by aggregated mono-6-(alkylamino)-. beta.-cyclodextrins. *J. Am. Chem. Soc.* **1990**, *112* (10), 3860-3868.
- (52) Tripodo, G.; Wischke, C.; Neffe, A. T.; Lendlein, A. Efficient synthesis of pure monotosylated beta-cyclodextrin and its dimers. *Carbohydr. Res.* **2013**, *381*, 59-63.

# Chapter 3: Mitigating *Pseudomonas aeruginosa* Biofilm Formation Using Self-Assembled Bactericidal Polymer Coatings

This chapter is based on work described in the following publication currently in preparation:

Yipei Zhang, Kejdi Kurti, Tarryn C. Trick, Mariah BoClair, Alexa R. Ribatt, Courtney Reichhardt\*, Jonathan C. Barnes\*. "Mitigating *Pseudomonas aeruginosa* Biofilm Formation Using Self-Assembled Bactericidal Polymer Coatings" *In Preparation*.

J.C.B. conceived the idea for the project, J.C.B., C.R., Y.Z. designed the experiments. Y.Z., T.C.T., and A.L.R. carried out the synthesis of the monomers, Y.Z. synthesized the polymers and polymer films. Y.Z. and T.C.T. characterized the monomers, polymers, and polymer films. K.K. and M.B. carried out biological experiments. J.C.B., C.R., Y.Z. and K.K. wrote the manuscript, and all authors contributed to the refinement of each document.



### 3.1 Abstract

Bacterial biofilms complicate the treatment of infections by enabling chronic colonization and antibiotic resistance. Infections that arise from contamination of surgical tools, medical implants, and catheters may be mitigated using antibacterial polymer coatings. Here, we describe a self-assembled polymer coating that consists of two bottlebrush copolymers which are synthesized through ring-opening metathesis polymerization. The formation of the polymer coating occurs via reversible host-guest interactions between adamantane and  $\beta$ -cyclodextrin and was shown to be stable on surfaces over several days in static salt solutions. Under dynamic flow conditions, the polymer coating efficiently prevented biofilm formation through a controlled delamination process, even after 96 h of exposure. Moreover, bactericidal properties were demonstrated through the slow release of antibiotics that were electrostatically loaded onto the positively charged oligoviologen side chains of the polymers. Growth inhibition was observed for up to 48 h under static conditions for the drug-loaded coatings. These results demonstrate a novel self-assembled polymer coating that was designed to possess both antifouling and bactericidal functionality under dynamic flow conditions, thus representing a novel platform with the potential to mitigate bacterial growth and biofilm formation on medical devices.

### 3.2 Introduction

The opportunistic pathogen *Pseudomonas aeruginosa* (*P. aeruginosa*) and other gram-negative bacteria are a rising public health threat due to their multi-drug resistance and ability to thrive in a range of environments.<sup>1,2</sup> *P. aeruginosa* is a main cause of medical device-associated infections, exacerbating hospital admissions and patient morbidity.<sup>3,4</sup> These characteristics can be attributed in part to the formation of multicellular bacterial communities called biofilms. Biofilms are aggregates of bacteria encased in an extracellular matrix that is typically comprised of extracellular DNA (eDNA), polysaccharides, and proteins.<sup>5</sup> Biofilm formation allows for stronger

adherence to surfaces, less susceptibility to environmental changes, and stronger tolerance toward antibiotics and the human immune system.<sup>6,7</sup> For example, biofilm bacteria can be up to 1000x more tolerant to antibiotics compared to their planktonic, or free swimming, counterparts.<sup>2</sup> Since targeting *P. aeruginosa* within the protective biofilm community can be challenging, preventing bacterial attachment and biofilm formation is a desirable therapeutic aim.<sup>8</sup>

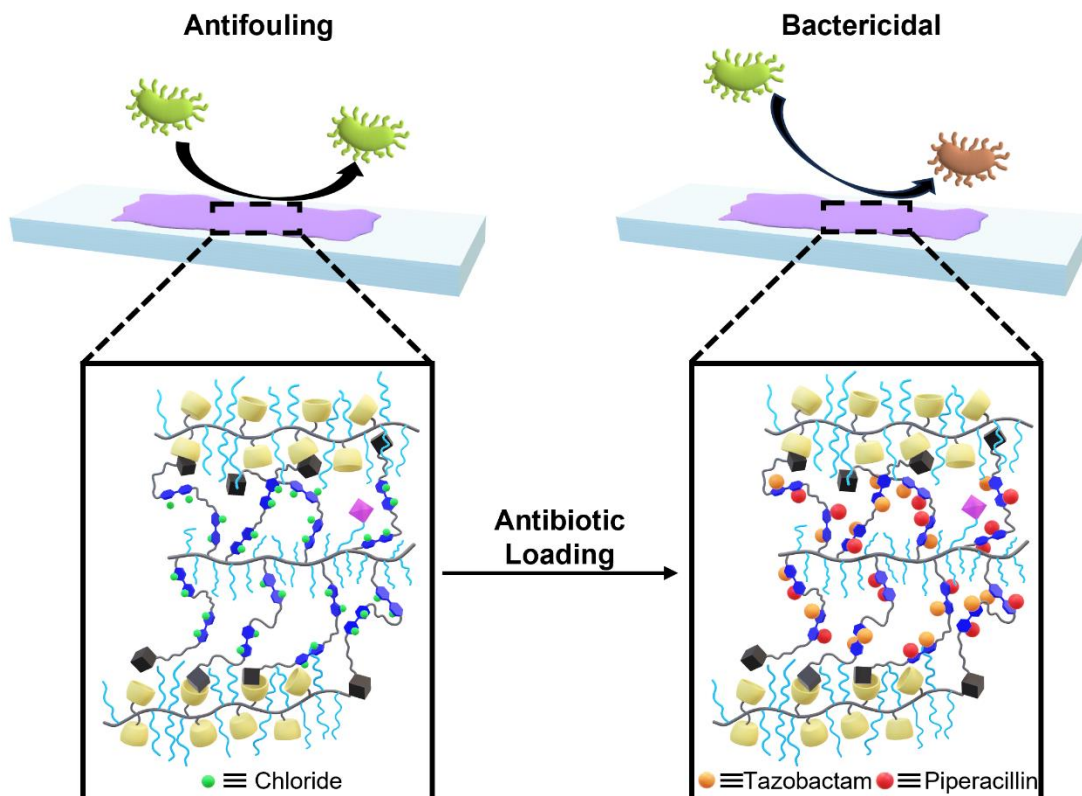


**Figure 3.1.** Schematic illustration of antifouling and bactericidal polymer coatings against bacterial adhesion and biofilm formation (top). Illustrations of the self-assembled polymer network before and after antibiotic loading is also shown (bottom).

Antibacterial polymer coatings have been widely used to prevent biofilm formation over the years.<sup>9,9</sup>

<sup>10</sup> The general mechanism to mitigate bacterial adhesion can be divided into two main categories of coatings: antifouling or bactericidal (**Figure 3.1**). Antifouling coatings function by inhibiting the bacterial attachment, while bactericidal coatings operate by killing the adhered bacteria.<sup>9, 10</sup>

Numerous hydrophilic polymers have been investigated as antifouling polymer coatings, including

polyethylene glycol (PEG),<sup>11-13</sup> zwitterionic polymers,<sup>14-16</sup> and polysaccharides.<sup>17-19</sup> The bactericidal coatings are generally designed to function through two different killing mechanisms.<sup>9</sup> The first involves a contact-active strategy, where the bacteria are killed upon direct contact with the coating. The majority of coatings that operate through this mechanism are cationic, such as antimicrobial peptides (AMPs),<sup>20</sup> quaternary ammonium compounds (QACs),<sup>21</sup> and quaternary phosphoniums.<sup>22</sup> The other mechanism involves the release of bactericidal agents, including antibiotics,<sup>23</sup> antiseptics,<sup>24</sup> AMPs,<sup>25</sup> etc. However, these types of coatings are not without limitations. For example, any bacterium that can attach to the antifouling coatings may still proliferate, whereas for bactericidal coatings, the gathering of dead bacteria and debris can lead to opportunities for other bacteria to colonize the surface. Therefore, a combination of antifouling and bactericidal coatings is often used to provide optimal protection against bacterial adhesion and biofilm formation.<sup>9</sup>

Herein, a novel self-assembled polymer coating is described which prevented *P. aeruginosa* bacterial cell attachment and biofilm formation on glass over a 96 h period through a controlled delamination process that was carried out under dynamic flow conditions (0.167 mL•min<sup>-1</sup>). The polymer coating consisted of two norbornene (Nb)-based bottlebrush copolymers (**A** and **B**) that formed a polymer film through reversible host-guest-based crosslinking between sidechain adamantane (Ad) and  $\beta$ -cyclodextrin ( $\beta$ -CD) functional groups. Polymer film **A+B** was fabricated by drop casting the polymer mixture dissolved in 90:10 MeOH:H<sub>2</sub>O onto glass slides and letting the solvent evaporate. Upon exposure to a static salt solution (100 mM NaCl), the polymer film displayed excellent stability over several days. However, the dynamic and reversible nature of Ad-CD host-guest complexes resulted in a controlled delamination of the **A+B** film during flow cell experiments, a controlled process which efficiently prevented *P. aeruginosa* biofilm formation over four days. Furthermore, copolymer **A** was loaded with tazobactam or piperacillin anions via electrostatic interactions with the constituent oligoviologen sidechains to yield bactericidal

copolymers **A<sub>t</sub>** and **A<sub>p</sub>**, respectively. The antibiotic-loaded polymer film **A<sub>t</sub>+A<sub>p</sub>+B** was then prepared (1:1 Ad:CD), which resulted in *P. aeruginosa* growth inhibition under static conditions for two days (as confirmed by confocal microscopy images and CFUs counts). The rate of release of the antibiotics from the polymer film **A<sub>t</sub>+A<sub>p</sub>+B** was studied indirectly under static conditions using MIC assays, ultimately demonstrating controlled release over a period of five hours. The ease with which the antibiotic-loaded polymer coating was fabricated, combined with its unique delamination-based antifouling mechanism under flow, suggests the self-assembled polymer coating platform reported here is an ideal candidate to mitigate bacterial growth on a range of biomedical device surfaces.

### 3.3 Results and Discussion

#### 3.3.1 Self-Assembled Polymer Film Design, Preparation, and Properties

The self-assembled polymer film was designed by cross-linking two separate PNB-based statistical copolymers through non-covalent host-guest interactions between Ad and  $\beta$ -CD. Specifically, copolymers **A** and **B** were synthesized using ring-opening metathesis polymerization (ROMP)<sup>26</sup> of functional Nb-based monomers (**Figure 3.2**). Copolymer **A** was designed to incorporate polar, dicationic viologen subunits that tether the Ad functional group to the polymerizable Nb group (**Nb-2V-Ad•4PF<sub>6</sub>**), while copolymer **B** was designed by linking the  $\beta$ -CD group to the Nb group with an ethylenediamine linker (**Nb-CD**). A tetraethylene glycol (TEG)-functionalized monomer (**Nb-TEG**) was polymerized together into each copolymer to promote the completion of the polymerization with bulky Ad or  $\beta$ -CD monomers, as well as increase the solubility of copolymers in polar solvents. An additional monomer functionalized with a zinc-based tetraphenylporphyrin (**Nb-TEG-ZnTPP**) was also added to copolymer **A** for the purpose of helping stabilize the self-assembled coating while also functioning as a dye to aid with visualizing the coating. The ratio of the different monomers in each copolymer was selected based on our

previous report,<sup>27</sup> which proved to be the most optimal in terms of polymerization efficiency, water solubility, and host-guest-based cross-linking between the two copolymers.

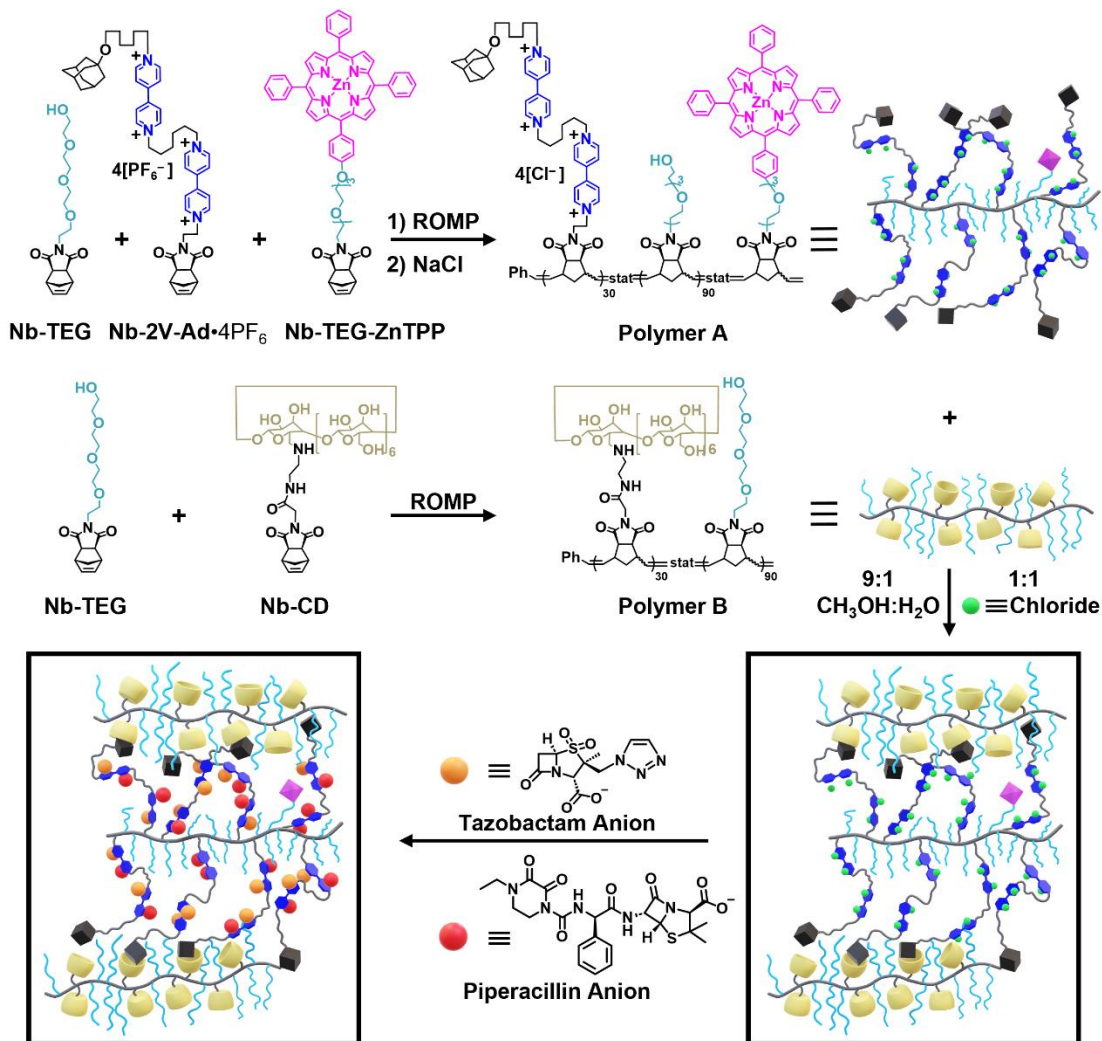


**Figure 3.2.** Ring-opening metathesis polymerization (ROMP) of norbornene-based functional monomers in DMF yielded a set of bottlebrush supramolecular copolymers **A** and **B** that, after dialysis, self-assembled 1:1 in a mixture of 90% MeOH and 10% H<sub>2</sub>O to afford a polymer coating, leading to a bactericidal polymer coating after counterion exchange with tazobactam and piperacillin anions.

Previously we reported<sup>27</sup> on the mechanism associated with the formation of viscous hydrogels prepared from copolymers **A** and **B** mixed in a 1:1 molar ratio in saltwater. The resultant hydrogel was confirmed to be cohesive and homogenous by SEM images, while exhibiting broad adhesive properties towards a variety of different surfaces. Here, rather than employing saltwater as the

solvent to afford the viscous hydrogels, copolymer **A** and **B** were dissolved in a 1:1 molar ratio in a combined solvent condition (90% CH<sub>3</sub>OH and 10% H<sub>2</sub>O). The choice of solvent in this instance better facilitated application to a glass slide using a pipette and a drop casting method to form the polymer film **A+B** after air drying (see Section 3.4.4, **Figure 3.8a**). A stability test of the polymer film **A+B** under static salt solutions (100 mM NaCl) was carried out over several days. Profilometry was used to determine the film thickness over several weeks. The results from this investigation confirmed that >90% of the polymer film remained after three weeks in static salt solutions and that the majority of the polymer film (≥79%) remained attached to the glass slide through 80 days (see Section 3.4.4, **Figure 3.8b** and **Table 3.1**). The effective stability of the **A+B** film in salt solutions suggested that the self-assembled copolymers could serve as an ideal antifouling coating, thus setting the stage for further biological studies of bacterial growth.

In addition to potentially functioning as an antifouling coating, a bactericidal polymer film was also successfully generated by loading negatively charged antibiotics into copolymer **A** through the ionic interactions with the positively charged viologen side chains (**Figure 3.2**). Copolymer **A** (with chloride ions as counter anions) was first converted to copolymers **A<sub>t</sub>** and **A<sub>p</sub>** by doing counteranion exchange with tazobactam and piperacillin anions, respectively. Proton nuclear magnetic resonance (<sup>1</sup>H NMR) revealed copolymer **A<sub>t</sub>** was approximately 60% loaded with tazobactam anions (see Section 3.4.3, **Figure 3.6**), while copolymer **A<sub>p</sub>** was approximately 45% loaded with piperacillin anions (see Section 3.4.3, **Figure 3.7**). The loading efficiency was comparable to our previous report of loading nalidixic acid anions into a cationic hydrogel also containing oligoviologens (~60% loaded).<sup>28</sup> We hypothesize the lack of complete loading of these two antibiotics into copolymer **A** was likely due to the larger size of either tazobactam or piperacillin anion compared to the original chloride ion, which led to some steric effects inside the copolymer chains. Moreover, this partial loading for both copolymers **A<sub>t</sub>** and **A<sub>p</sub>** was consistent with their relatively low solubilities as copolymer **A** was converted into the bactericidal polymer

film  $A_t+A_p+B$  (1:1:2 molar ratio of  $A_t:A_p:B$ ). SEM images for the  $A+B$  copolymer film (see Section 3.4.4, **Figure 3.9**) exhibited a smooth surface. However, small circles were observed on top of the surface for antibiotic-loaded polymer film  $A_t+A_p+B$  (see Section 3.4.4, **Figure 3.10**), which again, indicated that the larger size of the antibiotic anions (either tazobactam or piperacillin) decreased the solubility of the copolymers and thus led to incomplete loading of the antibiotics. Nevertheless, an adequate amount of antibiotics was loaded into the  $A_t+A_p+B$ , polymer film, effectively serving as a bactericidal coating suitable for further biological studies of bacterial growth.

### 3.3.2 Flow Cell Experiments

Based on the stability of the polymer film ( $A+B$ ) in saline solutions for several days under static conditions, the polymer film has the potential to serve as a physical barrier against bacteria growth. To test the effectiveness of the polymer film ( $A+B$ ) at preventing biofilm formation on a surface, we cultured biofilms in microfluidic devices called flow cells, which simulate an active flow environment similar to the environment in which a medical device may be placed. As shown in the schematic in **Figure 3.11** (see Section 3.4.5), for the flow cell growth setup, sterilized media is pumped at a constant rate through tubing, intercepted by a bubble trap, to the inlet port of a flow cell, and then waste passes through the outlet port. Bacteria are inoculated directly into the flow cell, where they attach to the glass coverslip and grow. The live biofilm can then be imaged using an inverted confocal microscope. First, to assess the potential autofluorescence of the polymer film, the flow cell was imaged without inoculation of bacteria. The polymer film ( $A+B$ ) exhibited autofluorescence across wavelengths. We predicted that the autofluorescence may be due to the porphyrin unit that is incorporated in the polymer film. However, autofluorescence was observed as well when a polymer film lacking the porphyrin unit ( $A_0+B$ ) was used to coat a coverslip (see Section 3.4.5, **Figure 3.12**). This result supports that another component of the film is resulting in autofluorescence.

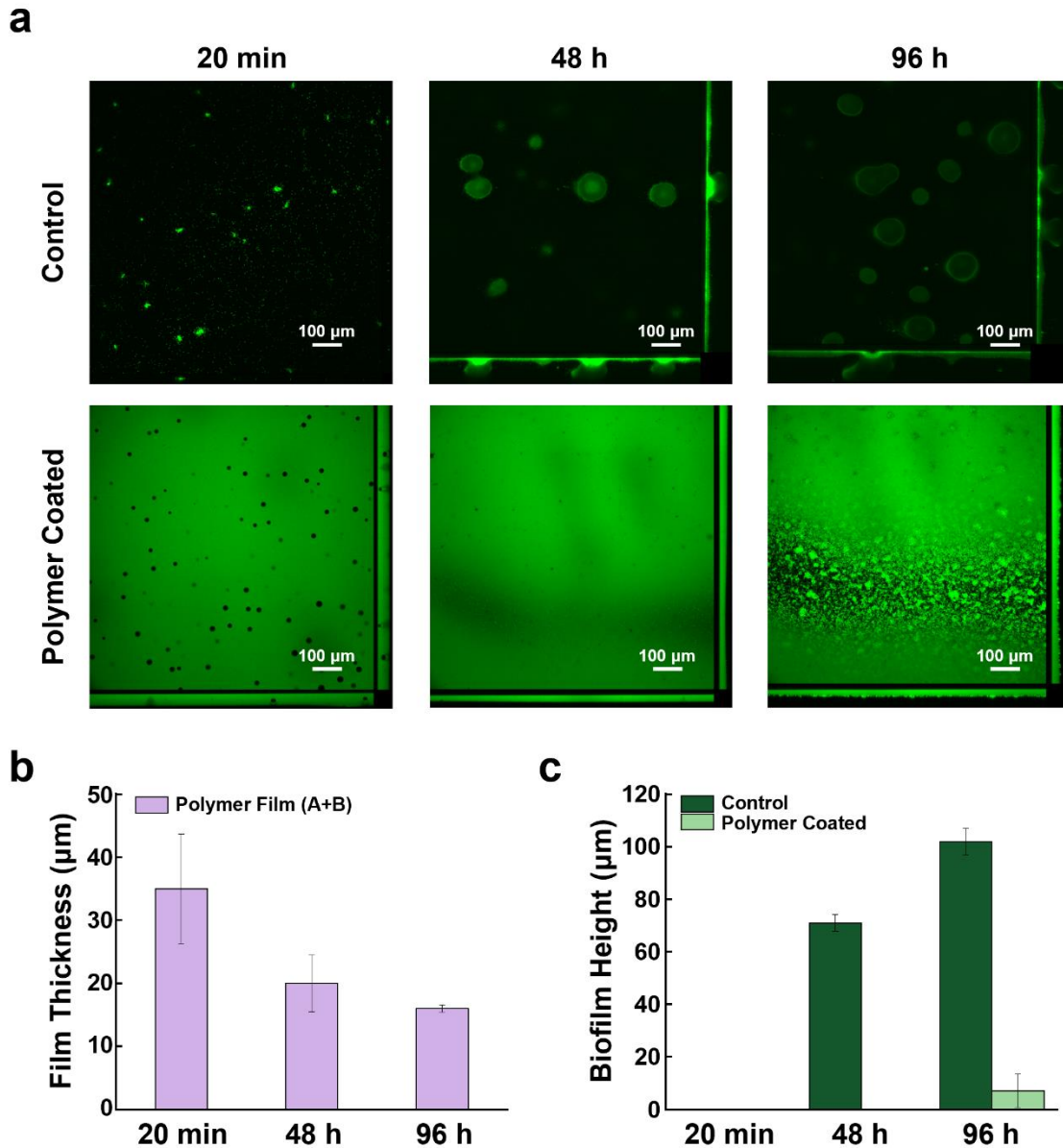


**Figure 3.3.** Flow cell biofilm experiments. (a) Representative confocal microscopy images of one replicate at 20 min, 48 h, and 96 h for control (no polymer) and polymer coated (**A+B**) experiments. The scale bar indicates 100  $\mu\text{m}$ . (b) Thickness of polymer film (**A+B**) on glass coverslip at 20 min, 48 h, and 96 h. (c) Biofilm height on glass coverslip for control and polymer coated (**A+B**).

Flow cells in which the coverslips were coated with polymer (**A+B**) (i.e., experimental group) and flow cells without the polymer coating (i.e., control group) were inoculated with a biofilm-overproducing *P. aeruginosa* strain that was engineered to constitutively express the fluorescent protein GFP, PAO1  $\Delta\text{wspF}$  Tn7 Gm::P(A1/04/03)::GFP. Growth medium for the flow cell experiments was supplemented with 50 mM NaCl to ensure integrity of the polymer. Confocal

microscopy images of the flow cells were collected at 20 min, 48 h, and 96 h after inoculation. As shown in **Figure 3.3a**, at 20 min, individual bacteria and small bacterial aggregates were attached to the flow cell coverslip without the polymer coating. However, for the case in which the coverslip was coated with polymer (**A+B**), at 20 min post-inoculation, it was unclear whether bacteria had attached due to the autofluorescence of the polymer. To overcome the issue of autofluorescence, the overall thickness of the polymer film + biofilm was monitored at subsequent timepoints. At 48 h post-inoculation, the flow cell without the polymer coating contained distinct biofilm aggregates with an average biofilm height of  $71 \pm 3.2 \mu\text{m}$  (three biological replicates, with three fields of view per replicate, **Figure 3.3c**). In contrast, distinct biofilm aggregates were not observed for flow cells in which the coverslip was coated with polymer (**A+B**), and only a thin layer of bacteria was observed on top of the polymer layer. Additionally, the polymer decreased in thickness from  $35 \pm 8.7 \mu\text{m}$  at 20 min post-inoculation to  $20 \pm 4.5 \mu\text{m}$  at 48 h post-inoculation (**Figure 3.3b**). By 96 h post-inoculation, biofilm aggregates with an average height of  $102 \pm 5 \mu\text{m}$  were observed in the flow cells with uncoated coverslips, and only small aggregates ( $7 \pm 6.4 \mu\text{m}$  tall) were observed in the flow cells with polymer-coated coverslips (**Figure 3.3c**). Additionally, by this time point, the polymer film thickness decreased to  $16 \pm 0.6 \mu\text{m}$  (**Figure 3.3b**). Overall, it was observed that the polymer film (**A+B**) inhibited large biofilm aggregates from forming, supporting that the polymer film (**A+B**) can serve as an antifouling coating under flow conditions (**Figure 3.1**). One possible mechanism contributing to the anti-biofouling properties of the film (**A+B**) is through delamination of the polymer film, which is supported by the decreasing thickness of polymer film over the course of the experiment (**Figure 3.3b**). Specifically, any bacteria that attach to the top of the polymer film will be removed with the delamination of the polymer film under the active flow system.

### 3.3.3 Static Growth Experiments

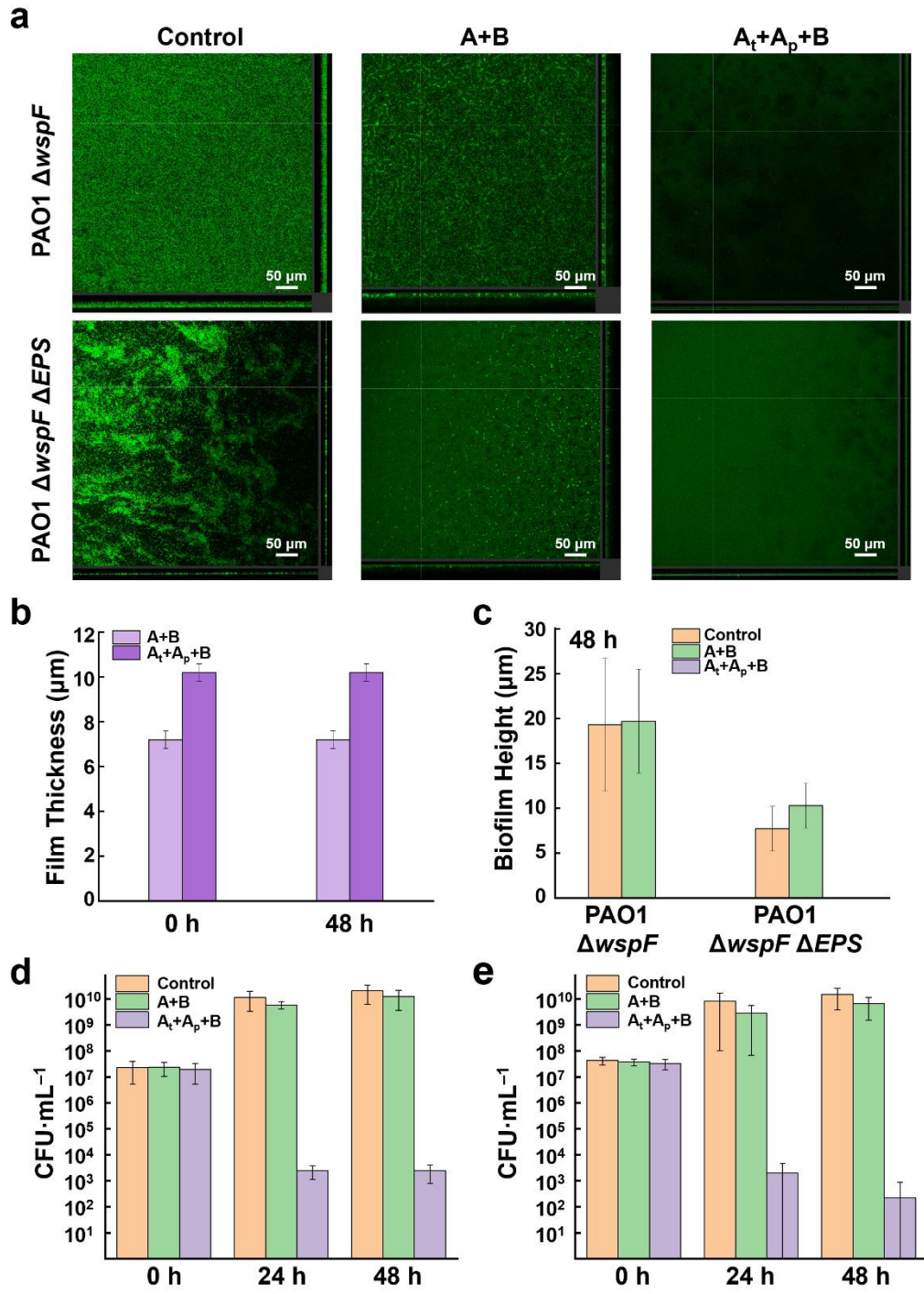


**Figure 3.4.** Static growth experiments. (a) Confocal microscopy images show biofilm formation of one replicate for no polymer film, polymer film (**A+B**) and antibiotic-loaded polymer film (**A<sub>t</sub>+A<sub>p</sub>+B**) at 48 h. The scale bar indicates 50  $\mu\text{m}$ . (b) Thickness of polymer film (**A+B**) and antibiotic-loaded polymer film (**A<sub>t</sub>+A<sub>p</sub>+B**) at 0 h and 48 h. (c) Biofilm formation at 48 h for no polymer film, polymer film (**A+B**) and antibiotic-loaded polymer film (**A<sub>t</sub>+A<sub>p</sub>+B**). CFUs of three biological replicates at 0 h, 24 h and 48 h for no polymer film, polymer film (**A+B**) and antibiotic-loaded polymer film (**A<sub>t</sub>+A<sub>p</sub>+B**) with PAO1  $\Delta wspF$  Tn7 Gm::P(A1/04/03)::GFP (indicated as “PAO1  $\Delta wspF$ ”) (d) and PAO1  $\Delta wspF \Delta pelF \Delta psi \Delta algD$  Tn7 Gm::P(A1/04/03)::GFP (indicated as “PAO1  $\Delta wspF \Delta EPS$ ”) (e).

Next, it was evaluated if the polymer film (**A+B**) exhibited similar anti-biofouling abilities under static growth conditions (i.e., no flow conditions). To do so, biofilm formation in 8-chambered glass slides was assessed, with the bottom of the chambers uncoated, coated with polymer (**A+B**), or coated with polymer that was loaded with the anionic, anti-*Pseudomonas* antibiotics, tazobactam and piperacillin (**A<sub>t</sub>+A<sub>p</sub>+B**). Before inoculating the 8-chambered glass slides with bacteria, the polymer films were imaged by confocal microscopy to determine the initial film thickness (**Figure 3.4 d**, see Section 3.4.5 for **Table 3.5-3.6**). As shown in **Figure 3.4d**, the thickness of the polymer film (**A+B**) was  $7.2 \pm 0.4 \mu\text{m}$ , and the polymer film loaded with antibiotics (**A<sub>t</sub>+A<sub>p</sub>+B**) was slightly thicker at  $10.2 \pm 0.4 \mu\text{m}$ . That the film formed by polymer (**A<sub>t</sub>+A<sub>p</sub>+B**) was thicker than that formed by polymer (**A+B**) is likely due to the larger size of the tazobactam and piperacillin anions relative to chloride. Both polymer coatings were observed to be uniformly distributed on the bottoms of the 8-chambered glass slides. Next, the 8-chambered glass slides were inoculated with the biofilm overproducing strain, PAO1  $\Delta wspF$  Tn7 Gm::P(A1/04/03)::GFP, or the isogenic, non-EPS-producing strain, PAO1  $\Delta wspF \Delta pelF \Delta psi \Delta algD$  Tn7 Gm::P(A1/04/03)::GFP, which serves as a negative control for biofilm formation. Bacteria were statically cultured for 48 h, without replenishing of media or removal of waste. Then, the non-adherent biomass and spent media were washed out before imaging the adherent biomass by confocal microscopy.

Biofilms with an average thickness of  $19.3 \pm 7.4 \mu\text{m}$  formed on the uncoated chambers that were inoculated with the biofilm overproducing strain, PAO1  $\Delta wspF$  Tn7 Gm::P(A1/04/03)::GFP (**Figure 3.4a, 3.4c**). This strain also formed biofilms in chambers that were coated with polymer film (**A+B**), with these biofilms having an average thickness of  $19.3 \pm 5.8 \mu\text{m}$  (obtained by

subtracting the initial thickness of the polymer from the total thickness observed at 48 h). In contrast, the polymer film loaded with antibiotics ( $A_t+A_p+B$ ) resulted in complete prevention of biofilm formation (i.e., no increase in thickness from the initial polymer thickness was observed). The thickness of both polymer films remained constant over the course of the 48-h experiment, and no delamination was observed under the static conditions (**Figure 3.4b**). This result matched findings from a separate experiment monitoring polymer film degradation (see Section 3.4.5, **Figure 3.8b**). As expected, the non-EPS producing strain, PAO1  $\Delta wspF \Delta pelF \Delta psl \Delta algD$  Tn7 Gm::P(A1/04/03)::GFP, formed minimal adherent biomass in both uncoated chambers ( $7.7 \pm 2.5 \mu\text{m}$ ) and in chambers coated with polymer film ( $A+B$ ) ( $10.3 \pm 2.5 \mu\text{m}$ ) (**Figure 3.4a, 3.4c**). Again, the polymer film loaded with antibiotics ( $A_t+A_p+B$ ) resulted in complete prevention any bacterial attachment.

Overall, the polymer film ( $A+B$ ) was not sufficient to prevent biofilm formation under static conditions. Instead, it appears that the polymer film ( $A+B$ ) may provide a surface for bacteria to attach and form biofilms. One possible explanation for this result is that copolymer **B** contains large amounts of  $\beta$ -CD, which is a sugar that *P. aeruginosa* could use as energy. To test this hypothesis, a similar experiment was set up in the 8-chambered slides, but instead of TSB media, sterile PBS buffer was used, which provides no carbon source for *P. aeruginosa*. Typically, *P. aeruginosa* cannot grow in PBS, but if the copolymer **B** acts as a carbon source, then we would expect to observe *P. aeruginosa* growth. By assessing bacterial growth by confocal microscopy and determining CFUs, it was clear that there was no bacterial growth in PBS alone, leading us to reject this hypothesis that copolymer B is serving as a carbon source (see Section 3.4.5, **Figure 3.19**). Another hypothesis to explain biofilm formation on the polymer film is that since the polymer film ( $A+B$ ) forms through dynamic host-guest interactions, swelling in the buffer might allow the dynamic bonds to move, providing some space for the bacteria to interact with the polymer film

(**A+B**) under static conditions. Similar findings previously were reported for bacterial attachment to another polymer (Herzberg and co-workers<sup>29</sup>).

However, the polymer film loaded with antibiotics (**A<sub>t</sub>+A<sub>p</sub>+B**) provided full protection. We predicted that this protection was due to release of the antibiotics from the polymer film to the growth medium in the chamber. To test this, colony-forming units (CFUs) in the liquid of each chamber were determined at 0, 24, and 48 h post-inoculation, providing a measure of the viable number of bacteria (**Figure 3.4d-e**). At 0 h post-inoculation, CFU values were approximately the same regardless of whether the chamber was coated or not, indicating that the same concentration of bacteria was added to each well. CFUs increased over time for liquid collected from both uncoated chambers and chambers coated with the polymer film (**A+B**). In contrast, for liquid collected from the chambers coated with the polymer film loaded with antibiotics (**A<sub>t</sub>+A<sub>p</sub>+B**), there was a significant drop in CFUs by 24 h post-inoculation, with CFUs plateauing to the 48 h timepoint. This plateau suggested that after 24 h, there was no more antibiotics released from the polymer film. To test this, additional experiments were performed to determine the release rate of the antibiotics.

### 3.3.4 Antibiotic Release Experiments

To better understand the release rate of the antibiotics from the static growth experiments, a Minimum Inhibitory Concentration (MIC) assay was performed. To do this, TSB media was added to 8-chambered slides, with the bottoms coated with polymer film loaded with antibiotics (**A<sub>t</sub>+A<sub>p</sub>+B**). Note that for this experiment, the slides were *not* inoculated with bacteria. At select time points, aliquots were collected by removing the entire media solution within a chamber and replacing it with fresh media. Then, these aliquots were added to a 96-well plate, inoculated with bacteria, and bacterial growth was assessed over 20 h by monitoring OD 600 nm. The negative control was TSB media without bacteria, and the positive control was TSB media with bacteria.

Only the PAO1  $\Delta wspF \Delta pelF \Delta psi \Delta algD$  Tn7 Gm::P(A1/04/03)::GFP strain was used to reduce aggregates from forming which would cause OD 600 nm values to be skewed.

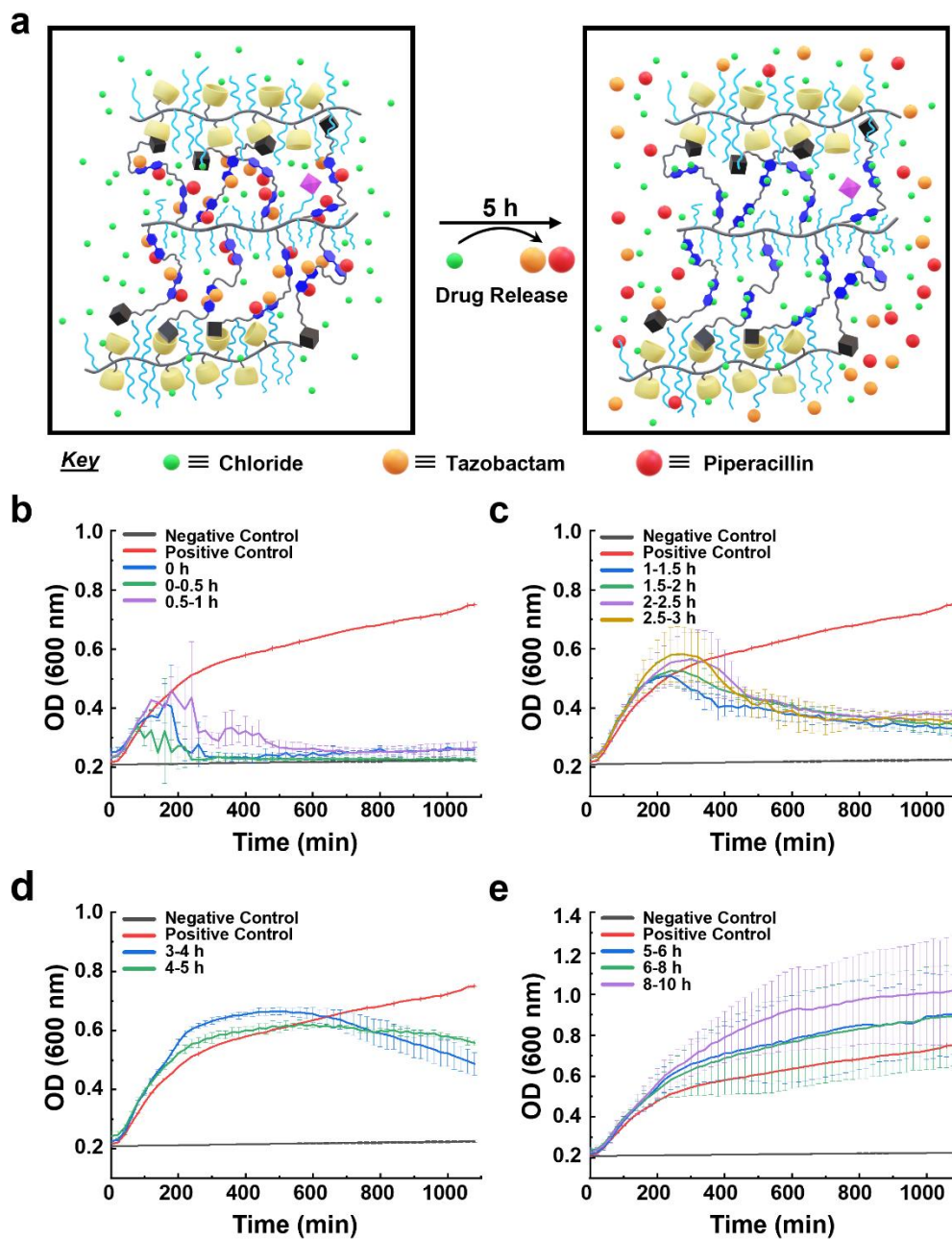


**Figure 3.5.** MIC assay experiments. (a) Graphical representation for the release of antibiotics via counteranion exchange for antibiotic-loaded polymer film ( $A_t+A_p+B$ ). (b-e) MIC assay results of aliquots collected at different time points from the solution with antibiotic-loaded polymer film ( $A_t+A_p+B$ ).

In the first run of this experiment, it was noted that most of the antibiotics were released between 0 and 4 h (see Section 3.4.5, **Figure 3.19a**). Subsequently, more time intervals were added within the first 4 h of the total 48 h of the experiment to determine the specific time range that the antibiotics were released (**Figures 3.5b-e**, see Section 3.4.5 for **3.20b**). The negative and positive controls were as expected, where the wells without bacteria showed no change in OD 600 nm, and the wells with TSB media and bacteria continuously grew throughout the 18 hours.

Bacterial growth was inhibited in the initial aliquot that was collected at 0 h, immediately after adding media, as well as in the aliquots collected from 0-0.5 h and 0.5-1 h (**Figure 3.5b**). This result suggests that the tazobactam and piperacillin anions were readily released upon media contact, which is consistent with the SEM image showing that these anions are present on the top layer of the polymer film (see Section 3.4.4, **Figure 3.10**). Bacterial growth was inhibited, albeit to a lesser degree, in aliquots collected from 1-1.5 h, 1.5-2 h, 2-2.5, and 2.5-3 h as illustrated in **Figure 3.5c**. By 3h, there was only minimal inhibition of growth, and no inhibition by 5 h (**Figure 3.5d**). These results support that antibiotic release from the polymer was rapid, and with media exchanges, occurred within the first 5 h.

## 3.4 Materials and Methods

### 3.4.1 Experimental Methods

All reagents were purchased from commercial suppliers and used without further purification unless stated otherwise. All reactions were performed under nitrogen (N<sub>2</sub>) or argon (Ar) gas unless otherwise stated. Column chromatography was carried out with silica gel (Sorbtech, 0.040–0.063 mm). Polymerization of all polymers was performed under an inert atmosphere of UHP N<sub>2</sub> in a glovebox using a modified Grubbs' 3<sup>rd</sup> generation catalyst that was prepared according to a previous reported protocol.<sup>30</sup> All nuclear magnetic resonance (NMR) spectra were recorded on Varian Inova-500 spectrometer at 25 °C, with working frequencies of 500 (<sup>1</sup>H) and 125 (<sup>13</sup>C) MHz.

Chemical shifts are reported in ppm relative to the signals corresponding to the residual non-deuterated solvents:  $\text{CDCl}_3$ :  $\delta_H = 7.26$  ppm and  $\delta_C = 77.16$  ppm;  $(\text{CD}_3)_2\text{SO}$ :  $\delta_H = 2.50$  ppm and  $\delta_C = 39.52$  ppm;  $\text{CD}_2\text{Cl}_2$ :  $\delta_H = 5.32$  ppm and  $\delta_C = 53.84$  ppm;  $\text{D}_2\text{O}$ :  $\delta_H = 4.79$  ppm;  $\text{CD}_3\text{OD}$ :  $\delta_H = 3.31$  ppm and  $\delta_C = 49.00$  ppm. High-resolution mass spectrometry (HRMS) data was recorded on a Bruker maXis 4G UHR-TOF mass spectrometer. Matrix assisted laser desorption/ionization time-of-flight mass spectrometry (MALDI-TOF-MS) was recorded on a Bruker Solaris 12T FT-MS, samples were prepared using 2,5-dihydroxybenzoic or  $\alpha$ -cyano-4-hydroxycinnamic acid matrices. Size exclusion chromatography (SEC) analyses were performed on an Agilent 1260 Infinity setup with three PSS NOVEMA MAX Lux analytical  $100 \text{ \AA}$  columns in tandem and  $0.025 \text{ M Na}_2\text{SO}_4$  in  $\text{H}_2\text{O}$  mobile phase run at  $23 \text{ }^\circ\text{C}$  with  $1.0 \text{ mL}\cdot\text{min}^{-1}$  flow rate. The differential refractive index (dRI) of each compound was monitored using a Wyatt Optilab T-rEX detector and the light scattering (LS) of each compound was monitored using Wyatt Dawn Heleos-II detector. The polymer films were all prepared by drop casting and the thickness of the films was determined by depositing the films on the center of a glass slide, leaving a border of glass on each side, followed by obtaining topographical data from a KLA-Tencor Alpha-Step D-100 Profilometer. Scanning electron microscopy (SEM) was conducted using a Thermofisher Quattro S ESEM apparatus with a high-stability Schottky field emission gun electron source providing electron resolution of  $0.7 \text{ nm}$  at  $30 \text{ keV}$ ,  $1.4 \text{ nm}$  at  $1 \text{ keV}$ .

For flow cell experiments, an upright confocal laser scanning microscope was used. Imaging was conducted using a Nikon AX Upright Laser Scanning Confocal Microscope. This microscope is equipped with a motorized stage and controlled by the Nis Element software. There is a custom stage made to allow for flow cells to be imaged. The microscope is equipped with a CFI Plan Apochromat Lambda 20x dry (NA 0.80) and a 40x oil immersion (NA 1.25). It contains 4 lasers that run from  $405 \text{ nm}$  to  $640 \text{ nm}$ . The scan head is a Nikon AX is a  $25 \text{ mm}$  FOV Galvano scanner

that supports bidirectional and line scan imaging. The microscope is stationed on a TMC vibrational control CleanBench laboratory table.

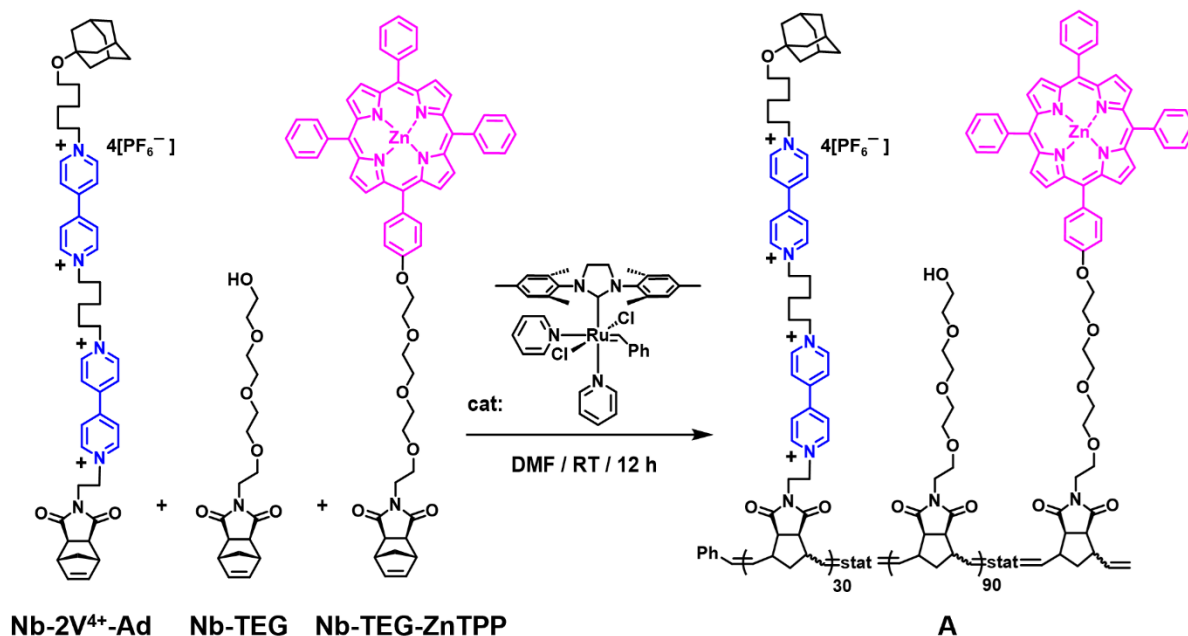
For static growth experiments, an inverted confocal laser scanning microscope was used. Imaging was conducted using a Leica SP8 Lightning Single Photon Laser Scanning Confocal Microscope. This microscope is equipped with a motorized stage and controlled by the Las X software. There are three piezo-driven adaptor plates that allow for multi-well plates to be imaged. The microscope is equipped with a HC PL APO CS2 10x dry (NA 0.40), 20x multi-immersion (NA 0.75), 40x oil immersion (NA 1.30), and 63x oil immersion (NA 1.40) objectives. It contains 5 lasers that run from 405 nm to 638 nm. Illumination is provided by a Broadband EL6000 mercury halide light source with 3 filter sets for DAPI, FITC, and Rhodamine. The scan head is a SP8 LIAchroics Compact RGB Tandem scanner (8000 Hz resonant scanner + 10-1800 Hz galvanometric scanner).

For the MIC assays, a 96-well plate reader was used. OD 600 nm measurements were taken by a ThermoFisher Scientific Varioskan LUX multimode microplate reader. There is an adaptor fitted for inserting 96 well plates into the machine. Incubation temperature of the machine can be set at a range of 0°C to 45°C. The microplate reader can be set to shake at light, moderate, heavy force modes to provide 0 to 1200 rpms. A Xenon flash lamp light source is used in connection to a Photomultiplier Tube (PMT) detector capable of reading OD measurements from 200 nm to 1000 nm. The microplate reader is connected to a PC Thermo Scientific SkanIt Software for data collection.

### 3.4.2 Synthetic Methods

The synthetic procedures of all the monomers used in this chapter (**Nb-2V<sup>4+</sup>-Ad**, **Nb-CD**, **Nb-TEG**, and **Nb-TEG-ZnTPP**) to make polymers can be found in Chapter 2. Statistical copolymers **A<sub>0</sub>**, **A**, and **B** are also reported in Chapter 2 but have a different letter abbreviation in this Chapter.

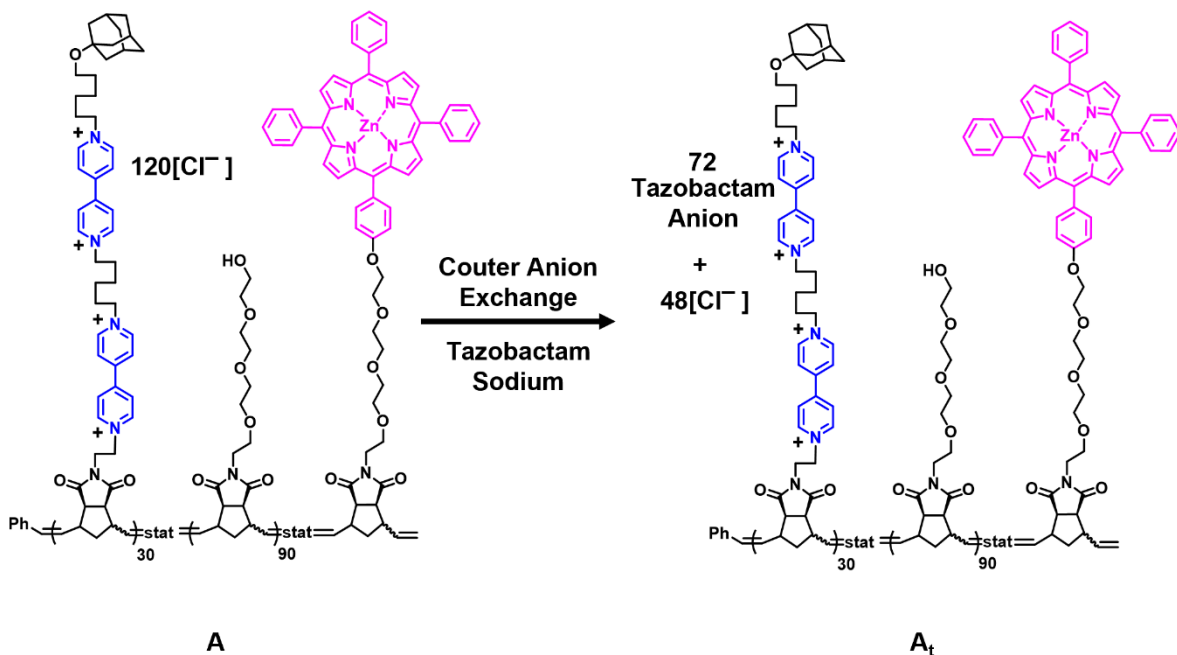




**Scheme 3.2.** Synthesis of statistical copolymer **A**: poly(2V<sup>4+</sup>Ad<sub>30</sub>-TEG<sub>90</sub>-ZnTPP)<sub>stat</sub>•120Cl.

A solution of modified G3 was freshly prepared in DMF. G3 (0.0595 mL, 0.86 mg, 1.19 μmol, 1 equiv.) was added to a solution of **Nb-2V<sup>4+</sup>-Ad** (50.1 mg, 35.7 μmol, 30 equiv.), **Nb-TEG** (36.4 mg, 107.2 μmol, 90 equiv.), and **Nb-TEG-ZnTPP** (1.21 mg, 1.19 μmol, 1 equiv.) in 1.370 mL DMF to give G3: **Nb-2V<sup>4+</sup>-Ad** ratio of 1:30 and a 0.025 M concentration of **Nb-2V<sup>4+</sup>-Ad**. The resulting solution was stirred for 12 h at room temperature. After the polymerization went to completion, the reaction was quenched by addition of EVE. Then, the reaction mixture was transferred to dialysis tubing (RC dialysis tubing, 1 kDa molecular weight cut-off, 38 mm flat-width) and was placed in a beaker with 500 mL H<sub>2</sub>O to remove the excess EVE and DMF. The dialysis continued for 12 h with H<sub>2</sub>O and was then switched to 500 mL saturated NaCl solution to do counter anion exchange from PF<sub>6</sub><sup>-</sup> to Cl<sup>-</sup> for 6 h. Then, the solution in the beaker was switched back to 500 mL H<sub>2</sub>O, followed by changing the H<sub>2</sub>O every 12 h for a total of two more times. After dialysis, copolymer **A** was lyophilized for 24 h to yield a purple solid (62.7 mg, 87% yield).

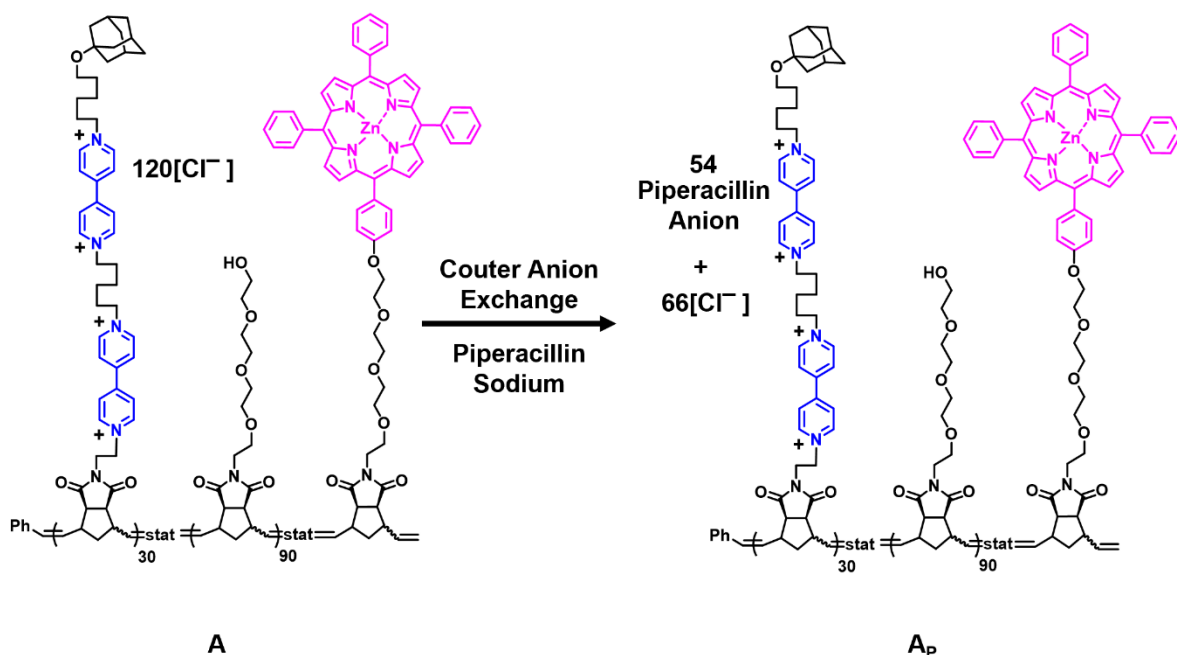
**Synthesis of Statistical Copolymer A<sub>t</sub>: poly(2V<sup>4+</sup>Ad<sub>30</sub>-TEG<sub>90</sub>-ZnTPP)<sub>stat</sub>•72Tazobactam•48Cl**



**Scheme 3.3.** Synthesis of statistical copolymer **A<sub>t</sub>**: **poly(2V<sup>4+</sup>Ad<sub>30</sub>-TEG<sub>90</sub>-ZnTPP)<sub>stat</sub>•72Tazobactam•48Cl**.

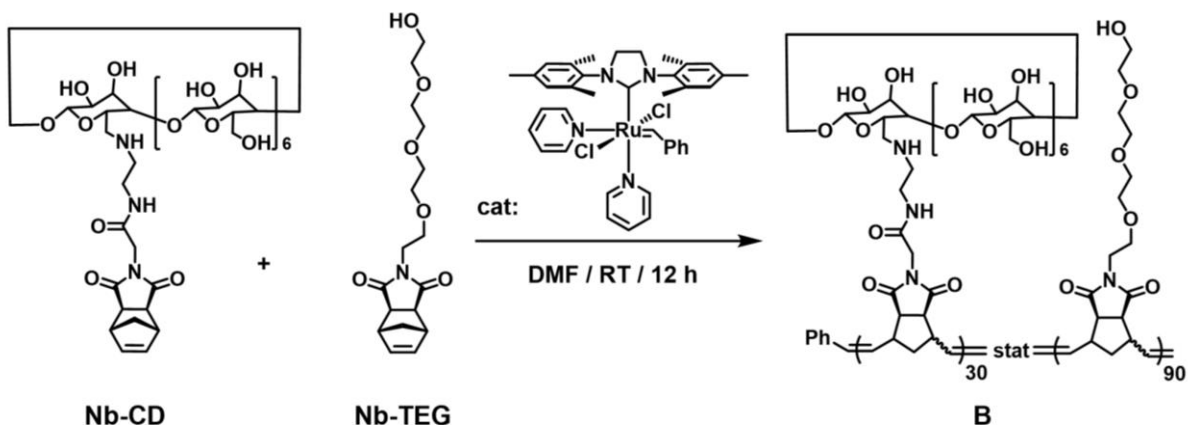
Copolymer **A** (27.7 mg, 0.0137 mmol, 1 equiv.) was dissolved in 2 mL H<sub>2</sub>O, then tazobactam sodium (106 mg, 0.33 mmol, 24 equiv.) dissolved in 5 mL H<sub>2</sub>O was added to the copolymer **A** solution to do counter anion exchange. The combined solution was then transferred to dialysis tubing (RC dialysis tubing, 1 kDa molecular weight cut-off, 38 mm flat-width), and was placed in a beaker with 500 mL H<sub>2</sub>O to remove the excess tazobactam sodium. The dialysis continued for 48 h and the H<sub>2</sub>O was changed every 12 h. After dialysis, copolymer **A<sub>t</sub>** was lyophilized for 24 h to yield a purple solid (33.9 mg, 78% yield). <sup>1</sup>H NMR confirmed that the counter anion exchange was about 60% with tazobactam for copolymer **A<sub>t</sub>** (**Figure 3.6**).

**Synthesis of Statistical Copolymer A<sub>p</sub>**: **poly(2V<sup>4+</sup>Ad<sub>30</sub>-TEG<sub>90</sub>-ZnTPP)<sub>stat</sub>•54Piperacillin•66Cl**



**Scheme 3.4.** Synthesis of statistical copolymer **A<sub>p</sub>**: **poly(2V<sup>4+</sup>Ad<sub>30</sub>-TEG<sub>90</sub>-ZnTPP)<sub>stat</sub>•54Piperacillin•66Cl**. Copolymer **A** (27.7 mg, 0.0137 mmol, 1 equiv.) was dissolved in 2 mL H<sub>2</sub>O, then piperacillin sodium (178 mg, 0.33 mmol, 24 equiv.) dissolved in 5 mL H<sub>2</sub>O was added to the copolymer **A** solution to do counter anion exchange, resulting in a purple solid that precipitated from solution after adding excess piperacillin sodium. The mixture was centrifuged, and the excess solution was poured out. The remaining purple solid was then dissolved in 2 mL CH<sub>3</sub>OH and transferred to dialysis tubing (RC dialysis tubing, 1 kDa molecular weight cut-off, 38 mm flat-width), and was placed in a beaker with 500 mL H<sub>2</sub>O to remove the excess piperacillin sodium. The dialysis continued for 48 h and the H<sub>2</sub>O was changed every 12 h. After dialysis, copolymer **A<sub>p</sub>** was lyophilized for 24 h to yield a purple solid (36.2 mg, 65% yield). <sup>1</sup>H NMR confirmed that the counter anion exchange was about 45% with piperacillin for copolymer **A<sub>p</sub>** (**Figure 3.7**).

**Synthesis of Statistical Copolymer B: poly(CD<sub>30</sub>-TEG<sub>90</sub>)<sub>stat</sub>**



**Scheme 3.5.** Synthesis of statistical copolymer **B**: poly(CD<sub>30</sub>-TEG<sub>90</sub>)<sub>stat.</sub>

A solution of modified G3 was freshly prepared in DMF. G3 (0.0479 mL, 0.69 mg, 0.96  $\mu\text{mol}$ , 1 equiv.) was added to a solution of **Nb-CD** (39.7 mg, 28.8  $\mu\text{mol}$ , 30 equiv.) and **Nb-TEG** (29.3 mg, 86.3  $\mu\text{mol}$ , 90 equiv.) in 1.103 mL DMF to give G3: **Nb-CD** ratio of 1:30 (the concentration of **Nb-CD** in solution was 0.025 M). The resulting solution was stirred for 12 h at room temperature. After the polymerization went to completion, the reaction was quenched by addition of EVE. Then, the reaction mixture was transferred to dialysis tubing (RC dialysis tubing, 1 kDa molecular weight cut-off, 38 mm flat-width), and was placed in a beaker with 500 mL H<sub>2</sub>O to remove the excess EVE and DMF. The dialysis continued for 24 h and the H<sub>2</sub>O was changed every 12 h. After dialysis, copolymer **B** was lyophilized for 12 h to yield a pale-yellow solid (51.5 mg, 75% yield).

### 3.4.3 Spectroscopy Characterization

#### Nuclear Magnetic Resonance (<sup>1</sup>H NMR)

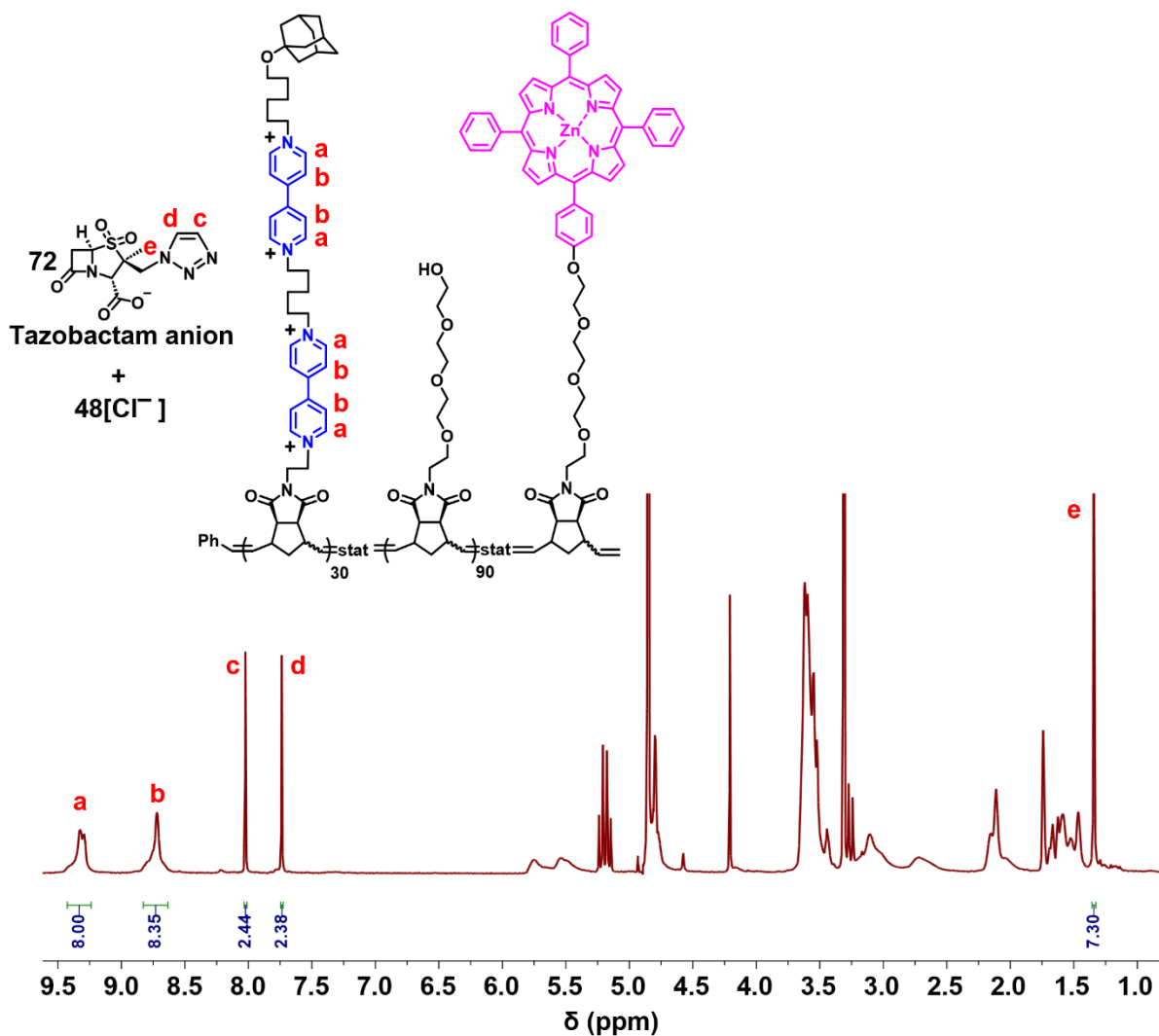


**Figure 3.6.**  $^1\text{H}$  NMR (500 MHz, 25 °C,  $\text{CD}_3\text{OD}$ ) spectrum of tazobactam loaded statistical copolymer **A<sub>t</sub>**. Each charged viologen side chain contained four positive charges and should bind to four tazobactam anions if fully loaded, when correlated with NMR integration, proton resonances a and b should be 8, and resonances c, d, e should be 4, 4, 12, respectively. By the integration shown above, copolymer **A<sub>t</sub>** is about 60% loaded with tazobactam anion.

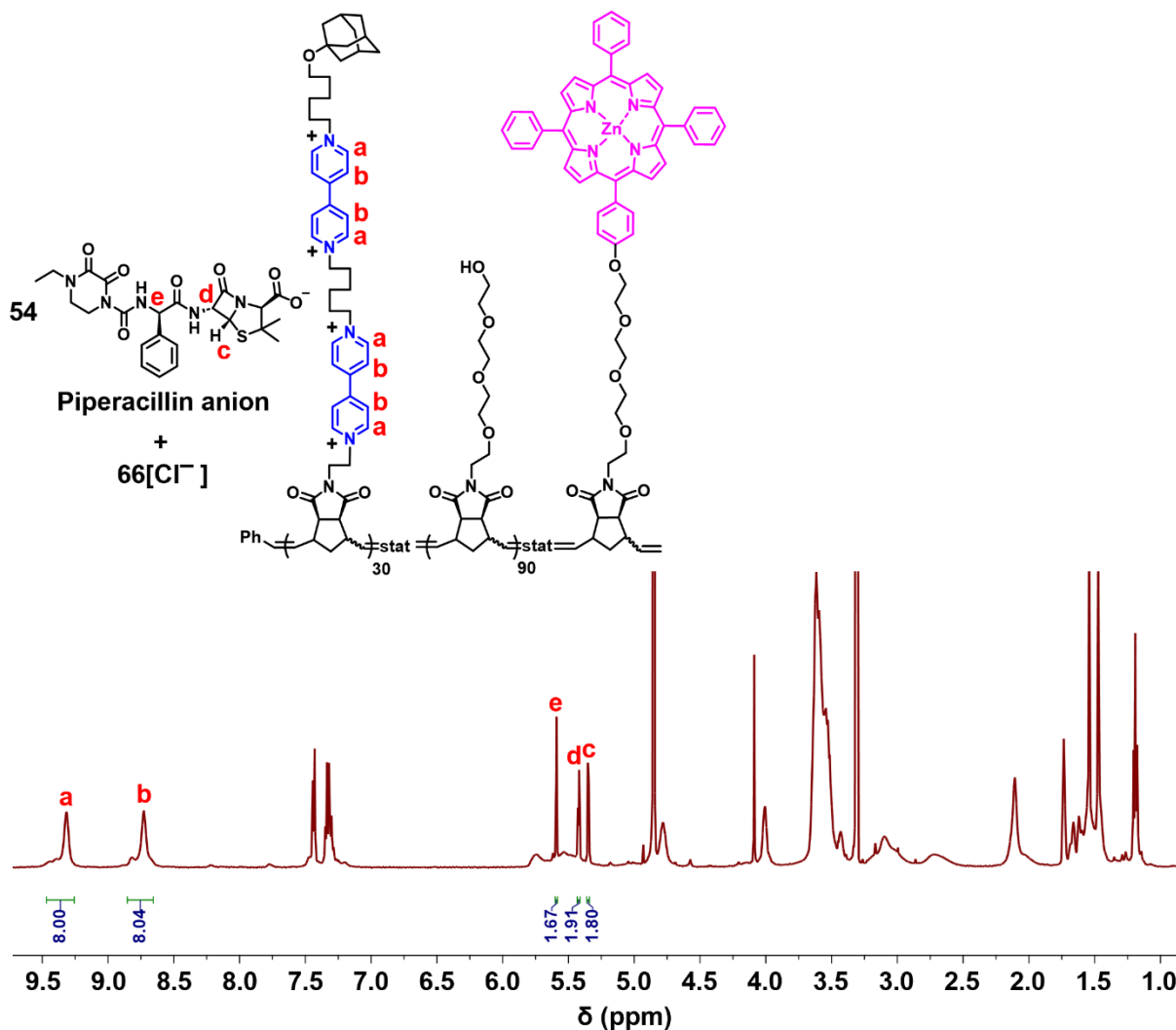


**Figure 3.7.**  $^1\text{H}$  NMR (500 MHz, 25 °C,  $\text{CD}_3\text{OD}$ ) spectrum of piperacillin loaded statistical copolymer **A<sub>p</sub>**. Each charged viologen side chain contained four positive charges and should bind to four piperacillin anions if fully loaded, when correlated with NMR integration, proton resonances a and b should be 8, and resonances c, d, e should be 4, 4, 4, respectively. By the integration shown above, copolymer **A<sub>p</sub>** is about 45% loaded with piperacillin anion.

### 3.4.4 Polymer Film Preparation and Evaluation of Properties

#### Profilometry

The guest copolymer **A** was dissolved in  $\text{CH}_3\text{OH}$ , and the host copolymer **B** was dissolved in a mixture of 80%  $\text{CH}_3\text{OH}$  and 20%  $\text{H}_2\text{O}$ . The solution of guest copolymer **A** was then added into the solution of host copolymer **B** (1:1 molar ratio of **A**:**B**) to form a mixture of **A**+**B** at a total concentration of  $50 \text{ mg}\cdot\text{mL}^{-1}$  in 90%  $\text{CH}_3\text{OH}$  and 10%  $\text{H}_2\text{O}$ . 150  $\mu\text{L}$  of the **A**+**B** solution was then

added to a glass slide by drop casting method and dried overnight before profilometry test (**Figure 3.8a**). The profilometry experiment was done on the middle part of the film with the direction of the arrow. This initial test was labeled as day 0. After this initial test, the glass slide with polymer film was submerged in 100 mM NaCl solution to continue testing over several days. The labeled days all include one day of drying before testing (e.g., day 4 represents three days in 100 mM NaCl solution and one day drying before being subjected to analysis by profilometry). Three replicates were done for this film degradation study and are summarized in **Table 3.1** and plotted in **Figure 3.8b**. The results showed that the polymer film was stable in the first week in static salt solutions and that the majority of the polymer film remained attached to the glass slide up to 80 days.

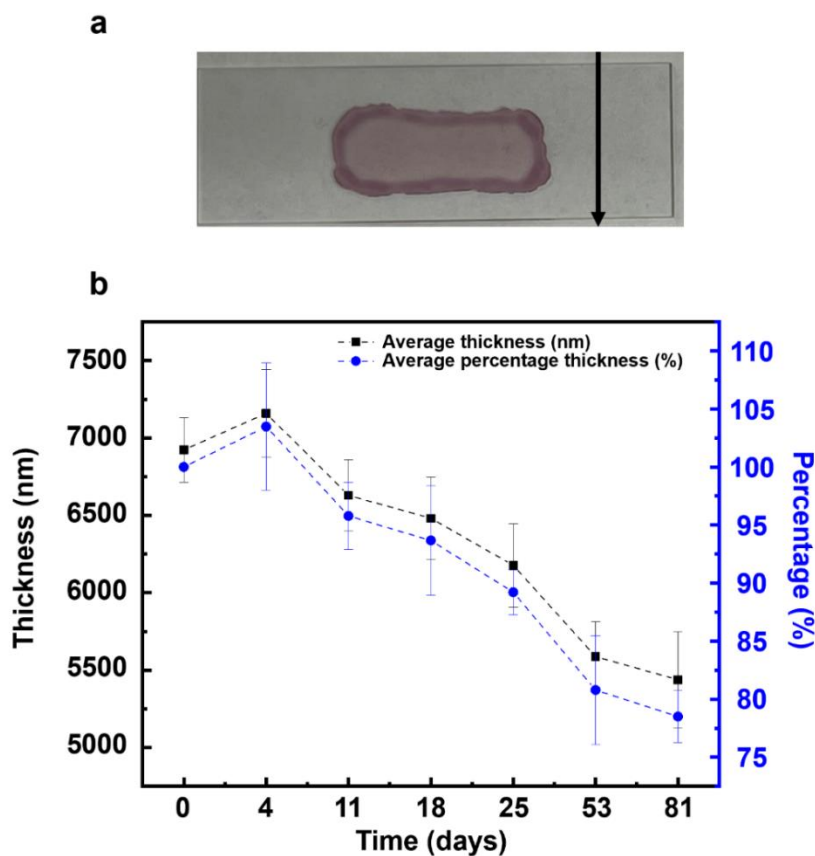


**Figure 3.8.** (a) Picture of polymer film on glass slide. (b) Summary of profilometry data for three replicates submerged in a salt solution (100 mM NaCl) over several days.

		<i>Thickness of film (nm)</i>					
<i>Replicates</i>	<b>Day 0</b>	<b>Day 4</b>	<b>Day 11</b>	<b>Day 18</b>	<b>Day 25</b>	<b>Day 53</b>	<b>Day 81</b>
<b>1</b>	7125	7313	6632	6667	6333	5667	5778
<b>2</b>	6706	7333	6400	6600	5867	5765	5167
<b>3</b>	6938	6833	6857	6176	6333	5333	5368
<b>average</b>	6923±210	7160±283	6629±229	6481±266	6177±269	5588±226	5438±311
		<i>Percentage of film (%)</i>					
<i>Replicates</i>	<b>Day 0</b>	<b>Day 4</b>	<b>Day 11</b>	<b>Day 18</b>	<b>Day 25</b>	<b>Day 53</b>	<b>Day 81</b>
<b>1</b>	100	103	93	94	89	80	81
<b>2</b>	100	109	95	98	87	86	77
<b>3</b>	100	98	99	89	91	77	77
<b>average</b>	100	103±5	96±3	94±5	89±2	81±5	79±2

**Table 3.1.** Summary of profilometry data for three replicates.

### Scanning Electron Microscopy (SEM) Imaging

Scanning electron microscopy (SEM) experiments were performed to see the differences in morphology between polymer film **A+B** and the antibiotics-loaded polymer film **A<sub>t</sub>+A<sub>p</sub>+B**. Two samples were prepared for SEM: 1) **A+B** (1:1 molar ratio of **A:B**) dissolved in 90% CH<sub>3</sub>OH and 10% H<sub>2</sub>O at 18.75 mg·mL<sup>-1</sup> was dropped onto clean gold wafer by pipette; 2) **A<sub>t</sub>+A<sub>p</sub>+B** (1:1:2 molar ratio of **A<sub>t</sub>:A<sub>p</sub>:B**) dissolved in 90% CH<sub>3</sub>OH and 10% H<sub>2</sub>O with the same molar amount of copolymer **B** as compared to **A+B** instead of the same concentration that was dropped onto a clean gold wafer by pipette. Both samples were air dried overnight, and the samples were then loaded into the SEM chamber. The sample chamber was evacuated using the HiVac setting, and images were recorded at 1000x, 5000x, 10000x, and 35000x magnification.

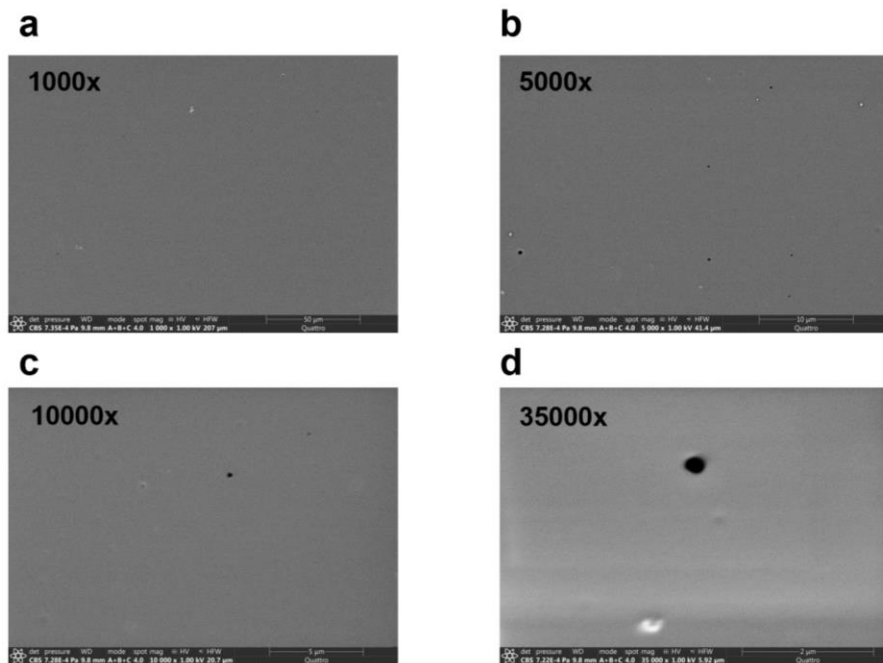


**Figure 3.9.** SEM images of **A+B** in 90% CH<sub>3</sub>OH and 10% H<sub>2</sub>O after being air dried overnight. (a) 1000x, (b) 5000x, (c) 10000x, and (d) 35000x.

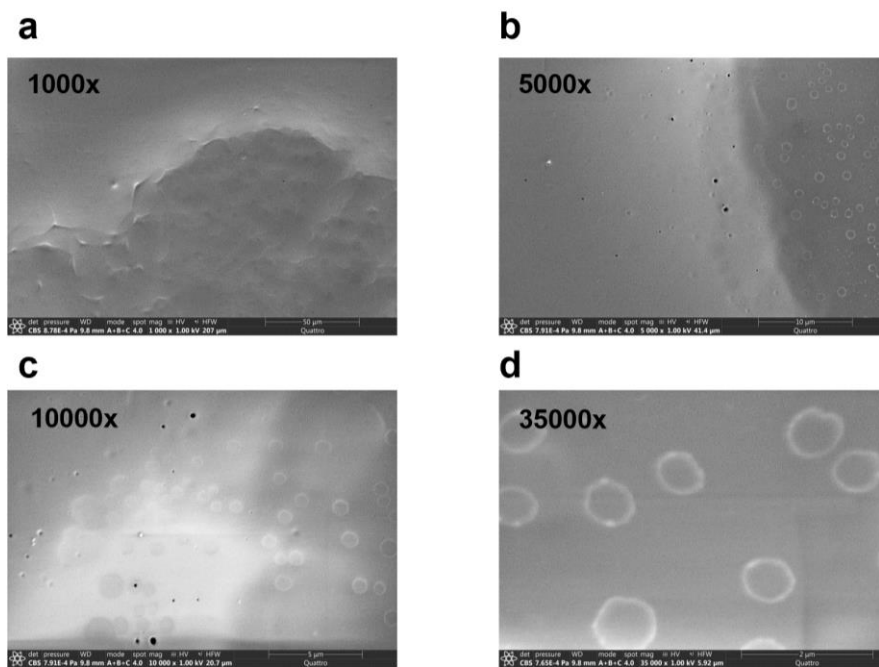


**Figure 3.10.** SEM images of **A<sub>t</sub>+A<sub>p</sub>+B** in 90% CH<sub>3</sub>OH and 10% H<sub>2</sub>O after being air dried overnight. (a) 1000x, (b) 5000x, (c) 10000x, and (d) 35000x.

### 3.4.5 Biological Experiments

#### Flow Cell Experiments

Polymer film (**A+B**) coated coverslips were prepared for flow cell experiments. The guest copolymer **A** was dissolved in CH<sub>3</sub>OH, and the host copolymer **B** was dissolved in a mixture of 80% CH<sub>3</sub>OH and 20% H<sub>2</sub>O. The solution of guest copolymer **A** was then added into the solution of host copolymer **B** (1:1 molar ratio of **A:B**) to form a mixture of **A+B** at a total concentration of 50 mg·mL<sup>-1</sup> in 90% CH<sub>3</sub>OH and 10% H<sub>2</sub>O. 150 μL of **A+B** solution was then added to each coverslip by drop casting method and dried overnight before flow cell experiments. Same preparation method of polymer film was used here as described for the profilometry experiments besides the glass coverslips were used instead of normal glass slides.

PAO1  $\Delta wspF$  Tn7 Gm::P(A1/04/03)::GFP was struck out onto Luria Broth (LB) agar plates from frozen glycerol stocks and incubated overnight at 37 °C. Tryptic Soy Broth (TSB) media was inoculated with a single colony and grown overnight with shaking at 37 °C. Overnight cultures were back-diluted 1/100 in TSB media and grown with shaking at 37 °C to mid-log phase. Mid-log cultures were then diluted in 1% TSB media supplemented with an additional 50 mM NaCl solution (i.e., 20 mL of 5 M NaCl were added to 2 L of media) to a final OD 600 nm of 0.01 in a 1 mL volume. Flow cells without coverslips were autoclaved, and then either glass coverslips without polymer coating (control) or polymer-coated glass coverslip was affixed to the flow cell using silicone sealant. The flow cells were inoculated with ~300 μL of back-diluted culture using a 1-mL syringe and incubated invertedly at 25 °C for 10 minutes. The flow cell was connected, and the initial rate was set at 40 mL·h<sup>-1</sup> for 20 minutes. After 20 minutes, the flow rate was reduced to 10 mL·h<sup>-1</sup> and imaged using an upright Nikon confocal laser scanning microscope. The 20x magnification objective was used with an excitation of 488 nm and an emission of 508 nm. After imaging, the flow cell was incubated in a dark room at 25 °C. On days 2 and 4, the flow cells were

imaged again. On each day of imaging, three stills and three z-stack images were taken of the middle portion of the flow cells.

The green fluorescence background of images for glass coverslips with polymer coating was first confirmed to not be due to the porphyrin component of copolymer **A** as illustrated in **Figure 3.12**, where polymer film **A<sub>0</sub>+B** (no porphyrin included) was imaged, and green fluorescence background was also observed.

Three replicates were performed for flow cell experiments using either glass coverslips without polymer coating (control) or polymer-coated glass coverslips. One representative z-stack image was chosen for each replicate and the images were shown in **Figure 3.13** and **Figure 3.14** for experiments using glass coverslips without and with polymer coating, respectively. The thickness of polymer film on the coverslip at 20 min, 48 h, and 96 h was summarized in **Table 3.2**, and polymer film delamination was observed in this set of flow cell experiments, probably due to the flow of buffer. The bacterial growth at 20 min, 48 h, and 96 h was summarized in **Table 3.3** and **Table 3.4** for glass coverslips without and with polymer coating, respectively.

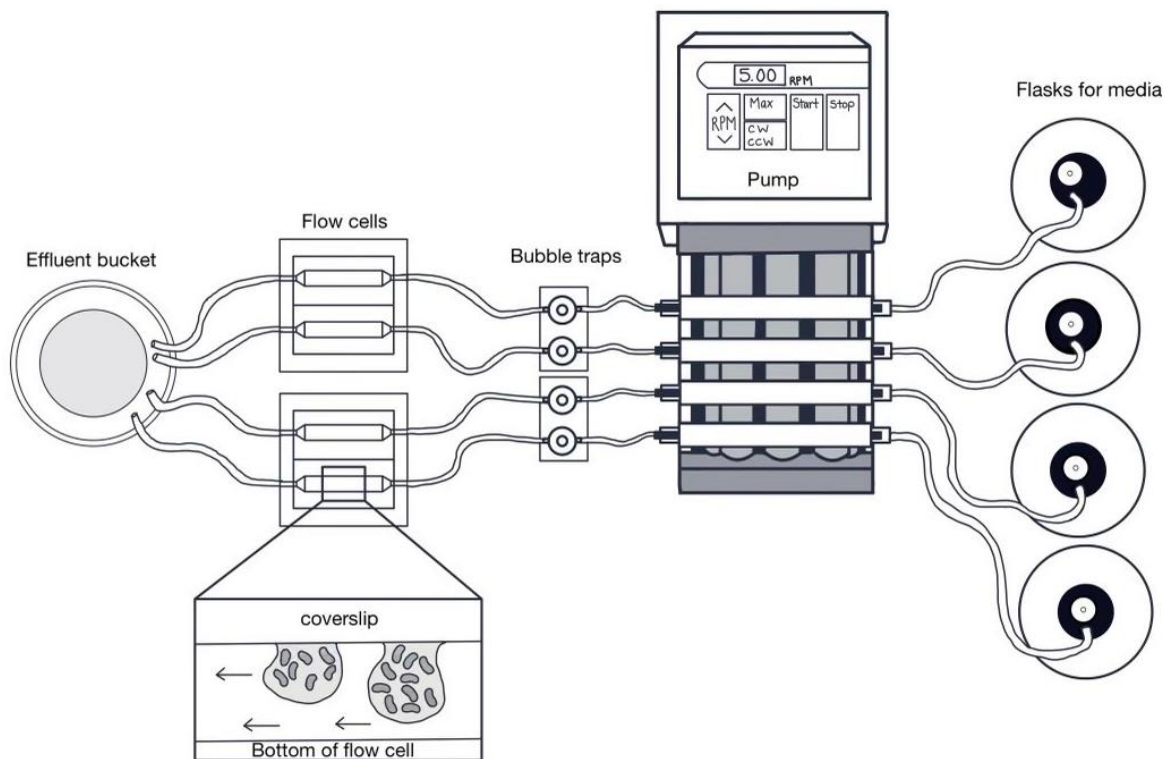


**Figure 3.11.** Set up of flow cells.

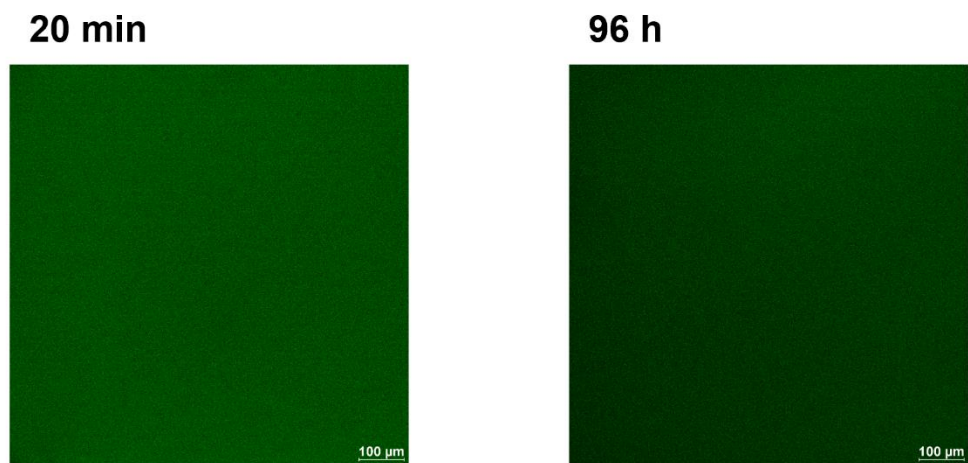
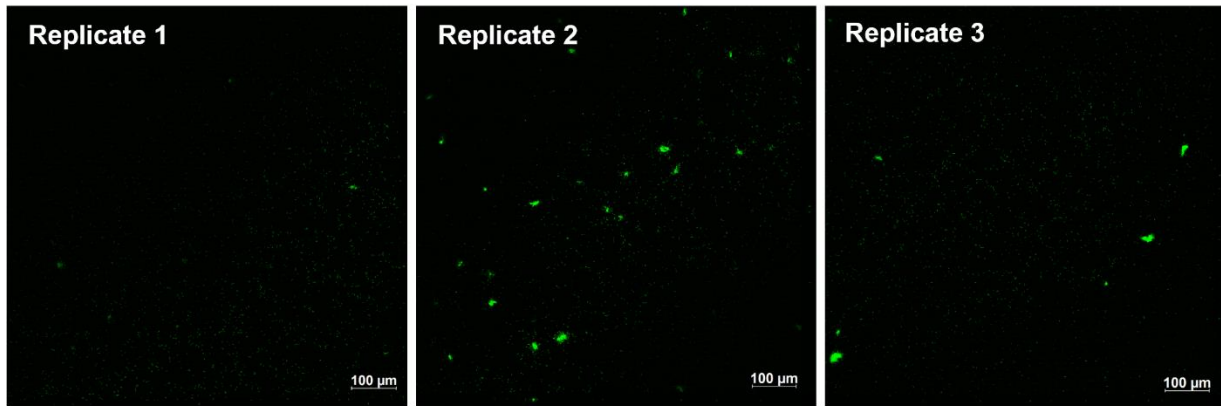
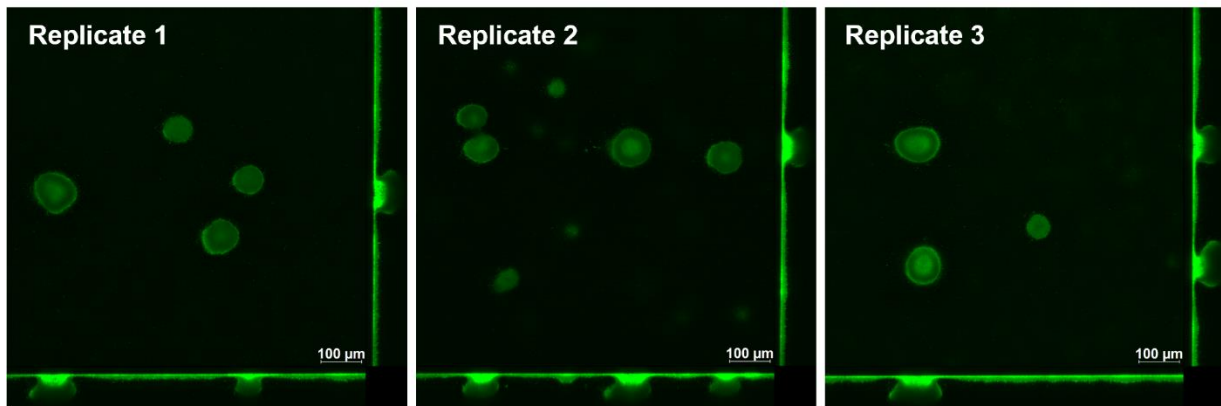


**Figure 3.12.** Images at 20 min and 96 h for flow cell experiments using glass coverslips coated with polymer film  $A_0+B$  (no porphyrin included).

20 min



48 h



96 h

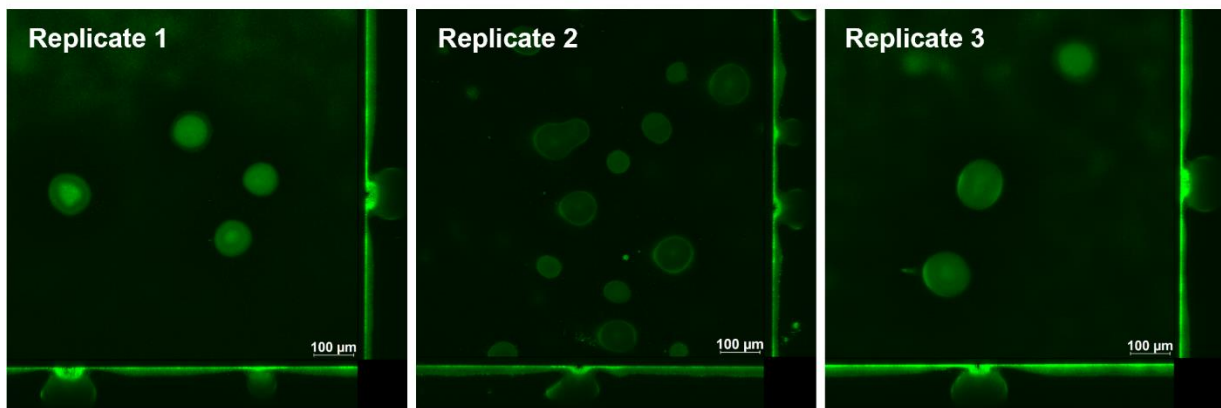
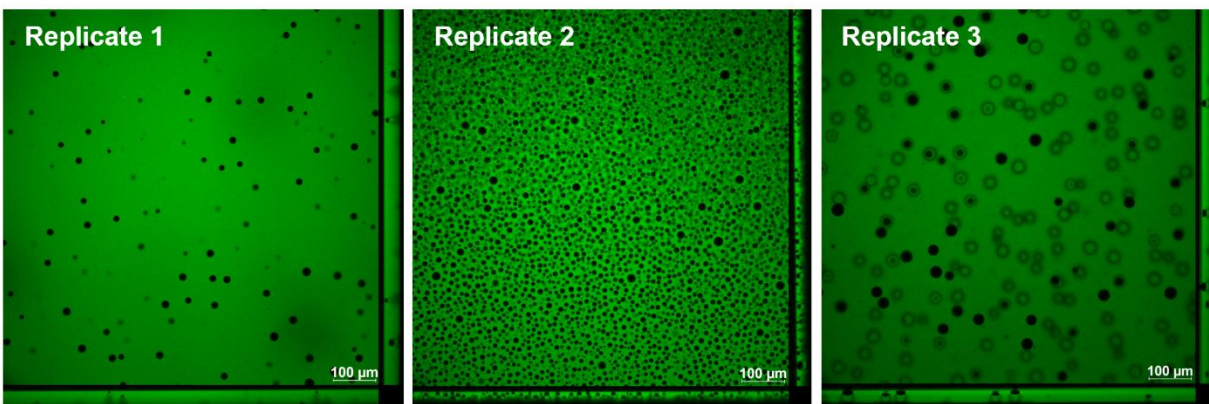
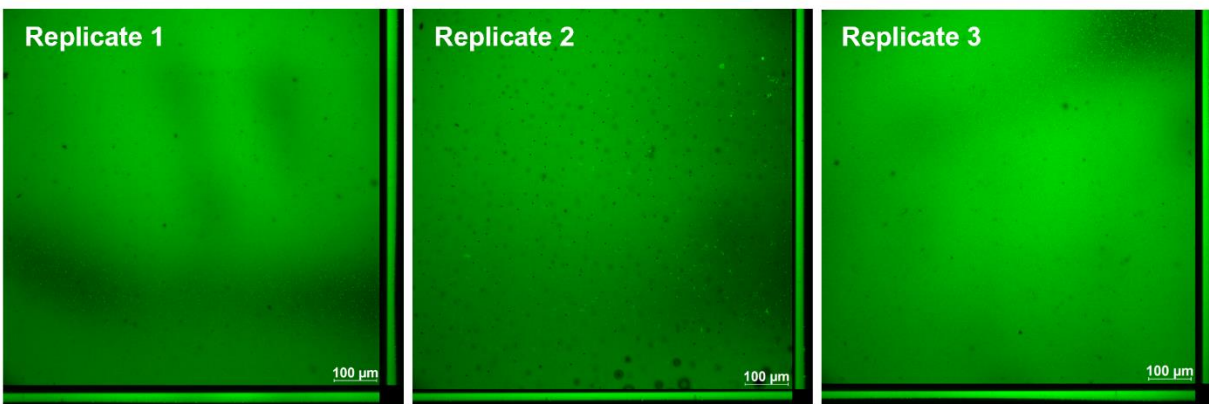


**Figure 3.13.** Representative z-stack images of each replicate at 20 min, 48 h, and 96 h for flow cell experiments using glass coverslips without polymer coating (control).

**20 min**



**48 h**



**96 h**

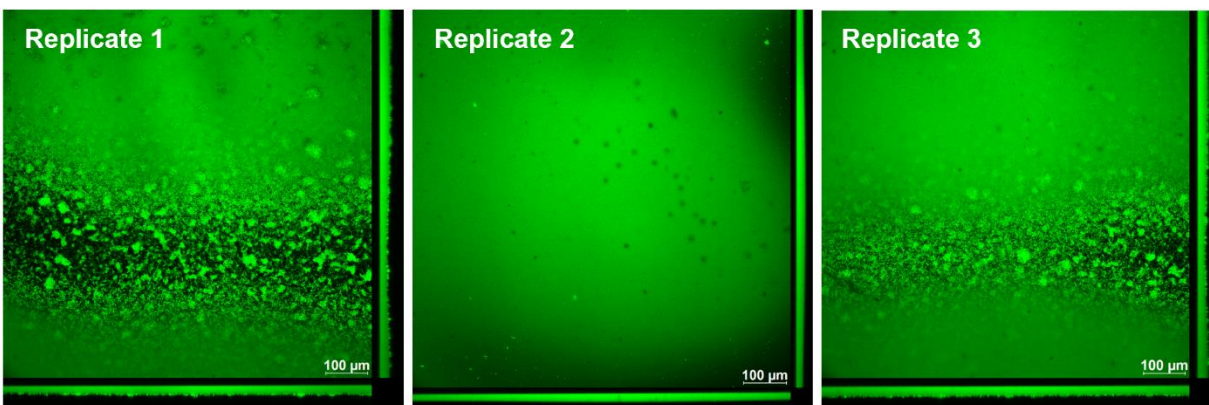


**Figure 3.14.** Representative z-stack images of each replicate at 20 min, 48 h, and 96 h for flow cell experiments using polymer-coated glass coverslips.

<b>Thickness of polymer film on glass coverslip (<math>\mu\text{m}</math>)</b>			
<b>Replicates</b>	<b>20 min</b>	<b>48 h</b>	<b>96 h</b>
<b>1</b>	40	25	17
<b>2</b>	25	16	16
<b>3</b>	40	20	16
<b>average</b>	$35\pm 8.7$	$20\pm 4.5$	$16\pm 0.6$

**Table 3.2.** Summary of thickness of polymer film (A+B) on glass coverslip at 20 min, 48 h, and 96 h.

<b>Bacteria growth on coverslip without polymer coating</b>			
<b>Replicates</b>	<b>20 min</b>	<b>48 h</b>	<b>96 h</b>
<b>1</b>	—	70 $\mu\text{m}$ biofilm	101 $\mu\text{m}$ biofilm
<b>2</b>	—	75 $\mu\text{m}$ biofilm	97 $\mu\text{m}$ biofilm
<b>3</b>	—	69 $\mu\text{m}$ biofilm	107 $\mu\text{m}$ biofilm
<b>average</b>	—	$71\pm 3.2$ $\mu\text{m}$ biofilm	$102\pm 5.0$ $\mu\text{m}$ biofilm

**Table 3.3.** Summary of bacterial growth on glass coverslip without polymer coating at 20 min, 48 h, and 96 h.

<b>Bacteria growth on coverslip with polymer coating</b>			
<b>Replicates</b>	<b>20 min</b>	<b>48 h</b>	<b>96 h</b>
<b>1</b>	—	—	10 $\mu\text{m}$ bacterial film
<b>2</b>	—	—	0 $\mu\text{m}$ bacterial film
<b>3</b>	—	—	12 $\mu\text{m}$ bacterial film
<b>average</b>	—	—	$7\pm 6.4$ $\mu\text{m}$ bacterial film

**Table 3.4.** Summary of bacterial growth on glass coverslip with polymer coating (A+B) at 20 min, 48 h, and 96 h.

## Static Growth Experiments

Cellvis 8 chambered #1.5 high performance cover glass wells were utilized for this experiment. Two of the glass wells were coated in a polymer film (**A+B**) while another two were coated in a polymer film loaded with antibiotics (**A<sub>t</sub>+A<sub>p</sub>+B**). **A+B** (1:1 molar ratio of **A:B**) was dissolved in 90% CH<sub>3</sub>OH and 10% H<sub>2</sub>O at 18.75 mg·mL<sup>-1</sup> and 200 μL was dropped into one glass well; **A<sub>t</sub>+A<sub>p</sub>+B** (1:1:2 molar ratio of **A<sub>t</sub>:A<sub>p</sub>:B**) was dissolved in 90% CH<sub>3</sub>OH and 10% H<sub>2</sub>O with the same molar amount of copolymer **B** as compared to **A+B** instead of the same concentration and 200 μL was dropped into one glass well. Then the well plate with 2 wells loaded with **A+B** solution (200 μL each) and 2 wells loaded with **A<sub>t</sub>+A<sub>p</sub>+B** solution (200 μL each) was put on a shaker to dry overnight before further experiments. Prior to inoculating bacteria, the polymer coatings were imaged using an inverted Leica confocal laser scanning microscope. The 20x magnification objective was used with an excitation of 488 nm and an emission of 508 nm. Three z-stacks were taken over the middle portion of the well.

PAO1  $\Delta wspF$  Tn7 Gm::P(A1/04/03)::GFP and PAO1  $\Delta wspF \Delta pelA \Delta psIBCD \Delta algD$  Tn7 Gm::P(A1/04/03)::GFP expressing strains were struck out onto Luria Broth (LB) agar plates from frozen glycerol stocks and incubated overnight at 37 °C. Tryptic Soy Broth (TSB) media was inoculated with a single colony and grown overnight with shaking at 37 °C. Overnight cultures were back diluted 1/100 in 100% TSB media and grown with shaking at 37 °C to an OD of 0.1. Then, 220 μL of back-diluted culture was added to each Cellvis well. The top row was inoculated with PAO1  $\Delta wspF$  Tn7 Gm::P(A1/04/03)::GFP culture and the bottom row was inoculated with PAO1  $\Delta wspF \Delta pelA \Delta psIBCD \Delta algD$  Tn7 Gm::P(A1/04/03)::GFP culture. At 0 h, CFUs were collected and plated on LB agar. Using an iPhone camera, a picture from the top of the wells was taken. The chamber was then placed in a covered Pyrex dish containing paper towels wet with deionized water to prevent dehydration, and then incubated in a dark room at 25 °C for 2 days. After 24 h and 48 h, CFUs and pictures of the top of the wells were taken again.

Prior to imaging the bacteria growth at 48 h, the wells were washed out by fully submerging the chamber in buffer (1x PBS, pH 7.4). The wells were tapped out on a paper towel to remove any excess liquid.

As for the CFUs for the well plates, a 200  $\mu$ L-multichannel pipette was used to place 90  $\mu$ L of 1x PBS solution into each 96 plate well. 10  $\mu$ L of the static glass well supernatant was carefully removed and added to the respective first column of the 96 well plate containing 90  $\mu$ L of PBS. Serial dilutions were performed by transferring 10  $\mu$ L from the first well to the adjacent well. This process was repeated to obtain a final dilution of 1:10<sup>8</sup>. A 20  $\mu$ L-multichannel pipette was then used to deposit 5  $\mu$ L from all eight wells of the respective row onto a room temperature LB agar plate, plated in triplicate. This step was repeated for each row. Drops on the LB agar plate was allowed to dry before being transferred to a 37 °C incubator to grow statically overnight. After 24 h, bacterial colonies were counted and CFU counts were calculated.

Three replicates were performed for this set of experiments. The images of the top of the wells were summarized in **Figure 3.15**. Confocal microscopy images of three biological replicates were summarized in **Figures 3.16-3.18**. Polymer film (**A+B**) thickness was summarized in **Table 3.5**. Antibiotic-loaded polymer film (**A<sub>t</sub>+A<sub>p</sub>+B**) thickness was summarized in **Table 3.6**. Bacterial growth was summarized in **Table 3.7** and **Table 3.8**.

Since bacteria grew in the well coated with polymer film (**A+B**), an additional set of control experiments was performed (**Figure 3.19**), which supported that the cyclodextrin part in copolymer **B** did not serve as food for bacteria growth, as no bacteria growth was observed with the polymer film (**A+B**) in PBS instead of TSB.

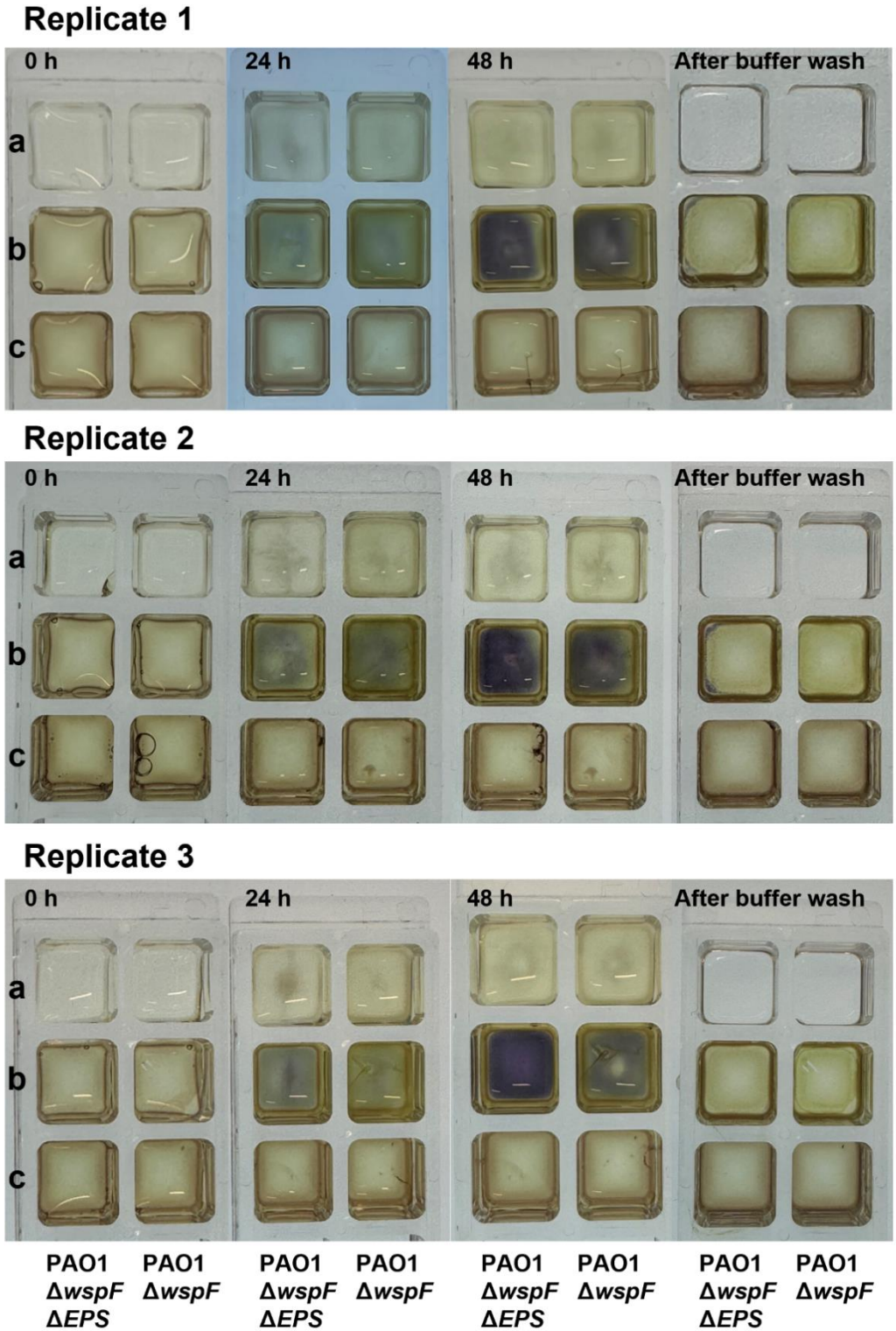


**Figure 3.15.** Images from the top of the wells for three replicates. In all three replicates, wells of lane “a” were with no polymer coating, wells of lane “b” were coated with polymer film ( $A+B$ ), and wells of lane “c” were coated with antibiotic-loaded polymer film ( $A_t+A_p+B$ ).

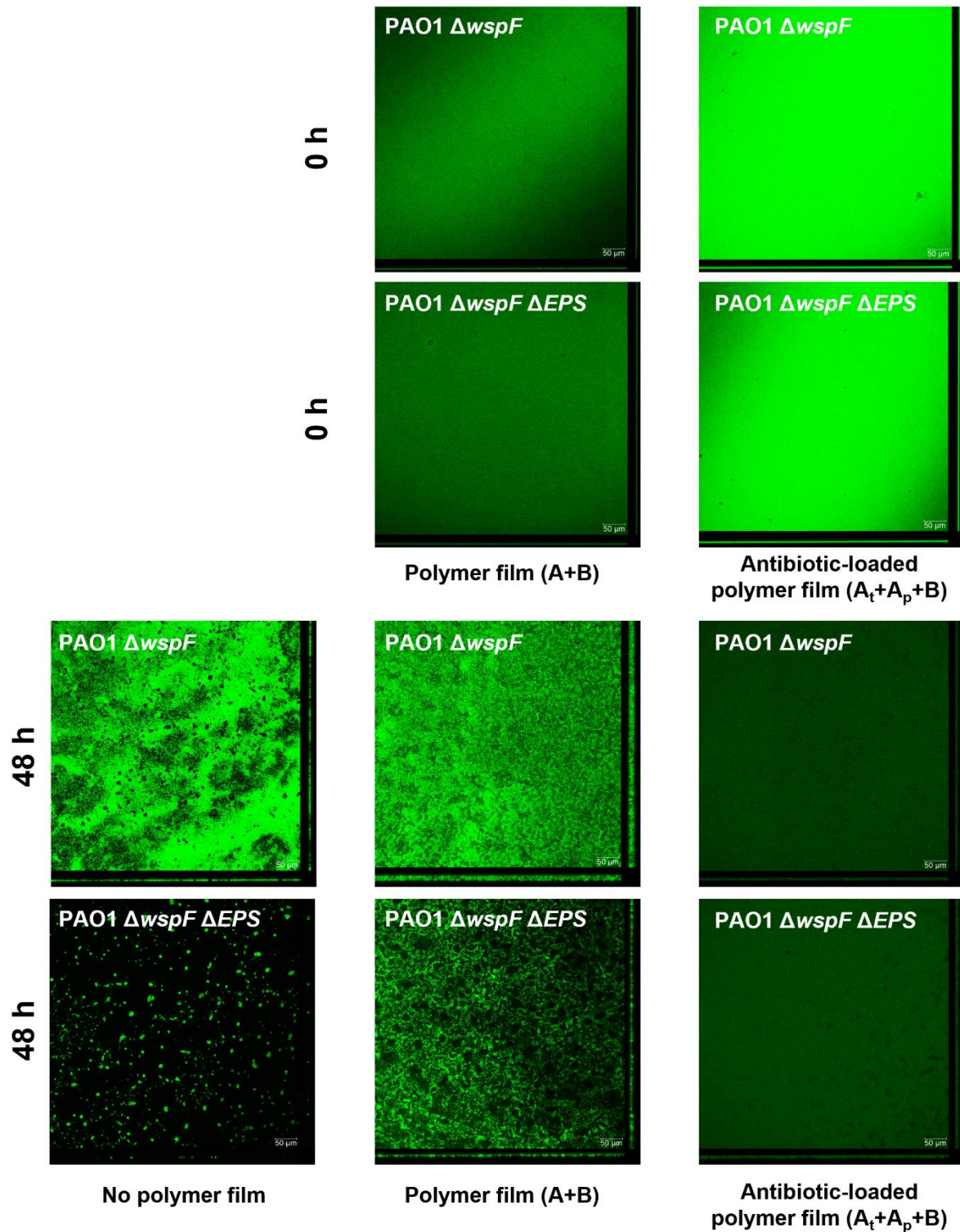


**Figure 3.16.** Confocal microscopy images (Replicate 1) of polymer film (A+B) and antibiotic-loaded polymer film (A<sub>t</sub>+A<sub>p</sub>+B) at 0 h; bacteria growth of no polymer film, polymer film (A+B) and antibiotic-loaded polymer film (A<sub>t</sub>+A<sub>p</sub>+B) at 48 h.

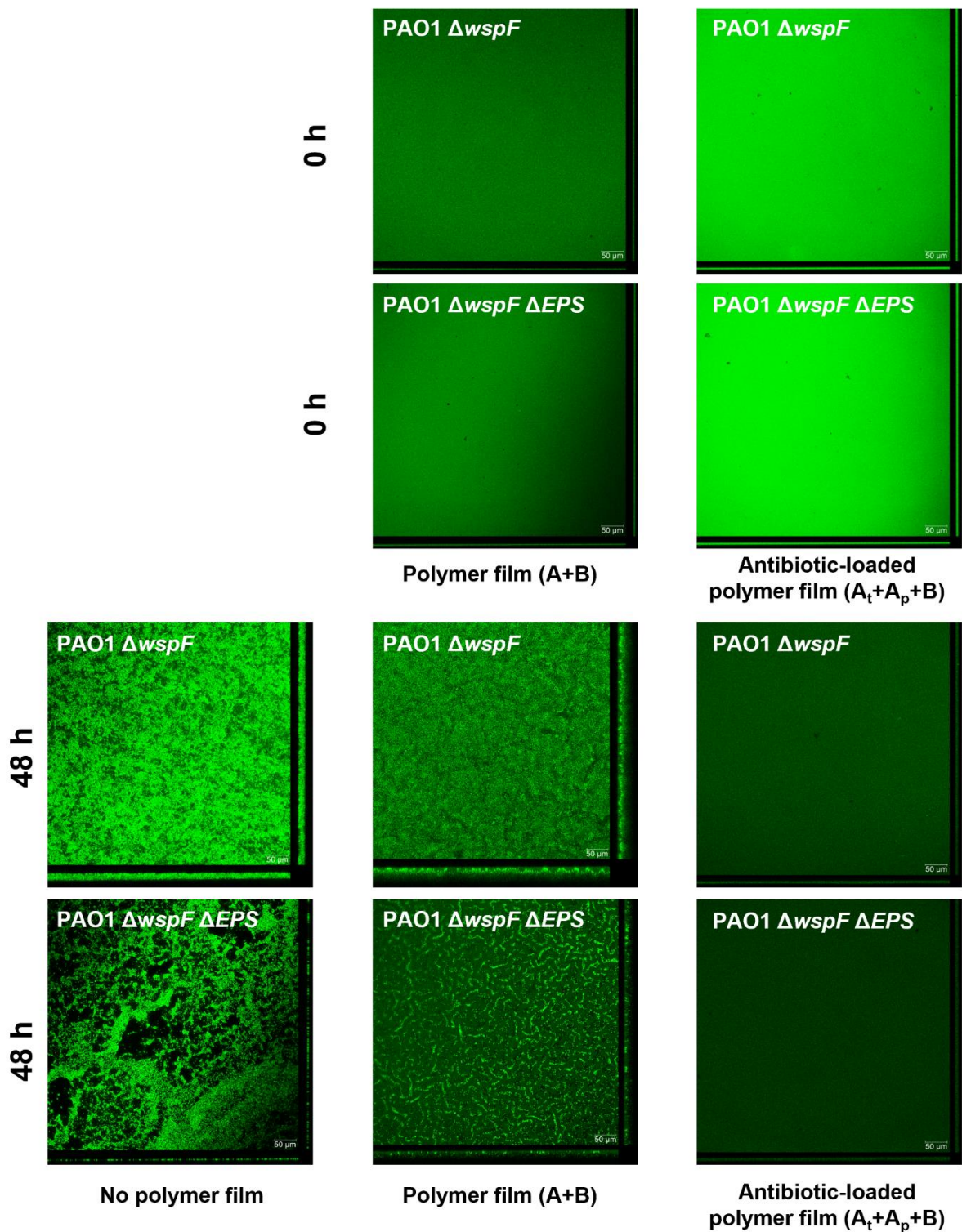


**Figure 3.17.** Confocal microscopy images (Replicate 2) of polymer film (A+B) and antibiotic-loaded polymer film (A<sub>t</sub>+A<sub>p</sub>+B) at 0 h; bacteria growth of no polymer film, polymer film (A+B) and antibiotic-loaded polymer film (A<sub>t</sub>+A<sub>p</sub>+B) at 48 h.

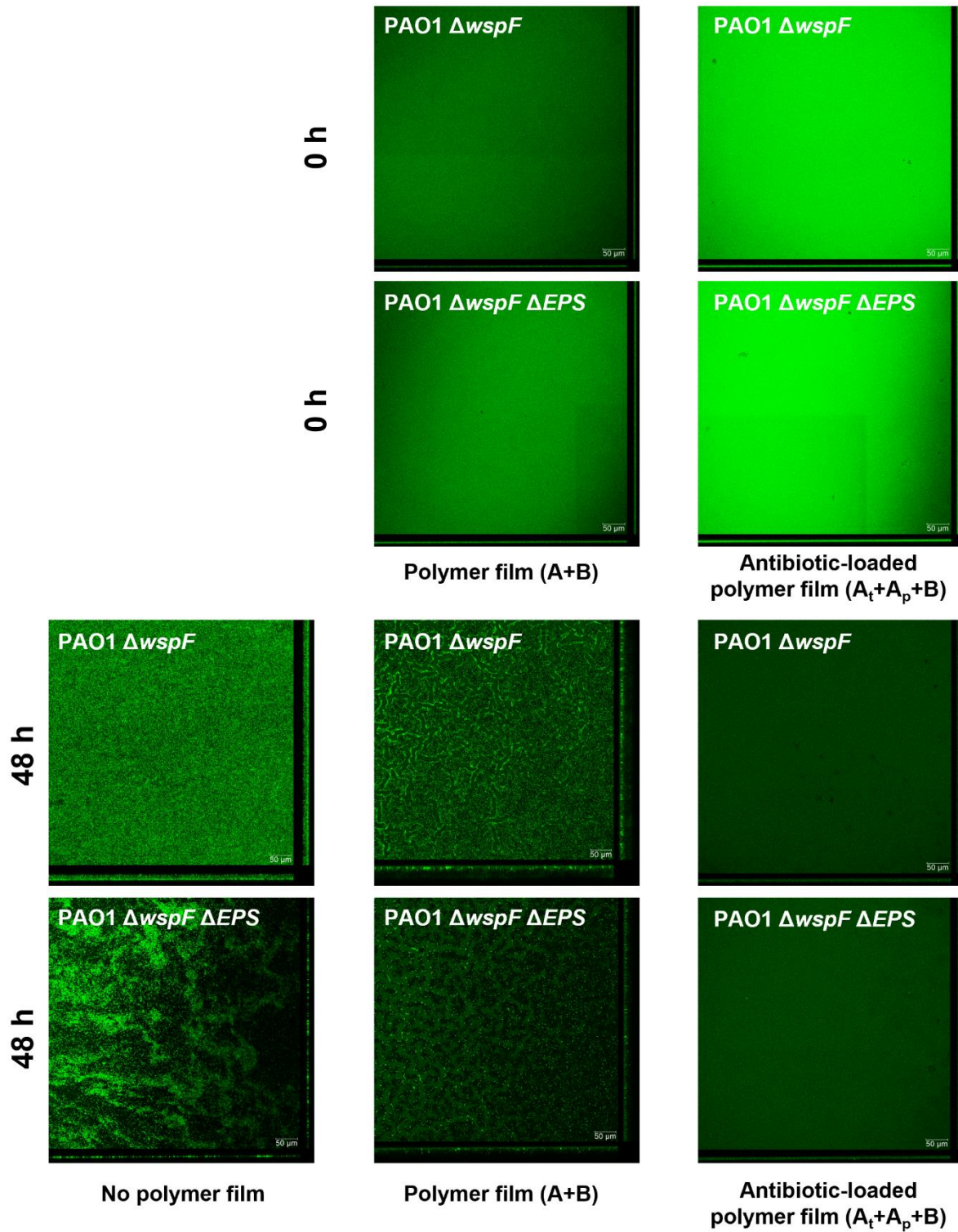


**Figure 3.18.** Confocal microscopy images (Replicate 3) of polymer film (A+B) and antibiotic-loaded polymer film (A<sub>t</sub>+A<sub>p</sub>+B) at 0 h; bacteria growth of no polymer film, polymer film (A+B) and antibiotic-loaded polymer film (A<sub>t</sub>+A<sub>p</sub>+B) at 48 h.

Replicates	Thickness of polymer film (A+B) ( $\mu\text{m}$ )			
	0 h (PAO1 $\Delta\text{wspF}$ )	48 h (PAO1 $\Delta\text{wspF}$ )	0 h (PAO1 $\Delta\text{wspF}$ $\Delta\text{EPS}$ )	48 h (PAO1 $\Delta\text{wspF}$ $\Delta\text{EPS}$ )
1	7	7	7	7
2	7	7	7	7
3	7	7	8	8
average	7 $\pm$ 0	7 $\pm$ 0	7.3 $\pm$ 0.6	7.3 $\pm$ 0.6

**Table 3.5.** Summary of thickness of polymer film (A+B) in well plates at 0 h and 48 h.

Replicates	Thickness of antibiotic-loaded polymer film (A <sub>t</sub> +A <sub>p</sub> +B) ( $\mu\text{m}$ )			
	0 h (PAO1 $\Delta\text{wspF}$ )	48 h (PAO1 $\Delta\text{wspF}$ )	0 h (PAO1 $\Delta\text{wspF}$ $\Delta\text{EPS}$ )	48 h (PAO1 $\Delta\text{wspF}$ $\Delta\text{EPS}$ )
1	10	10	10	10
2	10	10	10	10
3	10	10	11	11
average	10 $\pm$ 0	10 $\pm$ 0	10.3 $\pm$ 0.6	10.3 $\pm$ 0.6

**Table 3.6.** Summary of thickness of antibiotic-loaded polymer film (A<sub>t</sub>+A<sub>p</sub>+B) in well plates at 0 h and 48 h.

Replicates	Bacterial growth at 48 h for PAO1 $\Delta\text{wspF}$ ( $\mu\text{m}$ )		
	No polymer film	Polymer film (A+B)	Antibiotic-loaded polymer film (A <sub>t</sub> +A <sub>p</sub> +B)
1	11	13	0
2	25	23	0
3	22	23	0
average	19.3 $\pm$ 7.4	19.7 $\pm$ 5.8	0

**Table 3.7.** Summary of bacterial growth (PAO1  $\Delta\text{wspF}$ ) at 48 h for no polymer film, polymer film (A+B) and antibiotic-loaded polymer film (A<sub>t</sub>+A<sub>p</sub>+B) in well plates.

Replicates	Bacterial growth at 48 h for PAO1 $\Delta wspF \Delta EPS$ ( $\mu\text{m}$ )		
	No polymer film	Polymer film (A+B)	Antibiotic-loaded polymer film ( $A_t+A_p+B$ )
1	5	8	0
2	8	13	0
3	10	10	0
average	$7.7 \pm 2.5$	$10.3 \pm 2.5$	0

**Table 3.8.** Summary of bacteria growth (PAO1  $\Delta wspF \Delta EPS$ ) at 48 h for no polymer film, polymer film (A+B) and antibiotic-loaded polymer film ( $A_t+A_p+B$ ) in well plates.

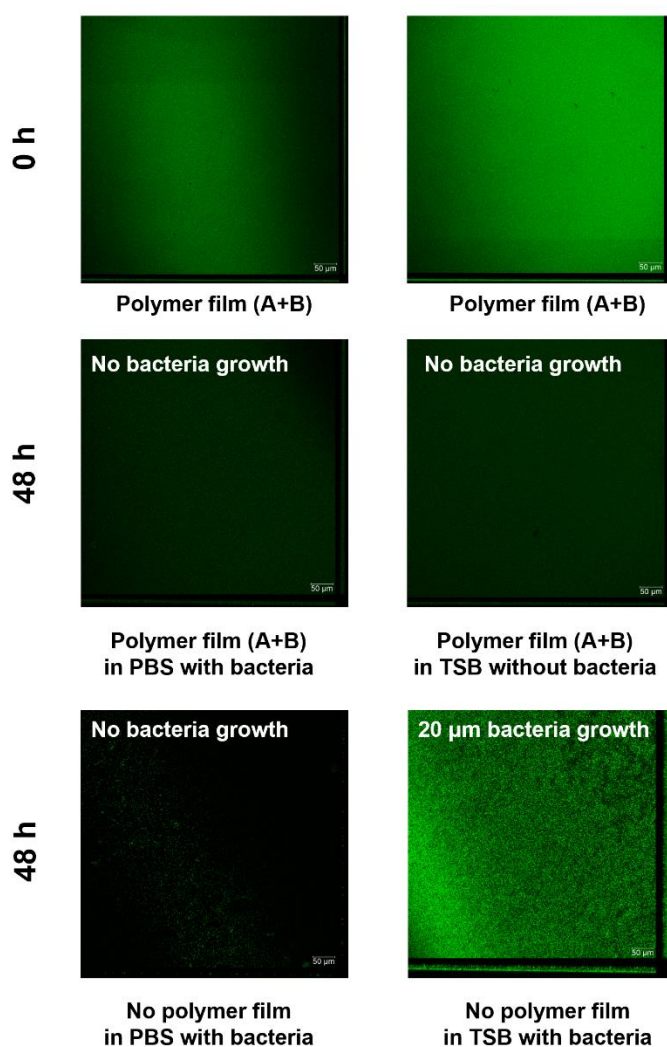


**Figure 3.19.** Confocal microscopy images of control experiments in the well plate: polymer film (A+B) with bacteria in PBS, polymer film (A+B) without bacteria in TSB, no polymer film with bacteria in PBS, and no polymer film with bacteria in TSB.

## Antibiotic Release Experiments

Since the results from the static growth experiments showed that the antibiotic-loaded polymer film ( $A_t+A_p+B$ ) inhibited bacteria growth, we then carried out experiments to analyze the rate of the antibiotics released from the polymer film into the solution in the well plate. The same amount of the antibiotic-loaded polymer film ( $A_t+A_p+B$ ) was used to coat each well for these antibiotic release experiments as was used previously in the static growth experiments.

To determine the release rate of antibiotics from the antibiotics loaded polymer film ( $A_t+A_p+B$ ) that coated the glass well, 220  $\mu$ L of 100% TSB was added to the well. Aliquots were taken at different time points to study the release rate of antibiotics. To remove aliquots, the entire 220  $\mu$ L solution was removed from the well and added to a sterile 1mL Eppendorf tube stored in a 4 °C refrigerator. Fresh 220  $\mu$ L of TSB was added back to the well. Between aliquot collection, the wells were stored in a covered Pyrex dish in a 25 °C room. After obtaining all aliquots, 180  $\mu$ L from the Eppendorf tube solution was added to individual wells on a 96 well plate.

The PAO1  $\Delta wspF \Delta pelA \Delta ps/BCD \Delta algD$  Tn7 Gm::P(A1/04/03)::GFP expressing strain was struck out onto LB agar plates from frozen glycerol stocks and incubated overnight at 37 °C. TSB media was inoculated with a single colony and grown overnight with shaking at 37 °C. Overnight cultures were back diluted 1/100 in TSB media and grown with shaking at 37 °C to an OD of 0.4. Then, 20  $\mu$ L of the back-diluted culture was added to each 96 well plate well.

A Breathe-Easy Sealing Membrane from Diversified Biotech was used to seal the 96 well plate. The well plate was inserted into the Thermoscientific Varioskan Lux well plate reader. The incubation temperature was set at 37 °C with light shaking at 240 rpm. The plate reader was set to measure the OD 600 nm at 20-minute intervals for a total of 18 h, with a pause of shaking during the readings. After 18 h, the well plates were removed from the reader.

Initially, aliquots were collected at 0 h, 4 h, 8 h, 12 h, 24 h and 48 h. As shown in **Figure 3.20a**, the majority of the antibiotics were released within 4 h. Further studies were conducted with additional collection time points. Specifically, aliquots were collected at 30-minute increments from 0 h to 4 h. Then additional aliquots were collected at 5 h, 6 h, 8 h, 10 h, 12 h, 24 h, and 48 h. Three replicates were performed for this experiment. The results were summarized in **Figures 3.5 and 3.20b**.

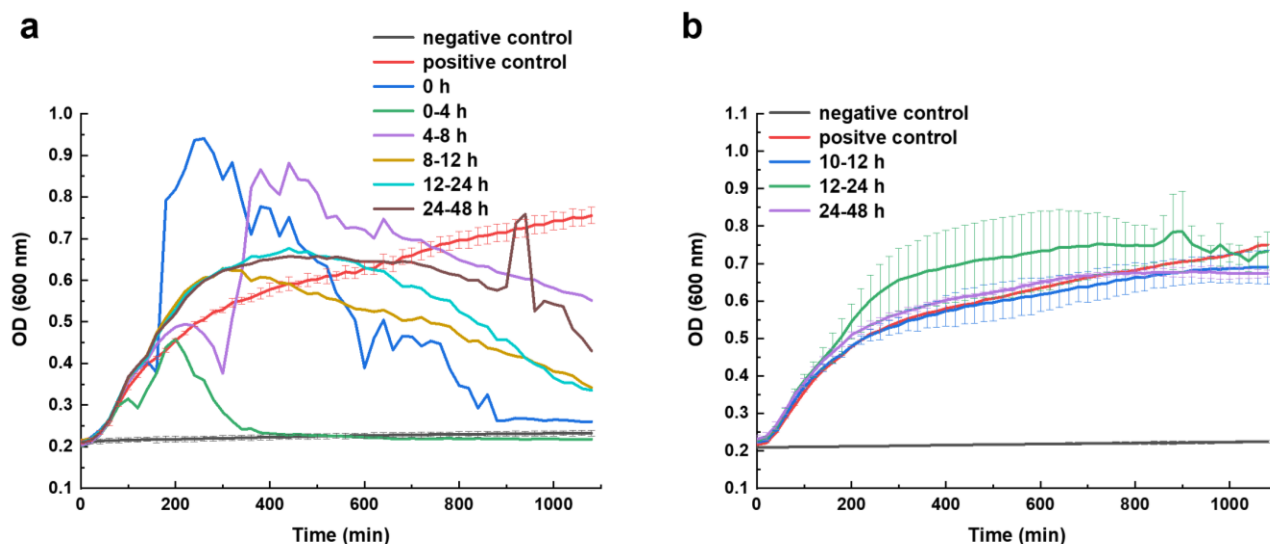


**Figure 3.20.** (a) Initial screening of MIC assay results of antibiotics released at 0 h, 0-4 h, 4-8 h, 8-12 h, 12-24 h, and 24-48 h. (b) MIC assay results of antibiotics released at 10-12 h, 12-24 h, and 24-48 h (three replicates).

### 3.5 Conclusions

The design, synthesis, loading, and release of antibiotics from a self-assembled polymer film/coating on a glass substrate is reported. The polymer coating was composed of two bottlebrush copolymers that were synthesized through ROMP, followed by self-assembly 1:1 via host-guest interactions between Ad and  $\beta$ -CD functional groups appended to the sidechains of each Nb-based copolymers, **A** and **B**, respectively. The polymer film (**A+B**) showed prominent prevention against bacterial cell attachment and biofilm formation over several days while under

a dynamic environment in a flow cell ( $0.167 \text{ mL}\cdot\text{min}^{-1}$ ). This successful outcome was attributed to a unique copolymer delamination mechanism, where >50% of the polymer film remained after four days (in contrast, >90% of the polymer film remained under static conditions). Furthermore, the antibiotic-loaded polymer film ( $\mathbf{A_t+A_p+B}$ ) mitigated bacterial growth under static conditions. The release of the antibiotics from the polymer film was achieved through diffusion-limited counteranion exchange with chloride ions in the buffered solutions, which was indirectly determined using MIC assays to go to completion within 5 h. Future efforts will focus on extending the antibiotic release time period of the polymer coatings to provide even longer protection, as well as investigating the potential for use in biomedical applications, such as in non-toxic, and biodegradable antifouling/bactericidal coatings for medical devices.

### 3.6 References

- (1) Nathwani, D.; Raman, G.; Sulham, K.; Gavaghan, M.; Menon, V. Clinical and economic consequences of hospital-acquired resistant and multidrug-resistant *Pseudomonas aeruginosa* infections: a systematic review and meta-analysis. *Antimicrob. Resist. Infect. Control* **2014**, *3* (1), 32.
- (2) Thi, M. T. T.; Wibowo, D.; Rehm, B. H. A. *Pseudomonas aeruginosa* Biofilms. *Int. J. Mol. Sci.* **2020**, *21* (22).
- (3) Costerton, J. W.; Stewart, P. S.; Greenberg, E. P. Bacterial biofilms: a common cause of persistent infections. *Science* **1999**, *284* (5418), 1318-1322.
- (4) Percival, S. L.; Suleman, L.; Vuotto, C.; Donelli, G. Healthcare-associated infections, medical devices and biofilms: risk, tolerance and control. *J. Med. Microbiol.* **2015**, *64* (Pt 4), 323-334.
- (5) Bjarnsholt, T.; Alhede, M.; Alhede, M.; Eickhardt-Sørensen, S. R.; Moser, C.; Kühl, M.; Jensen, P. Ø.; Høiby, N. The in vivo biofilm. *Trends Microbiol.* **2013**, *21* (9), 466-474.
- (6) Tseng, B. S.; Zhang, W.; Harrison, J. J.; Quach, T. P.; Song, J. L.; Penterman, J.; Singh, P. K.; Chopp, D. L.; Packman, A. I.; Parsek, M. R. The extracellular matrix protects *Pseudomonas aeruginosa* biofilms by limiting the penetration of tobramycin. *Environ. Microbiol.* **2013**, *15* (10), 2865-2878.
- (7) Doroshenko, N.; Tseng, B. S.; Howlin, R. P.; Deacon, J.; Wharton, J. A.; Thurner, P. J.; Gilmore, B. F.; Parsek, M. R.; Stoodley, P. Extracellular DNA impedes the transport of vancomycin in *Staphylococcus epidermidis* biofilms preexposed to subinhibitory concentrations of vancomycin. *Antimicrob. Agents Chemother.* **2014**, *58* (12), 7273-7282.
- (8) Gebreyohannes, G.; Nyerere, A.; Bii, C.; Sbhathu, D. B. Challenges of intervention, treatment, and antibiotic resistance of biofilm-forming microorganisms. *Heliyon* **2019**, *5* (8).

- (9) Mitra, D.; Kang, E.-T.; Neoh, K. G. Polymer-based coatings with integrated antifouling and bactericidal properties for targeted biomedical applications. *ACS Appl. Polym. Mater.* **2021**, *3* (5), 2233-2263.
- (10) Chu, X.; Yang, F.; Tang, H. Recent advance in polymer coatings combating bacterial adhesion and biofilm formation. *Chin. J. Chem.* **2022**, *40* (24), 2988-3000.
- (11) Faustino, C. M.; Lemos, S. M.; Monge, N.; Ribeiro, I. A. A scope at antifouling strategies to prevent catheter-associated infections. *Adv. Colloid Interface Sci.* **2020**, *284*, 102230.
- (12) Flavel, B. S.; Jasieniak, M.; Velleman, L.; Ciampi, S.; Luais, E.; Peterson, J. R.; Griesser, H. J.; Shapter, J. G.; Gooding, J. J. Grafting of poly (ethylene glycol) on click chemistry modified Si (100) surfaces. *Langmuir* **2013**, *29* (26), 8355-8362.
- (13) Banerjee, I.; Pangule, R. C.; Kane, R. S. Antifouling coatings: recent developments in the design of surfaces that prevent fouling by proteins, bacteria, and marine organisms. *Adv. Mater.* **2011**, *23* (6), 690-718.
- (14) Chen, W.-L.; Cordero, R.; Tran, H.; Ober, C. K. 50th anniversary perspective: Polymer brushes: Novel surfaces for future materials. *Macromol.* **2017**, *50* (11), 4089-4113.
- (15) Izquierdo-Barba, I.; Sánchez-Salcedo, S.; Colilla, M.; Feito, M. J.; Ramírez-Santillán, C.; Portolés, M. T.; Vallet-Regí, M. Inhibition of bacterial adhesion on biocompatible zwitterionic SBA-15 mesoporous materials. *Acta Biomater.* **2011**, *7* (7), 2977-2985.
- (16) Mi, L.; Jiang, S. Integrated antimicrobial and nonfouling zwitterionic polymers. *Angew. Chem. Int. Ed.* **2014**, *53* (7), 1746-1754.
- (17) Junter, G.-A.; Thébault, P.; Lebrun, L. Polysaccharide-based antibiofilm surfaces. *Acta Biomater.* **2016**, *30*, 13-25.
- (18) Mohan, T.; Kargl, R.; Tradt, K. E.; Kulterer, M. R.; Bračić, M.; Hribernik, S.; Stana-Kleinschek, K.; Ribitsch, V. Antifouling coating of cellulose acetate thin films with polysaccharide multilayers. *Carbohydr. Polym.* **2015**, *116*, 149-158.
- (19) Cao, X.; Pettit, M. E.; Conlan, S. L.; Wagner, W.; Ho, A. D.; Clare, A. S.; Callow, J. A.; Callow, M. E.; Grunze, M.; Rosenhahn, A. Resistance of polysaccharide coatings to proteins, hematopoietic cells, and marine organisms. *Biomacromolecules* **2009**, *10* (4), 907-915.
- (20) Nakatsuji, T.; Gallo, R. L. Antimicrobial peptides: old molecules with new ideas. *J. Invest. Dermatol.* **2012**, *132* (3), 887-895.
- (21) Jennings, M. C.; Minbiole, K. P.; Wuest, W. M. Quaternary ammonium compounds: an antimicrobial mainstay and platform for innovation to address bacterial resistance. *ACS Infect. Dis.* **2015**, *1* (7), 288-303.
- (22) Li, L.; Zhou, H.; Gai, F.; Chi, X.; Zhao, Y.; Zhang, F.; Zhao, Z. Synthesis of quaternary phosphonium N-chloramine biocides for antimicrobial applications. *RSC Adv.* **2017**, *7* (22), 13244-13249.
- (23) Wang, B.; Liu, H.; Wang, Z.; Shi, S.; Nan, K.; Xu, Q.; Ye, Z.; Chen, H. A self-defensive antibacterial coating acting through the bacteria-triggered release of a hydrophobic antibiotic from layer-by-layer films. *J. Mater. Chem. B* **2017**, *5* (7), 1498-1506.
- (24) Phuengkham, H.; Nasongkla, N. Development of antibacterial coating on silicone surface via chlorhexidine-loaded nanospheres. *J. Mater. Sci. Mater. Med.* **2015**, *26*, 1-11.
- (25) Alves, D.; Olívia Pereira, M. Mini-review: Antimicrobial peptides and enzymes as promising candidates to functionalize biomaterial surfaces. *Biofouling* **2014**, *30* (4), 483-499.

- (26) Bielawski, C. W.; Grubbs, R. H. Living ring-opening metathesis polymerization. *Prog. Polym. Sci.* **2007**, 32 (1), 1-29.
- (27) Zhang, Y.; Li, R.; Trick, T. C.; Nosiglia, M. A.; Palmquist, M. S.; Wong, M. L.; Dorsainvil, J. M.; Tran, S. L.; Danielson, M. K.; Barnes, J. C. Saltwater-Induced Rapid Gelation of Photoredox-Responsive Mucomimetic Hydrogels. *Adv. Mater.* **2023**, 2307356.
- (28) Dorsainvil, J.; Palmquist, M.; Yang, J.; Delawder, A.; Danielson, M.; Zhang, Y.; Saak, T.; Gruschka, M.; Kong, X.; Wencewicz, T. Electrostatic loading and photoredox-accelerated release of antibiotics from oligoviologen-crosslinked hydrogels using red light. *Mater. Today Chem.* **2024**, 35, 101847.
- (29) Ziemba, C.; Khavkin, M.; Priftis, D.; Acar, H.; Mao, J.; Benami, M.; Gottlieb, M.; Tirrell, M.; Kaufman, Y.; Herzberg, M. Antifouling properties of a self-assembling glutamic acid-lysine zwitterionic polymer surface coating. *Langmuir* **2018**, 35 (5), 1699-1713.
- (30) Love, J. A.; Morgan, J. P.; Trnka, T. M.; Grubbs, R. H. A practical and highly active ruthenium-based catalyst that effects the cross metathesis of acrylonitrile. *Angew. Chem. Int. Ed.* **2002**, 41 (21), 4035-4037.

## **Chapter 4: Innovative Drug Delivery**

### **Strategies to Treat Pediatric Kidney Disease**

This chapter describes efforts towards a new method to treat pediatric kidney disease by targeting therapeutics directly to the cells using custom, drug-loaded protein-polymer conjugates.

J.C.B. and J.H.M. conceived the idea. and J.C.B., J.H.M., Y.Z., and K.O. designed the experiments. Y.Z. and R.L. carried out the synthesis and characterization of monomers and polymers. K.O. carried out the synthesis, characterization, and biological studies of proteins. Y.Z. and K.O. carried out the characterization of protein-polymer conjugates.

#### **4.1 Abstract**

Chronic kidney disease, a kind of glomerular disease, has affected a significant number of individuals, including both adults and children. There are drug treatments available currently, but they are not highly effective at specifically targeting the kidneys. The primary challenge is that drugs with desired effects may also cause undesired side effects due to off-targeting in the body. Professor Jeffrey Miner's group at Washington University School of Medicine previously engineered a shortened version of Agrin, a protein derivative that they named "mini Agrin" which targets the glomerulus basement membrane (GBM). In this chapter, I describe an innovative approach to deliver drugs to the GBM of kidneys through the coupling of mini-Agrin with CD-based polymers. The design, synthesis, and characterization of a biotinylated CD-based polymer that could bind to a mini-Agrin protein modified with a monomeric streptavidin (mSA) domain is described. The biotinylated CD-based polymer was synthesized through ring-opening metathesis polymerization (ROMP) and monofunctionalized using a (bis)biotinylated olefin quenching agent. The polymer was characterized by both NMR spectroscopy and analytical GPC. The binding between the resultant polymer and streptavidin alone was confirmed by SDS-PAGE,

demonstrating a successful biotinylation of the CD-based polymer; ultimately setting the stage for formation of a novel protein-polymer conjugate for drug delivery.

## 4.2 Introduction

Chronic kidney disease, which is a kind of glomerular disease, has affected a large percentage of the population worldwide.<sup>1</sup> Currently, the systemic delivery of therapeutics for disease treatment frequently results in off-target toxicity and adverse side effects.<sup>2</sup> Ultimately, these off-target effects lead to reduced drug efficiency, necessitating the administration of multiple doses throughout a treatment regimen. An alternative delivery approach involves tethering drugs to higher molecular weight polymer carriers as illustrated in **Figure 4.1**, a strategy initially proposed by Ringsdorf in the mid-70s.<sup>3</sup> The advantages of this method include increased therapeutic bioavailability, more favorable pharmacokinetic and biodistribution properties and overall reduction in toxicity.<sup>4</sup> However, one potential problem of this method is incomplete or no conversion of the prodrug into free drug. Other strategies involving polymer-drug conjugates have also been explored as delivery vehicles for renal targeting,<sup>5, 6</sup> with some relying on localized enzymes in the kidney to release the prodrug from the polymer support.

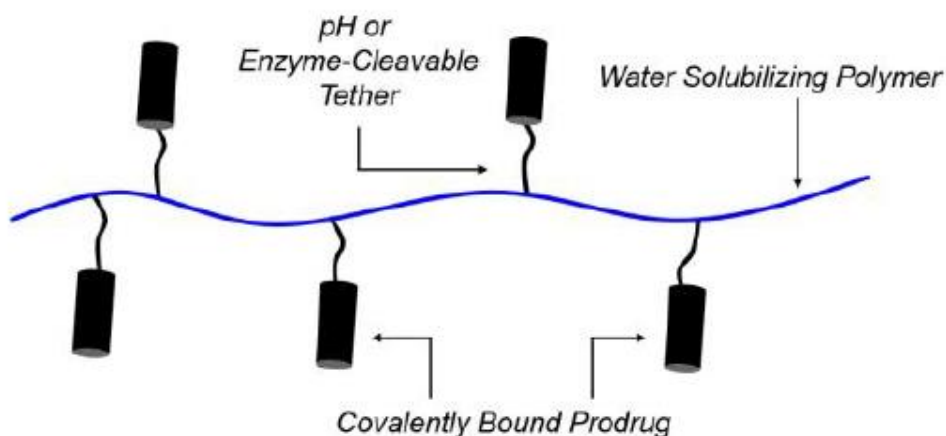


**Figure 4.1.** Cartoon representation of a polymer-drug conjugate.

PEGylation,<sup>7</sup> which refers to PEG conjugated to molecules such as proteins and peptides, is a general way to increase protein stability. By covalently attaching PEG to proteins, it is possible to lower the immunogenic response, increase blood half-life and usually there is no decrease in bioactivity. By using this method, Abuchowski and co-workers synthesized the first protein-polymer conjugate in 1977.<sup>8</sup> And so far, all FDA-approved protein-polymer conjugates that are used as therapeutics are PEGylated.<sup>9</sup> The first protein-polymer drug that gained FDA approval in 1990 is called Adagen, which is used for the treatment of severe combined immunodeficiency disease.<sup>10</sup>

In recent years, scientists have made great progress in the development of protein-polymer conjugates, which has provided a blueprint for future drug delivery platforms. Although there are many ways to design protein-polymer conjugates, with selectivity and efficiency being a primary focus when selecting a conjugation technique, it remains challenging to specifically target kidneys, as many nanomaterials often localize in the liver instead.<sup>11</sup> Here, I describe the design of a new protein-polymer conjugate that capitalizes on the high binding affinity between streptavidin and biotin ( $K_a \sim 10^{15}$ )<sup>12</sup> for the purpose of delivering therapeutics specifically to the GBM. (**Figure 4.2**) To achieve this goal, a diblock copolymer **poly(PEG<sub>5</sub>-ZnTPP)-(CD<sub>5</sub>-Me<sub>15</sub>)-biotin** was synthesized through ROMP with two steps and then mono-biotinylated using a (bis)biotin-functionalized olefin that also served as the termination agent. The PEG unit was included to increase the polymer's solubility in water, while the CD component is a great candidate for loading hydrophobic drugs through non-covalent host-guest interactions. The ZnTPP part as described in earlier chapters was also included as a fluorescent dye. The Miner lab has shown that a protein called "mini-Agrin" can accumulate specifically in the GBM when injected intravenously into mice. Thus, a new mini-Agrin protein that is fused to a monomeric streptavidin (mSA) domain was designed and engineered by them for the purpose of establishing the protein-polymer conjugate through biotin-streptavidin non-covalent interactions. In this study, we investigated the stability of this

bioconjugate in solution and *in vivo*, with an eye towards administering therapeutics in a mouse model used by the Miner group to simulate kidney disease.

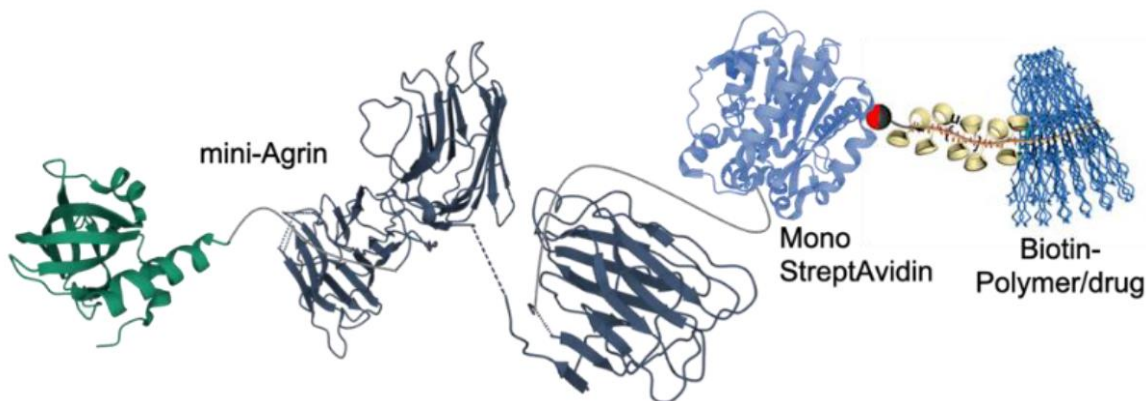


**Figure 4.2.** Schematic diagram shows the structure of the mini-Agrin protein (NtA; green + LG domains; gray) fused to mono-StreptAvidin (blue) to make mini-Agrin-mSA. The biotin (red) on the drug-carrying polymer at right binds to mSA, forming the complex that will be used to carry drugs to glomeruli *in vivo*.

## 4.3 Results and Discussion

### 4.3.1 Design, Synthesis, and Characterization of Biotinylated Diblock Copolymer

The diblock copolymer **poly(PEG<sub>5</sub>-ZnTPP)-(CD<sub>5</sub>-Me<sub>15</sub>)-biotin** was designed and synthesized through the ROMP of several norbornene (Nb) functionalized monomers using Grubbs' 3rd generation catalyst as illustrated in **Figure 4.3**. The first block was made by the copolymerization of **Nb-PEG** and **Nb-TEG-ZnTPP**, where **Nb-PEG** could significantly increase the water solubility of the block copolymer while **Nb-TEG-ZnTPP** was incorporated together to function both as a fluorescent dye and a metal carrying group. The former may be useful for imaging the polymer and protein conjugate, while the latter is anticipated to aid in determining the co-localization of the conjugate in the GBM *in vivo* on account of the metal content being detected down to the ppb level using a technique called inductively coupled plasma mass spectroscopy (ICP-MS). The second block was made by polymerizing **Nb-CD** and **Nb-Me** together, as the polymerization of **Nb-CD** alone could not go to completion, probably due to the steric effects of the CD macrocycles.

Normally, the polymerization was quenched by ethyl vinyl ether (EVE), however, here we used a (bis)biotin-functionalized olefin (Biotin Terminating Agent, **Biotin TA**) instead to quench the reaction. Therefore, the resulting diblock copolymer should have a biotin unit at the end of every polymer chain.

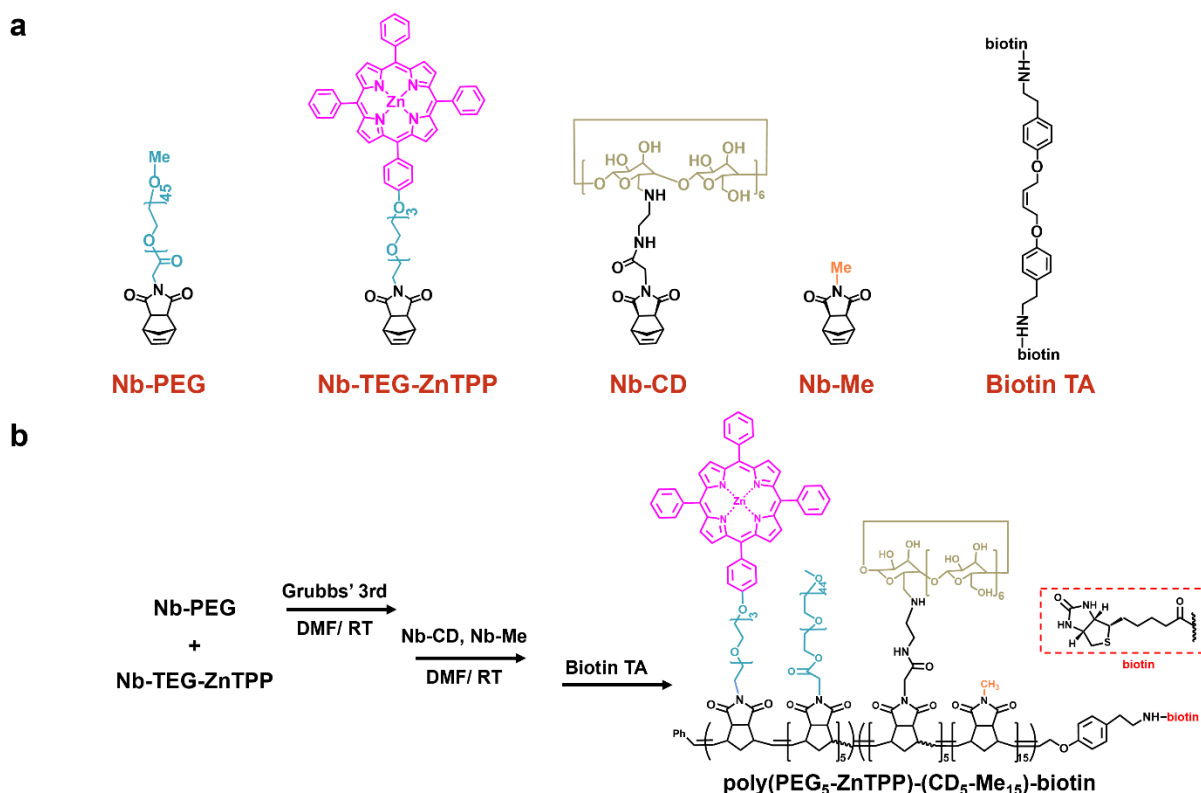


**Figure 4.3.** (a) Chemical structures of Nb-PEG, Nb-TEG-ZnTPP, Nb-CD, Nb-Me, and Biotin TA. (b) Synthetic strategy for poly(PEG<sub>5</sub>-ZnTPP)-(CD<sub>5</sub>-Me<sub>15</sub>)-biotin.

The multi-step polymerization was characterized by <sup>1</sup>H NMR spectroscopy (**Figure 4.4**). Specifically, the proton resonance close to 6.3 ppm should disappear over the course of the polymerization. The portions of the spectra inside the red box in **Figure 4.4** illustrates this point, where all the monomers showed a resonance around 6.3 ppm before polymerization, but not in either **poly(PEG<sub>5</sub>-ZnTPP)** or **poly(PEG<sub>5</sub>-ZnTPP)-(CD<sub>5</sub>-Me<sub>15</sub>)**. After the polymerization went to completion, excess **Biotin-TA** was added to quench the reaction to yield the desired diblock copolymer **poly(PEG<sub>5</sub>-ZnTPP)-(CD<sub>5</sub>-Me<sub>15</sub>)-biotin**, and the excess **Biotin TA** in the crude product

was removed by dialysis against DMF for three days before the product polymer was used for conjugation experiments, and the successful biotinylation was confirmed by  $^1\text{H}$  NMR spectroscopy as well with the peaks in the diblock copolymer after dialysis related to **Biotin-TA** (**Figure 4.5**). The polymerizations were also characterized by analytical GPC as shown in **Figure 4.6**. As shown in **Figure 4.6a**, there was an obvious shift for the polymers compared to the **Nb-PEG** monomer peak, which indicated the successful polymerization. After addition of the excess **Biotin-TA** into the polymerization, the peak of **Biotin-TA** showed up in the crude reaction mixture. While **Figure 4.6b** confirmed the removal of excess of **Biotin-TA** after dialysis with the disappearance of its peak.

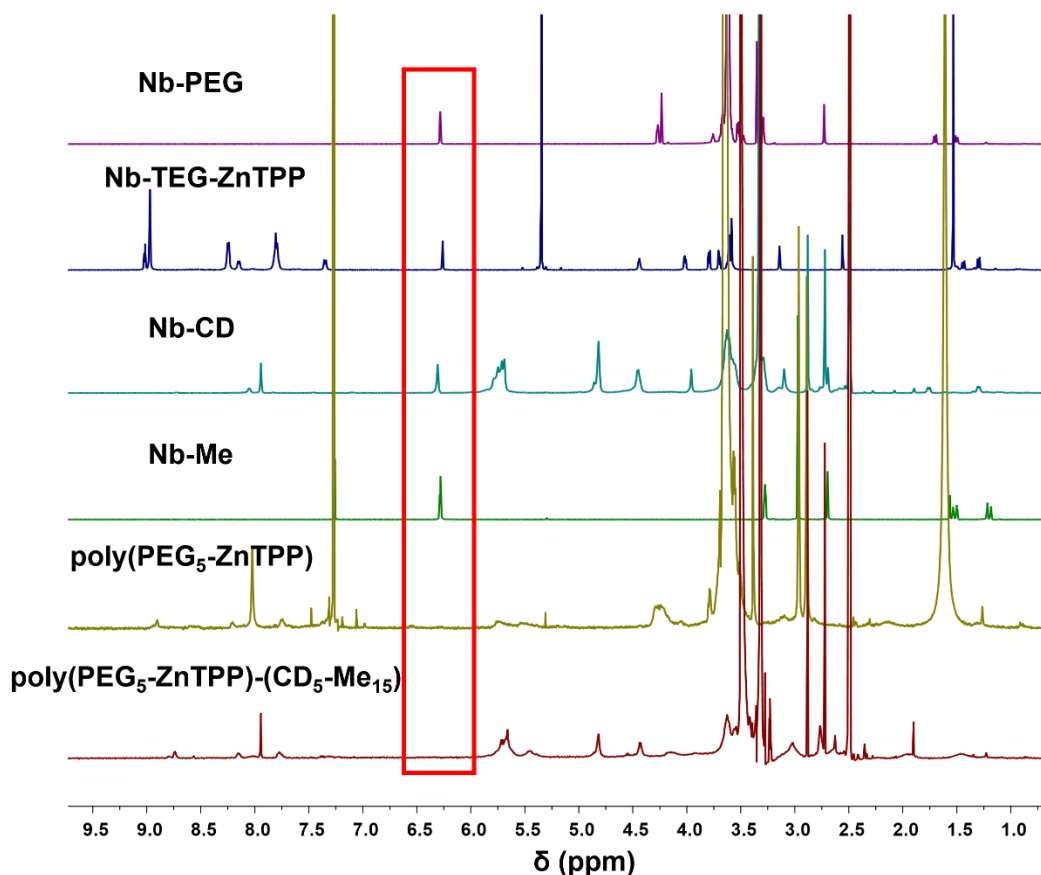


**Figure 4.4.**  $^1\text{H}$  NMR (500 MHz, 25 °C,  $(\text{CD}_3)_2\text{SO}$ ) spectra of Nb-PEG, Nb-TEG-ZnTPP, Nb-CD, Nb-Me, poly(PEG<sub>5</sub>-ZnTPP), poly(PEG<sub>5</sub>-ZnTPP)-(CD<sub>5</sub>-Me<sub>15</sub>) (from top to bottom).

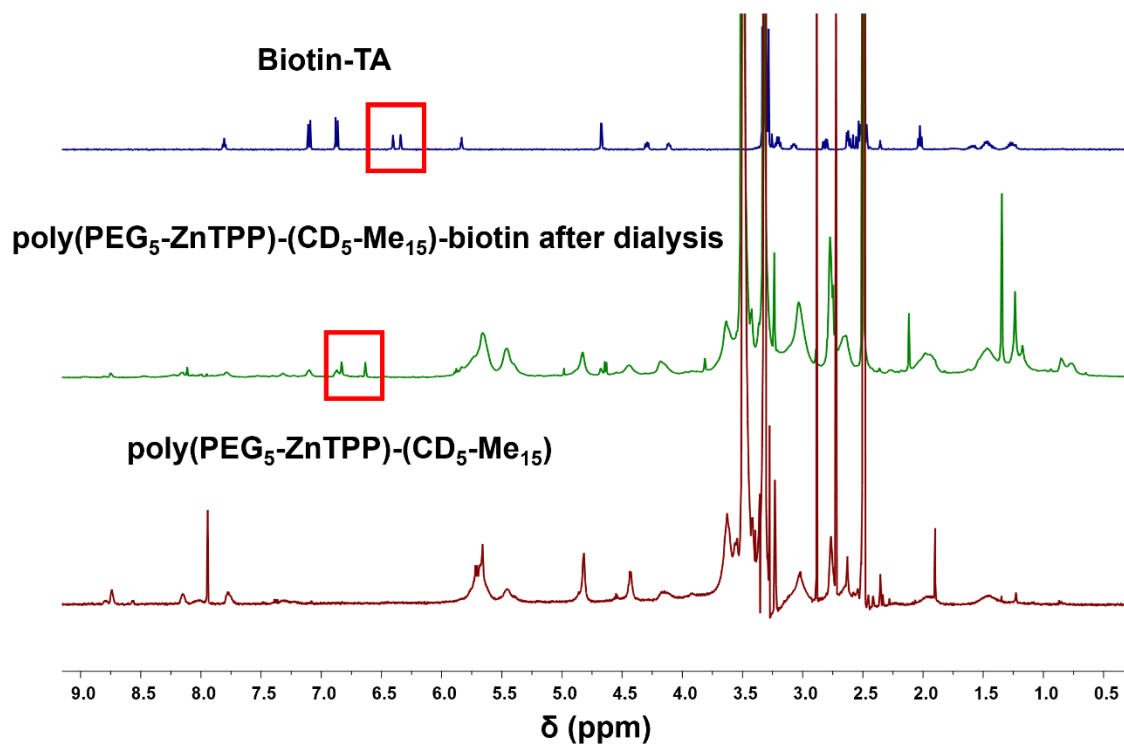


**Figure 4.5.**  $^1\text{H}$  NMR (500 MHz, 25 °C,  $(\text{CD}_3)_2\text{SO}$ ) spectra of **Biotin-TA**, **poly(PEG<sub>5</sub>-ZnTPP)-(CD<sub>5</sub>-Me<sub>15</sub>)-biotin** after dialysis, **poly(PEG<sub>5</sub>-ZnTPP)-(CD<sub>5</sub>-Me<sub>15</sub>)** (from top to bottom).

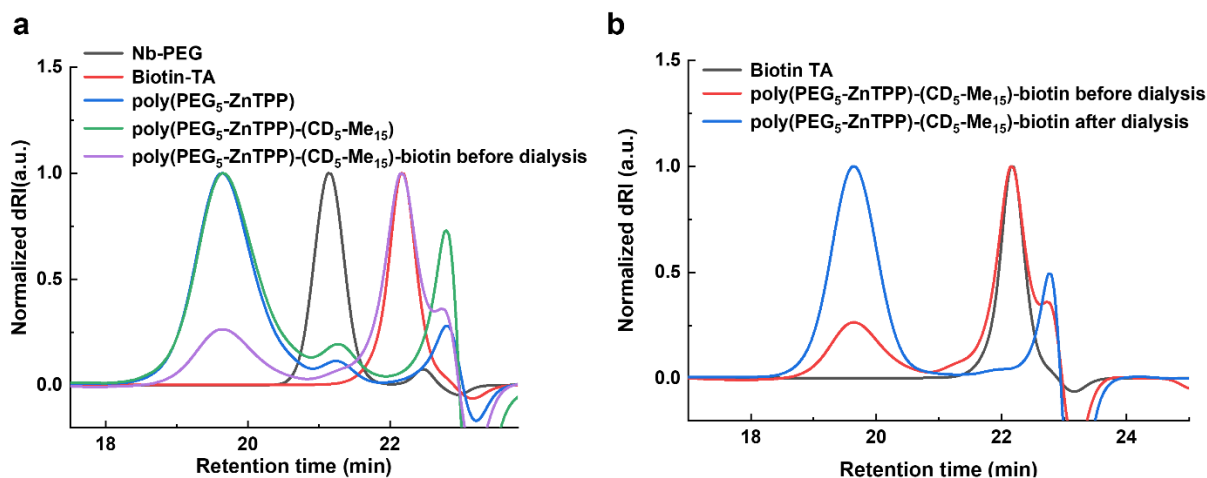


**Figure 4.6.** Overlay of analytical GPC traces in DMF with 0.025 M LiBr at 60 °C at 1.0 mL·min<sup>-1</sup>: (a) **Nb-PEG**, **Biotin-TA**, **poly(PEG<sub>5</sub>-ZnTPP)**, **poly(PEG<sub>5</sub>-ZnTPP)-(CD<sub>5</sub>-Me<sub>15</sub>)**, **poly(PEG<sub>5</sub>-ZnTPP)-(CD<sub>5</sub>-Me<sub>15</sub>)-biotin** before dialysis. (b) **Biotin-TA**, **poly(PEG<sub>5</sub>-ZnTPP)-(CD<sub>5</sub>-Me<sub>15</sub>)-biotin** before and after dialysis.

To further confirm the successful biotinylation of the diblock copolymer, SDS-PAGE analysis was carried out using the diblock copolymer **poly(PEG<sub>5</sub>-ZnTPP)-(CD<sub>5</sub>-Me<sub>15</sub>)-biotin** after dialysis and

commercially bought streptavidin. As previously reported by Mosebi and co-workers,<sup>13</sup> streptavidin itself will go through protein denaturation through boiling for 5 minutes and SDS treatment and thus separates into its monomeric subunits (~16 kDa). However, when streptavidin is bound with biotin, it will stay as a stable tetramer even treated with the same boiling and SDS treatment process. With this knowledge, I did the similar SDS-PAGE experiments, and the results were shown in **Figure 4.7a**. It was clear in lane A, streptavidin separated into the monomers as reported in the literature. While in lanes B and C, with the molar ratio of streptavidin to the diblock copolymer as 1:50 or 1:100, respectively, it was obvious there were almost no more monomer bands, meaning the biotinylated diblock copolymer bound to the streptavidin and stayed in the tetramer form. It was also confirmed that the small biotin molecules needed to be used in excess as illustrated in **Figure 4.7b**. Nevertheless, these results demonstrate the successful biotinylation of the diblock copolymer and its ability to bind streptavidin.

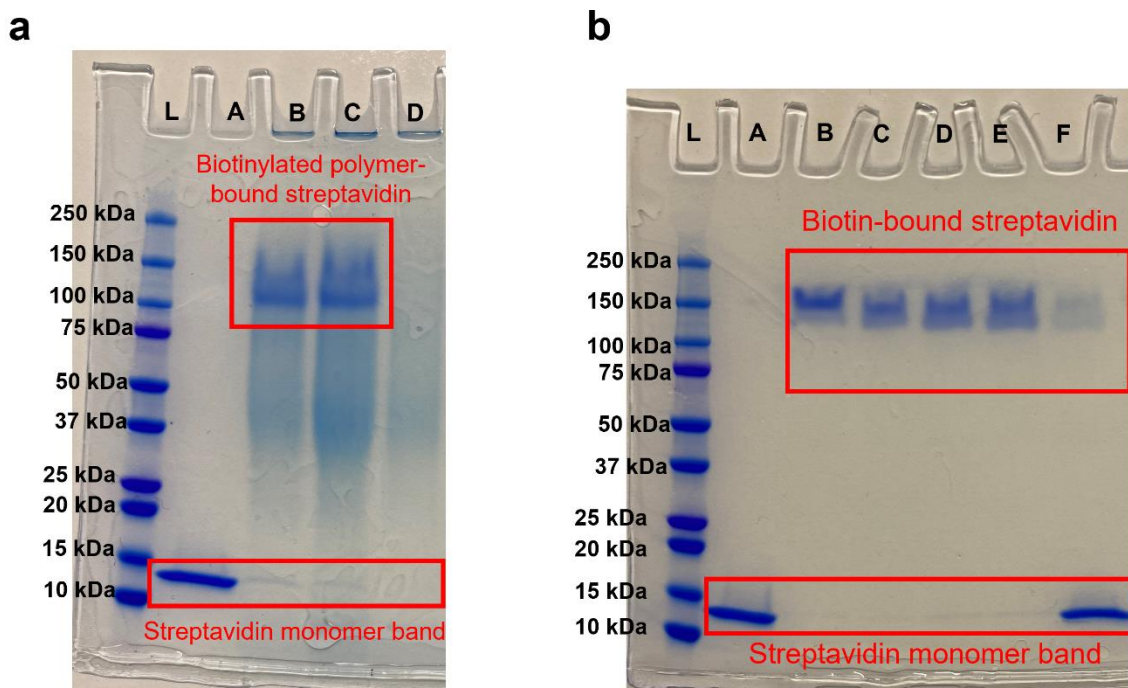


**Figure 4.7.** (a) SDS-PAGE results of streptavidin and diblock copolymer. Lane L: ladder; lane A: streptavidin; lane B: streptavidin mixed with diblock copolymer with a molar ratio of 1:50; lane C: streptavidin mixed with diblock copolymer with a molar ratio of 1:100; lane D: diblock copolymer. (b) SDS-PAGE results of streptavidin and small biotin molecule. Lane L: ladder; lane A: streptavidin; lane B: streptavidin mixed with small biotin molecule with a molar ratio of 1:50000; lane C: streptavidin mixed with small biotin molecule with a molar ratio of 1:5000; lane D: streptavidin mixed with small biotin molecule with a molar ratio of 1:500; lane E: streptavidin mixed with small biotin molecule with a molar ratio of 1:50; lane F: streptavidin mixed with small biotin molecule with a molar ratio of 1:5.

### 4.3.2 Characterization of mini-Agrin mSA

As for the protein side, the Miner Lab designed a new mini-Agrin protein that is fused to a mSA. Different amounts of mini-Agrin-mSA along with a negative control (PBS) were injected into different mice through retro-orbital sinus injection, which is an easy and reliable approach for intravascular delivery of various agents.<sup>14</sup> The kidneys of different mice used for this experiment were collected 1 h after injection and stained for the Myc tag (engineered in the mini-Agrin mSA sequence for purification and detection). As illustrated in **Figure 4.8**, the injected mini-Agrin-mSA protein successfully bound to the GBM in a dose-dependent fashion, as evidenced by the Myc tag staining signal in the GBM and no staining observed for the negative control. If the diblock copolymer could bind to the mini-Agrin-mSA to form a protein-polymer complex, and thus localize together in GBM in a mouse, it will be more effective in delivering drugs as the polymer has the ability to load drugs. Unfortunately, when the mini-Agrin-mSA was mixed with the biotinylated polymer with different molar ratios, there was no evidence of formation of the expected complex. However, it was tested that even a small fluorescently labelled biotin (i.e., Alexa488-PEG-biotin) did not bind the mini-Agrin-mSA. On the other hand, biotin-coated magnetic beads could pull-down mini-Agrin-mSA, suggesting the recombinant protein can bind biotin under certain circumstances, it was probably due to that the monomeric streptavidin incorporated into the mini-Agrin protein decreased the binding affinity with biotin compared to the tetramer streptavidin.

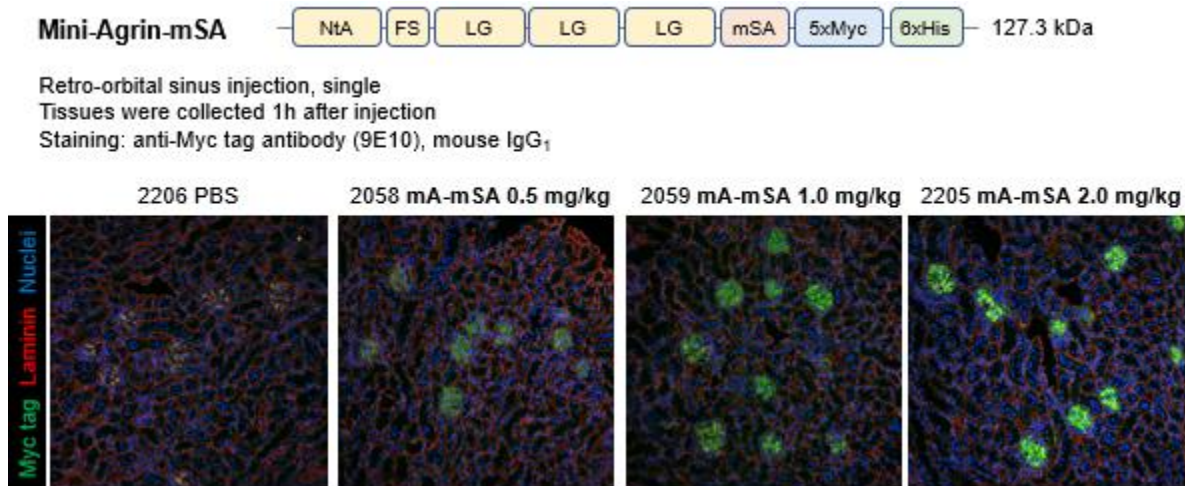


**Figure 4.8.** Schematic diagram (top) shows the domains of mini-Agrin-mSA and the epitope tags used for its purification and detection. Four different mice were injected i.v. with either PBS (left) or increasing doses of mini-Agrin-mSA. Kidneys were collected 1 h after injection and stained for the Myc tag. Increasing amounts of injected protein were detected in glomeruli.

## 4.4 Materials and Methods

### 4.4.1 Experimental Methods

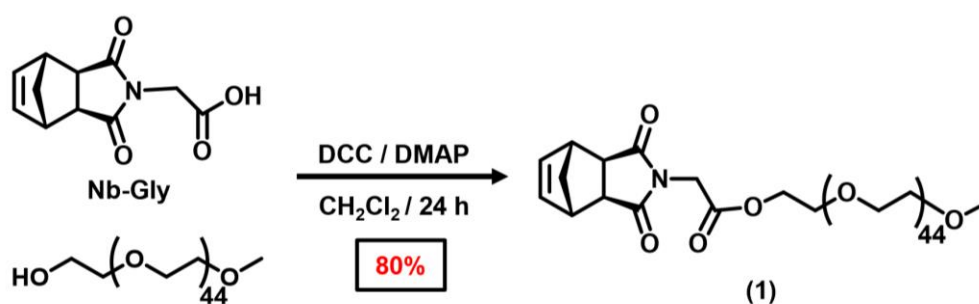
All reagents were purchased from commercial suppliers and used without further purification unless stated otherwise. All reactions were performed under nitrogen (N<sub>2</sub>) or argon (Ar) gas unless otherwise stated. Column chromatography was carried out on silica gel 60F (EMD Millipore, 0.040–0.063 mm). Polymerization of all polymers was performed under an inert atmosphere of UHP N<sub>2</sub> in glovebox using a modified Grubbs' 3rd generation catalyst that was prepared according to a previously reported protocol.<sup>15</sup> All nuclear magnetic resonance (NMR) spectra were recorded on Varian Inova-500 with working frequencies of 500 (<sup>1</sup>H) and 125 (<sup>13</sup>C) MHz. Chemical shifts are reported in ppm relative to the signals corresponding to the residual non-deuterated solvent: CDCl<sub>3</sub>:  $\delta_H = 7.26$  and  $\delta_C = 77.16$  ppm; (CD<sub>3</sub>)<sub>2</sub>SO:  $\delta_H = 2.50$  ppm and  $\delta_C = 39.52$  ppm; D<sub>2</sub>O:  $\delta_H = 4.79$  ppm. Matrix assisted laser desorption/ionization time-of-flight mass spectrometry (MALDI-TOF MS) was recorded on Bruker Solaris 12T FT-MS, sample was prepared using 2,5-dihydroxybenzoic as matrix. Preparative gel permeation chromatography (GPC) analyses were

performed on Japan Analytical Industry LaboACE instrument with one JAIGEL-2HR column and one JAIGEL-2.5HR column in tandem, running with dimethylformamide (DMF) at 8 mL/min. Size exclusion chromatography (SEC) analyses were performed on an Agilent 1260 Infinity setup with two Shodex GPC KD-806M columns in sequence and 0.025 M LiBr in DMF mobile phase run at 60 °C at 1.0 mL·min<sup>-1</sup>. The differential refractive index (dRI) of each compound was monitored using a Wyatt Optilab T-rEX detector and the light scattering (LS) of each compound was monitored using a Wyatt Dawn Heleos-II detector. SDS polyacrylamide gel electrophoresis (PAGE) was performed on 7.5% Mini-PROTEIN<sup>®</sup> TGX<sup>™</sup> precast protein gels (1.0 mm x 10 well; 65 min, 150 V, 1X SDS-PAGE running buffer, pH=8.8). Gels were stained with Coomassie Blue.

#### 4.4.2 Synthetic Methods

Monomers **Nb-PEG**, **Nb-TEG-ZnTPP**, **Nb-CD**, **Nb-Me**, and **Biotin-TA** were used for the synthesis of **poly(PEG<sub>5</sub>-ZnTPP)-(CD<sub>5</sub>-Me<sub>15</sub>)-biotin**. The synthetic procedures of **Nb-TEG-ZnTPP**, **Nb-CD**, **Nb-Me**, and **Nb-Gly** (which is used to make **Nb-PEG**) can be found in Chapter 2. The synthetic procedures of **Nb-PEG** and **Biotin-TA** will be described below. The synthesis of **Biotin-TA** is based on the paper published by Grubbs and coworkers.<sup>16</sup>

#### Synthesis of **Nb-PEG** (1)

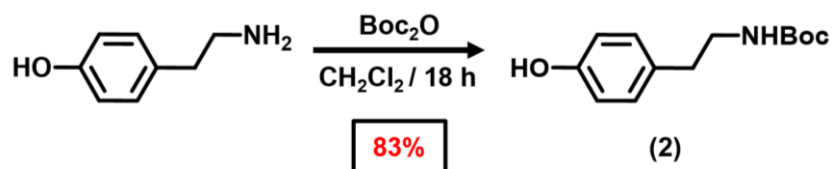


**Scheme 4.1.** Synthesis of **Nb-PEG**.

Compound **1** was synthesized according to a previously reported literature procedure.<sup>17</sup> To the mixture of **Nb-Gly** (165.9 mg, 0.00075 mmol, 1.5 equiv.), poly(ethylene glycol) methyl ether

( $M_n=2000$ , 1 g, 0.0005 mmol, 1 equiv.), dicyclohexylcarbodiimide (DCC, 123.8 mg, 0.0006 mmol, 1.2 equiv.), and 4-dimethylaminopyridine (DMAP, 14.66 mg, 0.00012 mmol, 0.24 equiv.),  $\text{CH}_2\text{Cl}_2$  (anhydrous, 10 mL) was added. After stirring at room temperature for 24 h, DCU was filtered, the crude product was purified by preparative GPC with DMF as eluent to yield the product **1** as a white solid (880 mg, 80% yield).  $^1\text{H NMR}$  (500 MHz,  $(\text{CD}_3)_2\text{SO}$ ):  $\delta_H$  6.32 (t,  $J = 1.5$  Hz, 2H), 4.21 – 4.18 (m, 4H), 3.66 – 3.63 (m, 2H), 3.61 – 3.58 (m, 3H), 3.57 – 3.48 (m, 160H), 3.43 (m, 3H), 3.38 – 3.35 (m, 3H), 3.24 (s, 4H), 3.13 (s, 2H), 1.60 (d,  $J = 9.4$  Hz, 2H), 1.36 (d,  $J = 9.7$  Hz, 2H). ESI-MS ( $m/z$ ): calculated for  $\text{C}_{14}\text{H}_{16}\text{NO}_5(\text{C}_2\text{H}_4\text{O})_{44}$ , 2217.2669; found, 2217.2710  $[M+H]^+$ .

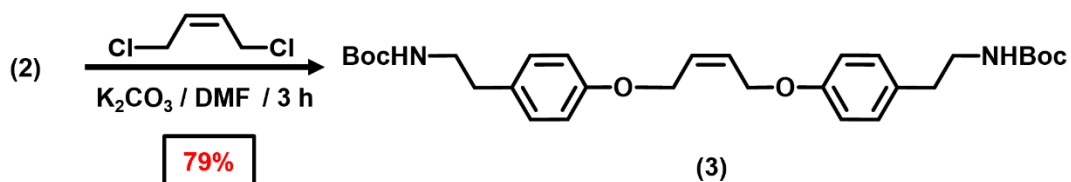
### Synthesis of Boc-Tyramine (2)



#### Scheme 4.2. Synthesis of Boc-Tyramine.

To a solution of 4-(2-aminoethyl) phenol (2g, 14.58 mmol, 1 equiv.) in dry  $\text{CH}_2\text{Cl}_2$  (25 mL),  $\text{Et}_3\text{N}$  (2.21g, 21.87 mmol, 1.5 equiv.) and Di-tert-butylidicarbonate ( $\text{Boc}_2\text{O}$ , 3.18g, 14.58 mmol 1 equiv.) was added at 0 °C. After stirring at 0 °C for 30 min, the reaction mixture was left to stir overnight at room temperature under  $\text{N}_2$ . The reaction mixture was treated with 30 mL saturated  $\text{NaHCO}_3$  solution. The organic layer was separated, and the aqueous layer was extracted with  $\text{CH}_2\text{Cl}_2$ . The combined organic layers were washed with brine, dried over  $\text{Na}_2\text{SO}_4$ , filtered and concentrated. Then the crude product was purified by column chromatography (silica gel, 7:3 hexane: EtOAc) as eluent to yield the desired product **2** as white solid (2.87 g, 83% yield).  $^1\text{H NMR}$  (500 MHz,  $\text{CDCl}_3$ ):  $\delta_H$  7.05 – 7.01 (m, 2H); 6.77 (d,  $J = 7.7$  Hz, 2H); 6.43 (s, 1H); 4.56 (s, 1H); 3.37 – 3.29 (m, 2H); 2.71 (t,  $J = 6.8$  Hz, 2H); 1.44(s, 2H).  $^{13}\text{C NMR}$  (125 MHz,  $\text{CDCl}_3$ ):  $\delta_C$  156.37, 154.86, 130.48, 129.93, 115.63, 79.75, 42.20, 35.39, 28.56.

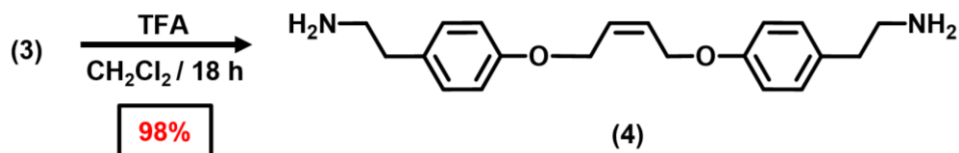
### Synthesis of Boc-Amine TA (3)



#### Scheme 4.3. Synthesis of Boc-Amine TA.

**2** (2.64g, 11.64 mmol, 2.12 equiv.), K<sub>2</sub>CO<sub>3</sub> (2.424g, 17.52 mmol, 3.3 equiv.) was added into a round-bottom flask with DMF (30 mL). Then 1,4-dichloro-cis-2-butene (0.713g, 5.4 mmol, 1 equiv.) was added and the reaction mixture was heated at 90 °C. After 3 h, the solvent was removed by rotary evaporation and the residue was re-dissolved in CH<sub>2</sub>Cl<sub>2</sub>. The mixture was washed with H<sub>2</sub>O and brine, and then dried over Na<sub>2</sub>SO<sub>4</sub>. The crude product was further purified by column chromatography (1% methanol in CH<sub>2</sub>Cl<sub>2</sub>) to yield the desired product **(3)** as white solid (2.9 g, 79% yield). <sup>1</sup>H NMR (500 MHz, CDCl<sub>3</sub>): δ<sub>H</sub> 7.13 – 7.07 (m, 4H); 6.87 – 6.83 (m, 4H); 5.93 (t, *J* = 3.5 Hz, 2H); 4.65 (d, *J* = 4.2 Hz, 4H); 4.55 (s, 2H); 3.34 (q, *J* = 5.8 Hz, 4H); 2.73 (t, *J* = 7.0 Hz, 4H); 1.43 (s, 18H). <sup>13</sup>C NMR (125 MHz, CDCl<sub>3</sub>): δ<sub>C</sub> 157.16, 156.00, 131.58, 129.92, 128.75, 114.91, 79.27, 64.35, 42.08, 35.44, 28.55.

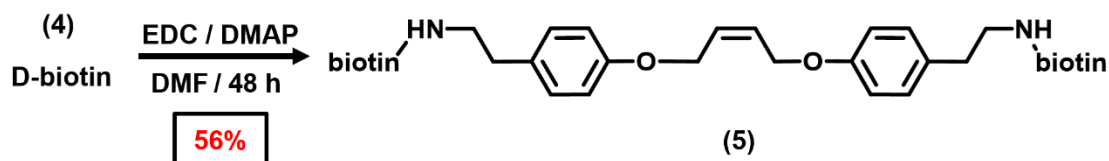
### Synthesis of Amine TA (4)



**Scheme 4.4.** Synthesis of **Amine TA**.

**3** (0.5 g, 0.95 mmol, 1 equiv.) and  $\text{CH}_2\text{Cl}_2$  (10 mL) was added. Trifluoroacetic acid (TFA, 1.5 mL, 9.8 mmol, 10 equiv.) was then added, and the flask was capped with a septum with a needle through it. The reaction was stirred overnight and then  $\text{CH}_2\text{Cl}_2$  was removed by rotary evaporation. Then it was quenched with 5% aqueous  $\text{NH}_4\text{OH}$  and diluted with  $\text{H}_2\text{O}$  and ethyl acetate was added. The organic layer with ethyl acetate was removed and the aqueous layer was washed with 15 mL ethyl acetate for 3 times. The organic layers were combined and dried over  $\text{Na}_2\text{SO}_4$ . The solvent was removed by rotary evaporation to afford the desired product **4** as yellow oil (305 mg, 98% yield).  $^1\text{H}$  NMR (500 MHz,  $\text{CDCl}_3$ ):  $\delta_{\text{H}}$  7.12 – 7.09 (m, 4H); 6.87 – 6.83 (m, 4H); 5.92 (t, 3.3Hz, 2H); 4.65 (d,  $J = 4.2$  Hz, 4H); 2.92 (t,  $J = 6.9$  Hz, 4H); 2.69 (t,  $J = 6.9$  Hz, 4H).  $^{13}\text{C}$  NMR (125 MHz,  $\text{CDCl}_3$ ):  $\delta_{\text{C}}$  157.02, 132.34, 129.93, 128.76, 114.84, 64.38, 43.75, 39.16.

**Synthesis of Biotin TA (5)**

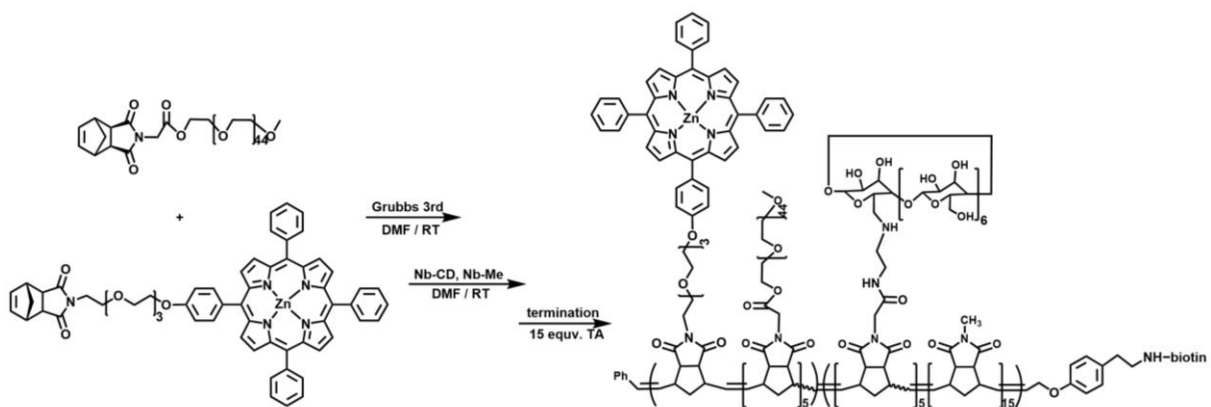


**Scheme 4.5.** Synthesis of **Biotin TA**.

D-biotin (173 mg, 0.71 mmol, 2.6 equiv.) and DMF (3 mL) was added to an oven-dried round-bottom flask, then EDC (160 mg, 0.85 mmol, 3.1 equiv.) and DMAP (6.6 mg, 0.05 mmol, 0.2 equiv.) was added. After stirring for 15 min, **4** (88 mg, 0.27 mmol, 1 equiv.) was added as a

solution in DMF (3 mL). The light-yellow reaction mixture was allowed to stir at 45 °C under argon. After 48 h the DMF was removed by rotary evaporation. The crude mixture was washed with sufficient H<sub>2</sub>O and filtered. Then the solid was washed with toluene/MeOH (4:1) to afford the desired product (**5**) as white solid (150 mg, 56 % yield). <sup>1</sup>H NMR (500 MHz, DMSO-*d*<sub>6</sub>): δ<sub>H</sub> 7.82 (t, *J* = 5.6 Hz, 2H); 7.11 (d, *J* = 8.6 Hz, 4H); 6.87 (d, *J* = 8.6 Hz, 4H); 6.42 (s, 2H); 6.35 (s, 2H); 5.84 (t, *J* = 3.6 Hz, 2H); 4.68 (d, *J* = 3.8 Hz, 4H); 4.31 – 4.28 (m, 2H); 4.14 – 4.10 (m, 2H); 3.23 – 3.18 (m, 4H); 3.11 – 3.06 (m, 2H); 2.83 – 2.78 (m, 2H); 2.65 – 2.56 (m, 6H); 2.03 (t, *J* = 7.4 Hz, 4H); 1.63 – 1.21 (m, 12H). <sup>13</sup>C NMR (125 MHz, DMSO-*d*<sub>6</sub>): δ<sub>C</sub> 171.89, 162.70, 156.48, 131.69, 129.56, 128.46, 114.50, 63.78, 61.04, 59.20, 55.43, 40.30, 35.20, 34.34, 28.18, 28.04, 25.30. MALDI-TOF calculated for C<sub>40</sub>H<sub>54</sub>N<sub>6</sub>O<sub>6</sub>S<sub>2</sub> (m/z) 778.35, found: 801 [*M*+Na]<sup>+</sup>.

#### Synthesis of diblock copolymer poly(PEG<sub>5</sub>-ZnTPP)-(CD<sub>5</sub>-Me<sub>15</sub>)-biotin



#### Scheme 4.6. Synthesis of diblock copolymer poly(PEG<sub>5</sub>-ZnTPP)-(CD<sub>5</sub>-Me<sub>15</sub>)-biotin.

A solution of modified Grubbs 3rd generation catalyst (G3G) was freshly prepared in DMF. G3G (0.097 mL, 1.41 mg, 1.94 μmol, 1 equiv.) was added to a solution of **Nb-PEG** (21.5 mg, 9.7 μmol, 5 equiv.) and **Nb-TEG-TPP-Zn** (1.97 mg, 1.94 μmol, 1 equiv.) in 0.097 mL DMF to give G3G: **Nb-PEG** ratio of 1:5 and the concentration of **Nb-PEG** in solution was 0.05 M. The resulting solution was stirred for 3 h at room temperature. Next, the reaction mixture was added to **Nb-CD** (13.39 mg, 9.7 μmol, 5 equiv.) and **Nb-Me** (5.16 mg, 29.09 μmol, 15 equiv.) dissolved in 0.194 mL DMF

and stirred at room temperature for 12 h. After the completion of the polymerization, the reaction was quenched by **Biotin TA** (22.63 mg, 29.09  $\mu\text{mol}$ , 15 equiv.) and stirred for 12 h. Then the reaction mixture was transferred to the dialysis tubing (RC dialysis tubing, 1 kDa molecular weight cut-off, 38 mm flat-width), and was placed in a beaker with 500 mL DMF to remove the excess **Biotin TA**. The dialysis was going on for 3 days. After 3 days, DMF was switched to  $\text{H}_2\text{O}$  in the beaker and the dialysis was continued in  $\text{H}_2\text{O}$  for another day. After the dialysis was completed, the diblock copolymer was yielded as purple solid after 12 h of lyophilization (34.5 mg, 78% yield).

## 4.5 Conclusions

The design, synthesis, and characterization of a biotinylated CD-based diblock copolymer is reported. The diblock copolymer was synthesized through ROMP and mono-biotinylated using a (bis)biotin-functionalized olefin quenching agent to yield the polymer terminated with a single biotin functional group that can be used as a coupling site for streptavidin. The successful biotinylation of the designed diblock copolymer was confirmed by the coupling to streptavidin by SDS-PAGE. The new engineered protein mini-Agrin-mSA was shown to localize in GBM in mice after 1h post-injection. However, the monomeric streptavidin incorporated into the mini-Agrin protein decreased the binding affinity with biotin compared to the tetramer streptavidin. Therefore, it was challenging to form the desired complex between the biotinylated diblock copolymer and mini-Agrin-mSA, perhaps the large molar masses of both the protein and diblock copolymer likely affected the stability of bioconjugate. In the future, alternative conjugation approach may be considered. For example, new biotinylated mini-Agrin (using the AviTag peptide and biotin ligase)<sup>18</sup> may be engineered and tetrameric avidin can be used to link together it together with the biotinylated diblock copolymer.

## 4.6 References

- (1) Kovesdy, C. P. Epidemiology of chronic kidney disease: an update 2022. *Kidney Int. Suppl.* **2022**, *12* (1), 7-11.
- (2) Langer, R. New Methods of Drug Delivery. *Science* **1990**, *249* (4976), 1527-1533.
- (3) Ringsdorf, H. Structure and properties of pharmacologically active polymers. *J. Polym. Sci., Polym. Symp.* **1975**, *51* (1), 135-153.
- (4) Larson, N.; Ghandehari, H. Polymeric Conjugates for Drug Delivery. *Chem. Mater.* **2012**, *24* (5), 840-853.
- (5) Zhang, Q.; Fu, Y.; Liu, R.; Gong, T.; Sun, X.; Zhang, Z.-R. Renal-specific delivery of prednisolone-folate conjugates for renal ischemia/reperfusion injury. *RSC Adv.* **2014**, *4* (92), 50828-50831.
- (6) Geng, Q.; Sun, X.; Gong, T.; Zhang, Z. R. Peptide-drug conjugate linked via a disulfide bond for kidney targeted drug delivery. *Bioconjug. Chem.* **2012**, *23* (6), 1200-1210.
- (7) Veronese, F. M.; Pasut, G. PEGylation, successful approach to drug delivery. *Drug Discov. Today* **2005**, *10* (21), 1451-1458.
- (8) Abuchowski, A.; van Es, T.; Palczuk, N. C.; Davis, F. F. Alteration of immunological properties of bovine serum albumin by covalent attachment of polyethylene glycol. *J. Biol. Chem.* **1977**, *252* (11), 3578-3581.
- (9) Duncan, R. The dawning era of polymer therapeutics. *Nat. Rev. Drug Discov.* **2003**, *2* (5), 347-360.
- (10) Alconcel, S. N. S.; Baas, A. S.; Maynard, H. D. FDA-approved poly(ethylene glycol)-protein conjugate drugs. *Polym. Chem.* **2011**, *2* (7), 1442-1448.
- (11) Ko, J. H.; Maynard, H. D. A guide to maximizing the therapeutic potential of protein-polymer conjugates by rational design. *Chem. Soc. Rev.* **2018**, *47* (24), 8998-9014.
- (12) González, M.; Bagatolli, L. A.; Echabe, I.; Arrondo, J. L. R.; Argaraña, C. E.; Cantor, C. R.; Fidelio, G. D. Interaction of Biotin with Streptavidin: THERMOSTABILITY AND CONFORMATIONAL CHANGES UPON BINDING\*. *J. Biol. Chem.* **1997**, *272* (17), 11288-11294.
- (13) Mpye, K. L.; Gildenhuis, S.; Mosebi, S. The effects of temperature on streptavidin-biotin binding using affinity isothermal titration calorimetry. *AIMS Biophys.* **2020**, *7* (4), 236-247.
- (14) Yardeni, T.; Eckhaus, M.; Morris, H. D.; Huizing, M.; Hoogstraten-Miller, S. Retro-orbital injections in mice. *Lab Anim (NY)* **2011**, *40* (5), 155-160.
- (15) Love, J. A.; Morgan, J. P.; Trnka, T. M.; Grubbs, R. H. A practical and highly active ruthenium-based catalyst that effects the cross metathesis of acrylonitrile. *Angew. Chem. Int. Ed.* **2002**, *41* (21), 4035-4037.
- (16) Matson, J. B.; Grubbs, R. H. Monotelechelic Poly(oxa)norborenanes by Ring-Opening Metathesis Polymerization Using Direct End-Capping and Cross-Metathesis. *Macromol.* **2010**, *43* (1), 213-221.
- (17) Li, R.; Li, X.; Zhang, Y.; Delawder, A. O.; Colley, N. D.; Whiting, E. A.; Barnes, J. C. Diblock brush-arm star copolymers via a core-first/graft-from approach using  $\gamma$ -cyclodextrin and ROMP: a modular platform for drug delivery. *Polym. Chem.* **2020**, *11* (2), 541-550.

(18) Fairhead, M.; Howarth, M. Site-specific biotinylation of purified proteins using BirA. *Methods Mol. Biol.* **2015**, *1266*, 171-184.

# **Chapter 5: Summary, Future Directions, and Final Thoughts**

## **5.1 Dissertation Summary**

In this dissertation, I have described the research endeavors, obstacles, and achievements that I have encountered during my graduate studies. Our group has been focused on developing next-generation polymeric materials with a broad range of applications. Specifically, I worked on the development of cyclodextrin (CD)-based shear-thinning hydrogels, polymer coatings, and a drug delivery platform through ROMP with potential biomedical applications.

In the introduction of this dissertation, Chapter 1, I started with a general overview of shear-thinning hydrogels, including definitions, properties, and the potential applications. Delving into the previous work in this field, it is clear that host-guest-based chemistry has been employed to a great extent. Particularly, CD is of great interest due to its suitable cavity size for accommodating a wide range of guest molecules, where researchers have investigated different CD-based systems for various applications. Although ATRP and RAFT are the most commonly used controlled polymerization methods to synthesize CD-based polymers, very few have been prepared using ROMP, even though it possesses the advantage of more functional group tolerance for the monomers. Therefore, there is considerable potential for innovation in using ROMP to make CD-based polymers.

In Chapter 2, I described a novel approach for creating shear-thinning hydrogels using ROMP, where a host-guest cross-linked network was soluble in deionized water but became kinetically trapped as a viscous hydrogel once exposed to saltwater. These hydrogels were composed of

polynorbornene-based bottlebrush copolymers with side chains containing porphyrin and oligoviologen units, and they were cross-linked through the reversible formation of  $\beta$ -CD/Ad inclusion complexes. The shear-thinning properties of the hydrogels were “switched on” in response to either heating or exposure to visible light. The viscous hydrogels displayed broad adhesive properties towards polar and non-polar surfaces, including glass, metal, and HDPE. Additional manipulation of the hydrogel’s mechanical properties and performance was attained through a low energy (blue light) photo-induced electron transfer process. We envision these injectable photoredox-responsive hydrogels may be useful in potential biomedical applications, such as in 3D(bio)printing and manufacturing, 4D tissue culture, therapeutic delivery, and regenerative medicine.

With the discovery of the viscous hydrogels described in Chapter 2, I then expanded the utility of these bottlebrush copolymers to fabricate antibacterial polymer coatings (Chapter 3). The self-assembled polymer coatings proved to be stable under static salt solutions over several days and efficiently mitigated the biofilm formation of *P. aeruginosa* under a flow environment. Additionally, the positively charged oligoviologen units inside the polymer chains allowed for the loading of negatively charged antibiotics through electrostatic interactions. The antibiotic-loaded polymer coatings inhibited the bacterial growth even under static conditions. These results demonstrated that the self-assembled bactericidal polymer coating has the potential to be applied to medical devices to mitigate the onset of bacterial infection.

In Chapter 4, I attempted to make protein-polymer conjugates through CD-based polymers, with the goal of treating pediatric glomerular disease. In this project, I designed and synthesized functional polymers that could bind to the protein called “mini-agrin”, which was an engineered protein that had the ability to target the glomerulus basement membrane (GBM). CD-based polymers containing designed functional groups capable of coupling to the protein were

synthesized and characterized. We demonstrated a possible way to delivery drugs to kidney glomeruli through innovative CD-based polymers.

## 5.2 Future Directions

As discussed in Chapter 1 on shear-thinning hydrogels, the cross-linking process does not involve chemical reactions and is predominately reliant on dynamic and inherently weak physical interactions. With the ease of injection for shear-thinning hydrogels, their mechanical strength is usually low. To overcome this, additional exploration has been conducted into secondary crosslinking techniques to enhance the stability of shear-thinning hydrogels, where photo-crosslinking has been used widely to the formation of covalent linkage of the polymeric materials.<sup>1</sup> Burdick and co-workers have investigated a lot in secondary photo-crosslinking by ultraviolet (UV) light. For example, as illustrated in **Figure 5.1**, methacrylates were incorporated into HA macromer that was either functionalized with Ad or CD. In addition to the physical crosslinking through host-guest interactions, a secondary crosslinking of methacrylates was realized with UV light exposure and a radical generating photoinitiator. With this second step, an increase in the storage modulus was observed, accompanied by the cessation of dynamic material behaviors.<sup>2</sup> However, I recognize that UV exposure may induce adverse effects for *in vivo* applications if not properly regulated,<sup>3</sup> therefore, visible light could be used alternatively to reduce harmful effects.<sup>4</sup>

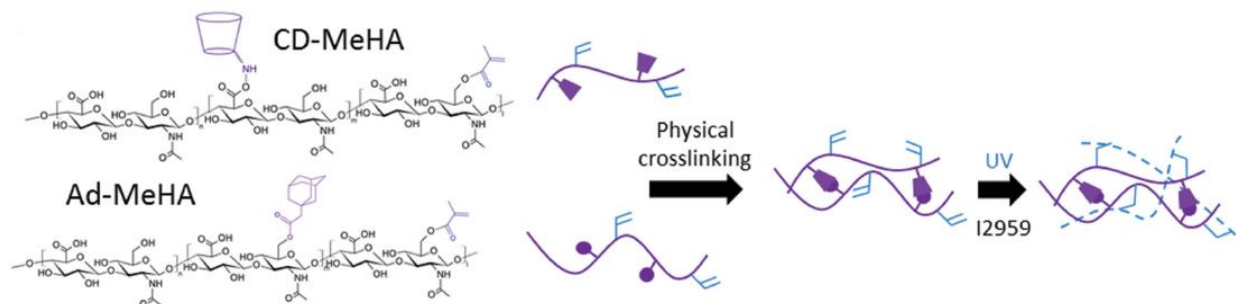


**Figure 5.1.** Hyaluronic acid modified with both methacrylates (blue) and guest and host molecules (purple). Ad-MeHA and CD-MeHA macromers crosslink by both physical bonding upon mixing and through a secondary crosslinking of methacrylates with UV light exposure. Reused with permission. <sup>2</sup>

With this knowledge in hand, we now want to introduce the secondary polymerization into our hydrogel network that was described in Chapter 2 for the purpose of studying the change in the gels' properties while also pursuing potential applications. Specifically, negatively charged ATRP initiators (**I**) (**Figure 5.2a**) will be introduced onto the positively charged oligoviologen sidechains of copolymer **A**: poly( $2V^{4+}Ad_{30}-TEG_{90}-ZnTPP$ )<sub>stat</sub>, similar to the loading of negatively charged antibiotics as described in Chapter 3. The synthesis of this initiator was previously reported by Haddleton and colleagues.<sup>5</sup> An acrylate monomer (**M**, **Figure 5.2a**) will be mixed with copolymer **B**: poly( $CD_{30}-TEG_{90}$ )<sub>stat</sub>, at varying weight percentages of **M**. Then, the two bottlebrush copolymers will be mixed to form the initial **A+B** viscous hydrogel containing both **M** and **I** (**Figure 5.2b**), with the latter two being evaluated at varying stoichiometries to ensure solubility and while also achieving the complete formation of a secondary interpenetrating polymer (**D**). To enable *in situ* polymerization, we will use visible-light-photoinduced ATRP (photo-ATRP),<sup>6, 7</sup> initially relying on the norbornene-based porphyrin monomer (**Nb-ZnTPP**) that we have already incorporated into the chain of copolymer **A**. However, other analogues such as **Nb-FeTPP** may be needed instead to reduce the initiator's C-Br bond and thus initiate the polymerization,<sup>7</sup> which should be synthesized in a similar way as **Nb-ZnTPP**. If the proposed secondary polymerization occurs, the resultant polymeric material's properties (e.g., rheological and adhesive properties) can be further investigated by modifying the polymerization conditions, such as the wavelength of light, the intensity of the light source, and the relative amounts of **I** to **A** and **I** to **M**.

Furthermore, a similar strategy of *in situ* photo-ATRP could also be investigated by adding a crosslinker (**XL**, i.e., PEG-diacrylate, PEG-DA) to copolymer **B** (including **M**) before mixing with copolymer **A** (which is also loaded with **I**) as illustrated in **Figure 5.2c**. We anticipate that incorporating PEG-DA will lead to the formation of a secondary interpenetrating covalent network (**E**), which could enhance the strength and stability of the original "host" **A+B** self-assembled network.

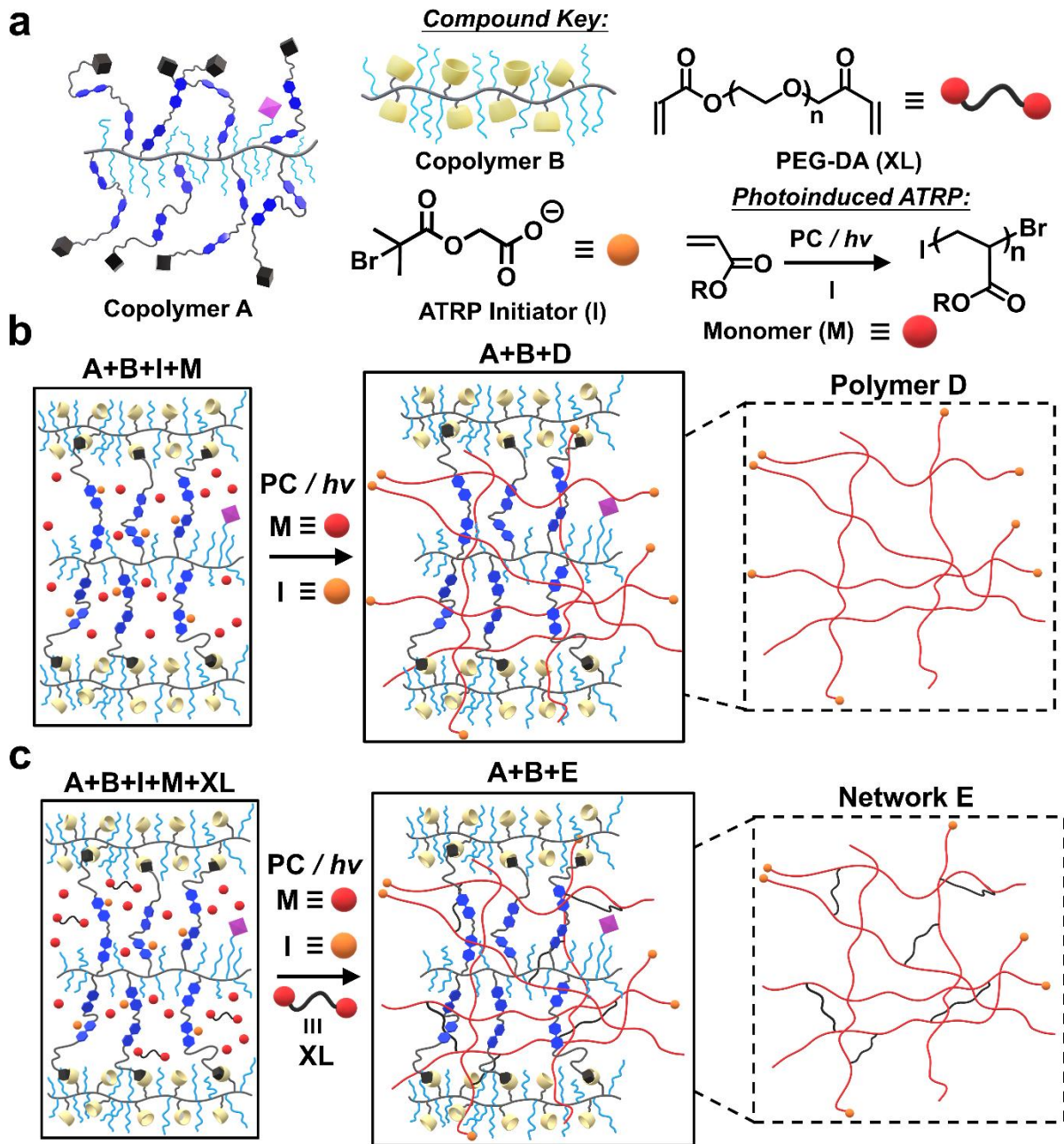


**Figure 5.2.** (a) Compound key showing copolymer **A**: poly( $2V^{4+}Ad_{30}$ -TEG $_{90}$ -ZnTPP) $_{stat}$ , copolymer **B**: poly( $CD_{30}$ -TEG $_{90}$ ) $_{stat}$ , negatively charged ATRP initiator (**I**), crosslinker (**XL**, i.e., PEG diacrylate: PEG-DA), and generic scheme showing photo-ATRP of an acrylate monomer (**M**). (b) Illustration showing the **A+B** viscous hydrogel in saltwater, where **I** has been electrostatically loaded onto the oligoviologen sidechains and **M** has been mixed in prior to a photoinduced ATRP to form *in situ* a second covalent polymer (**D**). (c) Illustration showing **A+B** hydrogel, where **M**, **I**, and **XL** have been mixed into the 'host' network prior to photo-ATRP to form a secondary covalent network (**E**).

We envision that by investigating the optimal ratio of the viscous hydrogel (**A+B**) and the secondary polymer (**D**) or polymer network (**E**), we will be able to controllably stiffen the initial

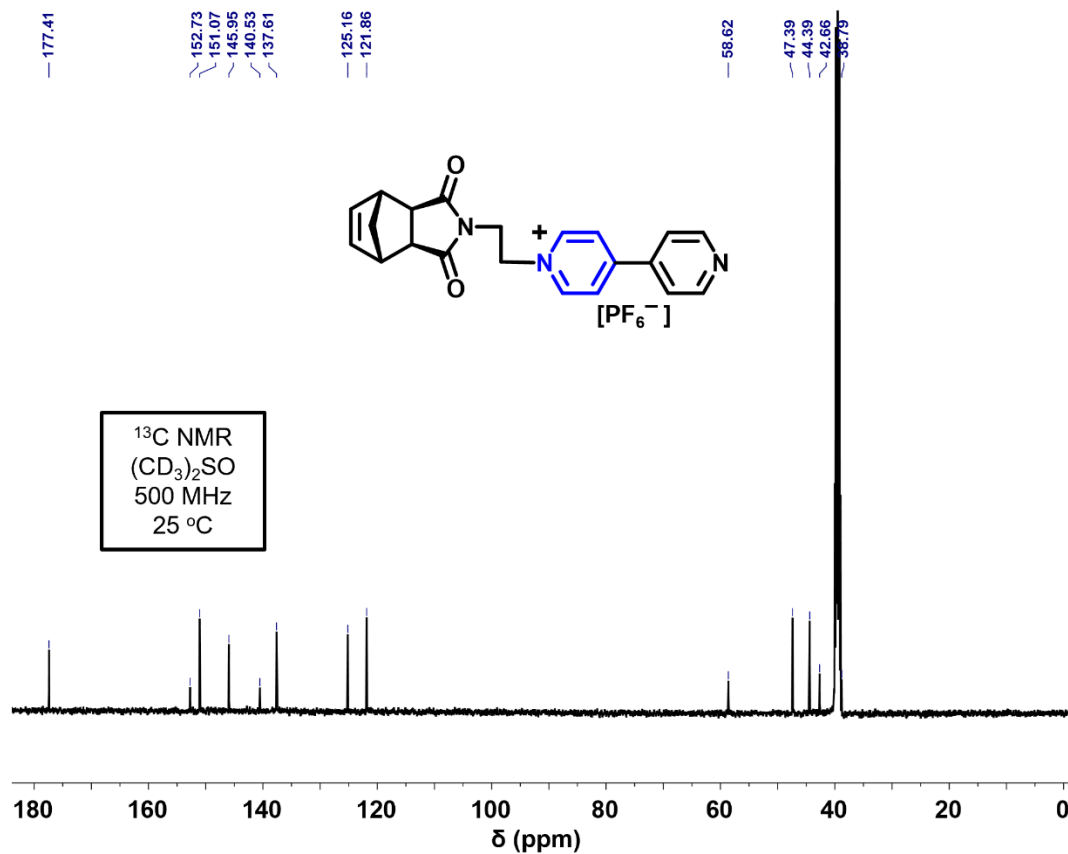
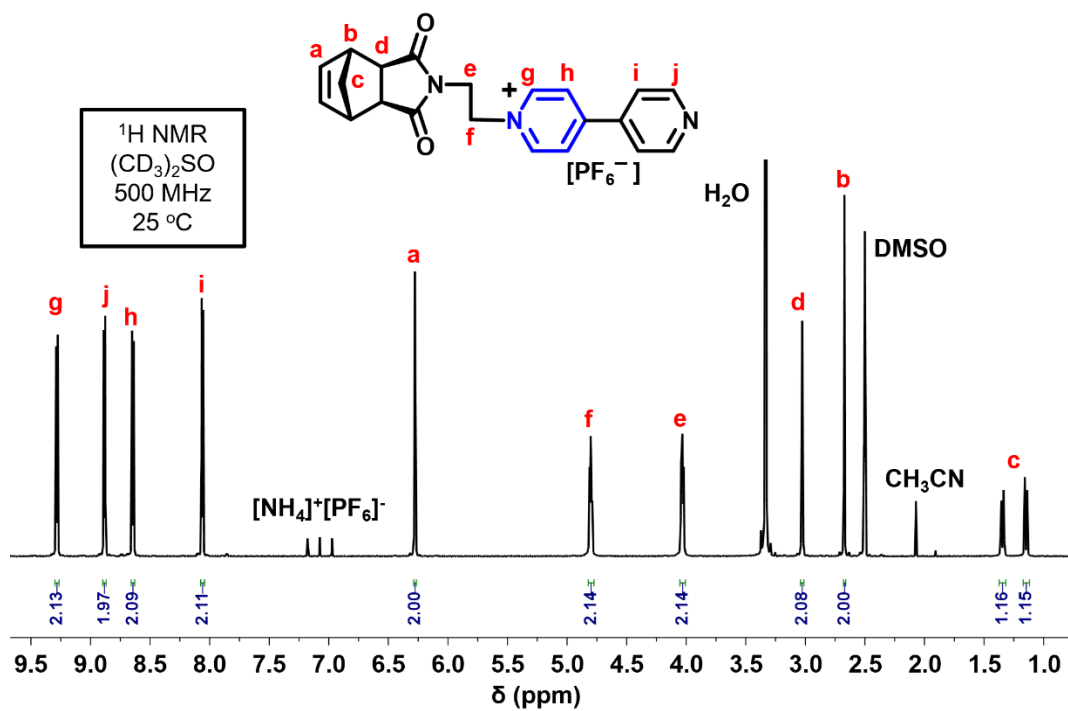
hydrogel network (**A+B**) in response to visible light. Therefore, this next-generation material will be potentially used in applications, such as coatings, injectable adhesives, and in additive manufacturing.

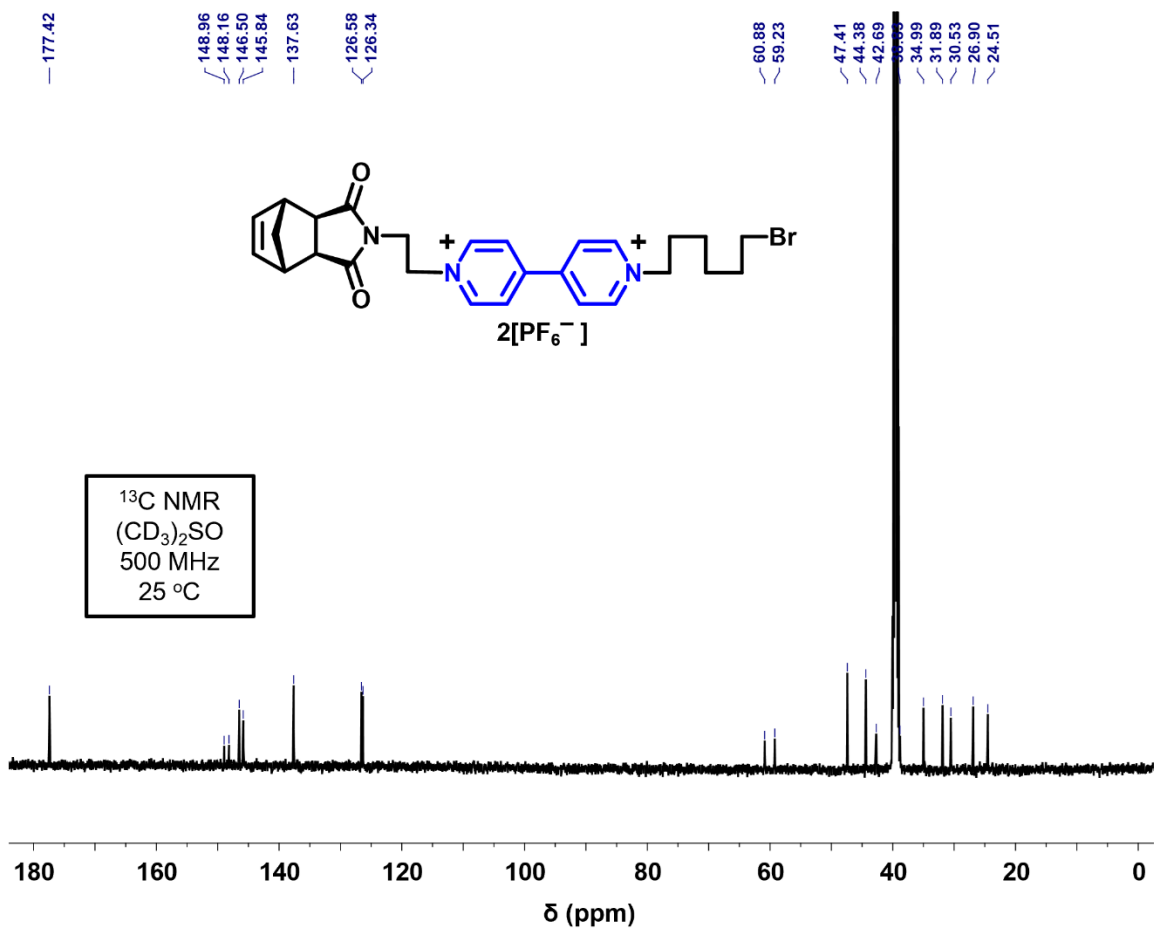
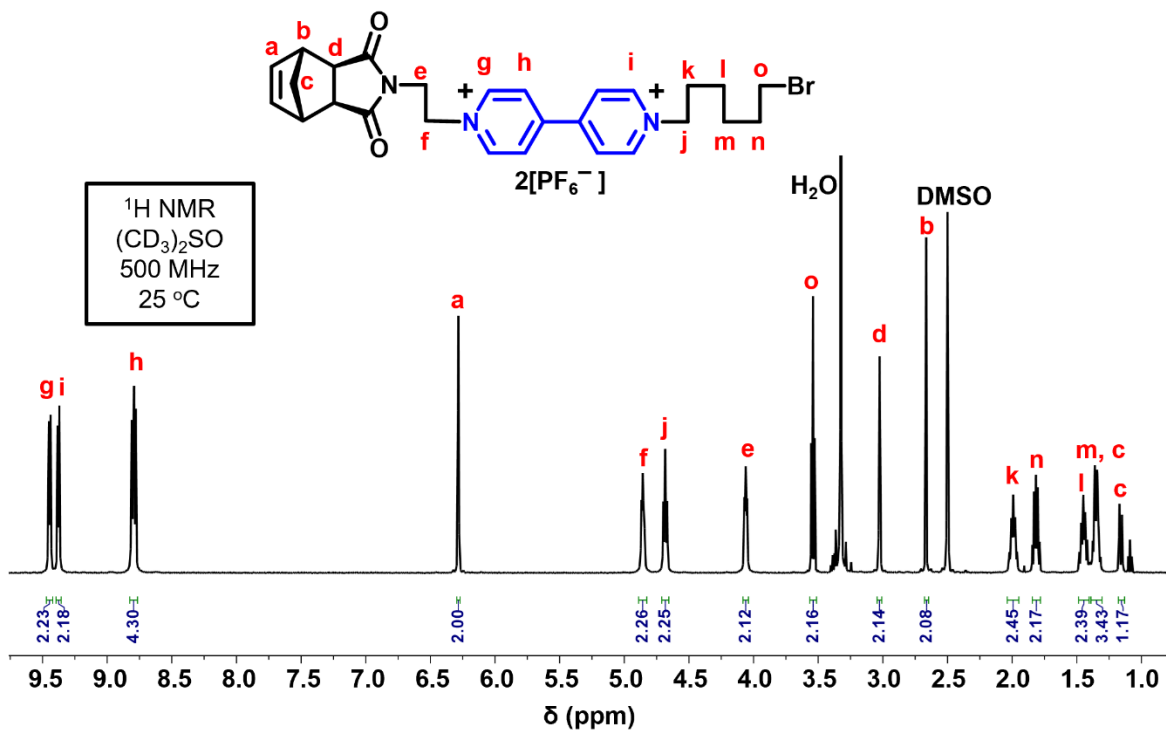
## 5.3 References

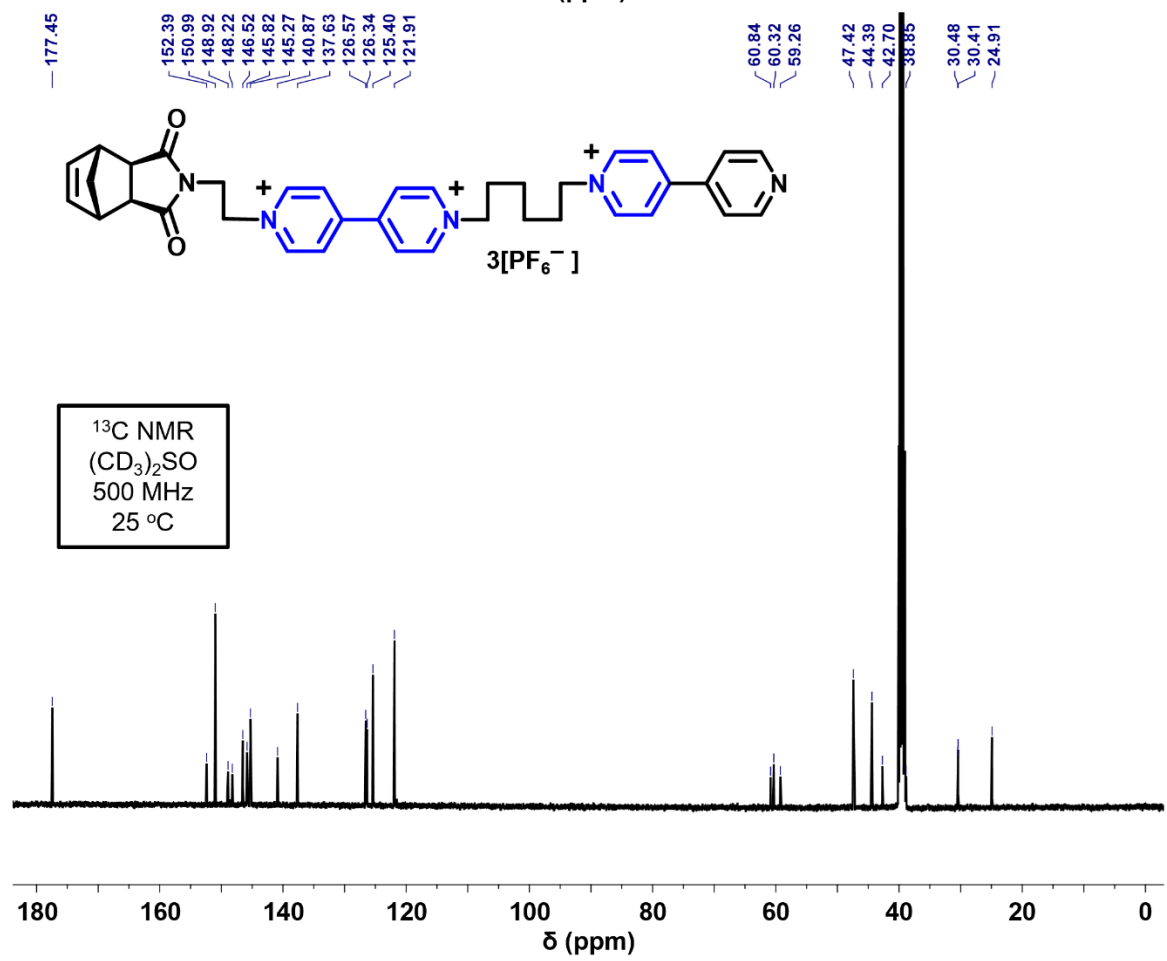
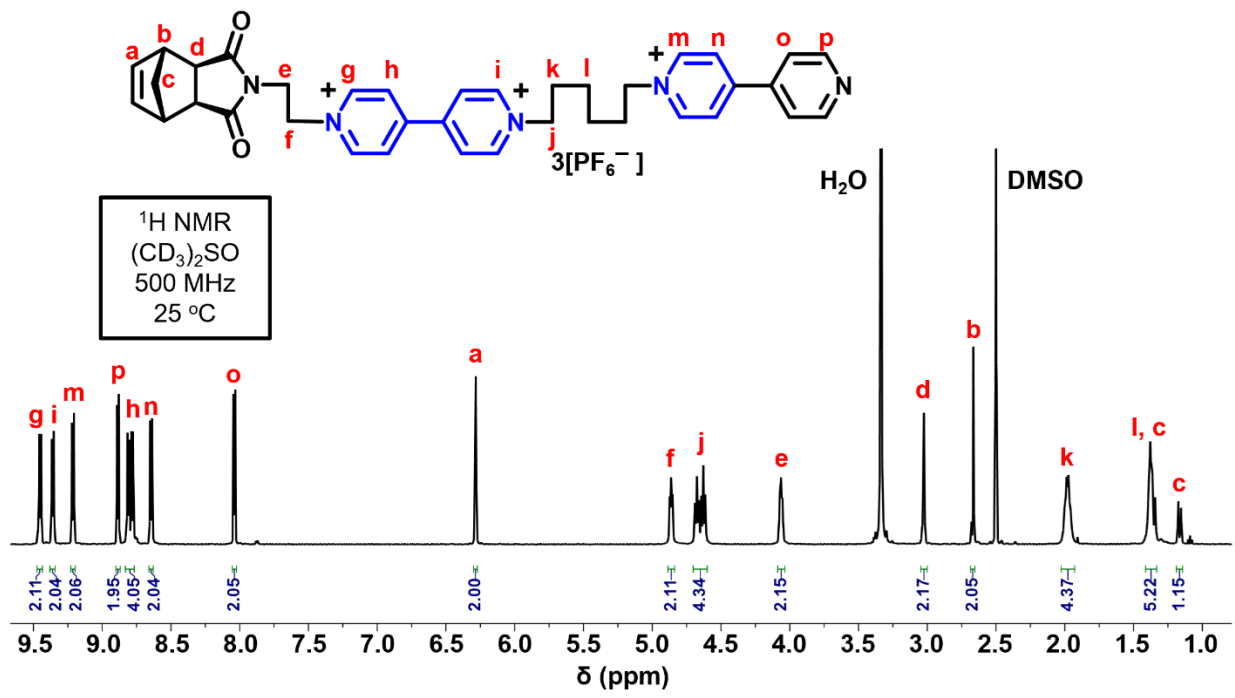
- (1) Jalalvandi, E.; Shavandi, A. Shear thinning/self-healing hydrogel based on natural polymers with secondary photocrosslinking for biomedical applications. *J. Mech. Behav. Biomed. Mater.* **2019**, *90*, 191-201.
- (2) Highley, C. B.; Rodell, C. B.; Burdick, J. A. Direct 3D Printing of Shear-Thinning Hydrogels into Self-Healing Hydrogels. *Adv. Mater.* **2015**, *27* (34), 5075-5079.
- (3) Fedorovich, N. E.; Oudshoorn, M. H.; van Geemen, D.; Hennink, W. E.; Alblas, J.; Dhert, W. J. A. The effect of photopolymerization on stem cells embedded in hydrogels. *Biomater.* **2009**, *30* (3), 344-353.
- (4) Hao, Y.; Shih, H.; Muñoz, Z.; Kemp, A.; Lin, C.-C. Visible light cured thiol-vinyl hydrogels with tunable degradation for 3D cell culture. *Acta Biomater.* **2014**, *10* (1), 104-114.
- (5) Zhu, C.; Schneider, E. K.; Nikolaou, V.; Klein, T.; Li, J.; Davis, T. P.; Whittaker, M. R.; Wilson, P.; Kempe, K.; Velkov, T.; et al. Hydrolyzable Poly[Poly(Ethylene Glycol) Methyl Ether Acrylate]-Colistin Prodrugs through Copper-Mediated Photoinduced Living Radical Polymerization. *Bioconjug. Chem.* **2017**, *28* (7), 1916-1924.
- (6) Treat, N. J.; Sprafke, H.; Kramer, J. W.; Clark, P. G.; Barton, B. E.; Read de Alaniz, J.; Fors, B. P.; Hawker, C. J. Metal-Free Atom Transfer Radical Polymerization. *J. Am. Chem. Soc.* **2014**, *136* (45), 16096-16101.
- (7) Fu, L.; Simakova, A.; Fantin, M.; Wang, Y.; Matyjaszewski, K. Direct ATRP of Methacrylic Acid with Iron-Porphyrin Based Catalysts. *ACS Macro Lett.* **2018**, *7* (1), 26-30.

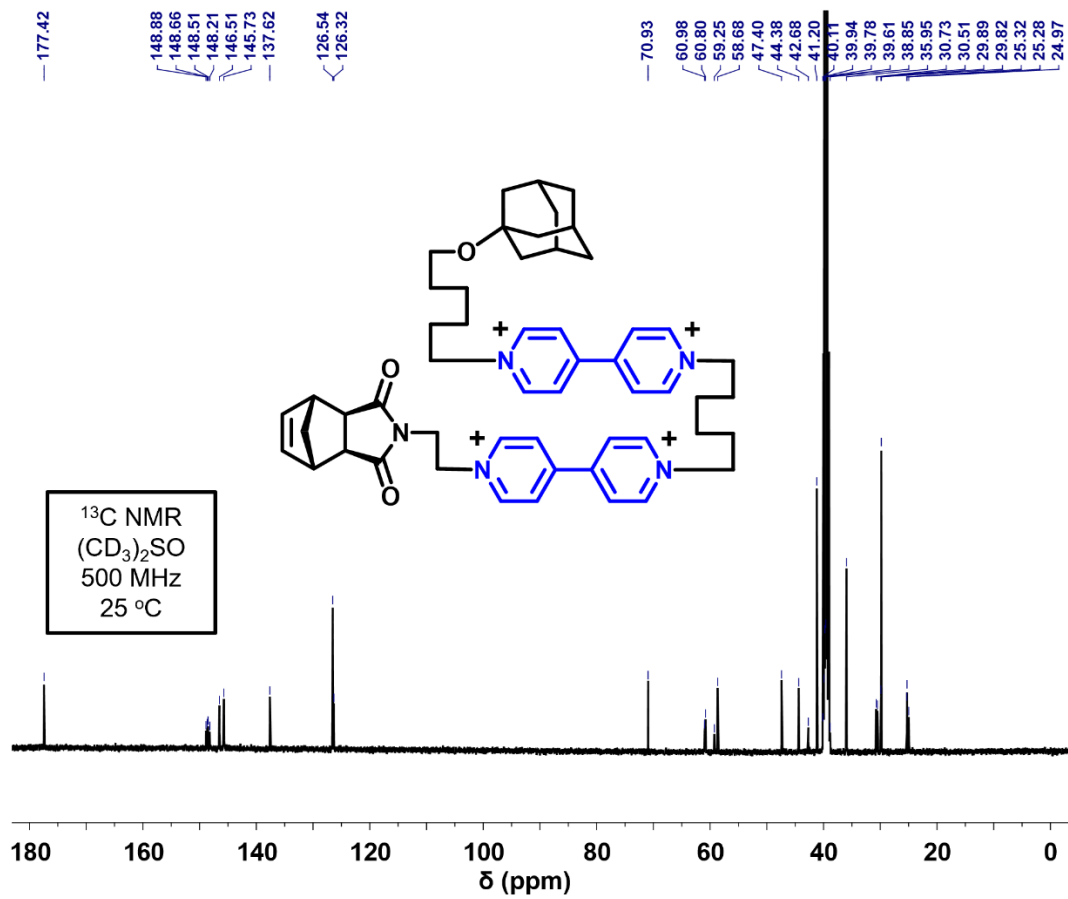
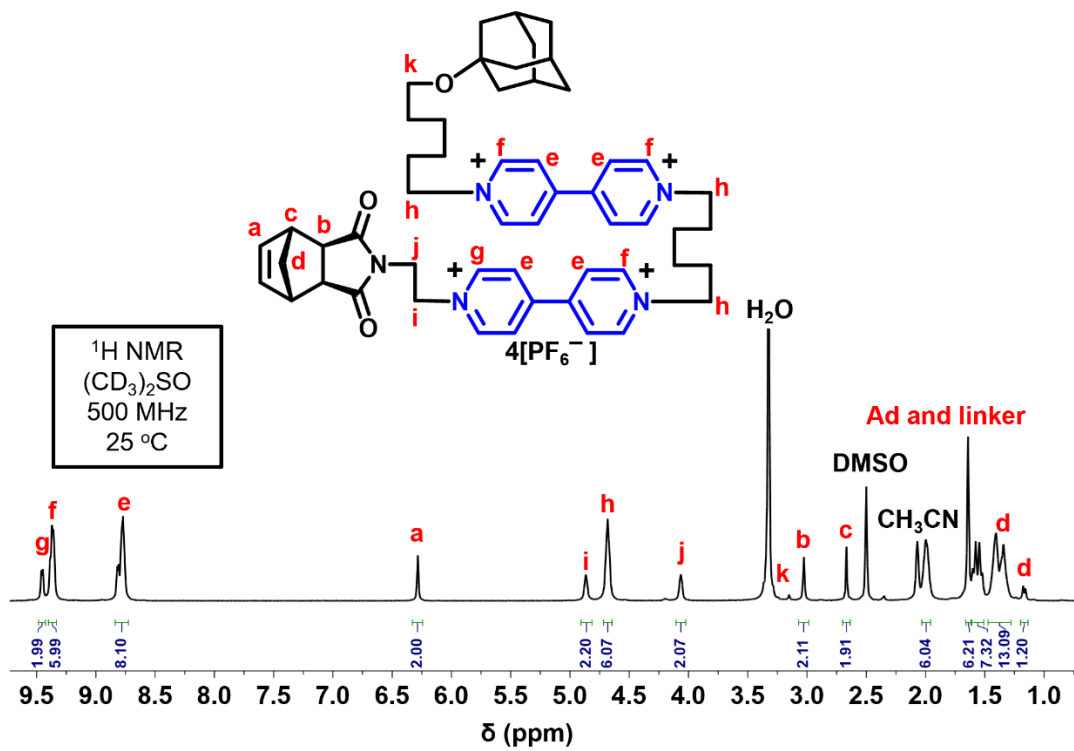
## **Appendix: NMR Spectra of Compound**

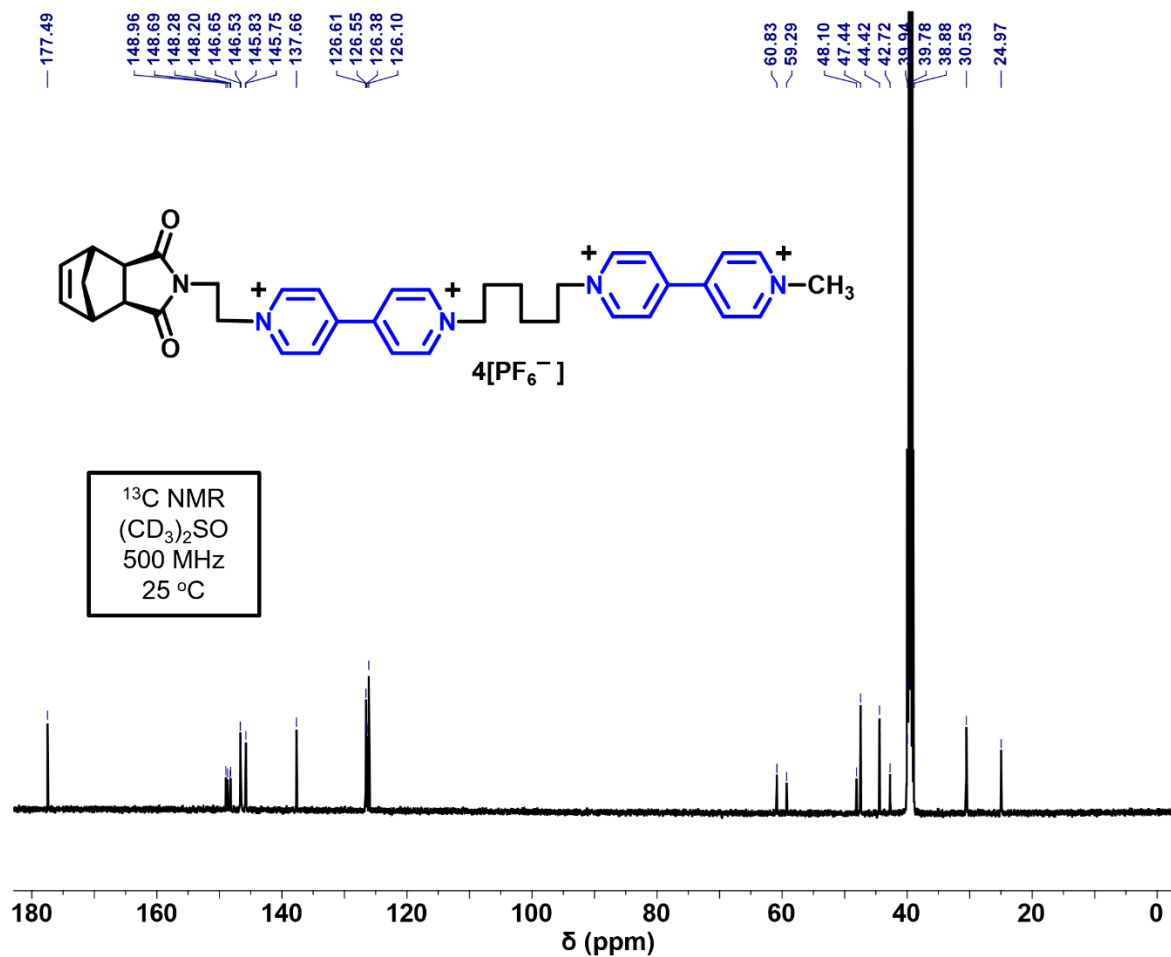
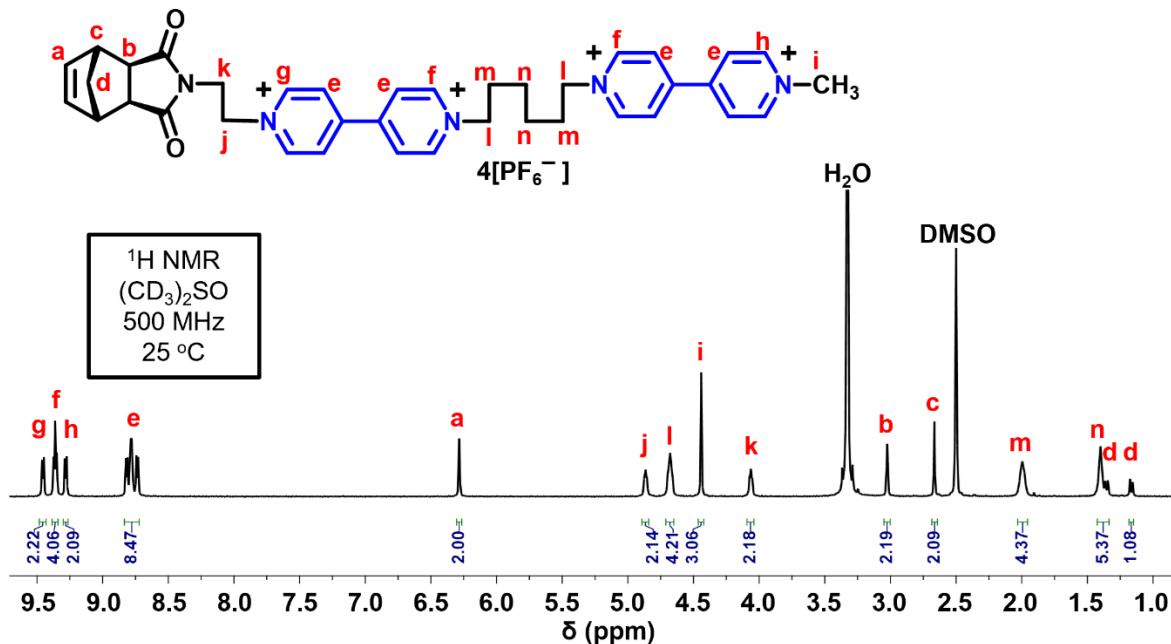
## Chapter 2:



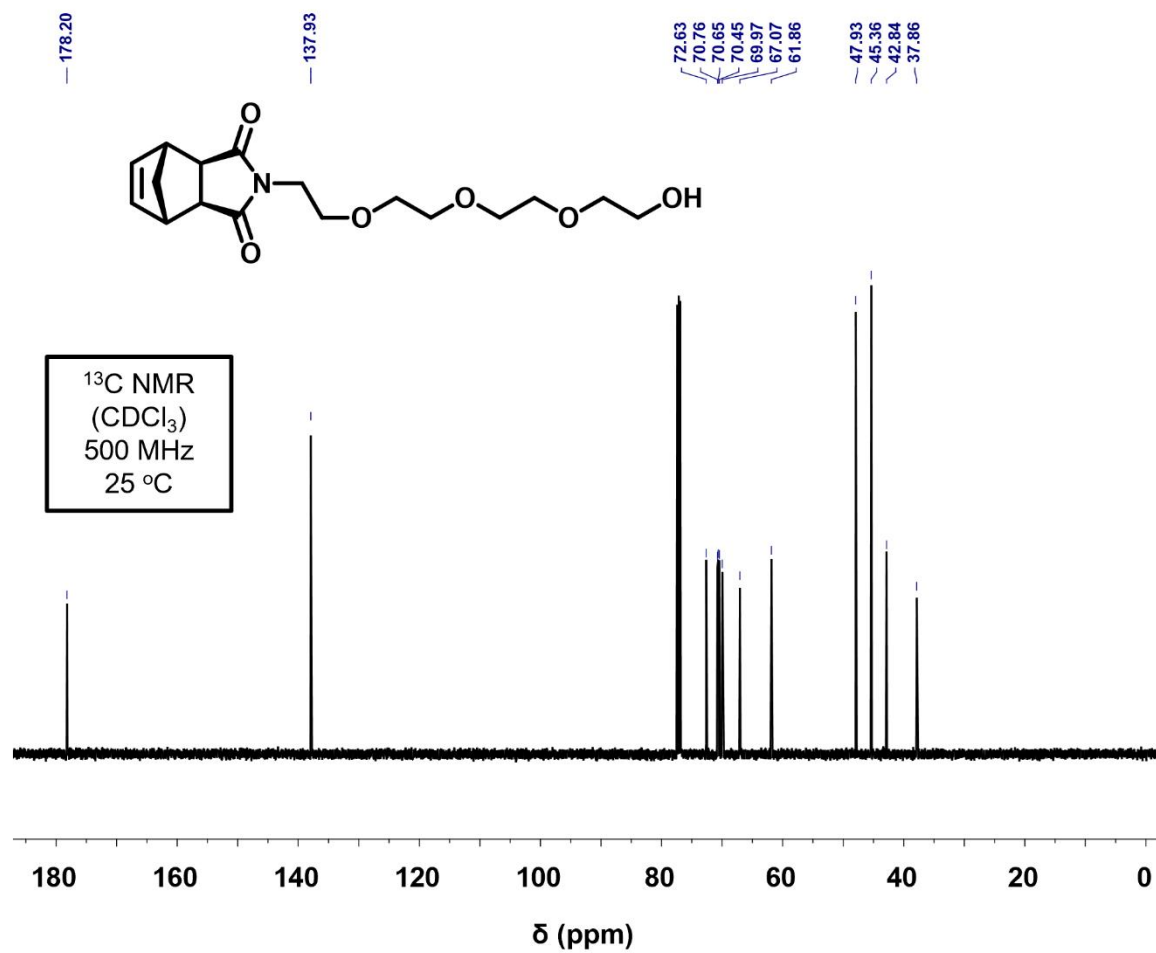
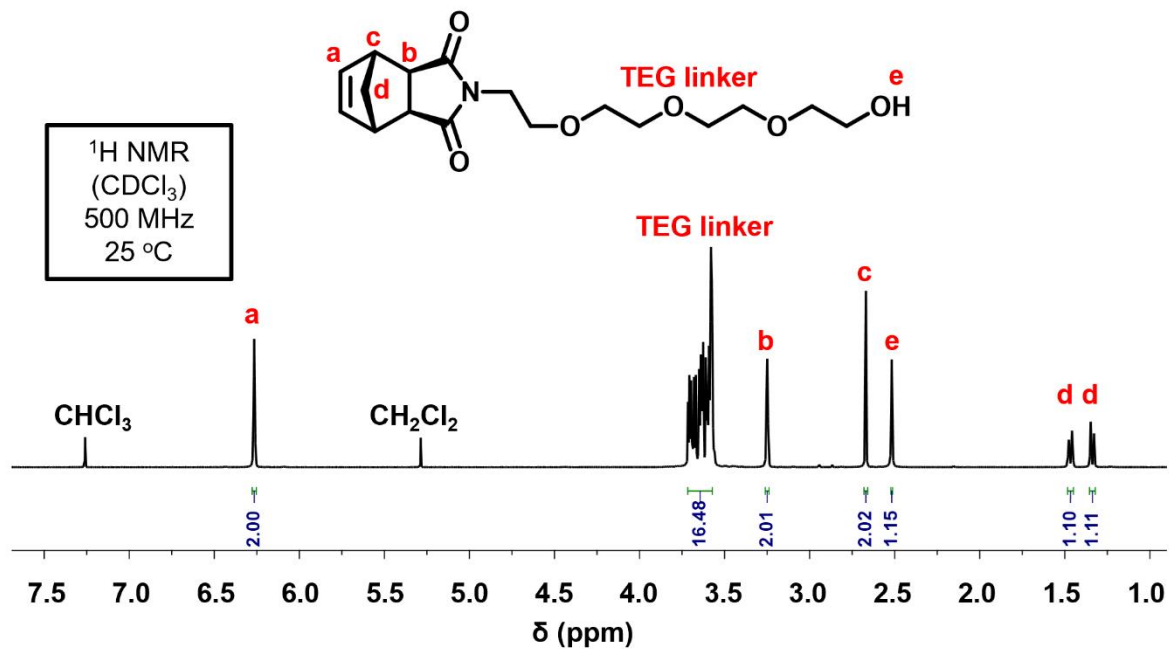


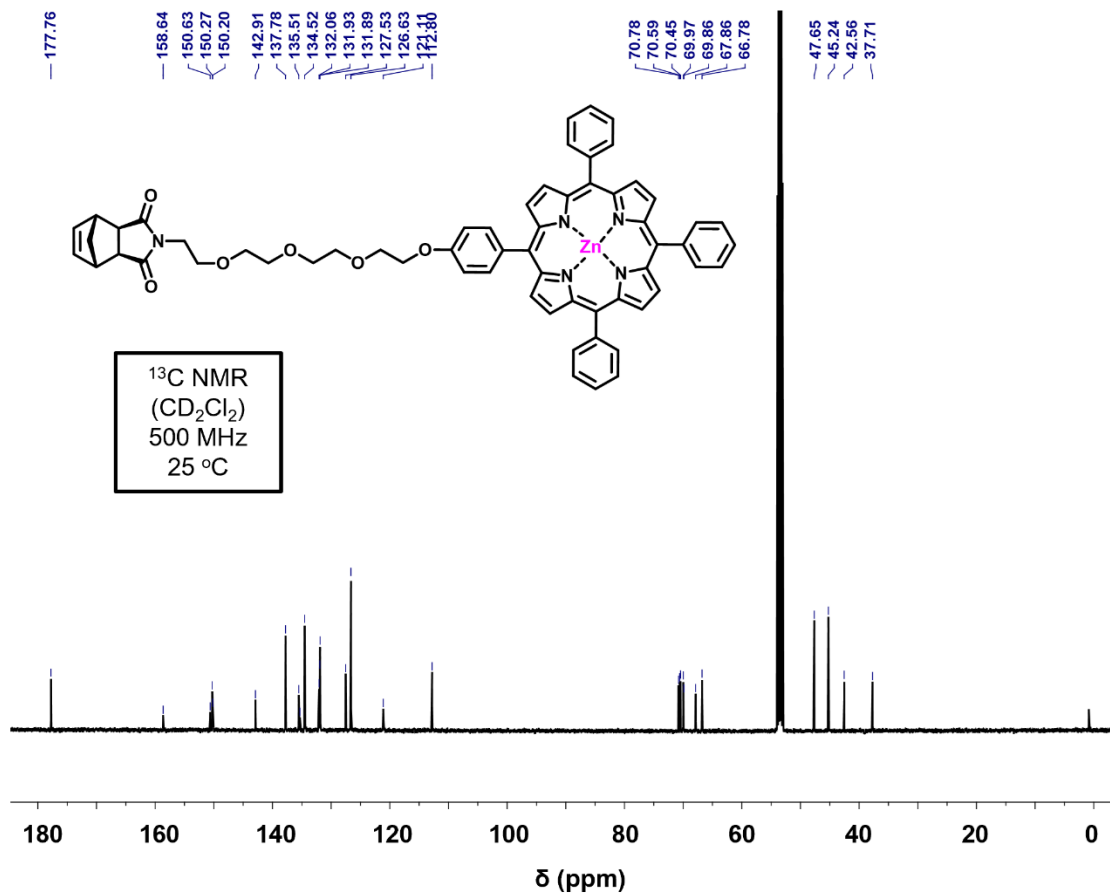
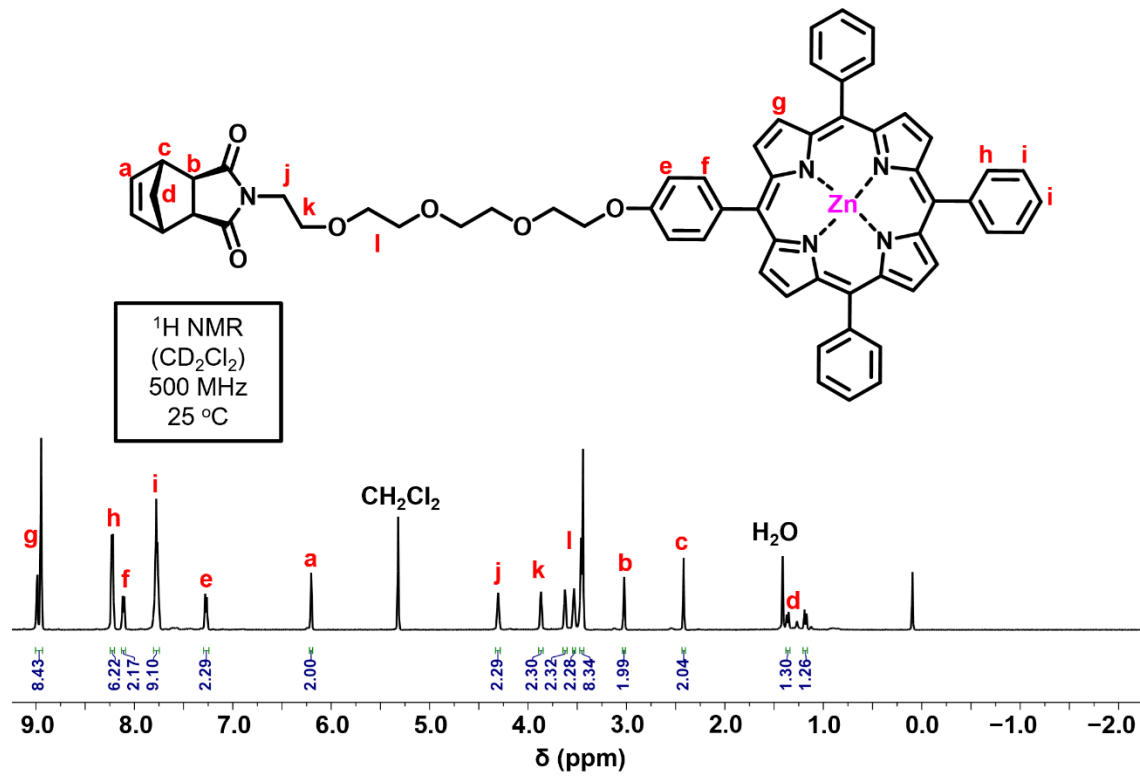


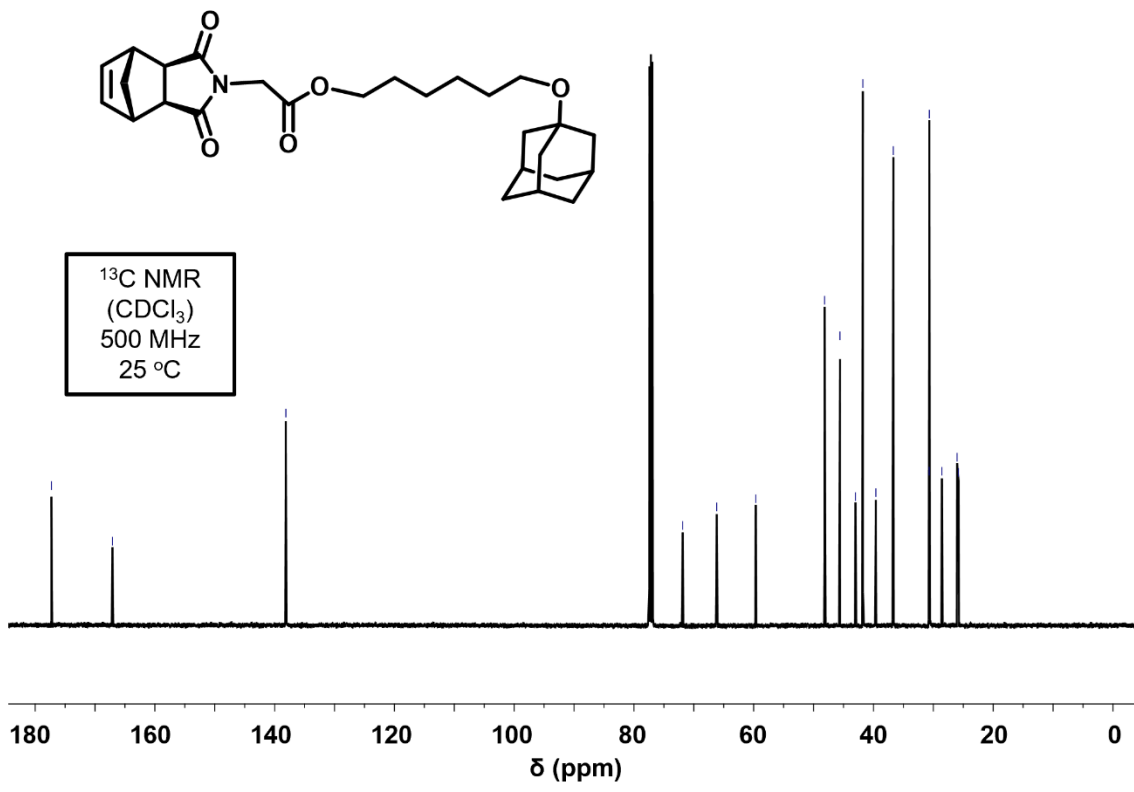
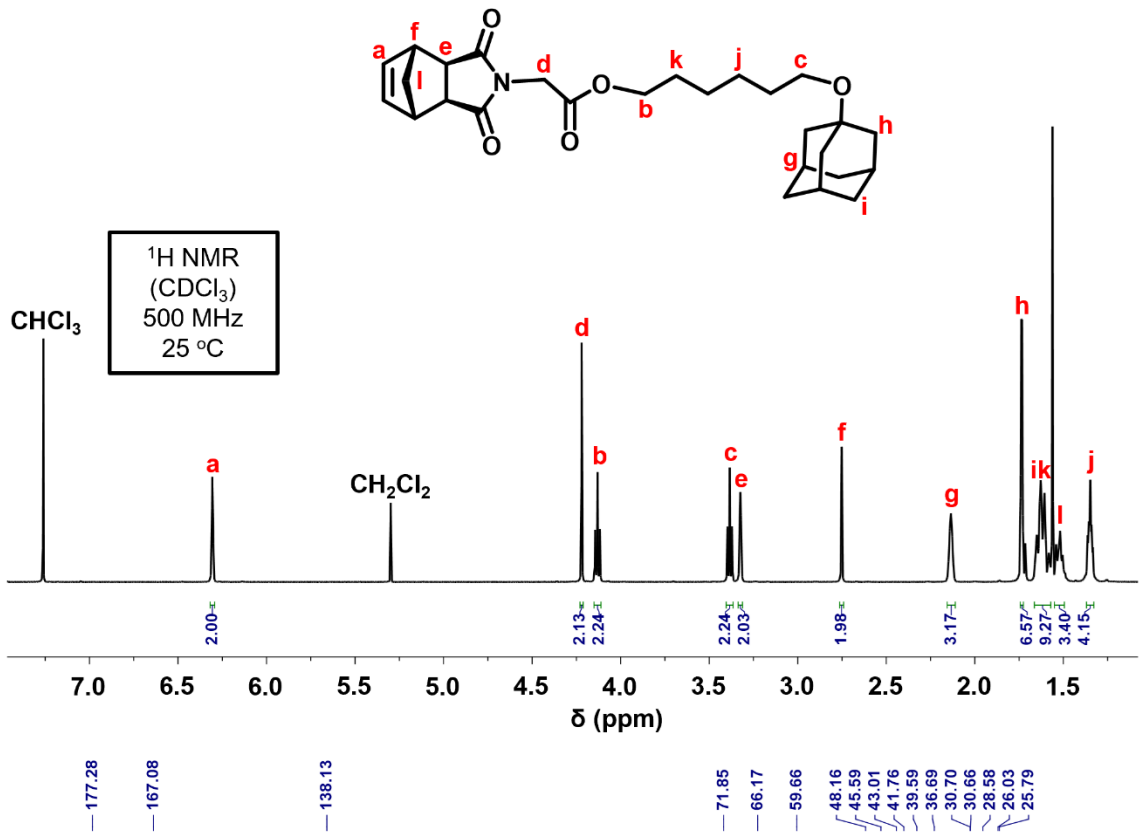


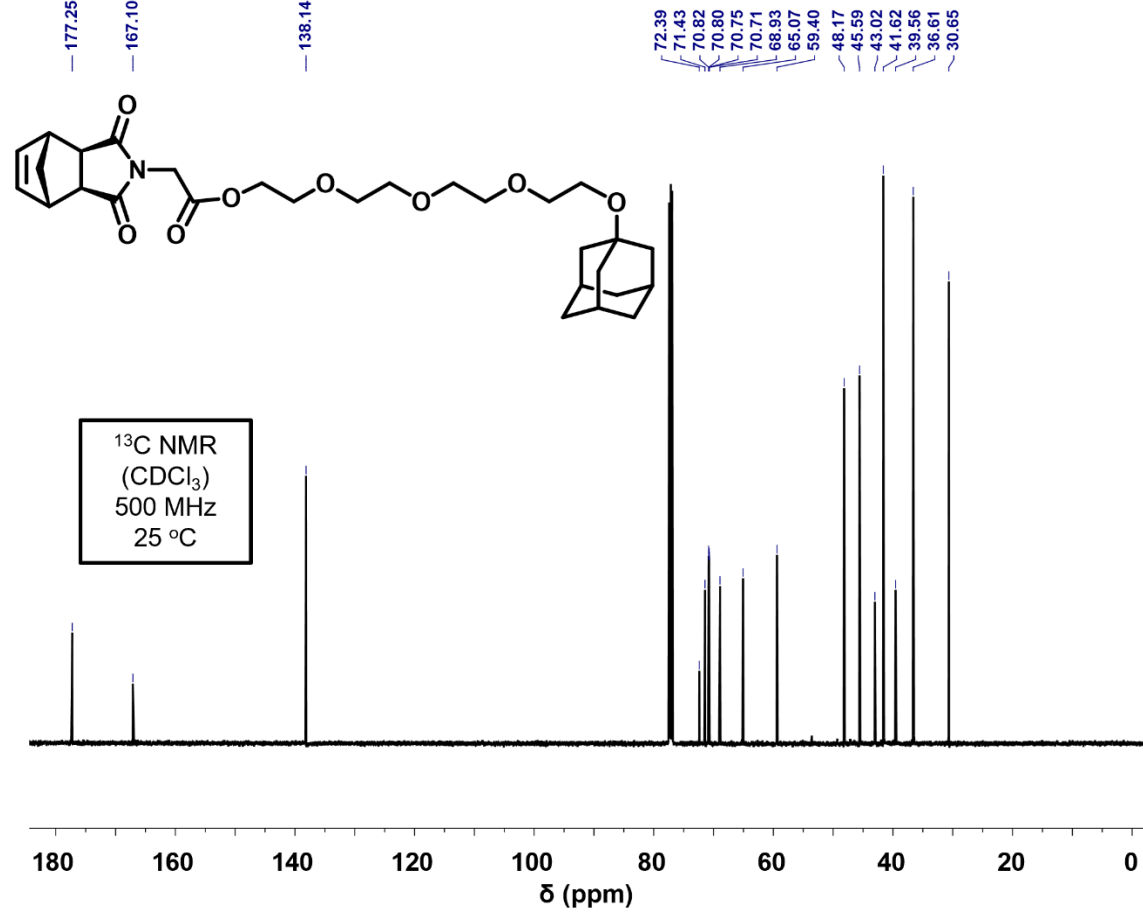
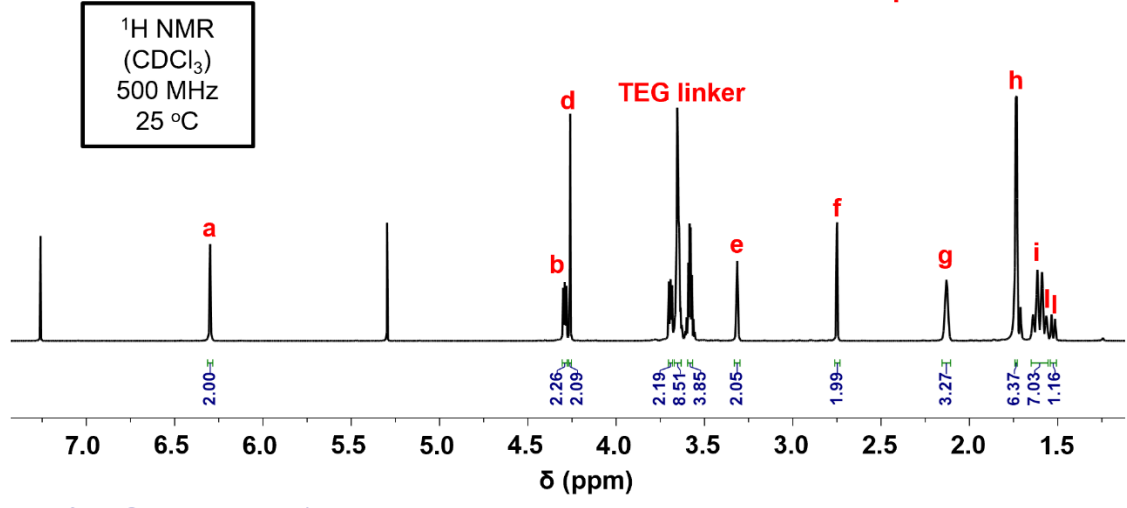
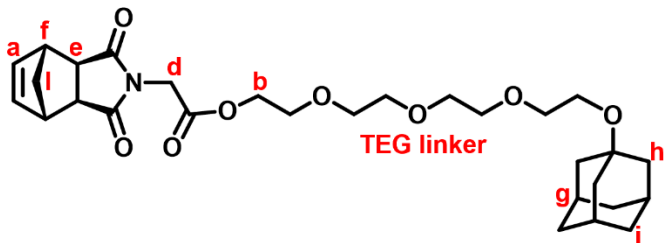












# Chapter 4:

